A SIMS And TEM Study Of Buried Oxide Layers In Silicon

A thesis submitted for the Degree of Doctor of Philosophy at the University of London

by

Christopher James Griffin

Department of Materials
The Royal School Of Mines
Imperial College of Science, Technology and Medicine
London SW7 2BP

April 1989

To my Mother and Father

"They are ill discoverers that think there is no land, when they can see nothing but sea."

"The knowledge of man is as the waters, some descending from above, and some springing from beneath, the one informed by the light of nature, the other inspired by divine revelation."

"If a man will begin with certainties, he shall end in doubts; but if he will be content to begin with doubts, he shall end in certainties."

Francis Bacon
Advancement of Learning
(vii.5, v.1, v.8)

Abstract

The formation mechanisms of buried silicon dioxide layers, made by high-dose, high-energy (150keV) oxygen ion implantation into silicon, have been studied using Secondary Ion Mass Spectroscopy (SIMS) and Transmission Electron Microscopy (TEM). The material was studied both in the as-implanted state and after annealing at 1300°C.

A mechanism has been proposed for the formation of the oxide layers as well as for the evolution of dislocations and other stable damage structures which exist after annealing. Further to this, the dislocations have been characterised in terms of their Burgers vectors, and stacking faults (extended dislocations) have been observed.

Since the SIMS analysis of high concentrations of oxygen in silicon is difficult to calibrate due to the enhancement of the secondary ion yields, a model has been put forward to simulate high dose implants. This has enabled the yield enhancement to be quantified so the actual oxygen concentrations can be derived directly from the experimental SIMS data. A phenomenological model for the enhancement mechanism is also postulated.

Finally, the effect of implantation temperature on the final microstructure has been studied for very high oxygen doses ($\approx 1.6 \times 10^{18} O^+/cm^2$). Although the defect levels in the material did not seem to be affected, some subtle changes were observed in and around the buried oxide layer in material annealed at 1300°C for 2 or 5 hours.

Background

Since the invention of the bipolar transistor by Bardeen and Brittain of the Bell Laboratories in 1948, there has been a rapid growth in the capability of solid state electronic devices. Over about the first ten years of development, great advancements were made in the technology required to produce the new electronic devices at low cost, and in the late 1950's it was possible to produce reliable integrated circuits with a small number of transistors fabricated in the same piece of material. While the bipolar transistor formed the basis of the early integrated circuits, and indeed many families of logic were produced using such devices, the complicated fabrication process and the relatively high power dissipation of the individual transistors produced severe limitations on the complexity of the circuits that could be produced.

To overcome these problems, the manufacture of the conceptually simpler Metal–Oxide–Semiconductor (MOS) device was developed in the mid 1960's, and it is this technology that has resulted in the production of today's highly complex microcomputer and large capacity memory circuits. However, as the sizes of discrete devices have decreased, it has become more difficult to achieve increased device performance by improved design or manufacturing processes. The limitations of the semiconducting materials now have an almost overriding importance on device performance.

At one time, gallium arsenide (and other compound semiconductors) were viewed as an alternative to silicon because, for example, their inherent carrier mobilities were higher, but the extra expense and the fact that silicon technology was so well–established meant that other than for certain specialised applications, silicon remained in a dominant position within the electronics industry

This thesis reports on the evolution of silicon–on–insulator structures for integrated circuit substrates. It is a good example of how materials science has been applied to allow processing of the silicon substrates to occur, prior to device fabrication, to give much improved device performance. The first chapter introduces semiconductors and SOI technology in general. The Literature Survey which follows gives a detailed background to the materials science of oxygen in silicon and how ion implantation and annealing can be used to produce good quality substrates, ultimately reflected in enhanced electronic device performance. Finally, the Results, Discussion and Conclusions sections explain how and why the buried oxides form from a materials science point of view. Hopefully this increased understanding will eventually enable better substrates and devices to be manufactured.

CONTENTS

Abstract		4
Background		5
Contents		6
List of Tables		10
List of Figures		11
List of Plates		16

Chapter 1

INTRODUCTION

1.1	Extrinsic Semiconductivity	20
1.2	MOSFETs	22
1.2.1	Band Bending And Inversion	22
1.2.2	PMOS	23
1.2.3	NMOS	25
1.2.4	Complementary MOS Technology	25
1.3	Silicon-On-Insulator	28
1.3.1	MOSFETs On Insulating Substrates	28
1.3.2	Current SOI Technologies	29
1.3.2.1	Silicon-On-Sapphire	29
1.3.2.2	Recrystallised Polysilicon	31
1.3.2.3	Full Isolation By Porous Oxidised Silicon	36
1.3.2.4	Separation By Implanted Oxygen	39
1.4	References for Chapter 1.	40

Chapter 2

LITERATURE SURVEY

2.1	The Nature Of Oxygen In Silicon	44
2.1.1	Oxide Precipitation And Growth	44
2.1.2	Thermodynamics Of The Silicon/Oxygen System	47
2.1.3	Oxygen-Induced Lattice defects	49
2.2	Manufacture Of SIMOX 1: Ion Implantation	51
2.2.1	Ion Ranges	52
2.2.2	Lattice Damage	57
2.2.3	Practical Ion Implantation	57
2.2.4	Oxygen Ion Implantation Into Silicon	60
2.2.4.1	Low Dose ($<10^{15}$ O^+/cm^2)	60
2.2.4.2	Medium Dose (10^{15}-10^{16} O^+/cm^2)	60
2.2.5	High Dose Implantation ($>10^{17}$ O^+/cm^2)	62
2.2.5.1	Oxygen Distribution/Redistribution	63
2.2.5.2	Microstructure 1: Oxide Precipitates	65
2.2.5.3	Microstructure 2: Crystallographic Defects	68
2.3	Manufacture Of SIMOX 2: Annealing	73
2.3.1	Low Dose	74
2.3.2	Annealing At 1150°C	75
2.3.3	High Temperature Annealing	76
2.3.4	Low Dislocation SIMOX	78
2.4	Electrical Characteristics	79
2.4.1	Subthreshold Characteristics	80
2.4.2	The Kink Effect	81
2.4.3	Oxygen-Related Donors	83
2.5	Non-Destructive Analysis	84
2.5.1	Photoluminescence	84
2.6	References for Chapter 2	88

Chapter 3

EXPERIMENTAL PROCEDURE

3.1	Oxygen Ion Implantation	97
3.2	High Temperature Annealing	97
3.3	Transmission Electron Microscopy	99
3.3.1	Cross Sectional TEM	99
3.3.2	Plan View TEM	101
3.3.3	TEM Observation	101
3.4	Secondary Ion Mass Spectrometry	102
3.4.1	The Ion Source	102
3.4.2	The Analysis Chamber	104
3.4.3	The Mass Spectrometer	104
3.5	Specimen Details	105
3.5.1	Incremental Doses	105
3.5.2	Defect and Impurity Analysis: SPIRE Wafers	106
3.5.3	Implantation Temperature Variation	107
3.6	References for Chapter 3	108

Chapter 4

RESULTS AND DISCUSSION

4.1	Calibration of High Dose Oxygen Implants	109
4.1.1	Introduction	109
4.1.2	Procedure	113
4.1.3	Quantification and Calibration	120
4.1.4	Cross-Sectional TEM	131
4.1.5	Discussion	131

4.2	The Evolution Of Buried Oxide Structures And Overlayer Threading Dislocations	137
4.2.1	SIMS Analysis	137
4.2.2	Cross-Sectional TEM	142
4.2.2.1	Low Doses: 0.1 to 0.25 x $10^{18}O^+/cm^2$	142
4.2.2.2	Medium Doses: 0.3 to 0.4 x $10^{18}O^+/cm^2$	145
4.2.2.3	High Doses: $\geq$0.45 x $10^{18}O^+/cm^2$	145
4.2.3	Discussion	147
4.3	Defect and Impurity Analysis: SPIRE Wafers	151
4.3.1	Dislocation Characterisation	151
4.3.2	Nitrogen Contamination	157
4.3.3	Dislocation Density	162
4.4	Implantation Temperature Variation	164
4.5	References for Chapter 4	171

Chapter 5

CONCLUSIONS

5.1	Calibration Of High Levels Of Oxygen In Silicon	173
5.2	Growth Mechanisms Of Buried Oxide Layers And Overlayer Threading Dislocations	173
5.3	Dislocation Characterisation	174
5.4	Nitrogen Contamination	174
5.5	Dislocation Density	175
5.6	Implantation Temperature Variation	175
5.7	Suggestions For Future Work	176
Acknowledgements		178

LIST OF TABLES

Chapter 2

Table 2.1
Characteristics of as-implanted SIMOX.

Chapter 3

Table 3.1
Table showing the wafer number and the total oxygen dose.

Table 3.2
Table showing the implantation and annealing treatments received by the "SPIRE" wafers.

Table 3.3
Table showing the implantation conditions of the high-dose wafers from the University of Surrey.

Chapter 4

Table 4.1
The measured peak shift from the experimental data.

Table 4.2
The simulated total swelling compared to previous experimental data

Table 4.3
Values of the constants in equation 4-6.

Table 4.4
Values of k' in equation 4-7b with standard deviations.

Table 4.5
Dislocation densities of the SPIRE wafers

Table 4.6
Overlayer and oxide thicknesses

LIST OF FIGURES

Chapter 1

Fig. 1.1
Intrinsic carrier concentration vs temperature in silicon

Fig. 1.2
Modified energy band structures of n- and p-type silicon

Fig. 1.3
Cross-section through a typical (p-channel) MOSFET

Fig. 1.4
Band bending and inversion at a positively charged silicon surface (n-channel MOSFET inset)

Fig. 1.5
Charge distribution in a p-channel enhancement-mode transistor

Fig. 1.6
Charge distribution in an n-channel depletion-mode transistor

Fig. 1.7
CMOS inverter: a) circuit, b) device cross-section

Fig. 1.8
Parasitic transistors: a) plan view, b) device cross-section

Fig. 1.9
Basic SOI CMOS device

Fig. 1.10
Bulk silicon CMOS inverter cross-section

Fig. 1.11
CMOS/SOS inverter cross-section

Fig. 1.12
Schematic showing implanting and annealing of SOS

Fig. 1.13

Typical starting substrate for "Recrystallised Polysilicon" SOI

Fig. 1.14

FIPOS process steps: a) selective p^+ layer formation, b) proton implantation, c) anodisation, and d) oxidation.

Chapter 2

Fig. 2.1

Position of an isolated oxygen atom in a [1 1 1] interstitial configuration

Fig. 2.2a

Oxygen solubility in silicon

Fig. 2.2b

Variation of the free energy of the Si–O system: a) oxygen solid solution, b) oxide precipitates.

Fig. 2.3

Schematic of typical ion implanter

Fig. 2.4

a) a "tree" of disorder for a typical implanted ion, and b) schematic of the range, R, projected range, R_p, uncertainty in R_p or straggle ΔR_p, and the lateral straggle $\Delta R_\perp$.

Fig 2.5

As-implanted depth profile of oxygen in silicon

Fig. 2.6

ZBL range diagram of oxygen in silicon

Fig. 2.7

Comparison of measured and theoretical ion and damage distributions

Fig. 2.8

SIMS profiles of as-implanted SIMOX: a) T_i=400°C, b) T_i=600°C.

Fig. 2.9

SIMS oxygen depth profile of 210keV 18–O implanted into a pre–formed 200keV 16–O buried oxide.

Fig. 2.10

Thicknesses of silicon and buried oxide layers as a function of dose

Fig. 2.11

Schematic microstructure of as–implanted SIMOX as a function of T_i, with Auger oxygen profiles

Fig. 2.12

Current–voltage characteristic of a SIMOX MOSFET showing kinks (arrowed)

Fig. 2.13

Carrier concentration and Hall mobility as a function of annealing temperature

Fig. 2.14

Photoluminescence spectra of SIMOX wafers annealed for 2 hours at 1150 (——— upper), 1200 (------), 1250 (——— lower) and 1275°C (— — —).

Chapter 3

Fig. 3.1

Diagram of wafer holder in the University of Surrey Implanter

Fig. 3.2

a) front and plan views of TEM cross–section ready to be mechanically thinned,

b) plan view of TEM cross–section mounted on grid.

Fig. 3.3

Schematic cross–section of the gas ion gun used to obtain a xenon primary beam.

Chapter 4

Fig. 4.1

a) Raw data from wafer 1

b) Raw data from wafer 7

Fig. 4.2

Calibrated profile for wafer 1

Fig. 4.3

Experimental intensity ratios as the dose increases from 0.1E18 to 0.55E18/sq.cm. Note the shift in peak depth.

Fig. 4.4

Wafer2: area used for swelling calculation

Fig. 4.5

Comparison of experimental and simulated data

Fig. 4.6

Comparison of experimental and simulated data near the onset of continuous buried layer formation

Fig. 4.7

Enhancement factor as a function of simulated oxygen concentration

Fig. 4.8

Enhancement factor as a function of measured intensity ratio

Fig. 4.9

Deconvoluted SIMS data showing real oxygen concentrations

Fig. 4.10

Plot to find the constants in equation 4-8. Data from wafers 9(·), 12(•) and 14(x).

Fig. 4.11

Plot to find the constants in equation 4-9. Data from wafers 9(·), 12(•) and 14(x).

Fig. 4.12

a) Calibrated profile for wafer 6 (dose = 0.45E18/sq.cm)

b) Measured and predicted O^- secondary ion intensities from the distribution shown above in Fig. 4.12a

Fig. 4.13

Calibrated profile for annealed wafer 1

Fig. 4.14

Calibrated profile for annealed wafer 3

Fig 4.15

Calibrated profile for annealed wafer 4

Fig. 4.16

a) calibrated profile for wafer 6 (no anneal)

b) calibrated profile for wafer 6 (annealed)

Fig. 4.17

Calibrated profile for wafer 7 (annealed)

Fig. 4.18

Calibrated profile for wafer 8 (annealed)

Fig 4.19

a) Nitrogen SIMS profiles of wafers SP10B and SP10C

b) Nitrogen SIMS profiles of wafers SP13B and SP13C

Fig. 4.20

Plot of Ln (nitrogen concentration) vs $(\text{distance})^2$ to determine the diffusion coefficient of nitrogen in buried oxides.

Fig. 4.21

SIMS profile of unannealed wafer implanted at 480°C.

Fig. 4.22

SIMS profile of wafer implanted at 540°C through a 70nm screening oxide and annealed for 5 hours at 1300°C.

List of Plates

Chapter 4

Plate 4.1

Cross-sectional TEM of (unannealed) wafer 2 (0.2 x $10^{18}O^+/cm^2$).

a) with SIMS overlay and showing near-surface damage region (D), defect-free silicon layer (M1) and two-phase microstructure of Si and SiO_2 (M2),

b) clearer view of regions M1 and M2.

Plate 4.2

Cross-sectional TEM of (unannealed) wafer 6 (0.45 x $10^{18}O^+/cm^2$).

a) showing regions D, M1 and M2 and a stacking fault (SF).

b) clearer view of stacking faults.

Plate 4.3

Cross-section of wafer 1 (0.1 x $10^{18}O^+/cm^2$), annealed at 1300°C for 5 hours showing faceted SiO_2 precipitates (p) and dislocations (d).

Plate 4.4

Cross-section of wafer 3 (0.25 x $10^{18}O^+/cm^2$), annealed at 1300°C for 5 hours showing how the oxide precipitates, mainly in one layer, have started to elongate.

Plate 4.5

Cross-section of wafer 3 (0.25 x $10^{18}O^+/cm^2$), annealed at 1300°C for 5 hours. This high-magnification image shows large precipitates in the lower layer and a smaller precipitate in the upper layer, all connected by dislocations (e.g. d). The dislocation double-images are due to multi-beam diffraction conditions.

Plate 4.6

Cross-section of wafer 5 (0.4 x $10^{18}O^+/cm^2$), annealed at 1300°C for 5 hours showing the discontinuous oxide network (white) and the holes in it. The layer almost constitutes a continuous buried oxide.

Plate 4.7

Cross-section of wafer 8 (0.65 x $10^{18}O^{+}/cm^{2}$), annealed at 1300°C for 5 hours showing a deep silicon protrusion into the buried oxide layer.

Plate 4.8

Cross-section of wafer 7 (0.55 x $10^{18}O^{+}/cm^{2}$), annealed at 1300°C for 5 hours. The upper interface (U) is very wavy compared to the lower one (L). Silicon inclusions (I) can be seen within the buried oxide, some of them twinned (T).

Plate 4.9

Cross-section of wafer 7 (0.55 x $10^{18}O^{+}/cm^{2}$), annealed at 1300°C for 5 hours showing a very distinct twin (T) growing upwards from the upper interface in one of the silicon isthmuses.

Plate 4.10

High-magnification cross-section of wafer 7 (0.55 x $10^{18}O^{+}/cm^{2}$) showing a wavy upper interface (U), a planar lower interface (L) and twinned silicon inclusions (T). A small stacking fault (SF) can be seen on one of the more planar areas of the upper interface.

Plate 4.11

Plan view TEM micrographs from wafer 10B, at different specimen orientations.

a) $(1\,1\,\bar{1})$ BF image showing five dislocations (A to E).
b) $(1\,1\,\bar{1})$ WB image showing clearer images of the dislocations A to E.
c) $(0\,\bar{2}\,2)$ BF showing the same dislocations.
d) $(0\,\bar{2}\,2)$ WB image
e) $(1\,\bar{1}\,\bar{1})$ WB image - dislocations A to E are no longer visible.
f) $(0\,\bar{4}\,0)$ WB image - again the dislocations A to E are invisible.

Plate 4.12

WB image using the $(1\,1\,\bar{1})$ planes, showing dislocation types 1 ($a/2\langle 1\,0\,1\rangle$) and 2 ($a/2\langle 1\,1\,0\rangle$). It has not been possible to characterise all of the others.

Plate 4.13

Micrographs to show the dissociation of two unit dislocations into partial dislocations, separated by a stacking fault.

a) BF image ([0 1 1] beam direction) of a complex dislocation structure, D.
b) (1 1 $\bar{1}$) WB image of D, now seen to comprise of dislocations (d_1, d_2, a and b) and stacking faults (SF).
c) (1 $\bar{1}$ 1) WB image of D showing the same features.
d) ($\bar{3}$ $\bar{1}$ 1) WB image showing no stacking fault contrast. Three very faint lines can be seen corresponding to partial dislocations with a separation of ≈15nm.

Plate 4.14

TEM images of widely-spaced dissociated dislocations.

a) (1 1 $\bar{1}$) WB image showing image of defect, D.
b) (1 $\bar{1}$ $\bar{1}$) WB image of the same structure showing stacking fault contrast in one of the dislocations.
c) ($\bar{1}$ 1 1) WB image showing a shift in the stacking fault contrast from one dislocation to the other.
d) (0 0 4) WB image showing triangular stacking faults formed at the dislocation nodes (SF1) and stacking faults along parts of dislocation lines (SF2).

Plate 4.15

Cross-sectional TEM of silicon implanted with oxygen to a dose of 1.6 x $10^{18}O^+/cm^2$ at 480°C (unannealed)

Plate 4.16

Cross-sectional TEM of silicon implanted with oxygen to a dose of 1.6 x $10^{18}O^+/cm^2$ at 540°C (unannealed)

Plate 4.17

Cross-sectional TEM of silicon implanted with oxygen to a dose of 1.6 x $10^{18}O^+/cm^2$ at 540°C through a 70nm screening oxide (unannealed)

Plate 4.18

High magnification image of the upper Si/SiO_2 interface for the 480°C specimen.

Plate 4.19

Microstructure of the 480°C wafer annealed for 5 hours at 1300°C showing a threading dislocation (d) and two rows of silicon inclusions (A and B) within the buried oxide.

Plate 4.20

TEM of 540°C wafer annealed for 5 hours at 1300°C showing a dislocation (d) and a lower layer of silicon inclusions (A).

Plate 4.21

540°C wafer, annealed for 2 hours at 1300°C showing a wavy upper Si/SiO_2 interface.

Plate 4.22

High magnification image of the upper Si/SiO_2 interface in Plate 4.21.

Chapter 1

Introduction

The electrical conductivity, σ, of a semiconductor is given by

$$\sigma = n_e q_e \mu_e + n_h q_h \mu_h \qquad (1-1)$$

where n is the carrier concentration, q is the charge on the carrier and μ the mobility. The subscripts e and h represent electrons and holes respectively.

Since the electron-hole pairs are thermally generated, n, the total charge carrier concentration increases exponentially with temperature [1] (section A of Fig. 1.1) and is therefore proportional to a Boltzmann factor i.e.

$$n = N \exp(-E_g / kT) \qquad (1-2)$$

where N is a constant, E_g the energy (band) gap, k the Boltzmann constant and T is absolute temperature. However at very low temperatures (section B of Fig.1.1) there is some deviation from this law due to electrically active impurities in the silicon single crystal.

1.1 Extrinsic Semiconductivity

Electrically active impurities, if added in small, controlled amounts (e.g. 1 part in 10^8), can dramatically alter the resistivity of silicon. When an arsenic atom, with five electrons in its outermost shell is added to silicon, which has four electrons, four of the As electrons are incorporated in covalent bonds with nearest neighbours. The fifth electron requires only a small amount of energy ($\approx$0.05eV) to be detached and join the conduction band. The presence of the As atom provides energy levels within the forbidden gap just below the conduction band as shown in Fig.1.2a. Such levels are called donor levels and the material is an n-type semiconductor because electric current in it is carried by negative charges (electrons).

If, on the other hand, gallium is incorporated into the silicon lattice, a different effect occurs. Ga atoms have only three electrons in their outermost shells and their presence leaves unoccupied states called holes in the electron structure of the crystal. An electron needs relatively little energy to enter a hole, but as it does so, it leaves

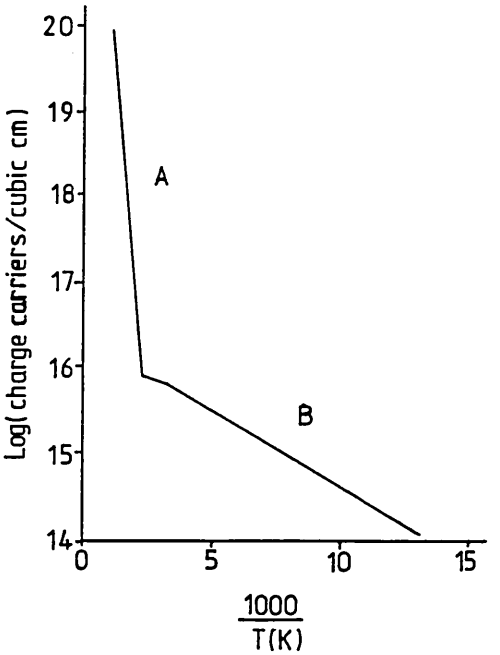


Fig.1.1 carrier concentration vs temperature in silicon [2]

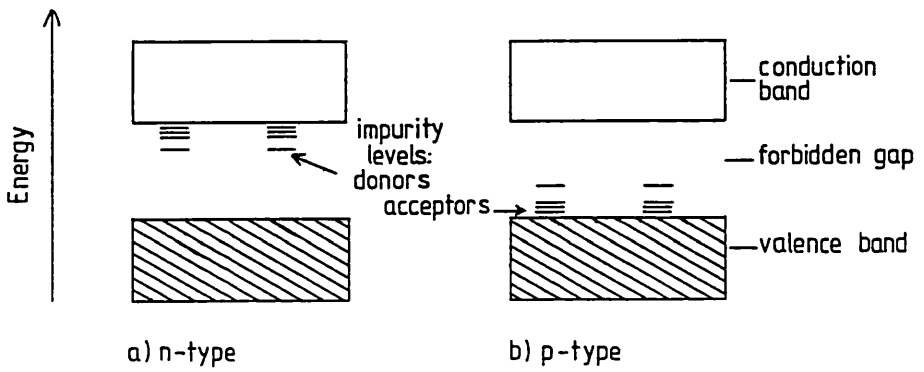


Fig.1.2 Modified energy band structures of n- and p-type silicon

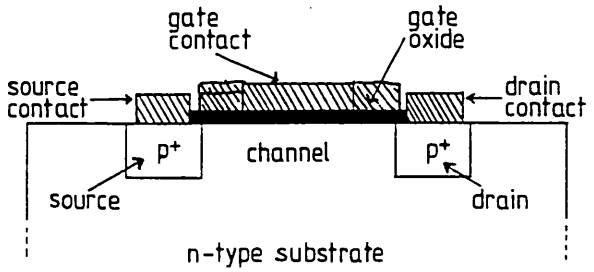


Fig.1.3 Cross-section through a typical (p-channel) MOSFET

a new hole in its former location. When an electric field is applied, electrons move to the anode by successively filling holes i.e. the flow of current can be described by the movement of holes, which act as positive charges. This type of material is called a p-type semiconductor. As shown in Fig. 1.2 b, the Ga atoms provide acceptor levels just above the top of the valence band. Any electrons which occupy these levels leave holes in the valence band which are able to move and conduct electricity.

1.2 MOSFETs [2,3]

Metal-Oxide-Semiconductor Field Effect Transistors (MOSFETs) are used in the production of most of today's complex micro-computer and large capacity memory circuits. The development of MOSFET technology has been responsible for the evolution of Very Large Scale Integrated (VLSI) circuits. The field effect principle of operation was first proposed in the early 1930's, although the first working MOSFET was not demonstrated until 1960 and commercial production was not achieved until the mid 1960's (a more detailed review is given in reference 2).

The structure of a typical MOSFET is shown in Fig. 1.3. The operation of the device involves the flow of current between the source and drain across the "channel" region, the conductivity of which is dramatically influenced by the transverse electric field established by applying a voltage between the source and gate electrodes. The gate-source voltage, V_{gs}, thus has a strong modulating effect on the drain-source current, I_{ds}, and it is this that gives the transistor its amplifying and switching properties. There must be no electrical conduction between the gate and the rest of the device - the interaction between the gate and the channel is purely by a "field-effect" mechanism. This electrical insulation is provided by the gate oxide. Using polysilicon for the gate contact rather than aluminium is a recent modification which gives improved switching speeds and lowered threshold voltages. The transistor shown in Fig. 1.3 is a p-channel (PMOS) device because conduction is due to the flow of holes between source and drain regions made from p-type silicon. Devices of this type were in wide commercial use in the early 1970's and were the basis of the first generation of Large Scale Integrated circuits (LSICs). More recently there has been a change from PMOS to NMOS (n-channel) devices which are inherently faster due to the higher mobility of electrons in silicon.

1.2.1 Band Bending And Inversion

The operation of MOSFETS involves the principle of band bending. When a positive

potential is applied to the gate contact in e.g. an n-channel MOSFET (inset on Fig.1.4), an equal and opposite charge will be induced on the p-type semiconductor surface across the (insulating) gate oxide. The space charge will reside in the negatively charged acceptor centres and any mobile carriers (electrons or holes) near the surface. The electron potential is shown in Fig.1.4. The diagram shows that the negative charge on the semiconductor surface arises not simply from the deficit of holes (repelled by the positive charge on the outer surface) and uncompensated acceptor impurities, but also from electrons attracted to the surface. This has the effect of altering the potential of the electrons and therefore bending the energy bands.

As the charge on the insulator is increased, band bending increases until there is a substantial electron density near the surface and a surface layer of thickness L is effectively "inverted", becoming n-type. Any further increase in charge is then taken up primarily by an increase in free-electron density at the surface since quite a small change in the degree of band bending, once an n-type surface has been achieved, results in a substantial change in electron density. Hence an n-type layer can be induced on a p-type substrate by applying an electric field across an insulating surface coating. If this layer connects two n-type regions, we have the elements of a unipolar transistor - a MOSFET.

1.2.2 PMOS

A PMOS transistor is shown in cross-section in Fig.1.5. It is effectively a 4-terminal device, with the substrate bias affecting device performance and protecting the gate oxide from damage which may be caused by excessive gate voltages. However, for this simplified discussion, assume both the source and substrate to be at ground potential (for a more detailed description see [2]).

An important feature of the device is the layer of fixed positive charge in the gate oxide close to the oxide-semiconductor interface. This charge may be mobile at elevated temperatures or when high field strengths are employed, and is introduced into the oxide during device fabrication as a consequence of contamination by alkali ions (e.g. Na^+) or by the formation of oxygen vacancies in the oxide structure. If the gate-source voltage is zero, the fixed oxide charge will induce compensatory negative charges on the gate electrode and at the silicon surface (Fig.1.5a). The semiconductor surface therefore becomes more n-type than the bulk and conduction is still not possible between the source and drain. If V_{gs} is negative, the structure behaves as a parallel plate capacitor, the metal gate acquiring a negative charge and inducing an equal and opposite charge in the silicon. The case of $|V_{gs}|$ being just

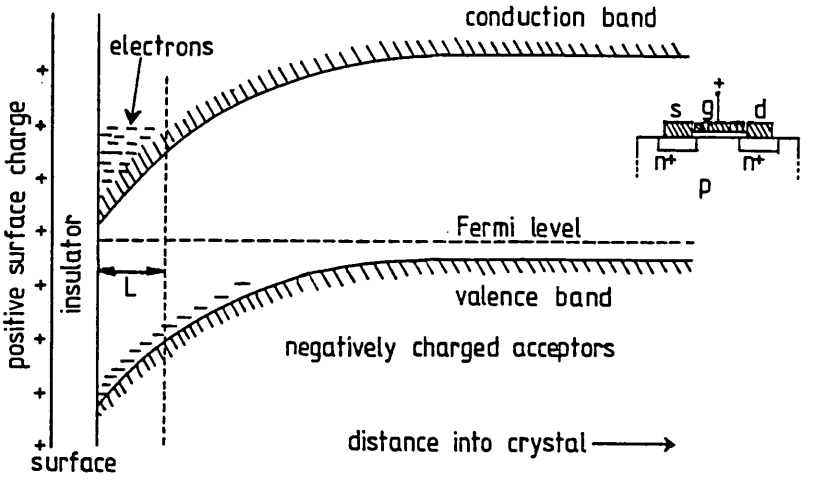


Fig.1.4 Band bending and inversion at a positively charged silicon surface (n-channel MOSFET inset)

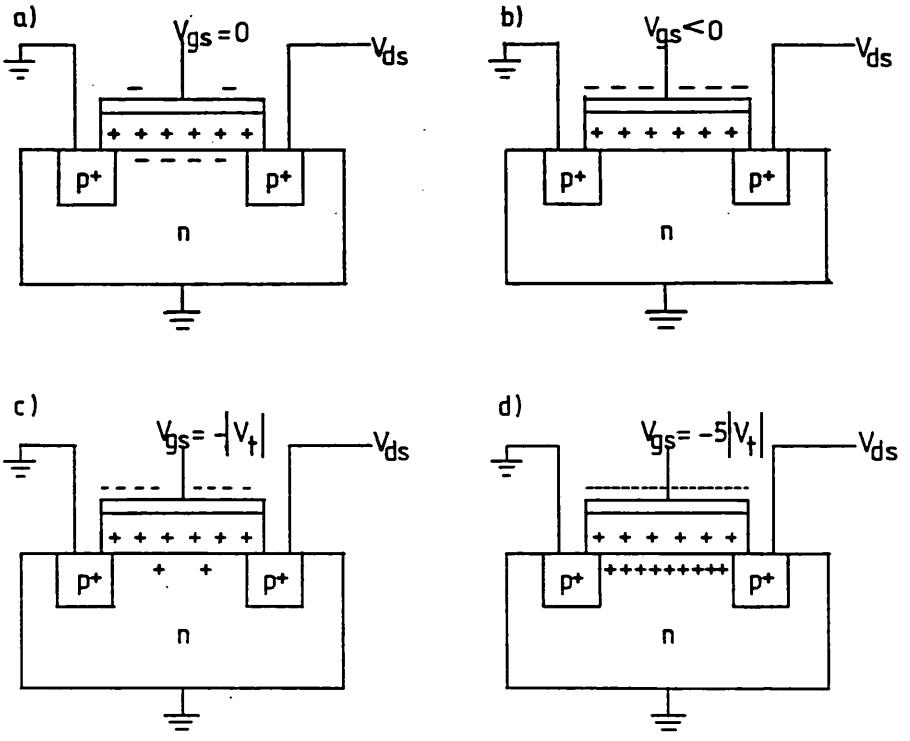


Fig. 1.5 Charge distribution in a p-channel enhancement-mode transistor.

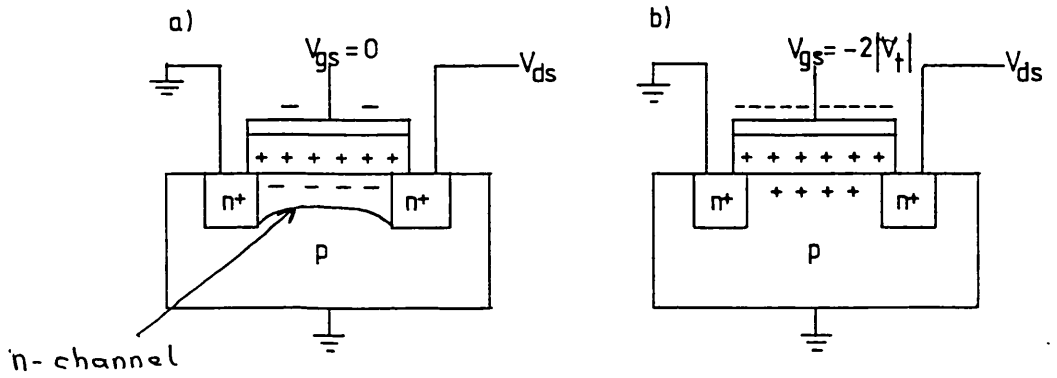


Fig. 1.6 Charge distribution in an n-channel depletion-mode transistor.

large enough to compensate for the fixed positive oxide charge is shown in Fig.1.5b. The silicon surface is now n-type with the same electron concentration as the substrate.

If $|V_{gs}|$ is further increased, positive charge (i.e. holes) is attracted to the silicon surface which takes on p-type character (Fig.1.5c). At this point (the "threshold"), conduction becomes possible between the source and drain via the effectively p-type channel. Further increases in $|V_{gs}|$ cause heavier inversion of the silicon surface (Fig.1.5d), a higher concentration of holes in the channel region and higher source-drain conductivity. This is described as an "enhancement mode" device because the transistor is "off" for zero gate voltage and is turned "on" by the application of a negative gate voltage.

1.2.3 NMOS

An alternative type of device may be fabricated using a p-type silicon substrate with n-type diffused source and drain regions as illustrated in Fig.1.6. All bias voltages and currents are in the opposite sense to those in the PMOS device (Fig.1.5), although the fixed oxide charge is still positive. As a consequence the silicon surface may be n-type (or even n^+) when V_{gs} is zero (Fig.1.6a), allowing conduction to occur. Making V_{gs} negative induces a positive charge in the silicon surface and turns the transistor "off" (Fig.1.6b). This is called a "depletion mode" device because it is "on" when V_{gs} is zero and can only be turned off by the application of a negative gate voltage to deplete the channel region of conduction electrons.

1.2.4 Complementary MOS Technology [2-4]

First introduced in 1963, complementary MOS (CMOS) technology provides both NMOS and PMOS transistors on the same chip. Early CMOS circuits used large substrate areas since the ratio of PMOS to NMOS transistors was 1:1 (the geometrical area of a PMOS transistor should be about three times that for the corresponding NMOS device to equate switching speeds, due to the different mobilities of holes and electrons). Current CMOS designs use more NMOS than PMOS transistors which conserves chip area. The great advantage of CMOS technology is its very low power consumption as explained below.

Fig.1.7a shows a basic CMOS (inverter) circuit with the corresponding device cross-section (Fig.1.7b) showing the p-well which acts as the NMOS transistor's substrate or back gate. The two devices are in series with their drains linked together and also their gates. The logic swing gate voltage, V_i, varies from zero

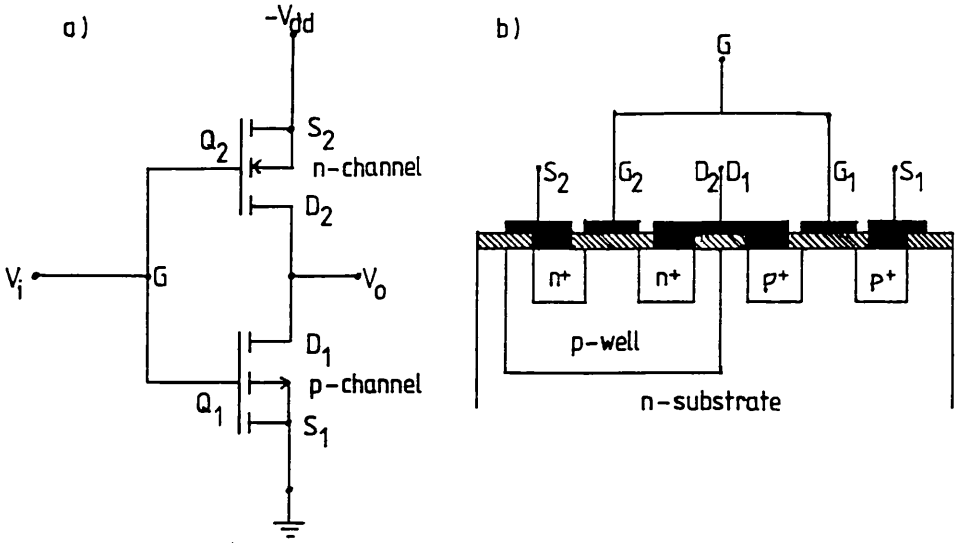


Fig.1.7 CMOS inverter. a) circuit, b) device cross-section.

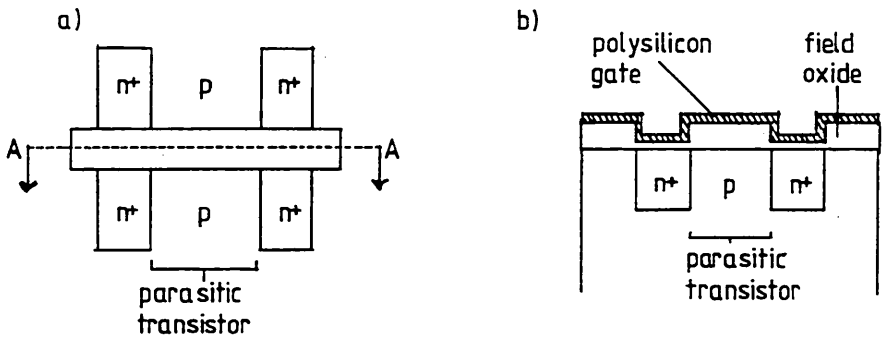


Fig. 1.8 Parasitic transistors. a) plan view, b) device cross-section.

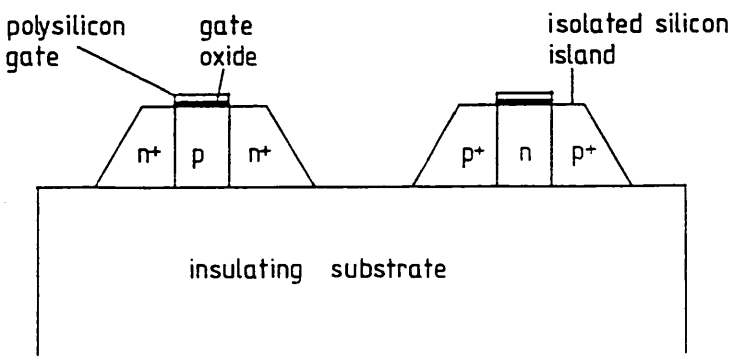


Fig. 1.9 Basic SOI CMOS device.

volts to the supply voltage, $-V_{dd}$. When $V_i = -V_{dd}$ (logic state "1"), transistor Q_1 is turned "on" (but draws no appreciable steady-state current) and Q_2 is turned "off". The output V_0 is then at zero volts (logic state "0") and the signal has been inverted. When zero voltage is applied to the input, the n-channel transistor, Q_2, is turned "on" (no steady-state current) and Q_1 is turned "off". Thus the output is at $-V_{dd}$. In either logic state, Q_1 or Q_2 is "off", meaning the quiescent power dissipation from this simple inverter is the product of the "off" leakage current and $-V_{dd}$, which is very low.

There may, however, be problems with CMOS technology. For example, if two adjacent NMOS transistors are close together on a p-type substrate, this may result in parasitic transistor action or "latch-up". Fig.1.8a shows a plan view of two such NMOS transistors with their channels shielded by the common gate contact. Fig. 1.8b is the corresponding device cross-section across AA. Both show the parasitic bipolar n-p-n transistor. If the parasitic transistor's threshold voltage is too low, an inversion layer can be formed between the induced n^+ regions of the individual transistors and tie them together. Hence the parasitic threshold should be made high enough to avoid the onset of sub-threshold conduction between the adjacent transistors. This can be achieved by having a thick field oxide (Fig.1.8b) and/or by raising the substrate doping level between the transistors.

As lateral device geometries are reduced, latch-up can be induced by α-particle minority carrier generation [5]. Incident α-particles can also induce "soft" errors in high-density circuits, "soft" errors being defined as, "random, non-recurring single bit errors in memory devices" [6,7]. The errors are not permanent, and show a complete recovery by the following write cycle with no greater chance of that bit showing a further error than any other bit of the device. Naturally occurring α-particles, with typical energies of 5MeV, can penetrate 10μm into the silicon. They travel nearly in straight lines and can excite electron-hole pairs within 2-3μm of the α-track. Unfortunately, these distances are comparable with current device dimensions and the number of induced electron-hole pairs is comparable with the number required to upset data in some dynamic memories (normal doses of β- and γ- radiation do not produce soft errors because of their relatively low energy-loss rates in silicon, although intense sources can cause catastrophic threshold shifts over long periods).

This susceptibility to radiation has proved to be a problem for military applications, space communication satellites and even for normal use where the low levels of thorium or uranium in integrated circuit packaging materials can decay to produce α-particles.

1.3 Silicon-On-Insulator

There are both physical and electrical advantages when manufacturing devices on insulating substrates, rather than on bulk silicon, as detailed in this section. However, as with most new technologies, Silicon-on-Insulator (SOI) substrates are more expensive than the bulk (silicon) substrates they are designed to replace, although SOI devices have a simpler fabrication sequence which helps to reduce the final cost. Silicon-on-sapphire (SOS) is the most well-established SOI technology in that SOS integrated circuits have been manufactured commercially for a number of years. SIMOX is currently second but is developing very rapidly, even to the extent that substrates are now commercially available, albeit in limited quantities.

1.3.1 MOSFETS On Insulating Substrates [2,4]

As already mentioned, details of the principal SOI technologies will be given later in this section, but at present is is sufficient just to consider the devices "sitting" on a planar insulating substrate. The basic structure of an SOI CMOS device is shown in cross-section in Fig.1.9, and it is immediately obvious that the individual devices are totally isolated from one another. This results in a number of advantages over bulk CMOS devices.

In Bulk CMOS technology, there is always a parasitic junction capacitance between devices and the substrate due to different doping levels. Also, heavily doped guard rings are sometimes employed to provide electrical isolation between individual devices, but these too have a parasitic junction capacitance which can limit the switching speed of a device. This limitation is overcome with SOI substrates where there can be no device-substrate parasitic capacitance and since no guard rings are necessary, their contribution to the parasitic capacitance is also eliminated. These factors, combined with the almost exclusive use of CMOS circuits, give SOI one of the lowest speed-power products of any semiconductor technology. The omission of guard rings also enables packing densities to be increased because the wasted area can now be used for active circuitry. Furthermore, the insulating substrate prohibits any parasitic transistor action.

It is still possible, however, for α-particles to induce soft errors in memory circuits, but since the silicon layers are so thin (typically $<0.5\mu m$), the interaction volume between an α-particle and a device is very small, considerably reducing the number of electron-hole pairs available to upset the circuit. Hence, compared to bulk silicon, SOI circuits have an increased radiation tolerance making them suitable for military applications and for circuits in space communications satellites.

1.3.2 Current SOI Technologies

1.3.2.1 Silicon-On-Sapphire

Silicon-on-sapphire (SOS) has been the most successfully exploited SOI technology with 3μm (channel length) devices being manufactured primarily for defence and space applications, where its high speed, low power and good radiation tolerance have outweighed its additional cost. However, the high cost of the substrates has so far precluded CMOS SOS from becoming a major commercial technology even though the devices require simpler processing than their bulk silicon equivalents. Bulk- and SOS-CMOS device cross-sections are shown in Figs. 1.10 and 1.11 respectively. The SOS device is simpler than its bulk silicon equivalent and therefore requires fewer processing steps.

SOS consists of a 0.3-0.6μm epitaxial $<100>$ silicon layer on a $<01\bar{1}2>$ single crystal sapphire (α-Al_2O_3) substrate grown by the Czochralski method, which results in a lattice mismatch of $\approx$6% at the Si/Sapphire interface. This misfit strain is reduced by the presence of a high density of twins and stacking faults at the interface, the density of which reduces sharply with distance into the silicon. These defects increase carrier scattering, reducing carrier mobilities and lowering device speeds. For example, electron mobility is $\approx$50% lower than that observed in the corresponding bulk silicon devices, reflecting the relatively low crystal quality of the 0.3μm films. However, the hole mobilities are very similar to those in bulk silicon, due in part to the action of internal shear stresses within the SOS films, which although degrading the electron mobilities, tend to enhance hole mobilities due to valence band splitting [10].

As lateral device geometries are reduced, it is also desirable to reduce vertical dimensions, hence the development of 0.3μm SOS (which superseded 0.6μm SOS). The active regions of the MOS transistors are then even closer to the interface where the density of defects is greatest. To help overcome this problem, Lau *et al* [11] implanted silicon ions into the as-grown epitaxial structures to amorphise most of the silicon but leaving the top layer as a single crystal. Subsequent furnace annealing was found to promote solid phase epitaxial regrowth in the layer with a significant reduction in the defect density. Fig.1.12 gives a diagrammatical representation of the process. This technique proved to be successful and was continued by other workers using different annealing techniques i.e. continuous wave argon lasers [12,13] and electron beams [8]. It was found that high temperature annealing or liquid phase epitaxial regrowth gave the greatest reduction in defect density but tended to increase the aluminium content of the layers, aluminium being an undesirable p-type impurity.

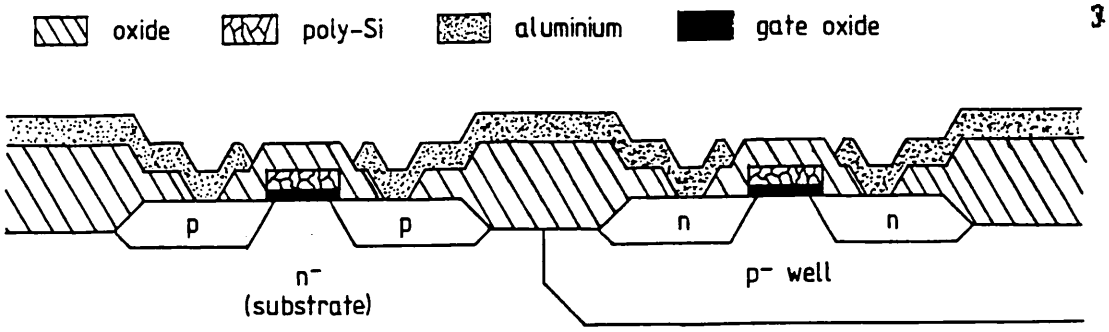


Fig.1.10 Bulk silicon CMOS inverter cross-section.

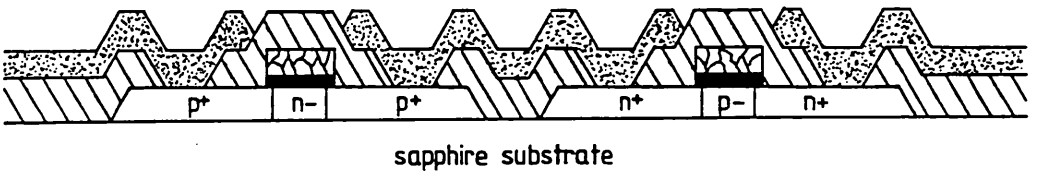


Fig.1.11 CMOS/SOS inverter cross-section.

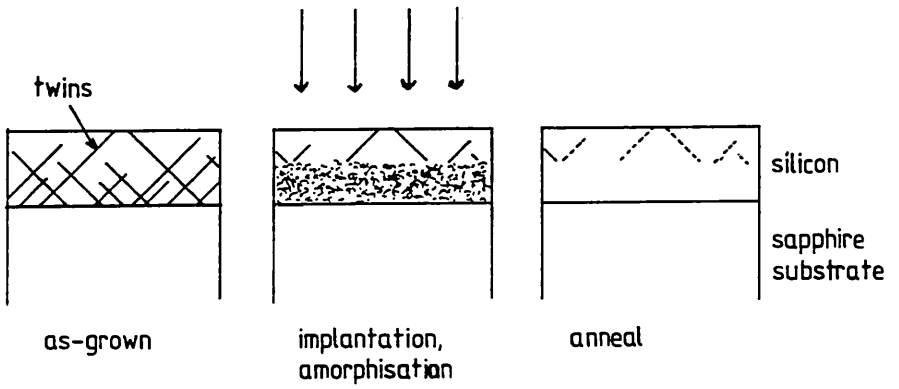


Fig.1.12 Schematic showing implantation and annealing of SOS.

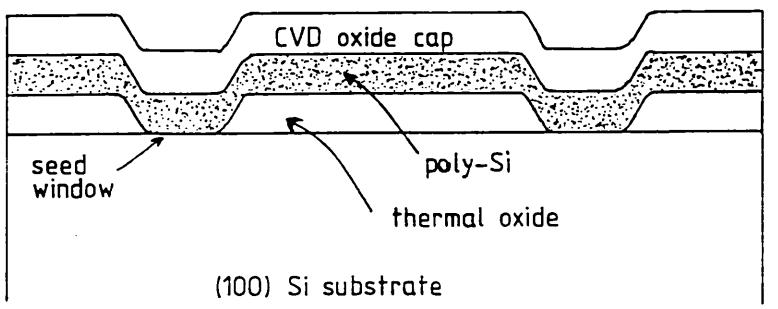


Fig.1.13 Typical starting substrate for "recrystallised polysilicon" SOI

Lower annealing temperatures gave the opposite results. No defect densities or aluminium levels were reported for the case of electron beam annealing [8], so a direct comparison cannot be made.

Overall, SOS has proved to be very successful in terms of small to medium scale production. So far, its electrical properties have outweighed its cost for certain specialised applications, but with recent developments and advances in the other main SOI technologies, it is likely to be superseded. Recrystallised Polysilicon, FIPOS and SIMOX have better fundamental electrical properties (e.g. mobilities) and are rapidly becoming cheaper.

1.3.2.2 Recrystallised Polysilicon

An alternative SOI technology is "Recrystallised Polysilicon". A typical starting substrate is shown in Fig.1.13. It consists of a 1μm layer of polysilicon deposited onto a thermally grown layer of SiO_2 (again $\approx$1μm) which has holes etched into it periodically so the polysilicon is in direct contact with the single crystal silicon substrate. In theory, the polysilicon melts during an annealing step and recrystallises to form a single crystal layer using the silicon substrate as a seed. The 1μm layer of CVD oxide is present to contain the polysilicon whilst it is molten.

The main problems associated with this technology are to do with defects in the silicon layers, such as twins, stacking faults, dislocations and surface inhomogeneities which are formed at distances of typically 50–100μm from the seed windows. To help overcome these problems, various annealing techniques have been developed, as described below.

a) Zone Annealing

Essentially, this technique involves heating the substrate to an equilibrium temperature below the melting point whilst scanning a graphite strip- or lamp-heater over the polysilicon layer.

As well as the substrate shown in Fig.1.13, fused quartz substrates have been used with polysilicon layers and an oxide cap. In these cases [14–16] there are obviously no seed windows and hence there are problems with attaining the desired crystallographic orientation. Graphite strip heaters have also been used to scan the front surfaces of the wafers (1700–2000°C) whilst the backs of the wafers were maintained at 1100–1300°C by either heated graphite strips or base plates. The final microstructure depended on a number of parameters such as temperature, temperature

gradient, scan direction, scan speed etc. but in each case the layers, although preferentially orientated in the <100> direction, were really just large-grained polysilicon.

A different starting substrate was used by Scharff *et al* [17] which consisted of small silicon islands deposited into grooves etched into a thermal oxide layer. Lamp annealing produced defect-free grains ≈30 x 300μm^2 although the orientations were in both the <100> and <110> directions.

Using a seeded substrate, back heating and a lamp heat-source under which the wafer was scanned [18], it was found that zone melting could be achieved with seeding from the substrate, the seed windows being 10μm-wide lines with a spacing of 1mm. Grains up to 100μm wide were formed along the scan direction, but there were problems when attempting to optimise the regrowth conditions e.g. low scan speeds produced larger grains but caused the silicon to agglomerate, whereas faster scans resulted in smaller grains and more low angle grain boundaries.

With thin (≈0.5μm) silicon films, the oxide cap was often found to break-up, causing the molten silicon to agglomerate into droplets. This was not the case for thicker (≈15μm) films, where holes in the oxide were found to be advantageous for layer homogeneity [19]. For thin films, the problem was overcome by using a double layer cap comprising of SiO_2 with a top layer of Si_3N_4. Further development work on the capping layers showed that by annealing the oxide-capped substrates in ammonia at 1100°C for 1 hour, an SiN_x surface layer could be produced [20]. Some nitrogen was found to diffuse through the cap to the polysilicon where it was believed to improve wetting during zone melting. The result was a silicon layer with a low defect density and good thickness uniformity.

A slight modification to the starting substrate involved patterning the lower (thermally grown) oxide by etching out SiO_2 islands before depositing a layer of polysilicon [21]. Subsequent annealing using two focussed halogen lamps (one above and one below) produced single crystal silicon layers over the 100 x 180μm^2 islands with no sub-grain boundaries. This proved to be a very successful technique with the possibility of a fast throughput and good power efficiency since no back-heating was required. However, there was a problem with wafer warpage.

Attempts have also been made to see whether the polysilicon layer can be recrystallised in the solid phase by heating to a temperature ≈200°C below the melting point [15,22]. Grain sizes of 50-100μm were achieved with heating at 1100-1200°C, but there were problems with the grain orientation which was found to

be predominantly <111> [17], or <100><110> in the large grains but with a more random orientation in the smaller grains [22]. The nature of the substrate was believed to have an effect, but this was not characterised. However, solid state recrystallisation was found to remove any problems of thickness uniformity or sub-grain boundaries which are associated with the liquid phase or the moving liquid/solid growth front. The process may well be further developed more if the misorientation problem can be overcome.

b) Laser Annealing

Laser annealing heats small areas of the surface of the material very quickly, hence seeding from the substrate is usually necessary. Since the heating time is small, and only the surface layer is melted, any problems with wafer damage due to prolonged heating near the melting point (as with strip heaters) will not occur [23]. This also means that lasers are only useful for thin (1-3μm) silicon films since at 5μm or above, the power required will tend to vaporise the surface before complete melting can occur. It has already been mentioned that it is the liquid/solid growth front which determines the final microstructure of the recrystallised silicon film, the growth front morphology depending on the heat-flow conditions, the temperature gradients and the nature of the heat source. A moving solidification front with a small radius of curvature is known to induce a higher density of defects as compared to a flat front [24], whereas a concave front is preferable if large, defect-free grains are to be produced [25].

Lasers can be scanned or reflected into different beam shapes which alter the shape of the growth front and the final microstructure. Scanned lasers can produce a continually moving growth front whereas pulsed lasers are only useful when small (1-3μm) grains are acceptable. A special scan was employed by Zorabedian *et al* [26] where the beam was scanned at an angle of 45° to the surface along seed window lines. A sensor located individual lines and directed the laser to them so the laser was only on "high-power" mode when scanning along the windows. This resulted in "stripes" of defect-free silicon ≈65μm wide. It is believed that the seed windows act as heat sinks [27] conducting the heat away from the molten silicon into the substrate, aiding defect-free growth. Further away from the windows where the silicon layer is only in contact with SiO_2, a poorer conductor of heat, the direction of heat-flow is different. This is believed to be one of the factors influencing grain or sub-grain boundary formation.

Another way of controlling the heat flow is to use lasers of different wavelengths (energies) which results in selective absorption e.g. CO_2 lasers are particularly suited

for the recrystallisation of silicon on fused quartz substrates where the SiO_2 absorbs more energy than the silicon. Pulsed visible and near-IR lasers can be used where substrate heating needs to be minimised and where grain boundaries can be tolerated. Continuous-wave (cw) visible lasers are limited to the recrystallisation of silicon films on top of previously diffused junctions and where few crystalline defects can be tolerated.

It is known that if the wafer is held at $\approx 1000^{\circ}C$ in a diffusion furnace during scanning, there are less thermal stresses [24]. Combined with a moving, planar growth front produced by a scanned cw argon laser, this gave 50μm lateral epitaxy with a low defect density, although a high substrate temperature can alter any impurity distributions. When two lasers ($\approx$50μm apart) were scanned over a substrate surface [28], it was found that grains 1.8mm long x 20μm wide could be achieved, even with the substrate held at room temperature. An alternative method [25] is to split the beam using a birefringence plate, which was found to give fairly large grains ($\approx$90 x 100μm^2) with no increase in the scanning complexity. A different "double-laser" technique [29] involved scanning with a Nd:YAG laser to obtain a $<100>$ texture in the polysilicon (i.e. the (100) plane is parallel to the substrate surface but the rotational orientation is random in the surface plane) and then scanning again using a cw argon laser using the $<100>$ grains as seed crystals. This gave good grain orientation but the grains were small. Also, the double-anneal process was more complex and hence more expensive.

The structure of the capping layer was found not only to alter the microstructure of the recrystallised silicon layer, but also the electrical characteristics [30], as determined from the performance of MOS devices. For three different caps, the following results were found:

a) a 6nm nitride cap allowed the widest range of power densities for successful laser recrystallisation, but led to the poorest interface characteristics,

b) a 64nm nitride layer on top of 20nm of CVD oxide gave the smoothest surface and the lowest interface charge density, but there was non-uniformity in the film's stress distribution, and

c) a 50nm nitride layer with thin stripes $\approx$10μm apart produced structures with less grain boundaries and effective control over their location as well as a more homogeneous stress distribution. This resulted in improved and more uniform device characteristics.

If three-dimensional integrated circuits are to be developed using recrystallised polysilicon, laser annealing is potentially the best technique since only the surface

layer is heated. However, the throughput is limited by the power density of unfocussed lasers – this means that the beams must be focussed to small spot sizes to be useful, so a long time is needed to process large areas.

c) Electron–Beam Annealing

There are a number of advantage of using electron beams, such as:

a) ease of generation and high power levels,
b) well–controlled and high–precision scanning with rapid switching on and off,
c) the specimens spend relatively little time at high temperature, minimising thermal effects such as wafer contamination and distortion,
d) very effective transfer of beam energy to the substrate with little loss to the surroundings – the beam power introduced into the substrate is independent of the substrate's crystallinity, surface condition, electrical resistivity, optical reflectivity etc. and the heating depth and area can easily be controlled by the acceleration voltage and the scanning method.
e) Finally, there is the possibility of a high throughput rate.

A relatively basic method involves holding the substrate at ≈400°C whilst mechanically scanning it through a high–power electron beam [31]. This gave defect–free silicon up to a distance of ≈50μm from the seed windows. Theoretical models presented in the same piece of work calculated that a maximum of 80–100μm could be achieved with 1μm polysilicon layers in their particular system.

Using a specially scanned, amplitude modulated electron beam, and back–heating the substrate with a tungsten covered quartz plate heated by a tungsten radiation lamp [32], it was found that a 4mm x 4mm area could be recrystallised, although it was believed that the defect–free regions only extended for ≈100μm from the seed windows. With similar apparatus, but sinusoidally scanning the electron beam [33] it was concluded that a stronger cap than just SiO_2 may be needed to produce much larger defect–free areas. A double layer cap of SiO_2/Si_3N_4 was proposed but not tried experimentally. Even so, the system was capable of producing 70 x 200μm areas with a scanned beam and 200 x 300μm areas using two beams with overlapping scans. Theoretical work on the capping layers [34] suggested that the recrystallisation process may be aided by a stepwise variation in the capping oxide thickness. This was only a model based on heat–flow calculations and was not proved experimentally.

A further annealing method has been evolved using a dual electron–beam system [4,5], where the wafer is held at an equilibrium temperature of 1000°C by means of a raster scanned electron beam on the back surface of the wafer. A second beam,

formed as a line by rapidly scanning a finely focussed spot, melts the polysilicon. This gave defect-free single crystal layers up to ≈150μm from the seed windows. At the edge of the scan, the material had seeded incorrectly and had twinned to produce a (211) orientation.

The main drawbacks with electron beams are that they require high-vacuum conditions and there are some problems with charging associated with insulating capping layers. However, the technique has proved to be extremely useful and may well supersede the use of lasers.

All of the work on recrystallised polysilicon has concentrated on optimising the annealing conditions and seed window geometries etc. to give the largest possible defect-free area. The problem has not been completely solved and work is continuing.

1.3.2.3 Full Isolation by Porous Oxidised Silicon (FIPOS)

One method of producing FIPOS is shown in Fig.1.14. It shows the formation of a network of thin p^+ layers by ion implantation and diffusion (Fig.1.14a) followed by proton implantation (Fig.1.14b). This results in an array of n-type silicon islands totally surrounded by p-type material (protons implanted into silicon produce donors after annealing at 400-500°C which disappear above 700°C [38]). During a subsequent anodic reaction in HF (Fig.1.14c), the p-type areas become porous but the n-type regions are unaffected. The n-type silicon islands are now separated from each other and from the substrate by porous silicon.

During an oxidation stage e.g. 1050°C in a wet oxygen ambient [38], the porous silicon is oxidised preferentially because its oxidation rate is much higher than that for single crystal silicon (the silicon islands usually often protected by a Si_3N_4 cap). However, the n-type islands revert back to p-type silicon because the donors produced by proton implantation disappear at the oxidation temperature (Fig.1.14d).

Imai *et al* [38], using a procedure similar to that described above, produced 0.5μm-thick silicon islands on a 7μm layer of porous oxidised silicon (POS), with a thickness uniformity of ±15% across a 3-inch wafer. The silicon islands were found to contain dislocations, the density of which depended on the concentration of HF e.g. a 45% solution gave 8 x $10^8/cm^2$ whereas a 20% solution gave 6 x $10^6/cm^2$. This variation occurs because as the HF concentration increases, the density of the porous silicon and the POS also increases resulting in a greater stress between the POS and the single crystal islands. This stress from volume expansion can also result

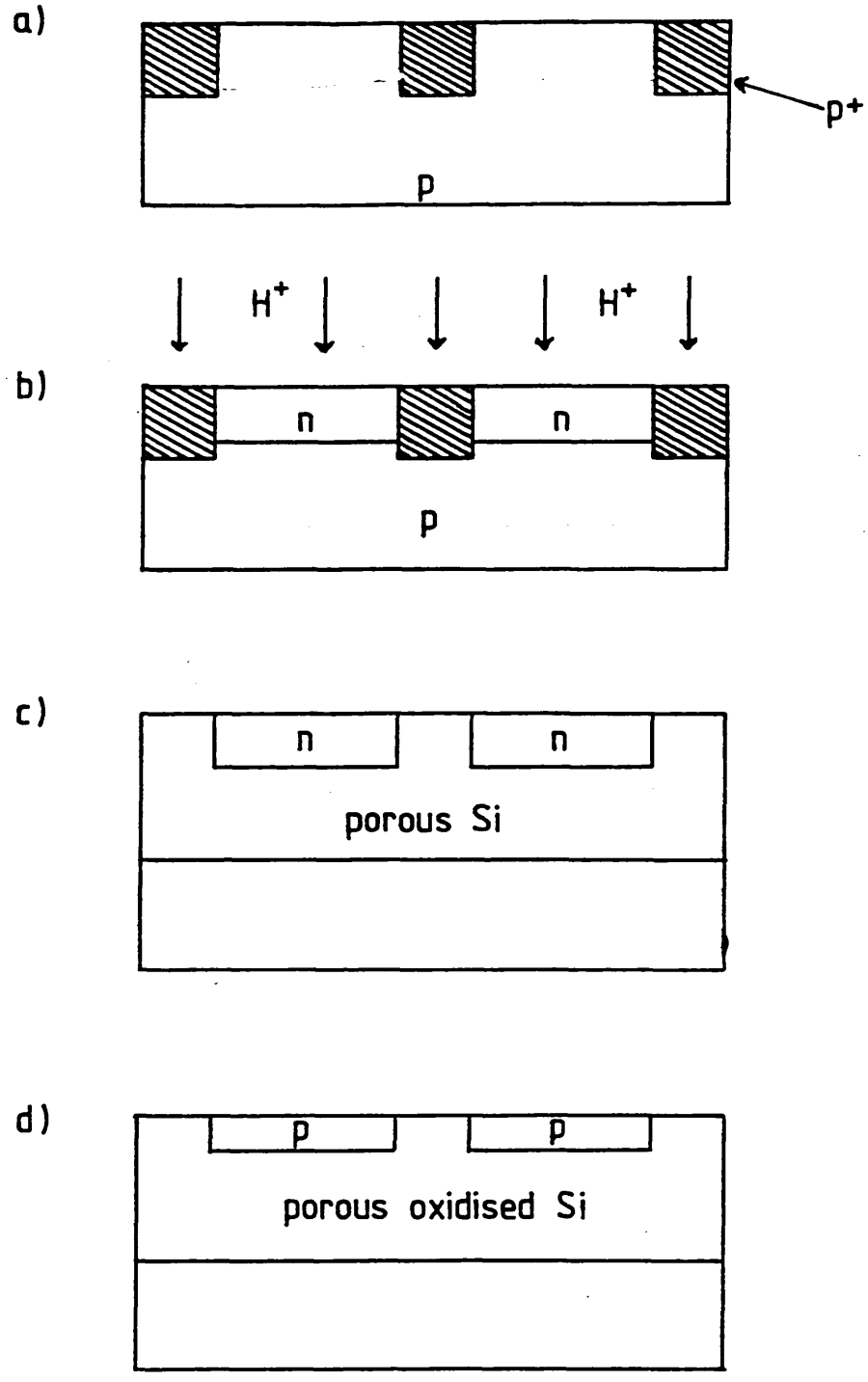


Fig. 1.14 FIPOS process steps: a) selective p+ layer formation, b) proton implantation, c) anodisation, and d) oxidation.

in wafer warpage, which appears to be inevitable with thick (≈10μm) porous oxidised layers [39].

There are also difficulties with the anodisation step [40], because the current spreads out in all directions from the windows, hence a thick porous layer is needed to isolate even small islands. Also, as anodisation proceeds, the area being anodised increases, resulting in a decreasing current density leading to a variation in the porous silicon density with depth. Furthermore, it was found that the silicon islands are attatched to the substrate by stalks of unanodised material. Oxidation then causes spikes at the bottom of the islands and on the substrate beneath them. This can set up considerable stresses, which are likely to aid the formation of dislocations within the islands. However, the dislocation densities are approximately 2-3 orders of magnitude lower than those reported for other SOI techniques, and electrical measurements showed that they had very little influence since carrier mobilities were very similar to those in bulk silicon.

An alternative approach is to grow a molecular beam epitaxial (MBE) layer on a previously anodised silicon layer, since the porous silicon is still single crystal [41]. This means that the silicon layer can be grown at ≈750°C which is desirable since the porous structure collapses at ≈800°C and its complete oxidation becomes difficult. 350μm x 2mm SOI structures have been fabricated in this way by using a two-step oxidation technique [42]: the first at 750°C oxidises the large-pore silicon underlayer to avoid the collapse of the porous structure and to secure the lateral oxygen supply channels in the porous oxide, whilst the second oxidation is performed at 950°C to oxidise the remaining porous silicon and to ensure uniform oxidation at the bottom of the MBE layer. The electrical properties of these layers were very good but there was no mention of defects such as dislocations or stacking faults which may be expected. This technique may be limited by the high cost of the MBE process.

A more recent method of producing FIPOS [43] is to epitaxially deposit a silicon layer on a heavily n^+ doped substrate. Then, either an n^+ or etched trench grid is produced in the epi-layer down to the n^+ layer. The n^+ regions can be made porous selectively leaving the remnant epitaxial regions on top of a porous layer which is subsequently oxidised to yield good quality SOI material. This method has problems with good layer thickness control and vulnerability to contamination of the porous parts. However, it has the advantage of using cheaper equipment than other SOI techniques even though an epitaxial deposition step is required.

1.3.2.4 Separation By Implanted Oxygen

This SOI technique involves implanting high doses of oxygen ions into silicon at high energies to form a continuous buried layer of SiO_2. Subsequent high-temperature annealing gives the buried oxide layer sharp interfaces leaving a thin, single crystal silicon overlayer at the surface, which has a low oxygen content. This technology is proving to be very successful in terms of production development. The material has electrical characteristics which are extremely good although there is still concern about the relatively high dislocation density.

A more detailed description of the production techniques and the material quality are given in Chapter 2.

1.4 References For Chapter 1

[1] G.L.Pearson and J.Bardeen, "Electrical properties of pure silicon and silicon alloys containing boron and phosphorous", Phys. Rev. 75 (1949) 865.

[2] A.D.Milne, "MOS Devices: Design and Manufacture", (Edinburgh University Press, 1982).

[3] J.Millman and C.Halkias, "Integrated Electronics: Analog and Digital Circuits and Systems", 23rd printing (McGraw Hill, Tokyo, 1981).

[4] S.M.Sze, "VLSI Technology", 2nd printing (McGraw Hill, Singapore, 1984).

[5] H.E.Oldham and S.L.Partridge, "A comparison of MOS processes for VLSI", G.E.C. J. Res. 1(1) (1983) 2.

[6] T.C.May and M.H.Woods, "Alpha-particle-induced soft errors in dynamic memories", I.E.E.E. Trans. Electron Devices, 26(1) (1979) 2.

[7] D.S.Yaney, J.T.Nelson and L.K.Vanskike, "Alpha-particle tracks in silicon and their effect on dynamic MOS RAM reliability", I.E.E.E. Trans. Electron Devices, 26(1) (1979) 10.

[8] D.J.Smith, L.A.Freeman, R.A.McMahon, H.Ahmed, M.G.Pitt, and T.B.Peters, "High resolution electron microscopy of Si-implanted and electron-beam annealed silicon on sapphire", Inst. Phys. Conf. Ser. Nº 67, section 2, (1983) 83.

[9] J.L.Hutchison, G.R.Booker and M.S.Abrahams, "Transmission high-resolution electron microscopy studies of silicon-sapphire epitaxial layer structures", Inst. Phys. Conf. Ser. Nº 60, section 3, (1981) 139.

[10] E.C.Ross and G.Warfield, "Superlinear current density vs electric field in p-type silicon-on-sapphire", J. Appl. Phys. 41 (1970) 2657.

[11] S.S.Lau, S.Matteson, J.W.Mayer, P.Revesz, J.Gyulai, J.Roth, T.W.Sigmon and T.Cass, "Improvement of crystalline quality of epitaxial silicon layers by ion implantation techniques", Appl. Phys. Lett. 34(1) (1979) 76.

[12] I.Golecki, G.Kinoshita, A.Gat and B.M.Paine, "Recrystallisation of silicon-on-sapphire by cw Ar laser irradiation: comparison between the solid- and liquid-phase regimes", Appl. Phys. Lett. 37(10) (1980) 919.

[13] R.E.Reedy and T.W.Sigmon, "Characterisation of defect reduction and aluminium redistribution in silicon implanted SOS films", J. Crystal Growth, 58 (1982) 53.

[14] M.W.Geiss, H.I.Smith, B-Y.Tsaur, J.C.C.Fan, D.J.Silversmith and R.W.Mountain, "Zone-melting recrystallisation of Si Films with a moveable-strip-heater oven", J. Electrochem. Soc. 129(12) (1982) 2812.

[15] E-H.Lee, "<100> and <111> textures in seeded, strip heater recrystallised silicon-on-insulator", Appl. Phys. Lett. 48(2) (1986) 180.

[16] S.Fujita, M.Okamoto, H.Yamamoto and A.Sasaki, "Effects of heating-temperature gradient and scanning direction on crystallographic properties of zone-melting recrystallised silicon on square-shaped fused quartz", J. Appl. Phys. 56(10) (1984) 2986.

[17] W.Scharff, J.-W.Erben, A.Wolf, M.Heber, C.Hamann, C.Weissmantel, M.Voelskov, J.Matthäi, R.Kögler, R.Klabes and E.Weiser, "Growth of single-crystalline regions on amorphous insulating substrates by zone-melting recrystallisation", Phys. Stat. Sol. (a), 82 (1984) K5.

[18] H.E.Cline, "Silicon thin films formed on an insulator by recrystallisation", J. Appl. Phys. 55(8) (1984) 2910.

[19] L.Pfeiffer, T.Kovacs and K.W.West, "Si-on-insulator films of high crystal perfection by zone melting under a SiO_2 cap provided with vent openings", Appl. Phys. Lett. 47(2) (1985) 157.

[20] C.K.Chen, M.W.Geis, M.C.Finn and B-Y.Tsaur, "New capping technique for zone-melting recrystallisation of silicon-on-insulator films", Appl. Phys. Lett. 48(19) (1986) 1300.

[21] J.Sakurai, "Focussed lamp zone melting recrystallisation of silicon on insulator substrates", J. Elecrtrochem. Soc. 133(7) (1986) 1485.

[22] H.E.Cline, "A single-crystal silicon thin film formed by secondary recrystallisation", J. Appl. Phys. 55(12) (1984) 4392.

[23] G.K.Celler, "Laser crystallisation of thin Si films on amorphous insulating substrates", J. Crystal Growth, 63 (1983) 429.

[24] J.Shappir and R.Adar, "Polycrystalline silicon recrystallisation by combined cw laser and furnace annealing", J. Electrochem. Soc. 131(4) (1984) 902.

[25] N-A.Aizaki, "Recrystallisation of silicon film on insulating layers using a laser beam split by a birefringent plane", Appl. Phys. Lett. 44(7) (1984) 686.

[26] P.Zorabedian, T.I.Kamins and C.I.Drowley, "Laser scan registration for lateral epitaxy on silicon-on-insulator stripes on silicon substrates", J.Appl. Phys. 57(12) (1985) 5262.

[27] S.Kawamura, N.Sasaki, M.Nakano and M.Takagi, "Laser recrystallisation of Si over SiO_2 with a heat-sink structure", J. Appl. Phys. 55(6) (1984) 1607.

[28] N.Sasaki, R.Mukai, T.Izawa, M.Nakano and M.Takagi, "Melt-width enhancement in the recrystallisation of polycrystalline silicon-on-insulator by twin-laser-beam-induced substrate interheating", Appl. Phys. Lett. 45(10) (1984) 1098.

[29] K.Egami, M.Kimura and T. Hamaguchi, "Crystallographic orientation control of silicon stripes in SiO_2 grooves using a new double laser annealing technique", Appl. Phys. Lett. 44(10) (1984) 962.

[30] H.E.Lu, J.T.Boyd, H.E.Jackson and J.H.Janning, "Characterization of the effects of different capping layer structures on the laser recrystallization of silicon by using electrical test structures and Raman spectroscopy", J. Appl. Phys. 60(12) (1986) 4273.

[31] J.A.Knapp, "Silicon-on-insulator structures formed by a line-source electron beam: experiment and theory", J. Appl. Phys. 58(7) (1985) 2584.

[32] T.Hamasaki, T.Inoue, I.Higashinakagawa, T.Yoshii and H.Tango, "Highly controllable pseudoline electron-beam recrystallisation of silicon on insulator", J. Appl. Phys. 59(8) (1986) 2971.

[33] H.Ishiwara, K.Ohyu, S.Horita and S.Furukawa, "Recrystallisation of silicon-on-insulator structures by sinusoidally-scanned electron beams", Japan. J. Appl. Phys. 24(2) (1985) 126.

[34] I.N.Miaoulis and B.B.Mikić, "Temperature distribution of silicon-on-insulator systems during recrystallisation processing", J. Appl. Phys. 59(5) (1986) 1663.

[35] R.A.McMahon, H.Ahmed, D.J.Godfrey and M.G.Pitt, "Application of electron beams in thermal processing of semiconductor materials and devices", G.E.C. J. Res. 1(3) (1983) 146.

[36] J.R.Davis, R.A.McMahon and H.Ahmed, "Characterisation of the dual e-beam technique for recrystallising polycrystalline silicon films", J. Electrochem. Soc. 132(8) (1985) 1919.

[37] Y.Ohmura, Y.Zohta and M.Kanazawa, "Shallow donor formation in Si produced by proton bombardment", Phys. Stat. Sol. (a), 15 (1973) 93.

[38] K.Imai, H.Unno and H.Takaoka, "Crystalline quality of silicon layer formed by FIPOS technology", J. Crystal Growth, 63 (1983) 547.

[39] K.Barla, R.Herino and G.Bomchil, "Stress in oxidised porous silicon layers", J. Appl. Phys. 59(2) (1986) 439.

[40] J.D.Benjamin, J.M.Keen, A.G.Cullis, B.Innes and N.G.Chew, "Large area, uniform silicon-on-insulator using a buried layer of oxidised porous silicon", Appl. Phys. Lett. 49(12) (1986) 716.

[41] S.Konaka, M.Tabe and T.Sakai, "A new silicon-on-insulator structure using a silicon molecular beam epitaxial growth on porous silicon", Appl. Phys. Lett. 41(1) (1982) 86.

[42] T.L.Lin and K.L.Wang, "New silicon-on-insulator technology using a two-step oxidation technique", Appl. Phys. Lett. 49(17) (1 986) 1104.

[43] K.J.S.Cave, I.E.E. Tutorial meeting, "Silicon On Insulator - Current Status And Future Potential", London, March 1987.

Chapter 2

Literature Survey

2.1 The Nature Of Oxygen In Silicon

2.1.1 Oxide Precipitation and Growth

Vacuum fusion analysis [1] has shown as-grown Czochralski silicon (Cz-Si) to be supersaturated with approximately 10^{18} oxygen atoms/cm^3. This "frozen-in" oxygen occupies interstitial positions and forms bonds with two neighbouring silicon atoms. With an O-Si bond length of 0.16nm, and assuming the Si-Si distance to be unchanged at 0.234nm, the bond angle would be $\approx 100^\circ$, which was believed to be quite feasible. Subsequent work on the sense of the stress induced dichroism in the 9μm infared absorption band [2] confirmed that oxygen is nestled interstitially in a bonded $<111>$ Si-O-Si configuration between two nearest neighbour silicon atoms as shown in Fig. 2.1. In addition to this dissolved, dispersed oxygen, Kaiser [3] believed that a partial grouping of oxygen atoms occurs during the normal cooling process after crystal growth. These microprecipitates, of what was believed to be SiO_2, nucleate continuously during the cooling process [4] and have a continuous size distribution depending on when they were nucleated.

The magnitude of the absorption coefficient at 9μm in silicon is known to depend on the amount of dissolved oxygen [1]. Heat treatment of the silicon for 60 hours at 1000°C was found to decrease the absorption coefficient but to cause an increase in optical scattering [3]. This was believed to be due to the growth of oxide precipitates, taking the oxygen out of solution. The oxide precipitates were calculated to be $\approx 0.1\mu$m in diameter with a density of $\approx 5 \times 10^{10}$ /cm^3.

However, the proof that the precipitates were SiO_2 (or SiO_x where x is close to 2) was not provided until Yang *et al* [5] studied them in the TEM using electron energy loss spectroscopy (EELS). The EEL spectra of the precipitates showed features similar to those found in thermally grown SiO_2 but not in the precipitate-free silicon matrix. Furthermore, energy filter images showed the precipitates to be bright indicating they had a high oxygen content or were indeed SiO_2.

The rate of oxide precipitation (or the rate of removal of oxygen atoms from optically active sites) was found to increase by introducing a high density of dislocations into the silicon [6]. Hence the grown-in dislocations were believed to act

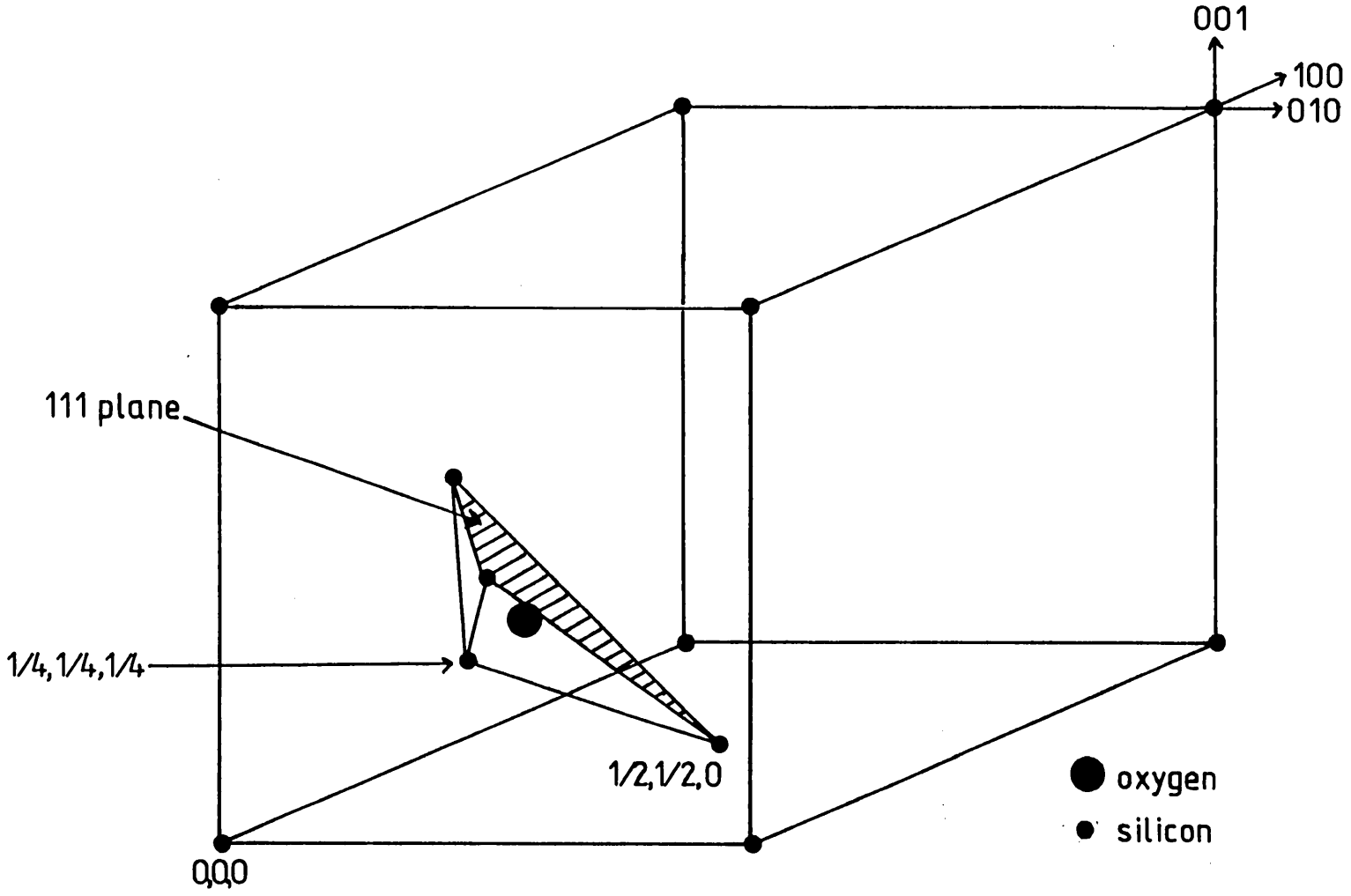


Fig. 2.1 Position of an isolated oxygen atom in a [111] interstitial configuration.

as heterogeneous nucleation sites, although their density was not great enough to account for all of the oxide precipitates. There has been speculation about the effects of impurities such as carbon, but more recent work [7] has shown the oxide precipitation and growth to be independent of the carbon concentration whereas other contempory work has disagreed [8]. The position has still not been clarified.

An analysis of the nucleation and growth of oxide precipitates [9] using classical nucleation theory [10] introduced the oxygen equilibrium temperature (see section 2.1.2) which has a value of 1230°C at an oxygen concentration of $8 \times 10^{17}/cm^3$. In the same specimen, 1150°C was the highest temperature at which oxide particles were observed to nucleate, giving a value of 80°C for the supercooling. At lower annealing temperatures (e.g. 700°C) the critical radius for precipitate growth is so small that there is always a very high precipitate density, but at 1150°C the critical radius is ≈1nm which corresponds to approximately 200 atoms. From this it was concluded that the precipitates must nucleate homogeneously. Later work [4] calculated the undercooling to be ≈300°C which gave further proof that homogeneous nucleation was the dominant process.

After a 5-day anneal at 650°C, TEM analysis revealed long (≈μm) ribbon-like defects (RLDs) approximately 2nm thick. These defects were believed to be coesite, a high-pressure silica polymorph [8,11] which nucleated homogeneously from a small oxygen complex in the form of a <110> elongated chain on the {100} planes. They were unstable and were not present after annealing at 870°C. A more detailed (HREM) analysis [12] has revealed that the RLDs in fact exist primarily on the {311} habit planes rather than on the {100} planes. However, coesite precipitates on {100} habit planes tend to have sections along {311} - conversely RLDs on {311} habit planes formed after annealing at 485°C for over 900 hours sometimes show signs of continuing growth along {100}. This suggests the defects are the same, namely coesite; {311} being the preferred habit plane during the initial stages of growth, with the {100} becoming more favourable in order to minimise the strain energy for larger precipitates.

Bourret [13] later disproved the conclusions about RLDs by postulating that they are not coesite, but thin strips of an hexagonal silicon phase made up from an agglomeration of silicon interstitials which are a *result* of oxide precipitation. This wurtzite-type silicon structure is metastable with only a small energy difference from the diamond cubic phase, and is modified above ≈800°C to form a dislocation loop.

Conventional TEM has shown that small (≈2nm) black dots in the image co-exist with RLDs at the lower annealing temperatures (≈650°C) [8]. They have a density

of $\approx 10^{15}/cm^3$ and are believed to grow into ≈10nm silicon platelets ($1.3 \times 10^{14}/cm^3$) at 870°C. Their instability under electron bombardment in the TEM [11] led workers to believe that they are due to silicon interstitials, but the idea of them being small oxide precipitates cannot be discounted *because* they are so small and because they are very likely to contain oxygen.

After annealing at 870°C for 5 days [8], amorphous SiO_2 platelets were found to form on the {100} planes. They had a mean diameter of ≈10nm and a density of $1.3 \times 10^{14}/cm^3$. These precipitates were similar to those reported earlier by Tice and Tan [14], although the latter varied from 100–1000nm in diameter with densities as low as 10^4–$10^5/cm^3$, probably due to the higher annealing temperature (1050°C). The basic precipitate morphology was a square platelet on one of the {100} planes with edges parallel to the two <110> directions in that plane. From TEM observations, the earliest observable stage of precipitation was the formation of a cross-shaped ribbon with two <100> branches. Dendritic growth of these branches in the <110> directions eventually completed the square plate. The platelets were reported as having thicknesses of 1.5nm [8] tapering to one atomic layer at the edges or 4nm [15] which did not increase until their diameters were greater than ≈1 μm.

These results show that after annealing, even the relatively small amount of oxygen in Cz-Si segregates to form stable SiO_2 precipitates. The nucleation mechanism depends on impurity concentrations and defect densities, both of which are low in Cz-Si, meaning that homogeneous nucleation is the dominant process. However, the size and density distributions of the precipitates are determined by the thermodynamics of the Si–O system, of which a brief description is given below.

2.1.2 Thermodynamics Of The Silicon/Oxygen System

Fig. 2.2a gives the solubility of oxygen as a function of temperature. When the system is at thermal equilibrium, each value of the temperature, T_e, corresponds to a certain value of the oxygen concentration. When oxygen is in supersaturation at temperature T ($T < T_e$), the degree of supersaturation corresponds to a value T_e–T, the supercooling. Fig. 2.2b represents the variation of free energy per unit volume (G_V) of the Si/O system as a function of temperature. Curve "a" corresponds to a solid solution of oxygen in silicon, whereas curve "b" corresponds to a silicon matrix with SiO_2 precipitates. This shows that as the temperature decreases, a two-phase microstructure becomes energetically favourable. However, this requires the formation of an Si/SiO_2 interface with a corresponding surface energy, σ. Since SiO_2 precipitation is also accompanied by a volume increase, a stress will be produced in the matrix, with a further increase in energy.

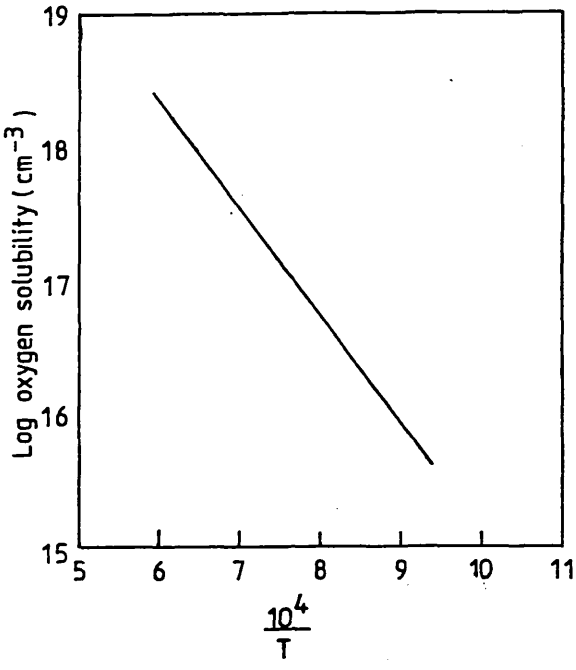


Fig.2.2a Oxygen solubility in silicon

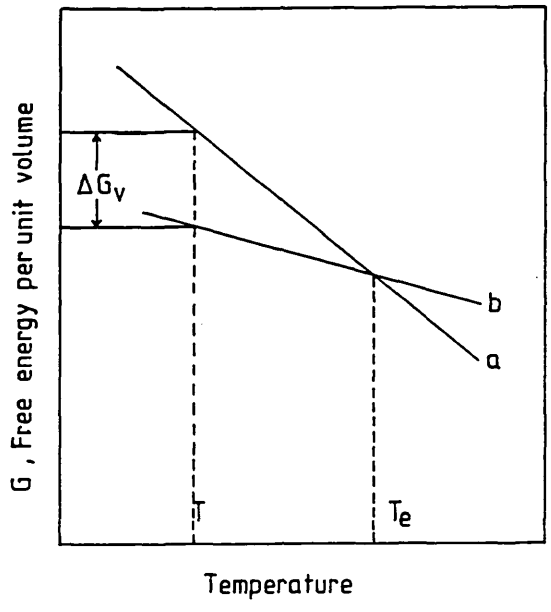


Fig.2.2b Variation of the free energy of the Si-O system. a) oxygen solid solution, b) oxide precipitates.

The total free energy change, ΔG, on precipitation at temperature T is given by

$$\Delta G = 4/3\ \pi r^3 \Delta G_v + 4\pi r^2 \sigma + \text{elastic strain energy} \qquad (2\text{-}1)$$

for a spherical precipitate of radius r.

The increase in surface energy means that small precipitates consume more energy than they release but larger precipitates do the opposite. There is a critical radius, r_c, at which precipitates become stable, but below r_c they are unstable and dissolve. This value is given by

$$r_c = \frac{2\sigma}{\Delta H_v} \quad \frac{T_e}{(T_e - T)} \qquad (2\text{-}2)$$

where ΔH_v is the enthalpy of formation of the SiO_2 phase per unit volume and T_e is the equilibrium temperature. This shows that the critical radius depends on temperature and (T_e-T), the supercooling, which is a measure of the interstitial oxygen supersaturation.

When annealed at high temperature, the number of precipitates decreases and their sizes increase: the larger ones grow at the expense of the smaller ones. This process is known as "Ostwald Ripening" [10,16] and requires the diffusion of solute atoms from regions surrounding the small precipitates to those surrounding the larger ones. The overall driving force for this process is a reduction in Si/SiO_2 surface energy.

2.1.3 Oxidation-Induced Lattice Defects

In 1964, Patel [17] pointed out the possibility of SiO_2 precipitation and the nucleation of dislocations by these precipitates. Tice and Tan [14] observed such dislocations and believed them to be generated by the mechanism of prismatic punching caused by a compressive misfit stress introduced into the silicon matrix. The stress field was believed to arise from misfit strain associated with oxide precipitation and from differential contractions between precipitates and the silicon matrix during wafer cooling after heat treatment, although the latter effect is likely to be less significant [18]. Two prismatic loops (of opposite nature) are generated, accomplished by the expansion of existing generator loops around a glide prism. The interstitial loop ($a/2\langle 110\rangle\ \{110\}$) is punched out along the glide direction while the vacancy loop moves onto the precipitate surface where it is annihilated, thereby reducing the misfit strain. Some of the glide systems are more difficult to operate than others, depending on the platelet orientation, which explains why some were not seen on certain planes in the TEM. The perfect dislocation loops have been found

to be rhombus shaped with edges parallel to the <110> and <112> directions [18].

At 550–750°C [11], there is a high density of dislocation dipoles, but the number decreases sharply at lower temperatures. The majority are 60°, although a smaller number of 90° dipoles are also present. This is because the complexity of bond rearrangement is greater for 90° dipoles than for 60° dipoles. Both types consist of two parallel dislocations in <110> directions with a separation of 25–35nm. The dislocations were found to be undecorated.

Further work [11,19,20] has shown that a variety of defects, always associated with precipitates, are produced at higher temperatures i.e. Frank and a/6<114>-type stacking faults, elongated dislocation loops and polygonal prismatic loops. The a/6<114> stacking faults were all associated with perfect dislocation loops and are believed to be formed from the transformation of double Frank stacking faults by the reaction

$$2a/3\ [111] \rightarrow a/6\ [114] + a/2\ [110] \qquad (2\text{–}3)$$

which is energetically favourable due to the lowering of dislocation line energy. In some cases, the polygonal <114> stacking faults can annihilate to form perfect dislocation loops.

The elongated dislocation loops are aligned along the <110> directions but they are less straight than the ones observed at lower temperatures, and have 60° burgers vectors. They lie on the {100} planes and are believed to form by climb and glide out of the 60° dipoles.

All of the defects mentioned are interstitial in nature [18], consistent with the idea that they are formed as a result of silicon interstitial emission from the growing precipitates. Analysis of experimental results has found that the free energy change accompanying precipitation is not large enough to compensate for the strain due to volume expansion; this strain is relieved by dislocation formation at the precipitate/matrix interface. After the precipitation stage, growth occurs by oxygen diffusing to that interface. The volume change (an increase of ≈2.2x) means that silicon atoms, in the form of interstitials, must be displaced from the interface. These excess interstitials can collapse to form an extrinsic (Frank) stacking fault which grows by a Bardeen–Herring climb mechanism. An alternative theory is that the dislocation associated with the precipitate dissociates as follows,

$$a/2\,[1\,1\,0] \rightarrow a/6\,[1\,1\,\bar{2}] + a/3\,[1\,1\,1] \qquad (2\text{-}4)$$

to form a Shockley and a Frank partial. The former can easily glide away in the precipitate's strain field leaving the Frank partial surrounding a stacking fault. For either mechanism, silicon interstitial formation and diffusion away from the interface to the dislocation surrounding the fault was found to be the rate-determining step at 1000–1200°C. This was confirmed in an analysis of the stacking fault morphology by Leroy [22]. The self-diffusion coefficient for silicon interstitials was determined to be 10^{-10} to 10^{-12} cm^2/s at 1200 to 1000°C, with an activation energy of 3.6eV [23], although later work over a greater temperature range [24] gave a value of 4.66eV. Also, the silicon interstitial concentration was found to be almost independent of temperature over the range 1000 to 1400°C, at $\approx 10^{17}/cm^3$.

Plougonven *et al* [25] and Takaoka *et al* [23] favoured the interstitial-collapse model since the $a/6[1\,1\,2]$ Shockley partials had never been observed. Two possible models for the stacking fault growth were then postulated:

i) the Frank loops climb by trapping silicon interstitials as they are emitted from the growing precipitate, or

ii) the silicon vacancies required at the growing interface are supplied as the Frank loops climb.

No conclusion was reached as to which mechanism is the correct one. However, it was concluded that since the rate of stacking fault growth was found to be proportional to $t^{\frac{1}{2}}$ where t is the annealing time, and the rate of oxide platelet growth also varies as $t^{\frac{1}{2}}$, that both are limited by silicon interstitial emission and diffusion. Hence the formation of stacking faults and dislocations is a direct result of oxide precipitation and growth.

nb. This section gives only a very brief description of the behaviour of oxygen in silicon, since literally thousands of papers have been published on the subject over the past thirty years. For more information, the reader is refered to the reviews in references 7, 11 and 15.

2.2 Manufacture of SIMOX 1 (Ion Implantation) [26]

The theory of ion implantation (i.e. the interaction between energetic ions and solids) is extremely complex since it has to take account of many different aspects of various interactions such as electronic excitation of the atoms, nuclear interactions, displacement of lattice ions by energetic collisions (lattice damage) and the production of plasmons and phonons in the solid by passing ions. The two main overall processes which cause the ions to lose energy are electronic and nuclear stopping.

Since the turn of the century, many models have been put forward to simulate and quantify the overall process in real solids (i.e. range and damage distributions) by, for example, considering atomic nuclei to have a finite size as opposed to being point charges. However it was not until 1963 that a single model brought all the points together to create a unified theory for a wide range of ions, targets and energies. This was the Lindhard-Scharff-Schott (LSS) theory, a statistical model which incorporated a number of bridging approximations where necessary.

The LSS theory was the last comprehensive study based on statistical models of atom-atom collisions. Since then, improvements have been made by applying numerical methods techniques and by removing the remaining approximations. This has obviously been aided by the use of computers. A good model currently available is called TRIM (the Transport of Ions in Matter) [26], which allows ion ranges and defect distributions to be calculated to within 10-20%. This Monte Carlo simulation has been very useful although it does not take account of very high-dose implantations where, for example, there is diffusion of the implanted species (thermal and/or radiation-enhanced), surface swelling, density changes or where compound formation occurs (as with SIMOX). A more recent model [27] does take account of these effects and appears to predict high-dose implantation profiles quite accurately. For further information, see reference [26] which gives an extremely comprehensive review of the theory of Ion Implantation.

2.2.1 Ion Ranges [26-31]

As briefly mentioned earlier, an individual implanted ion undergoes scattering events with electrons and atoms in the target, reducing the ion's energy until it comes to rest. Point defects and even small amorphous zones may result (Fig.2.3a). The total path length of the ions is called the range, R (Fig.2.3b). A typical ion stops at a distance normal to the surface, called the projected range, R_p. Some ions undergo less or lower energy interactions and come to rest beyond the projected range, whereas others may undergo more or higher energy interactions and come to rest between the surface and the projected range, or may even be backscattered from the target. The fluctuation or straggle in the projected range is ΔR_p. There is also a fluctuation in the final ion's position perpendicular to its incident direction, called the lateral straggle, $\Delta R_\perp$. A typical as-implanted depth profile of oxygen implanted into silicon is shown in Fig.2.4.

The depth distribution or profile of stopped ions can be approximated by a symmetric Gaussian distribution. The concentration of implanted ions as a function of position is:

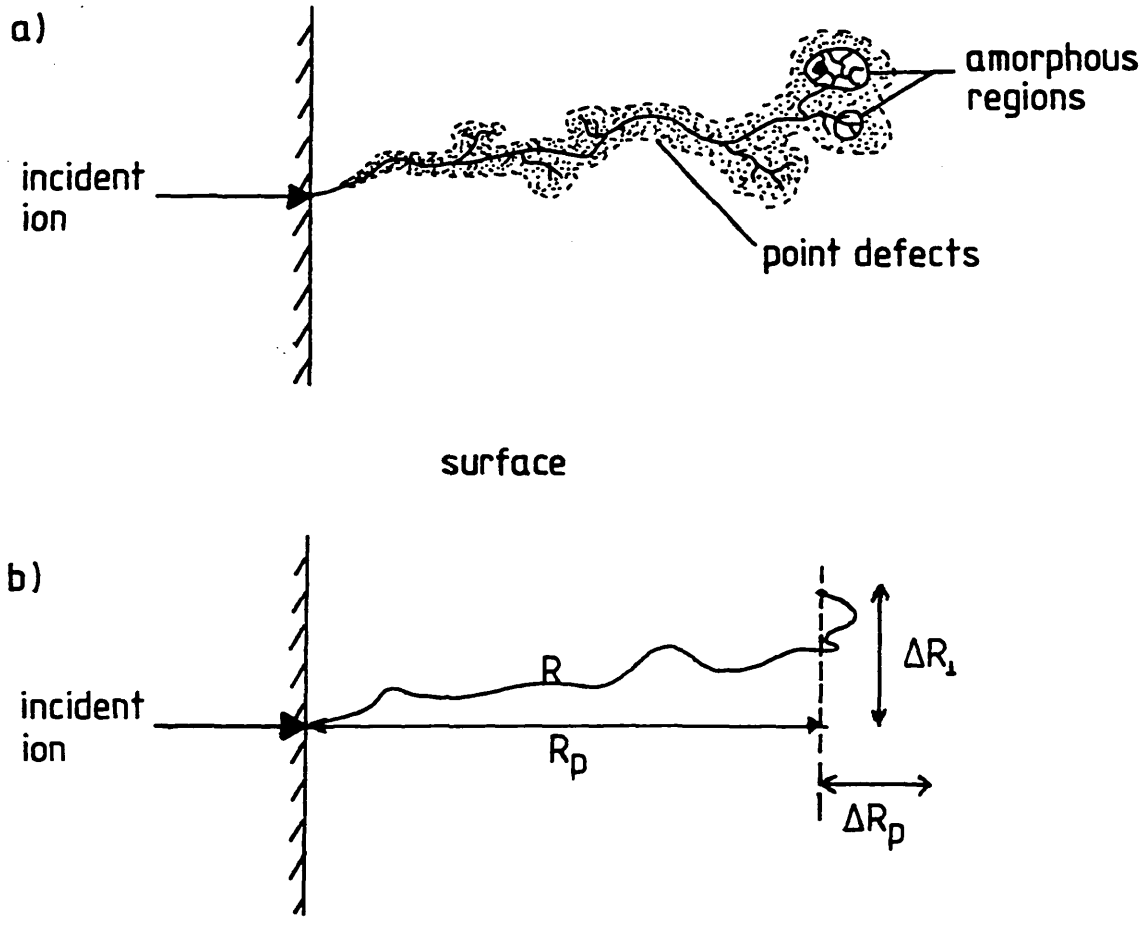


Fig.2.3 a) "tree" of disorder for a typical implanted ion, and b) schematic of the range, R, projected range, R_p, uncertainty in R_p or straggle ΔR_p, and the lateral straggle, $\Delta R_\perp$.

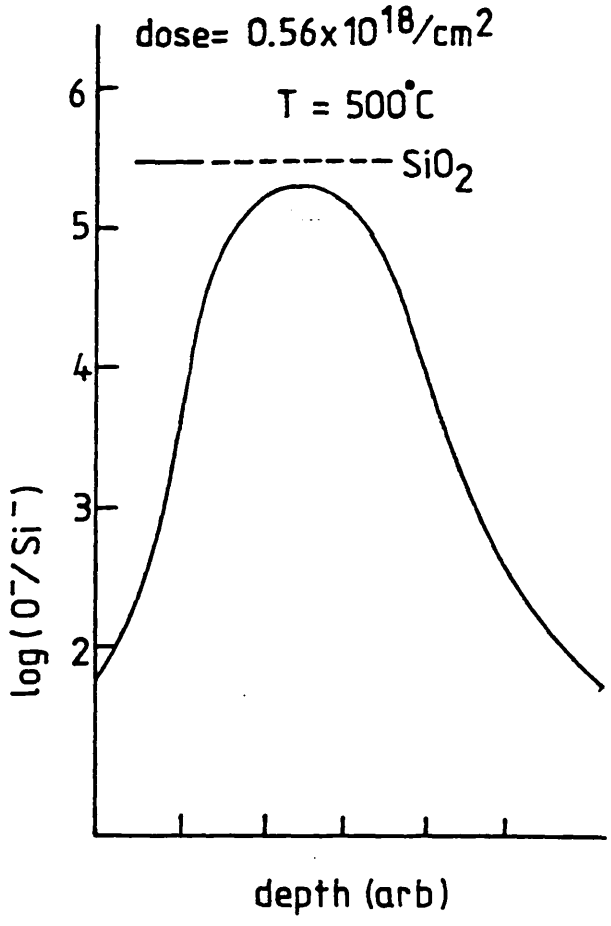


Fig. 2.4 As-implanted depth profile of oxygen in silicon [56].

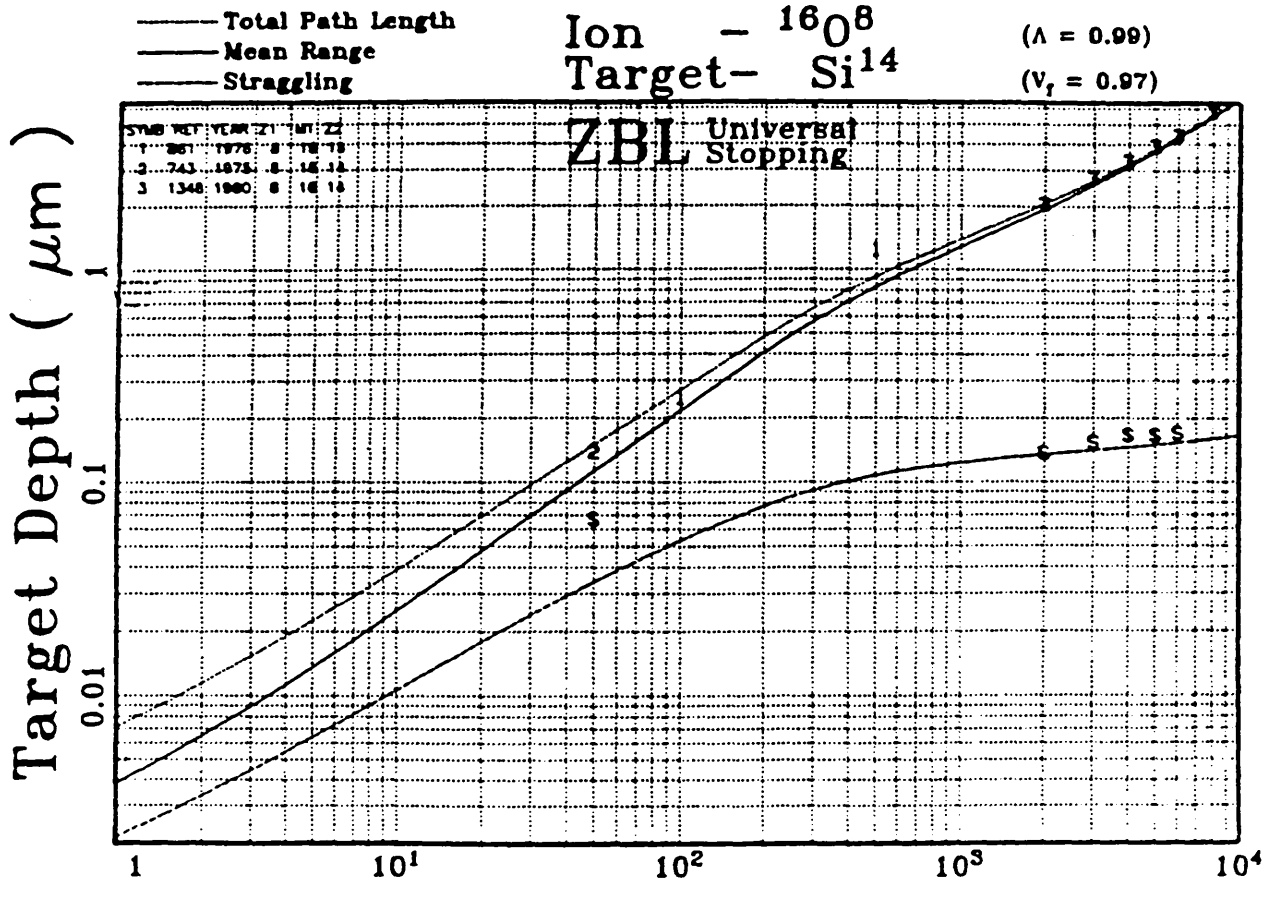


Fig. 2.5 Ion range table, from Ziegler et al [26]

$$n(x) = n(R_p) \exp\left[-\frac{(x-R_p)^2}{2\,\Delta R_p^2}\right] \qquad (2\text{-}5)$$

where the maximum concentration occurs at $x = R_p$, and ΔR_p is the standard deviation or "straggle" in the distribution. Clearly, the integral of n(x)dx gives the dose, Ψ, and the maximum concentration, $n(R_p)$, can be written as

$$n(R_p) = \frac{\Psi}{(2\pi)^{\frac{1}{2}}\,\Delta R_p} \approx \frac{0.4\,\Psi}{\Delta R_p} \qquad (2\text{-}6)$$

This Gaussian fit is almost always good near the peak, but there is a pronounced skewness in the actual distributions. To account for this skewness and any tailing character, higher moment distributions are needed.

A three-moment approach [29] uses two Gaussians, each with their own straggle, ΔR_{p1} and ΔR_{p2}. The Gaussians are joined together at their modal range, R_M. From the three fundamental calculated parameters, R_p, ΔR_p and the third moment ratio CM_{3p}, it is possible to calculate ΔR_{p1}, ΔR_{p2} and R_M. A distribution is then obtained by joining of two Gaussians:

$$n(x) = \frac{2\Psi}{(2\pi)^{\frac{1}{2}}\,(\Delta R_{p1} + \Delta R_{p2})} \exp\left[-\frac{(x-R_M)^2}{2\Delta R_{p1}^2}\right] \qquad x \geq R_M \qquad (2\text{-}7)$$

$$n(x) = \frac{2\Psi}{(2\pi)^{\frac{1}{2}}\,(\Delta R_{p1} + \Delta R_{p2})} \exp\left[-\frac{(x-R_M)^2}{2\Delta R_{p2}^2}\right] \qquad x \leq R_M \qquad (2\text{-}8)$$

A more exact description uses the "four moment" approach [30]: first (R_p), second (ΔR_p), third - skewness (γ) - and fourth - kurtosis (β). Kurtosis describes the tail character of the distribution. This approach is based on a Pearson IV type distribution giving a very complex result summarised in [28]. Excellent fits to the implanted distributions can be made using this approach.

Using the ZBL (Ziegler-Biersack-Littmark) theory to calculate stopping powers for ions in solids [26], graphs can be produced to predict projected ranges and straggles at various implantation energies. Such a graph for oxygen implanted into silicon is

shown in Fig.2.5, from which peak oxygen concentrations can be estimated quite accurately using equation 2-6. This computer simulation is known as TRIM (transport of ions in matter). It has been developed for determining ion range and damage distributions as well as angular and energy distributions of backscattered and transmitted ions. This is achieved mainly by applying an analytical formula for determining nuclear scattering angles and by suitably expanding the distance between collisions at high energies.

This method consists of following a large number of individual ion or particle "histories" in a target. Each history begins with a given energy, direction and position. The particle is assumed to change direction as a result of binary nuclear collisions and move in straight line free-flight-paths between collisions. The energy is reduced as a result of nuclear and electronic (inelastic) energy losses, and a history is terminated either when the energy drops below a pre-specified value or when the particle's position lies outside the target. The target is considered amorphous with atoms in random locations and thus the directional properties of the crystal lattices are ignored.

The nuclear and electronic energy losses are assumed to be independent. Thus, particles lose energy in discrete amounts in nuclear collisions and lose energy continuously from electronic interactions.

However, some modifications to the previous approaches may be necessary if ion channeling occurs [31]. This is when an incident ion finds entry into an open space between planes of atoms. Once the ion is inserted, steering forces of the atomic row potentials become operative and guide the ion towards the centre of the open space (channel). The ion is stably guided along the channel over considerable distances whilst it gradually loses energy through its gentle, glancing collisions on the edges of the channel and eventually scatters out of the channel. Channeled penetration distances can be several times the penetration in amorphous targets since the ions' energy loss rates are lower. Channeling is usually undesirable in ion implantation and its effects can be minimised by orienting the target so the incident ions enter in directions of high atomic density, although this is likely to increase the backscattered yield.

One other process which occurs is the "knock-on" effect. This is most obvious when ions are implanted through surface layers e.g. oxide or nitride caps. The atoms within the capping layers can be knocked into the underlying material by incident ions. This mixing is often undesirable but also unavoidable. Likewise, ions implanted into a material comprising of a number of thin layers tend to "smear" the

layers so that they are no longer clearly defined.

2.2.2 Lattice Damage

When ions enter a silicon crystal, they undergo electronic and nuclear scattering but only the nuclear interactions result in displaced silicon atoms.

Light and heavy implanted ions have a qualitatively different distribution of disorder along the stopping track. Light ions which enter the surface initially suffer electronic stopping. They gradually lose energy until nuclear stopping becomes dominant. Whilst undergoing nuclear stopping, they displace silicon atoms and also change direction. The displaced atom profile has a buried concentration peak. In contrast to this, heavy ions enter the surface and immediately encounter a relatively higher fraction of nuclear stopping and displace large numbers of silicon atoms near the surface. As they slow down, the nuclear stopping power of the primary incident ion is nearly constant over most of the energy values although recoiled atoms transfer deposited energy to greater depths. The final damage density profile exhibits a broad buried peak which is a replica of the recoiled range distribution.

If the energy transferred to a given silicon atom is much greater than the amount required to displace it, there will be multiple secondary (recoil or knock–on) displacements accompanied by defect clusters. Some of the highest density disorder regions may be locally amorphous, especially for heavy mass implanted ions, as in Fig.2.3a.

The nature of the disorder in the lattice is complex and depends on many factors such as target orientation and temperature. At room temperature there may be vacancies, divacancies, vacancy–impurity complexes etc. but above $\approx 500^{\circ}C$ dislocations may form [32]. In general, the disorder peak lies between the surface and the projected range peak.

2.2.3 Practical Ion Implantation

Fig.2.6 is a schematic diagram of a typical ion implanter. It shows the gas source into which a gas of the required ion is fed e.g. CO_2 for oxygen ion implantation. Next is the ion source containing an ion plasma with a variety of ions e.g. O^+, O_2^+, CO^+ at a pressure of $\approx 10^{-3}$mBar. The low pressure is to aid beam transport by reducing the amount of ion scattering. This whole section of the equipment is at a high potential, typically ≈50kV.

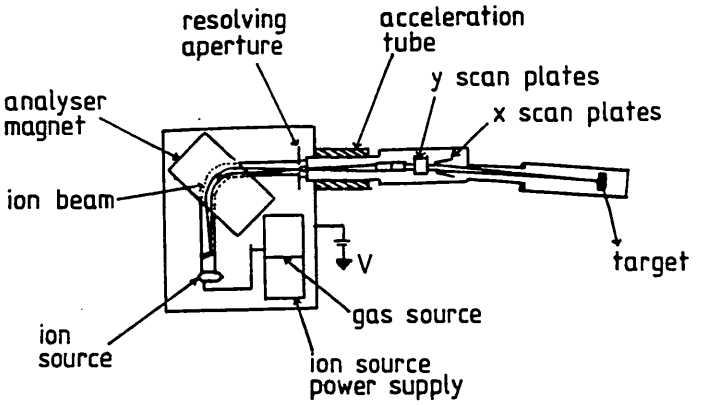


Fig.2.6 Schematic of typical ion implanter.

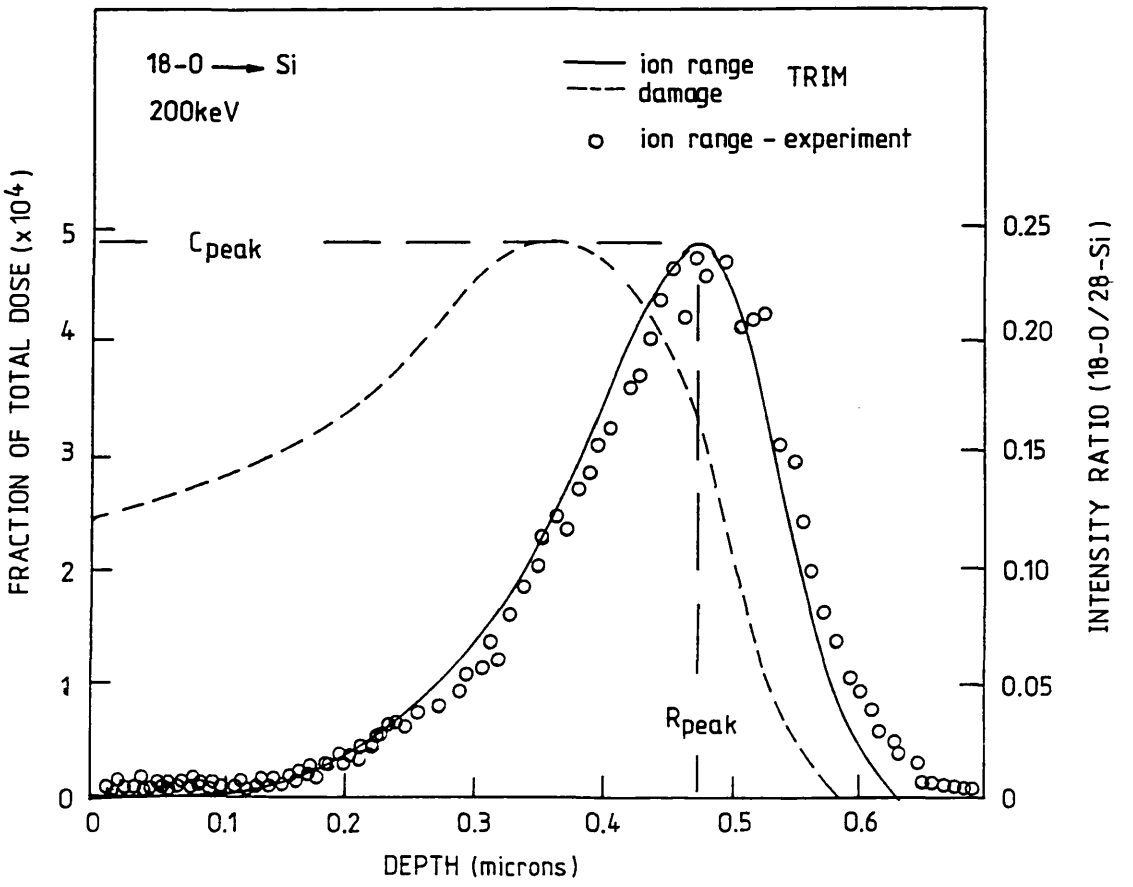


Fig. 2.7 Comparison of measured and theoretical ion and damage distributions.

The 50keV ion beam then passes through an analyser magnet which selects the required ion species by its charge/mass ratio, and rejects all other species. The selected ion beam enters the accelerator column, via a resolving slit (aperture), where it is accelerated to the desired final energy and onto the target.

The incident beam is always scanned over the surface of the target to give a uniform dose over the whole wafer. This is either done using x and y plates (electrostatic scanning as in Fig.2.6) or by maintaining a stationary beam and mechanically moving the wafer through it (mechanical scanning).

The designs of ion implanters obviously vary between manufacturers, but the above description is very general and describes the main features of most instruments.

A report of an ion implanter, specifically designed to produce SIMOX commercially, appeared in 1986 [32] using a rotating end station onto which the wafers were clamped, so that up to 19 wafers could be implanted simultaneously. Unfortunately, the beam current at that time (≈mA) was too low to make the process viable. However, a commercial SIMOX ion implanter has been developed and manufactured [33]. The basic design is essentially the same as above, but particular design requirements are necessary for this specialised application if it is to succeed commercially; they are summarised below:

i) beam energy of 150–200keV,
ii) dose uniformity better than ±5%,
iii) wafer temperature of 500–750°C,
iv) wafer pre-heating (if deemed necessary),
v) high beam current (>100mA), and
vi) ability to process 4- to 6-inch wafers.

To achieve these operating conditions, there is a two-chamber plasma generator, one containing the filament surrounded by argon and the second containing an oxygen plasma contained by a strong axial magnetic field. This allows a very high beam current to be generated (150–200mA) whilst still achieving an acceptable filament lifetime (25–40hours). The beam is extracted at 40–50keV and passes through a 90° analyser magnet although there is a also a post-acceleration magnetic analyser to increase the purity of the final beam, which is elliptical and stationary. The target wafers are mounted on a water-cooled revolving drum rotating at ≈200rpm (mechanical scanning).

Although the nitrogen content of the wafers produced by this implanter has been shown to be below 2 x 10^{17}atoms/cm^3 [34], there have been problems with surface carbon contamination and metallic impurities [35]. By removing all the graphite components in the end station and replacing them with polysilicon ones, the carbon level at the surface has been reduced by almost an order of magnitude. The metallic impurities such as Fe, Cu, Cr and Ni, which can cause high leakage currents in devices, were found to arise when the ion beam struck the beam-line in the dipole magnet which deflects the beam into the end station. The beam line was subsequently lined with polysilicon, which significantly reduced the level of contamination.

This implanter has been used successfully to produce good quality SIMOX material, but the amount of operating experience is still believed to be fairly limited.

2.2.4 Oxygen Ion Implantation Into Silicon

Fig.2.5 gives the projected range and straggle of oxygen ions implanted into silicon over a wide range of energies. For commercial SIMOX technology, the 150-200keV energy range is of most interest. However, as the implanted dose is increased, the table becomes increasingly inaccurate since no account is taken of sputtering, surface swelling and changes in the target's density and composition.

2.2.4.1 Low Dose Implantation (<10^{15} O^+/cm^2)

Fig.2.7 shows a TRIM [26] Monte Carlo simulation of the final ion distribution of $^{18}O^+$ ions implanted into silicon at 200keV. It compares very well with the experimentally determined SIMS results [38]. The distributions are skewed negative towards the surface, corresponding to the implant of light ($^{18}O^+$) ions into a heavier (^{28}Si) matrix. The peak oxygen concentration is ≈5 x 10^{18} atoms/cm^3, only just greater than the oxygen impurity level in as-grown Cz-Si [1], hence ^{18}O was used to clearly distinguish between the implanted atoms and the oxygen already present in the silicon. The TRIM simulation also shows that the defect depth distribution is more markedly skewed towards the surface.

2.2.4.2 Medium Dose Implantation (10^{15} - 10^{16} O^+/cm^2)

The production of lattice defects and localised amorphous regions with this skewed distribution means that at a dose, Ψ = 10^{15} O^+/cm^2, an amorphous layer will form near the peak of the ion distribution.

For SOI substrate applications (and indeed for nearly all semiconductor applications) it is essential that the surface silicon layer remains a single crystal, with the same crystallographic orientation as the substrate. If the silicon temperature is allowed to rise during the implant, either by beam-induced or external heating, the formation of an amorphous layer will be suppressed. It has been shown that if the wafer temperature exceeds 100°C, there is no dose up to $5 \times 10^{17}/cm^2$ which will create a buried amorphous layer [38], although one was believed to be observed at a dose of $10^{16}O^+/cm^2$ at 40keV with a wafer temperature of 170°C [39]. It is likely that this was due to the total damage being confined to a very small layer at such a low energy.

For most SIMOX production, implantation temperatures of 500–600°C are used [e.g. 40,41] so the amorphised regions continually revert to single crystal silicon by solid phase epitaxial regrowth. This regrowth is a thermally activated process with an activation energy of 2.3eV [42] or 2.7eV [43], giving regrowth rates of 1.1, 3.1, 8.3 and 23.8 nm/min at 500, 525, 550 and 575°C respectively for the $<110>$ and $<100>$ directions [36].

At very low oxygen concentrations, the oxygen atoms occupy bonded interstitial sites which bridge pairs of normal lattice atoms [1]. However, at the peak of the implanted oxygen distribution, the oxygen concentration greatly exceeds the solid solubility limit, which, at implantation temperatures of 500–600°C, will give rise to the precipitation of oxygen. These precipitates are expected to be very small (3–6nm [37] or 0.6–2.4nm [7]), although their size will obviously increase with the oxygen content as individual particles start to coalesce. Initially it was believed that the precipitates were coesite [44], but these particular features were later proved to be small regions of an hexagonal silicon phase [13] (see section 2.1.1), co-existing with amorphous oxide precipitates.

Compounds cannot be formed if they are unstable under ion impact [43], and a report by Kelly [45] classified SiO_2 as being chemically stable under ion bombardment but structurally unstable. Hence SiO_2 precipitates would be expected to be amorphous. Also, the infared absorption spectra of as-implanted material exhibited shoulders in the 8–9μm range [46], similar to features found in the spectra of amorphous SiO_2. As a result the small oxide precipitates are believed to be amorphous.

2.2.5 High Dose Implantation (>10^{17} O^+/cm^2)

At high doses, the oxygen content as measured by the peak of the ion range distribution is directly proportional to the dose until the peak value of the oxygen/silicon ratio approaches 2 [39,47]. At this point, SiO_2 precipitates overlap near the peak of the implanted distribution forming an amorphous SiO_2 layer. Further dose increases cause the oxygen concentration to increase mainly in the region between the surface and the buried layer (most probably due to radiation-enhanced diffusion), resulting in an increase in the oxide layer thickness.

High doses of oxygen also cause surface swelling, since Si-O compounds are formed even at concentrations of oxygen below the stoichiometric value of SiO_2 [43,48]. This leads to a volume expansion as mentioned in section 2.1.1. A dose of 1.5 x 10^{18} O^+/cm^2 at 200keV was found to cause the surface to swell by 100nm. Swelling tends to push the implanted depth profile effectively deeper into the substrate by moving the surface, whereas the sputtering, generally a less significant effect at 200keV, moves the profiles towards the surface. At 40-60keV [39] the sputter erosion at a dose of $10^{18}O^+/cm^2$ was believed to be ≈30nm, but higher implantation temperatures can increase the sputter yield [48].

The effects of swelling and sputtering (and substrate composition change) have been shown to cause discrepancies between measured and calculated depth distributions [49]. For example at 200keV, the oxygen and damage range peaks were calculated to be 425 and 340nm respectively but from SIMS and TEM measurements, they were believed to be 480±30 and 320±20nm respectively.

The critical dose, Ψ_{crit}, required to form a continuous buried oxide layer during implantation is, 1.4 x 10^{18} O^+/cm^2 [50] or 1.2-1.3 x $10^{18}O^+/cm^2$ [40] at 200keV, and is calculated to be ≈0.7 x 10^{18} O^+/cm^2 at 150 keV [26].

Although it has been difficult to prove categorically that the small precipitates are stoichiometric SiO_2, continuous buried layers are much larger and hence much easier to study. Watanabe and Tooi first formed oxide layers by ion implantation [51] and proved that they were stoichiometric SiO_2 using infared absorption techniques. Further infared analysis has confirmed this [39,52] as has work using SIMS [40] and a combination of Auger Electron Spectroscopy (AES) and X-ray Photon Spectroscopy (XPS) [53].

For implantation at room temperature, stoichiometry was never exceeded in the buried layers due to the rapid diffusion of excess oxygen to the wings of the

implanted distribution [40]. Even with implantation at liquid nitrogen temperatures (77K) [54], super-stoichiometry was not achieved. However, a recent report by Scanlon *et al* [55] suggests that super-stoichiometric implants can be achieved with implants performed at liquid helium temperature (6K). The nature of this excess oxygen is unknown at present.

2.2.5.1 Oxygen Distribution/Redistribution

Early work on oxide formation by low energy implantation (40-60keV) [39] suggested that the change from a skew-Gaussian to a flat-topped distribution occurs because once a stoichiometric oxide is formed, no more chemical bonds are available and any further implanted oxygen diffuses rapidly to the sub-stoichiometric regions around R_p. This redistribution of oxygen was seen to occur mainly in the region between R_p and the surface and was believed to be strongly influenced by implantation damage i.e. radiation-enhanced diffusion (RED). The oxygen was believed to diffuse all the way to the surface at low implantation energies. At higher energies it was observed to oxidise the silicon on either side of the buried layer since after the formation of a continuous layer, the Si/SiO_2 interfaces became more abrupt [43].

With a dose of $2 \times 10^{18} O^+/cm^2$ at 200keV, Rutherford Backscattering (RBS) analysis [47] showed the buried oxide to be 400nm thick, centred around a depth of 550nm. The buried oxide layer thickness has, to a first approximation, been shown to increase linearly with dose [56]. Hence, each incremental dose increase leads to a proportional increase in the volume of SiO_2 formed by the oxidation of silicon atoms. The gradients of the oxygen depth profile at the upper and lower interfaces were a decade in 170nm and a decade in 95nm respectively i.e. the upper interface is broader, in agreement with RED which will be greater in the highly disordered region nearer the surface.

Redistribution of the implanted oxygen was also seen to occur at sub-stoichiometric doses [41] where profile flattening was observed even though a stoichiometric oxide layer was not present. The effect was more prominent as T_i, the implantation temperature, increased. T_i was also found to have an effect on the oxygen distribution for stoichiometric implants [57]. A surface build-up of oxygen was seen at T_i values of 325-400°C (Fig.2.8a), but not at 500-600°C Fig.2.8b), and the plateau region of the oxygen distribution was found to be flatter at higher temperatures.

By implanting an ^{18}O tracer into an as-implanted ^{16}O SIMOX structure, Kilner *et al* [40] showed conclusively that there is isotope mixing and RED between the buried

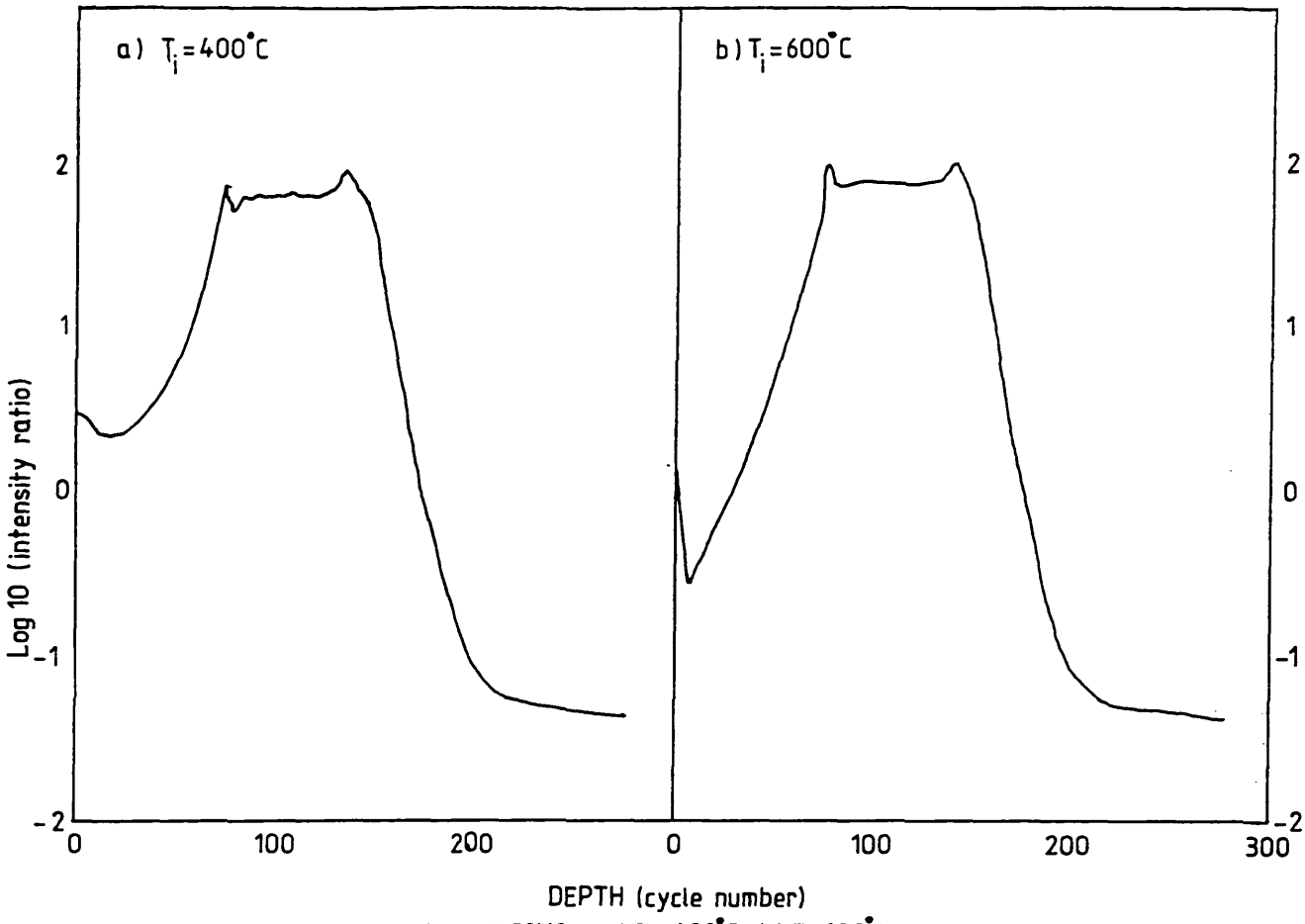


Fig. 2.8 SIMS profiles of as-implanted SIMOX: a) T_i=400°C, b) T_i=600°C.

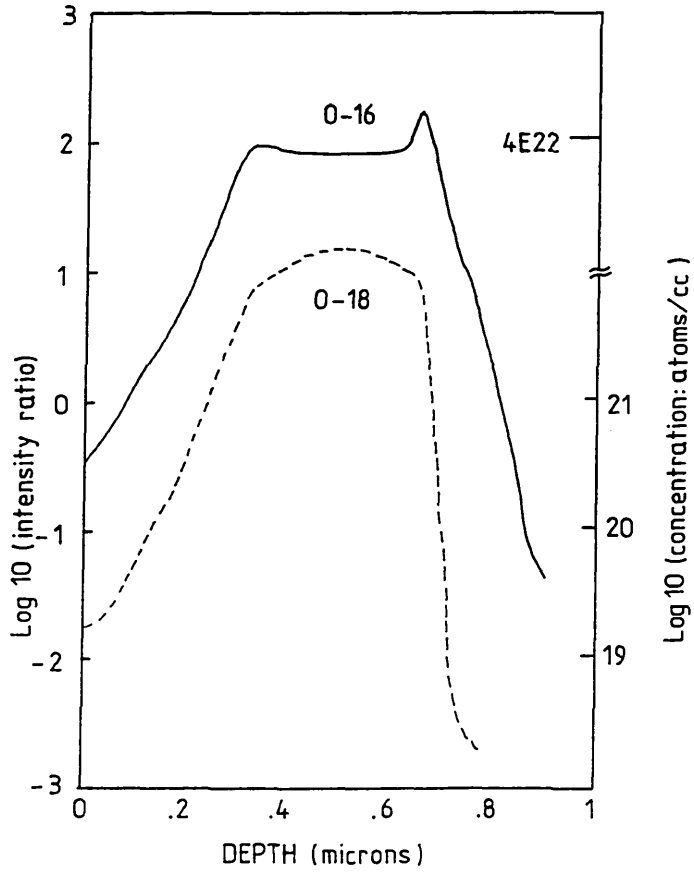


Fig. 2.9 SIMS oxygen depth profile of 210keV 18-O implanted into a pre-formed 200keV 16-O buried oxide.

oxide and the wafer surface. It was also shown that there is isotope exchange within the buried layer. However the most important feature of this work was the abrupt tailing-off of the ^{18}O distribution near the lower interface as shown in Fig.2.9. This indicated that once the oxygen is implanted into the buried oxide region, most of it diffuses to the upper Si/SiO_2 interface causing the oxide to grow towards the surface rather than towards the bulk. This is in agreement with work where buried oxides were formed near the surface of a silicon wafer already containing a deep buried nitride marker [36]. The distance between the lower (Si/SiO_2) interface and the marker was found to be virtually unchanged when the dose was increased from 1.6 to 2.0 x $10^{18}O^+/cm^2$, even though the oxide thickness increased. The distance between the surface and the marker also increased indicating that swelling was more prominent than sputtering.

In summary, it appears that once a continuous buried oxide layer has been formed, further implanted oxygen ions do not make the layer superstoichiometric; they diffuse very quickly to the interfaces partly by exchanging with oxygen atoms already in the buried layer. Most internal oxidation of the silicon occurs at the upper interface because there is more implantation damage which promotes radiation enhanced diffusion. This means that the silicon overlayer is consumed by the growing oxide. Furthermore, only by implanting high energy (300keV) $^{18}O^+$ ions into a buried $Si^{16}O_2$ layer formed at 200keV [58], was the ^{18}O found to penetrate the back interface and cause oxide growth to occur there.

2.2.3.2 Microstructure 1: Oxide Precipitates

In a typical high-dose ($\approx$1.8 x $10^{18}O^+/cm^2$) 200keV specimen, the oxygen concentration increases from $\approx 10^{20}/cm^3$ at the surface to $\approx$4 x $10^{22}/cm^3$ in the stoichiometric buried oxide [49]. Since this is well above the solid solubility limit, oxide precipitation occurs. In regions where the oxygen concentration is equal to that in stoichiometric SiO_2, a continuous layer of SiO_2 is formed. On both sides of this layer, SiO_2 precipitates nucleate either homogeneously, or heterogeneously on defects and/or impurities.

The thicknesses of the buried oxide and silicon overlayers have been measured by a number of workers, and their results are summarised in Table 2.1. It is clear that for the same dose, the layer thicknesses vary with implantation energy (c.f. Fig.2.5). Hemment *et al* [56] produced Fig.2.10 showing the oxide and corresponding silicon overlayer thicknesses for different doses at 200keV. This confirms, to a first approximation, that once a continuous oxide layer has been formed, each incremental dose of oxygen leads to a proportional increase in the volume of SiO_2 formed by the

Implantation Energy keV	Layer Thickness (nm)		Dose x1E18	T_i °C	Source
	Si	SiO_2			
180	300	450	2.0	475	Holland et al [63]
200	420	180	1.5	700	Jassaud et al [16]
200	400	200	1.7	600	Bruel et al [59]
200	+	300	1.8	550	Krause et al [49]
200	+	400	2.4	550	Krause et al [49]
200	180	650	3.0	500	Jassaud et al [62]
300	510	350	2.5	550	van Ommen [64]

+ not reported

Table 2.1 Characteristics of as-implanted SIMOX.

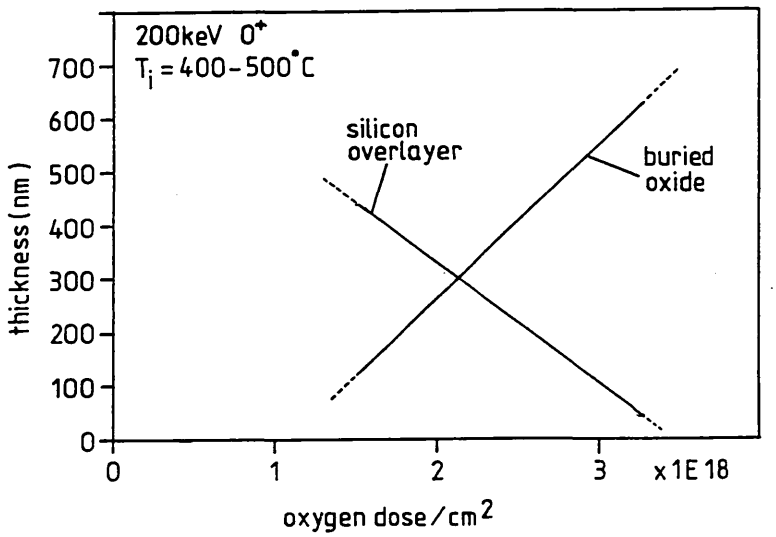


Fig 2.10 Thicknesses of silicon and buried oxide layers as a function of dose.

oxidation of silicon atoms.

The oxide precipitates have been studied near the upper and lower Si/SiO_2 interfaces, although the former is clearly more important since it is in this region that the electronic devices will ultimately be fabricated.

A TEM investigation of the silicon overlayer [59] has shown that a thin layer near the surface contains no precipitates, although the central region exhibited a granular contrast attributed to a network os small SiO_2 precipitates. These precipitates were observed to increase in size and decrease in density towards the upper Si/SiO_2 interface. The larger precipitates near the interface became elongated along the $<100>_{Si}$ axes, their diameters decreasing in the direction towards the surface. This gave a banded structure in the TEM similar to that observed near the lower interface [60] and in high-energy sub-stoichiometric implants [61].

A more detailed high-resolution TEM (HREM) analysis of the silicon overlayer [49] showed that the size of the oxide precipitates ranged from ≈12nm at the upper interface to ≈2nm 0.1μm away. The centre-to-centre distance decreased from 15nm to 6nm at 0.1μm from the interface giving precipitate densities ranging from 10^{17}–$10^{19}/cm^3$. Higher implantation temperatures gave larger precipitates at a given distance from the interface in the range 450–550°C.

The diffusion distances of oxygen during a 3-hour implant were calculated to be 0.4nm and 17nm at T_i values of 450 and 550°C respectively [49], although they are likely to be larger due to radiation-enhanced diffusion. With such small diffusion distances and high oxygen concentrations, a high density of small precipitates would be expected, which is in agreement with experimental observation.

In some instances, the small oxide precipitates have been observed to form a periodic structure as described below. This is important since during subsequent annealing, these structures evolve to give defect-free silicon overlayers.

In 1984, a TEM study by Holland *et al* [63] revealed that a region of "rippled" contrast was present after implanting to a dose of 1.5 x $10^{18}O^+/cm^2$ at 150keV. The dose, surprisingly, was not high enough to form a continuous buried oxide layer, but between 380 and 510nm there was a band containing large, randomly distributed precipitates in a single crystal silicon matrix. However, the precipitates located between 160 and 380nm were much smaller and were arranged in a periodic manner along the $<100>_{Si}$ directions.

Implanting with a very stable, low beam current, van Ommen *et al* [64–66] produced an ordered network of 2nm precipitates. These precipitates were also aligned along the $<100>_{Si}$ directions, forming a simple cubic superlattice with a periodicity of 5nm. The precipitates were believed to align themselves along the $<100>_{Si}$ directions, since these accommodate the strain most easily. This was proved by Raman scattering experiments [65] which showed that no residual stress was present with a precipitate superlattice, although there was stress with randomly distributed precipitates.

It was believed that the homogeneous distribution of precipitates could be attributed in some way to the emission of silicon interstitials at the Si/SiO_2 interfaces. At the lower interface, there is a region supersaturated with interstitials, but at the upper interface they can migrate to the surface, creating an excess of vacancies. These vacancies are believed to help create an accommodation volume for stress-free precipitation [16]. This explanation is possibly true for the special implantation conditions employed.

2.2.5.3 Microstructure 2: Crystallographic Defects

Implanting at elevated temperatures preserves the crystallinity of the silicon overlayer, although lattice defects are formed as a result of implantation damage and silicon interstitial emission from the growing oxide. The effect of substrate temperature was found to be critical in determining the crystalline quality of the silicon overlayer [63]. At 450°C, RBS measurements showed that a considerable amount of implantation damage remained, but this damage was not present at 475°C and above where defect clustering is inhibited (clustering at lower temperatures can lead to the nucleation of dislocation loops, stacking faults [67] and other stable damage structures). This is consistent with the work of Minear *et al* [68] and Matthews and Ashby [69] who only found defect clustering to occur below 500 and 450°C respectively. Irradiating the silicon specimens with protons or electrons below these temperatures produced clusters of point defects such as $\{311\}$-type defects, believed at the time to be associated with impurity precipitation. At high enough temperatures the point defects, once generated, can diffuse away from the region of high defect generation, but at lower temperatures they cluster and as a result, the effects of radiation-enhanced diffusion are reduced. The RBS spectra for 550°C-implanted wafers actually showed a *decrease* in the degree of crystallinity, but this was an overall measurement taking account of the presence of large, amorphous oxide precipitates.

TEM analysis showed the near-surface regions of the 450°C-implanted specimens to contain a high density of dislocation loops and tangles consistent with

radiation-induced damage: this was characteristic of all the low temperature implants. However, measurements showed that the wafer surface temperature often exceeded 800°C due to instantaneous beam heating, but dislocations were still present. This was attributed to dislocation nuclei being formed during the warm-up period at the start of the implant. Once nucleated, they are relatively stable and provide trapping sites for subsequently generated point defects, even at higher temperatures.

By heating the wafer to 500 or 600°C before implantation (pre-heating) [59,62], this "warm-up" period was eliminated with the result that the surface region became free from crystallographic defects, although some were present near the upper interface as well as large rod-like defects believed to be Frank dipoles located in the {111} planes, their depth corresponding to the peak of the damage distribution. The latter defects, however, were not identified unambiguously using HREM. They are believed to nucleate from implantation damage and grow by trapping silicon interstitials from the growing oxide.

The most comprehensive study of the microstructure of as-implanted SIMOX as a function of T_i has been carried out by Tuppen *et al* [60]. For a dose of 1.8 x $10^{18}O^+/cm^3$ at 200keV, there were two features common to all specimens implanted between 350 and 550°C: a 100nm surface silicon layer with a low oxygen content ($\leqslant$1 atomic %) and a dislocation density of $\approx 10^9/cm^2$, and a stoichiometric, amorphous buried oxide layer. The greatest effects of varying T_i were found in the regions on either side of the buried layer.

Fig.2.11 is a schematic representation of the microstructure as a function of T_i, with the corresponding Auger (oxygen) profiles for the highest and lowest temperature implants. At T_i=350°C, the regions numbered 1 to 8 were characterised as follows:

1. oxygen denuded zone with good quality crystalline silicon,
2. a band of damage coinciding with a "hump" in the oxygen depth profile; the dislocations in this region appeared to be generated by the SiO_2 precipitates,
3. a thin oxygen-free zone, also free from precipitates,
4. a narrow ($\approx$10nm) interfacial region composed of a discontinuous band of oxide, producing a spike in the oxygen profile,
5. a polycrystalline layer whose overall oxygen concentration is high, but below that of stoichiometric SiO_2, and which contains many, mainly randomly orientated silicon crystallites. Most of the oxygen in this layer is present as SiO_2.
6. A stoichiometric, amorphous buried oxide layer,
7. a polycrystalline silicon layer similar to 5, and

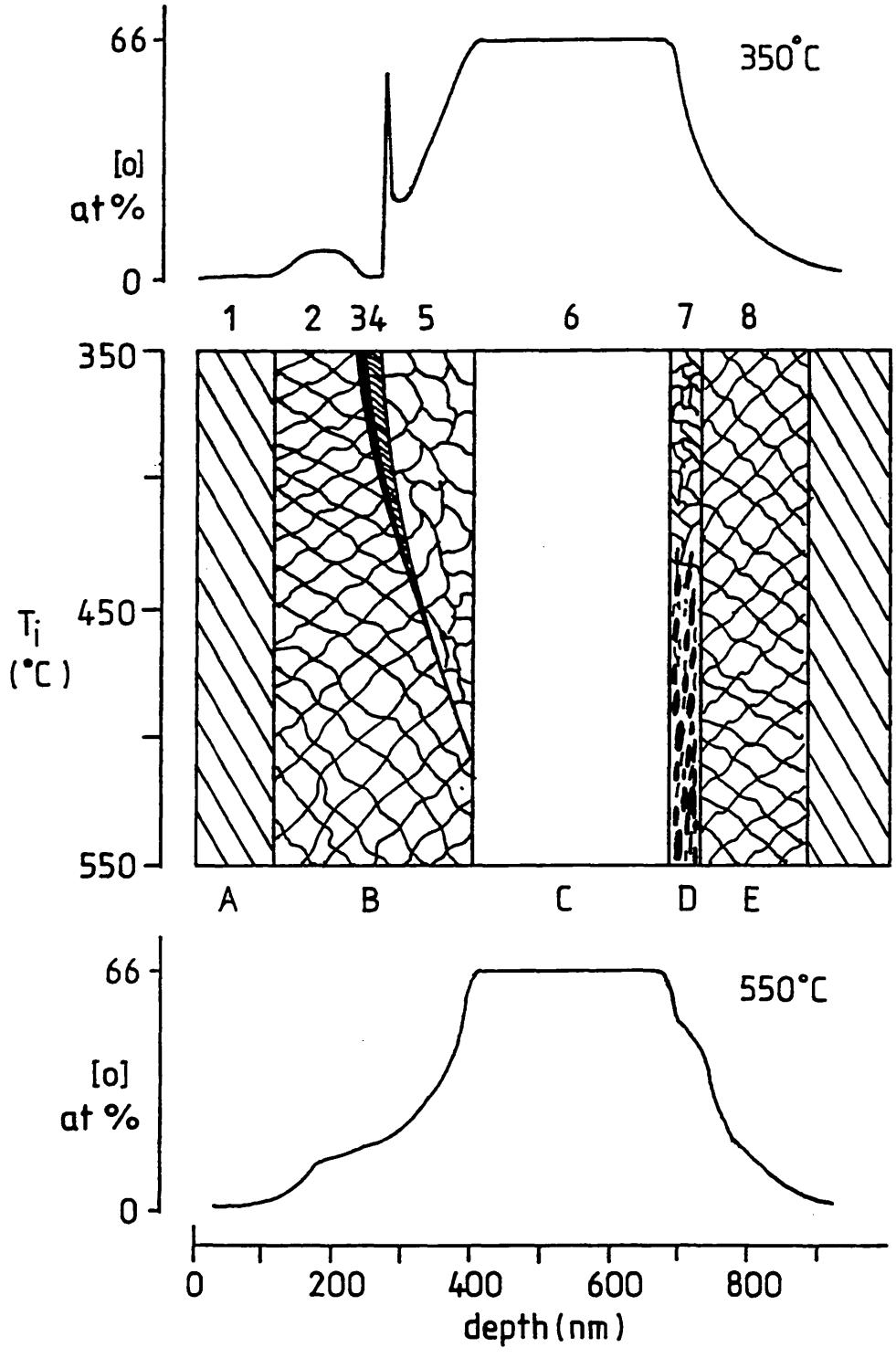


Fig.2.11 Schematic microstructure of as-implanted SIMOX as a function of T_i, with Auger oxygen profiles.

8. a damage zone.

The high-T_i implanted wafers have less structure; five regions are labelled A to E in the diagram. It can be seen that the damage region in the surface single crystal silicon layer (B) extends from the edge of the oxygen denuded zone (A) to the stoichiometric oxide (C). The lower Si/SiO_2 interface shows a banded structure corresponding to kinks in the oxygen profile.
These results suggest that there is some amorphisation of the silicon during the lower temperature implantation, resulting in regions of polycrystalline material, although this is eliminated at 500°C and above, which is in agreement with later work where twinned regions were found after a room temperature implant and an anneal at 725°C [61].

Reeson *et al* [70] gave a detailed report of the as-implanted microstructure for a range of 200keV doses implanted at ≈550°C. Essentially, six different regions were characterised (in order of depth from the surface) as follows:

1. A very thin surface layer of good quality single crystal silicon.
2. A thin layer with a high defect density.
3. A high quality single crystal layer with considerably fewer defects than region 2.
4. A highly defective layer (not present at high doses because it is consumed by the growing oxide).
5. A layer of very high oxygen content (stoichiometric at high doses).
6. A layer of highly defective silicon containing a high density of {311}-type defects.

The boundary between regions 2 and 3 is always at approximately the same depth, corresponding to the peak of the damage distribution. Stacking fault pairs were found in this region - one extrinsic and one intrinsic - which are likely to be due to the agglomeration of silicon interstitials and vacancies from implantation-induced Frenkel pairs.

The damage regions (2, 4 and 6) increase in thickness as the dose increases, but region 3 becomes smaller. Region 1 also increases in thickness with dose and is believed to be due to a reconstruction of the surface as the oxidation-induced silicon interstitials migrate there.

van Ommen [65,66] confirmed that the density and distribution of dislocations were closely related to the point defects created in the silicon overlayer, and also found the precipitate distribution to be important. He believed that the dislocations nucleate

from the Frenkel pairs caused by the collision cascades of the incident oxygen ions, which occur around the peak of the damage distribution between the buried oxide and the surface.

As internal oxidation proceeds, silicon interstitials are emitted and are trapped by the dislocation nuclei causing them to grow. The result is usually a random distribution of precipitates and a high density of dislocations, together with a high stress in the overlayer. However, when an ordered precipitate superlattice is present in the centre of the overlayer, there is no stress to aid dislocation formation in this region and the dislocations ($\approx 10^9/cm^2$) are confined to a region near the upper interface. As the dislocations grow, they reduce the supersaturation of silicon interstitials, allowing the precipitates to grow to larger sizes. Hence the two proceses are related.

With a sub-stoichiometric dose, dislocation loops (≈10nm) are found at a depth greater than the peak range [71]. However, once a continuous buried oxide layer has been formed, no dislocations are seen near the lower interface, although there are some defects on the {311} planes. van Ommen believed these to be coesite, but they were later found to be a consequence of the precipitation of silicon self-interstitials, which induces a local cubic-diamond → hexagonal distortion in the silicon lattice [13]. The absence of dislocations occurs for two reasons: firstly, there is very little implantation damage at this depth, and secondly, since most of the buried oxide growth occurs at the upper interface, less interstitials are produced.

During buried oxide formation, the point defects created by oxide growth (interstitials) are more dominant than those created by implantation in the region of the lower interface. Once the buried oxide becomes continuous, the interstitials can no longer be annihilated at the surface since the diffusion coefficient of silicon in SiO_2 is very low ($\approx 10^{-29} cm^2/s$) [72], so they have to diffuse to the back surface of the wafer, a distance three orders of magnitude greater. This significantly reduces the oxidation rate at the lower interface hence dislocations would not be expected to form.

In summary, dislocations nucleate from the implantation damage and grow by trapping interstitials, allowing oxide precipitates to grow at the same time. With a low beam current and a high implantation temperature (as suggested earlier by Minear *et al* [68]), a "steady state" is achieved allowing precipitates to nucleate homogeneously forming a superlattice. Any fluctuation in the implantation parameters can cause a supersaturation of point defects resulting in dislocations, heterogeneous nucleation of oxide on those dislocations, and no superlattice.

More recently, microvoids or cavities (≈3–13nm in diameter) have been found in some as–implanted SIMOX structures. They are believed to be caused by the coalescence of vacancies, which are in supersaturation, but only over a limited temperature range of 600–675°C [73]. Below 600°C, there is insufficient vacancy migration so that either vacancy–interstitial recombination is enhanced or the vacancies diffuse over smaller distances to oxide precipitates which act as sinks. However, above 675°C the supersaturation of vacancies is believed to be reduced because of the higher equilibrium vacancy concentration, making conditions more unfavourable for cavity nucleation. This last point seems rather unlikely since the equilibrium concentration of vacancies will still be minute compared to the number of vacancies produced by the implantation process.

The voids described above are in a random array, but by using a very high dose rate (≈mA/cm^2) with no screening surface oxide, regular arrays of cavities were found within ≈100nm of the surface. These cavities were aligned in columns along the direction of implantation, even though this was away from any of the major crystallographic axes in the silicon. It is believed that the voids are nucleated along the incident ion tracks, a high current density meaning that a large number of vacancies are available for nucleation and growth. The proximity of the cavities to the surface enables interstitials to migrate there which prevents recombination. However, no cavities were found when a screening oxide was present, probably because the surface then becomes a less–efficient interstitial sink. At lower dose rates (as in [73]), there are fewer vacancies, so although the nucleation rate may be as high, there are not enough vacancies to sustain the growth of them all. The result is that a large number of the cavities dissolve leaving a random array.

The cavities are believed to be stabilised by a high oxygen pressure. As well as taking oxygen atoms out of solution, this reduces the stress in the overlayer, thus reducing two causes of defect generation. It should be emphasised that cavities are not seen regularly and they only occur for a limited range of implantation conditions.

2.3 Manufacture Of SIMOX 2: Annealing

The as–implanted SIMOX substrates contain a high density of crystallographic defects and oxide precipitates making them unsuitable for device fabrication. Annealing at temperatures between ≈1050 and 1405°C for up to 10 hours greatly improves the quality of the silicon layers: the defect density is reduced and the oxide precipitates evolve by an Ostwald Ripening of the microstructure (section 2.1.2).

The first circuits reported on SIMOX [75] were processed on material annealed at 1150°C. This temperature seemed to be established as a standard value for 2–3 years, using resistively heated furnaces with a typical warm–up rate of 1.9°C/s over the range 900–1150°C [50]. This temperature was sufficient to give a silicon layer good enough for device fabrication or as a seed for subsequent epitaxial growth [e.g. 76]. By using higher temperature anneals e.g. 1210°C [62] or 1300°C [77], the silicon overlayer quality was improved. The highest annealing temperature reported was 1405°C [78] where lamp heaters heated the silicon surface almost to the melting point, taking 1 minute to heat from 200–1405°C.

Annealing was usually carried out in dry nitrogen, which caused severe pitting of the wafer surface (the same effect was present with vaccuum annealing) [61]. This was due to small amounts of residual oxygen, producing the volatile SiO phase which is favourable at low oxygen partial pressures and high temperatures. Capping the wafer with a low–temperature (≈725°C) CVD oxide protected the silicon overlayer but not the back surface of the wafer. To overcome the problem, ≈1% oxygen was added to the annealing ambient (White *et al* [61] used argon) which produces a thin (≈20nm) protective SiO_2 layer on the silicon surface. This is now standard practice for most workers, even when an oxide cap is also employed.

2.3.1 Low Dose

Annealing a 200keV specimen, implanted to a dose of 0.1 x $10^{18}O^+/cm^2$, at 1405°C for 30 minutes gave an oxygen distribution with two distinct bands [70,79,80]. These were found to be due to two layers of discrete oxide precipitates, one at a depth of 300nm and one at 490nm. The precipitates in the lower layer were larger, being typically 110nm across compared to ≈80nm in the upper layer. They all had the same morphology – truncated octahedra, bounded by the four $\{111\}_{Si}$ planes and the $(100)_{Si}$ plane parallel to the wafer surface. No threading dislocations were found, (i.e. between the precipitates and the surface) although there were dislocations connecting individual precipitates, within the layers and between them.

The layer depths correspond to peaks in the implantation profiles. The lower layer is at the same depth as that of the projected range peak which would have the highest oxygen concentration (and the largest oxide precipitates) after implantation whereas the upper layer is close to the damage peak. This region would have the highest point defect concentration, enhancing oxide precipitation and growth.

As the dose was increased to 0.25 x $10^{18}O^+/cm^2$, the precipitates in the lower band elongated in the direction parallel to the wafer surface and had a density of 4 x

$10^9/cm^2$ whilst the density of the upper band was 2 x $10^9/cm^2$. With a further increase in dose (to 0.35 x $10^{18}O^+/cm^2$), the lower precipitates continued to elongate, but the precipitate density in the upper layer decreased to 9 x $10^8/cm^2$. Dislocations still connected the precipitates but there were no overlayer threading dislocations.

2.3.2 Annealing at 1150°C

Annealing over the range 750–1150°C, after a low-temperature implant, resulted in a layer of twins and, as the annealing temperature increased, a layer of polysilicon between the monocrystalline silicon surface layer and the buried oxide [55]. At higher implantation temperatures, the annealed microstructure revealed no twins or polysilicon regions, only a single crystal silicon layer with a high defect density [81] indicating that no amorphisation of the silicon had occurred. Higher annealing temperatures were found to result in a more complete recovery of the silicon overlayer. For these 150keV-implanted specimens, no large oxide precipitates were found in the overlayers after annealing because they were consumed by the growing oxide layer. After this, most early work on the annealing of buried oxides used conditions consistent with device fabrication facilities. A typical set of conditions was 1150°C for 2 hours in dry nitrogen or argon [41].

For a dose of 1.8 x $10^{18}O^+/cm^2$ at 200keV, the annealed oxygen depth profiles show that oxygen diffuses from the wings of the distribution to the buried oxide and the surface, leaving a single crystal silicon overlayer with an oxygen concentration of $\approx 10^{18}$atoms/cm^3. If any instantaneous amorphisation does occur, this layer will regrow epitaxially using the surface as a seed [47]. The overlayer contained a high density of SiO_2 precipitates near the upper interface associated with dislocation loops and $\approx 10^{10}$ threading dislocations/cm^2. The precipitates were 10–50nm in size and had the same morphology as those described in section 2.3.1 [62]. The upper and lower interfaces were relatively rough and were characterised by a diphasic microstructure of SiO_2 bands in a silicon matrix. The bands were elongated parallel to the wafer surface – in a similar way to the buried oxide layer – suggesting that the oxidation rate is lowest on the {100} planes [79]. For higher implantation temperatures, the microstructures of the interfacial regions were found to be less complex, although the interfaces were still wavy.

For high doses ($\geq$1.8 x $10^{18}O^+/cm^2$), there is less or no banding at the lower interface, although it is still present at the upper interface, possibly due to radiation-enhanced oxidation. This is consistent with observations that most of the buried oxide growth occurs at the upper interface [40,55] for the same reasons as

those given in section 2.2.5.1 i.e. interstitials are trapped near the lower interface, suppressing further oxide growth there. Also, the microtwins and stacking faults at the upper interface in the as-implanted material are consumed by top oxide growth during annealing [49]. However stacking faults well above the buried oxide and {311} defects below disappear due to dispersal of the excess silicon interstitials from which they were formed.

The remaining dislocations (in an epitaxial layer grown on the overlayer) were found to be of the $a/2<110>$ type, possibly dissociated although this was not proved conclusively, and the overlayer dislocations have still never been characterised exactly.

There is still no general model for dislocation formation in SIMOX, but some of the proposed mechanisms are as follows :

i) the expansion of dislocation loops present in the as-implanted material,

ii) the formation and propagation of dislocation nuclei from the buried oxide's upper interface due to thermal stresses and the stresses associated with oxide growth, and

iii) the generation of excess interstitials during high-temperature annealing.

It seems likely that all three mechanisms contribute in some way to the formation of threading dislocations.

In most cases, rows of silicon inclusions are found in the buried oxide close to the lower interface [82]. The inclusions are all aligned in a single crystal orientation, with a misorientation of less than 1° from the substrate. They are faceted in cross-section (TEM) but are circular in plan view.

2.3.3 High-Temperature Annealing

The best material produced at $1150^{\circ}C$ is still far from the ideal structure in that the interfaces are broad and the overlayers still contain high-densities of precipitates and dislocations, even after annealing for 24 hours [79]. At a temperature of $1185^{\circ}C$ [59], there are fewer oxide precipitates. This reduction is even more apparent at $1210^{\circ}C$ [62] and $1250^{\circ}C$ [79], although in the former case the dose was 3 x $10^{18}O^{+}/cm^{2}$, meaning that the damage peak lay within the buried oxide towards the end of the implantation process. The remaining oxide precipitates increased in size in agreement with Ostwald Ripening where the precipitates with the largest radii are the most stable. The increased annealing temperature was also found to result in a slight reduction in dislocation density.

Two types of dislocation were observed after annealing: threading dislocations and dislocations between precipitates. The threading dislocations are very stable and do not disappear even after very high temperature annealing. However the dislocations pinned on precipitates are eliminated or become threading dislocations when the precipitates dissolve, which takes 4 hours at 1300°C or 30 minutes at 1405°C [16].

Annealing in the range 1200–1405°C resulted in a reduction in the dislocation density from $5 \times 10^9/cm^2$ to $3 \times 10^8/cm^2$, whilst the oxide layer thickness increased at the expense of the silicon overlayer [79]. In the same report, increasing the annealing time did not cause a very significant improvement in the structures compared to a 50°C increase in the isochronal annealing temperature.

At 1405°C, the interfaces were found to be very sharp, although there were $\approx 10^9$ defects/cm^2 at the upper interface. These 30nm defects were found to be microtwin lamallae and stacking fault tetrahedra [80].

Overall, as the annealing temperature increases, the dislocation and precipitate densities decrease and the interfaces become sharper.

The change in precipitate size and density occurs because the largest precipitates are the most stable. Once a buried oxide with flat interfaces has formed, it is effectively a precipitate with infinite radius and hence it becomes the *only* stable precipitate. This is most obvious at moderate doses, where continuous buried oxide layers are not formed during implantation. Annealing at 1405°C can result in a stoichiometric oxide layer at a dose of $0.6 \times 10^{18} O^+/cm^2$ [50] or $0.5 \times 10^{18} O^+/cm^2$ at 1400°C [61], at an implantation energy of 200keV. This is a result of the oxygen atoms being very mobile, allowing all of the smaller precipitates to dissolve. These buried layers, however, are characterised by wavy interfaces and large silicon inclusions [50,79]. It is believed that the high warm-up rate associated with these anneals is too fast to allow the Si/SiO_2 system to equilibrate resulting in the growth of a small number of large precipitates which coalesce to produce a very wavy interface. At higher doses, where the nucleation rate is increased, the interfaces are a result of the coalescence of a large number of small precipitates, making them much more planar.

After 6 hours at 1300°C [16] silicon inclusions, with approximately the same orientation as the substrate, are present at an almost constant distance of 25nm from the lower interface. They all have well-developed facets along the $\{100\}_{Si}$ and $\{111\}_{Si}$ planes, probably due to a lowering of surface energy and different oxidation rates along different crystallographic directions. These inclusions form from the regions where the lamellar structure existed prior to annealing. During annealing, the

SiO_2 precipitates coalesce and trap small volumes of silicon, which cannot be oxidised due to the very low diffusivity of Si in SiO_2. At 1405°C [80], the silicon inclusions were found to be misoriented from the substrate by as much as 5–10°. This suggests that the oxide becomes more fluid at this temperature so the inclusions can move or rotate under the influence of local stresses. This may also reduce stress in the overlayer giving a lower dislocation density.

2.3.4 Low Dislocation SIMOX

From the previous sections, it is clear that the threading dislocations cannot even be eliminated by annealing at ≈7°C below the melting point of silicon. Hence it is the microstructure of the as-implanted material which is critical in determining the microstructure after annealing. van Ommen has produced dislocation-free SIMOX (i.e. $\leq 10^5$ dislocations/cm^2) under special conditions, with great emphasis placed on the fact that a low beam current density of 1.5μA/cm^2 was necessary. Such a low beam current means the process will not be suitable to scale-up for commercial applications.

More recently, there have been reports of low dislocation SIMOX using multiple low-dose implants with intermediate anneals. One such report [84] used 6 doses of 0.3 x $10^{18}O^+$/cm^2 at 150keV, with 16 hour anneals at 1275°C between implants. This dose was chosen since doses of up to 0.6 x $10^{18}O^+$/cm^2 are known to result in dislocation-free overlayers at 150keV after a 2 hour anneal at 1150°C [83]. This was found to decrease the dislocation density by ≈4 orders of magnitude and gave excellent sructures with sharp interfaces. However, in a commercial environment, the long anneals make this processing unfeasible. Also, a 2 hour anneal after the first implant revealed two layers of oxide precipitates (rather than one layer after 16 hours) suggesting that longer anneal times (or higher annealing temperatures) really are necessary.

Another process used three implants of 6, 6 and 5 x $10^{17}O^+$/cm^2 at 150keV with intermediate 5 minute anneals at 1360°C [85]. This type of anneal was chosen to give short process times and good wafer-to-wafer control. Also, if anything should go wrong during the annealing cycle, only a single wafer would be affected. The best results were achieved by capping the wafer prior to each anneal. This process was found to decrease the dislocation density to below 10^5/cm^2, although more work is needed to produce planar interfaces and to remove all the SiO_2 precipitates from the silicon overlayer.

It could be suggested that by combining these techniques to have low incremental doses with rapid thermal processing at 1360°C, good quality SIMOX substrates may be produced more readily.

2.4 Electrical Characterisation

The first major electrical study of oxides formed by ion implantation and annealing (900°C), found them to be very similar to thermally grown SiO_2 [52]. The dielectric constant was 3.45 x 10^{-13}F/cm (c.f. 3.453 x 10^{-13} for thermally grown SiO_2) with a breakdown field strength of 5.3MV/cm (c.f. 5.5MV/cm). Later work [85] gave 5.9MV/cm, with a higher annealing temperature increasing the breakdown strength. The dopant concentration of the substrate was found to be unaffected by the implantation process but the oxide–semiconductor fixed charge density increased with implantation energy, having a value 9.7 x 10^{11}/cm^2 at 80keV. However, the density of surface states for the oxide/semiconductor interface was an order of magnitude greater than for thermally grown SiO_2, although the values were comparable after an 1100°C anneal, suggesting that implantation damage was responsible for the difference.

It was the work of Izumi *et al* [75] which caused a surge of interest in SIMOX in 1978. This report concerned a 19–stage CMOS ring oscillator fabricated in epitaxial silicon–on–SIMOX. A delay of 960ps/stage was reported (with a power dissipation of 406μW/stage), which was twice as fast as the equivalent circuits in bulk silicon.

When CMOS devices were fabricated in SIMOX implanted to a dose of 1.4 x $10^{18}O^+$/cm^2 (annealed 1150°C/2 hours), there was found to be a thin buried oxide containing silicon inclusions surrounded by diphasic SiO_2 regions [87]. The silicon inclusions were believed to provide an electrically conducting path through the oxide, giving a leakage current of 1μA/cm^2 at only 0.9V. In comparison, a dose of 2 x $10^{18}O^+$/cm^2 resulted in a thicker oxide with a leakage current of 0.1pA/cm^2 at 20V. The optimum dose was considered to be 1.8 x $10^{18}O^+$/cm^2. A similar dose–leakage dependence was found by Hemment *et al* [47] on 250 x 250μm^2 etched mesa structures, with resistivities similar to bulk SiO_2 ($\approx 10^{15}\Omega$cm) at a dose of 1.8 x $10^{18}O^+$/cm^2, annealed at 1150°C for 2 hours. Furthermore, with 270 x 270μm^2 islands (2 x $10^{18}O^+$/cm^2), enhancement mode NMOS devices exhibited channel mobilities of 360cm^2/Vs.

Improvements in device performance were shown to be possible by increasing the annealing temperature from 1150–1200–1250–1405°C [82]. Long channel mobilities of 590 and 175cm^2/Vs were reported for electrons and holes respectively at the highest annealing temperature. This is similar to another report [50] of electrical activity

and Hall mobilities being within 90% of bulk silicon values. The leakage currents were reported to be 1pA per micron channel width at 5V but this was improved to 0.1pA when care was taken to reduce metallic contamination during implantation [87]. In the same report, mobilities identical to those in bulk silicon were reported, although this was in an epitaxial silicon layer grown on the SIMOX overlayer, which would be expected to be better than in SIMOX alone. From Van der Pauw measurements over the temperature range 77–300K [88], the Hall mobilities of specimens annealed at high temperature were found to vary in the same way as in bulk silicon i.e. the mobilities increase with temperature when ionised impurity scattering prevails ($\lesssim$150K) followed by a decrease as soon as accoustic phonon scattering becomes dominant. However, annealing in nitrogen gave lower mobilities than in argon due to a background donor generation of $\approx 5 \times 10^{16}/cm^3$ increasing the scattering rate on ionised impurity centres.

Back–channel mobilities were still a problem where oxide precipitates were present near the upper interface (particularly for 200keV implants), but this was overcome by e.g. implanting boron into that region or annealing at higher temperatures to dissolve the precipitates. In this way, delay times as low as 250ps were achieved.

Thinner overlayers were found to enhance device performance because of an increase in the ratio of gate–controlled depletion charge to that controlled by the source and drain regions [89]. With 0.4μm gate length devices on 180nm silicon layers, delay times of 30ps at 4V and 19ps at 7V were achieved. However the minority carrier lifetime is reduced in SIMOX due to the threading dislocations, limiting its use, at present, for bipolar applications [90].

2.4.1 Subthreshold Characteristics

In order to maximise the drive current available from transistors, so obtaining the highest possible speed, it is necessary to set the threshold voltages to the lowest values consistent with being able to turn the transistor "off". Thus the slope of the subthreshold characteristic, expressed as the change in gate voltage required to reduce the drain current by an order of magnitude, is an important parameter in MOS device characterisation.

The characteristics of SIMOX MOSFETS differ significantly from those of bulk silicon transistors in two important ways:

i) as the drain voltage is increased, the subthreshold slope becomes steeper, which is the opposite to what would be expected in bulk, and

ii) as the gate length is reduced, the subthreshold slope improves, again in

contrast to bulk behaviour.

For one particular SIMOX/NMOS transistor [91], with a 3μm gate length, the slope improved from 140mV/dec at a drain voltage of 0.1V to 98mV/dec at 3V. For a similar device, the slope for a 10μm gate length was 130mV/dec compared to 73mV/dec for 1.5μm [82] with 50mV/dec being achieved at higher drain voltages. These figures are better than those expected for an "ideal" bulk device with the same dimensions and dopant levels. For a comparison, the very high speed 0.4μm channel-length transistors of Vasudev *et al* [89] had slopes of ≈60mV/dec at a drain voltage of ≈0.4V.

There is still conduction in the back-channel transistor i.e. in the silicon close to the Si/SiO_2 interface. This can either be suppressed by applying a substrate bias to invert the layer, or by implanting the oxygen at a temperature below ≈450°C to give an oxygen-rich polysilicon layer with a high resistivity after annealing. This is in contrast to section 2.4, where efforts were made to *increase* back-channel mobilities rather than decrease them.

A good review of the subthreshold characteristics, their cause and effect, is given in reference [92].

2.4.2 The Kink Effect

Channel carriers in an SOI MOSFET, operating at a high applied voltage, generate electron-hole pairs by impact ionisation near the drain region. The generated holes travel to the source, lowering the potential barrier for electrons flowing from the source to the channel, which results in an abrupt decrease in the drain-current vs drain-voltage characteristic (a kink) as shown in Fig.2.12 for an n-channel transistor [93]. The kink effect is one of the characteristics of SOI MOSFETS.

The kink effect shows its maximum at gate voltages somewhat lower than the drain voltages, since this is when the generation of holes induced by the avalanche process is at a maximum. The carrier accumulation due to the avalanche process produces an abrupt increase in the drain current. An increased recombination rate, subsequent to this process, suppresses a further increase in the current.

Although the kink is usually observed in the saturation regime, it also occurs in the subthreshold region [91]. There is a strong minimum in the kink-voltage vs gate-voltage relationship near the threshold voltage, due to the competing effects of increased drain current and reduced ionisation efficiency as the gate voltage increases.

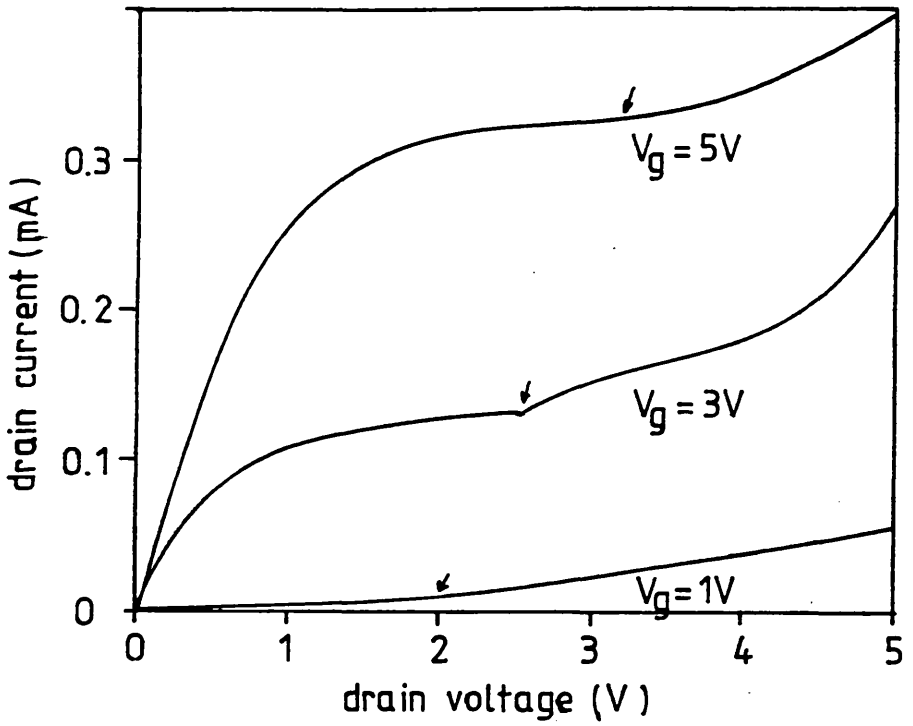


Fig. 2.12 Current-voltage characteristic of a SIMOX MOSFET showing kinks (arrowed).

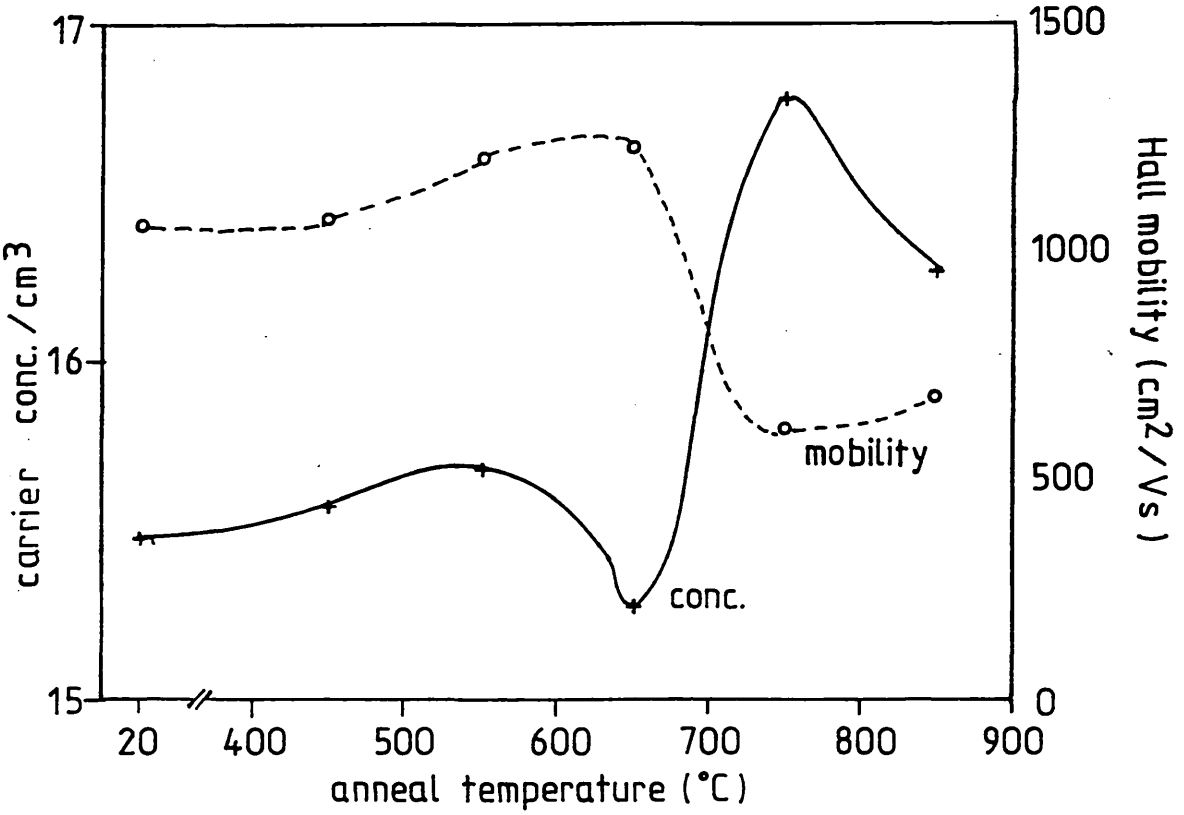


Fig. 2.13 Carrier concentration and Hall mobility as a function of annealing temperature.

Thus, in the subthreshold region, increasing the gate voltage produces an exponential increase in the drain current (available for impact ionisation) which dominates over the decrease in ionisation efficiency caused by the confinement of the channel current to a thinner inversion layer. The drain current increases more slowly above threshold, allowing the reduction in ionisation efficiency to produce a smaller avalanche current. It is the magnitude of the avalanche current which determines the source–body voltage and hence the occurrence of the kink.

For a fixed drain voltage, below but close to saturation, the transistor is operating more deeply towards the kink minimum as the gate voltage is increased from zero towards the threshold voltage, thus rapidly reducing the drain voltage. This is the origin of the steep subthreshold slopes described in section 2.4.1.

The kink effect has been thought of as a disadvantage of SOI technologies. While this may be the case for analog applications, the effect could be employed to advantage in high–speed switching circuits where it produces an increase in the current drive capability in the "on" state, and allows the threshold voltage to be set to a low value while retaining the ability to turn the device "off".

2.4.3 Oxygen–Related Donors

Interstitial oxygen within the silicon matrix can be electrically activated by annealing. Two types of donor are formed: Thermal Donors (TD) at 400–550°C and New Donors (ND) at ≈750°C. The generated electrons remain mobile even after cooling to room temperature or below, which is very important in SIMOX due to the high oxygen levels. Even after annealing at 1150°C, short anneals at 450 or 750°C are sufficient ot reduce the overlayer resistivity by 2 or 4 orders of magnitude respectively [88]. This can lead to an intolerable level of compensation or overdoping when TD are produced during normal MOS device fabrication.

Fig.2.13 shows the carrier concentrations of specimens annealed at 1340°C and then re–annealed between 450 and 850°C. There is a small amount of TD formation at 450°C ($\approx 10^{15}/cm^3$) with a smooth maximum at 550°C ($2–3 \times 10^{15}/cm^3$) [88]. The small increase at 450°C may be due to a limited number of TD formed during the cooling process after the high–temperature post–implantation anneal. The donors are completely destroyed at 650°C. There is then a very intense generation of ND at 750°C ($\approx 10^{17}/cm^3$), but at 900°C, these too are annihilated and the specimen recovers its initial resistivity [94]. The donor generation rates are $5 \times 10^{11}/cm^3s$ and $2 \times 10^{13}/cm^3s$ for TD and ND respectively. This correlates well with Hall mobilities (also shown on Fig.2.13), which are generally very high, and the region of

high mobility corresponds to the region of low carrier oncentration.

The generation of TD is related to the formation of Si–O complexes, but there is still uncertainty about ND generation. They are believed to result from SiO_x precipitates which contain a fixed positive charge and donor interface states. As a result, the energy bands are bent down and an accumulation layer is formed (in n–type material), this being the source of ND. The ND are essentially generated in the very early stages of annealing although this behaviour is modified by the level of carbon, which accentuates their formation. The main portion of the ND are likely to be situated around very small oxide precipitates and in a narrow region close to the buried oxide.

2.5 Non–Destructive Analysis

All of the analysis techniques mentioned so far are destructive. To a certain extent, even some electrical measurements are destructive in that they require e.g. metallisation or dopant implantation/diffusion to ensure a good contact. Since SIMOX has reached the production stage, there is a need to assess the quality of substrates quickly and accurately.

The main criteria for non–destructive analyses (NDA) are that they should be able to quantify overlayer thickness, defect levels, residual stress and impurity levels. To date, the principal methods reported are:

i) Photoluminescence,
ii) Raman spectroscopy,
iii) infared absorption, and
iv) optical interference.

In this section, the results of photoluminescence analysis will be discussed, which have been shown to be capable of characterising SIMOX substrates, at least semi–quantitatively.

2.5.1 Photoluminescence

Work on the photoluminescence spectra of deformed silicon single crystals [95] has shown that four distinct luminescence lines, called D1, D2, D3 and D4, appear at photon energies of 0.812, 0.875, 0.934 and 1.000eV respectively (Fig.2.14). As the dislocation density decreases from 10^6 to $5 \times 10^4/cm^2$, high resolution spectra have shown D1 and D2 to become narrower and have a fine structure of two components.

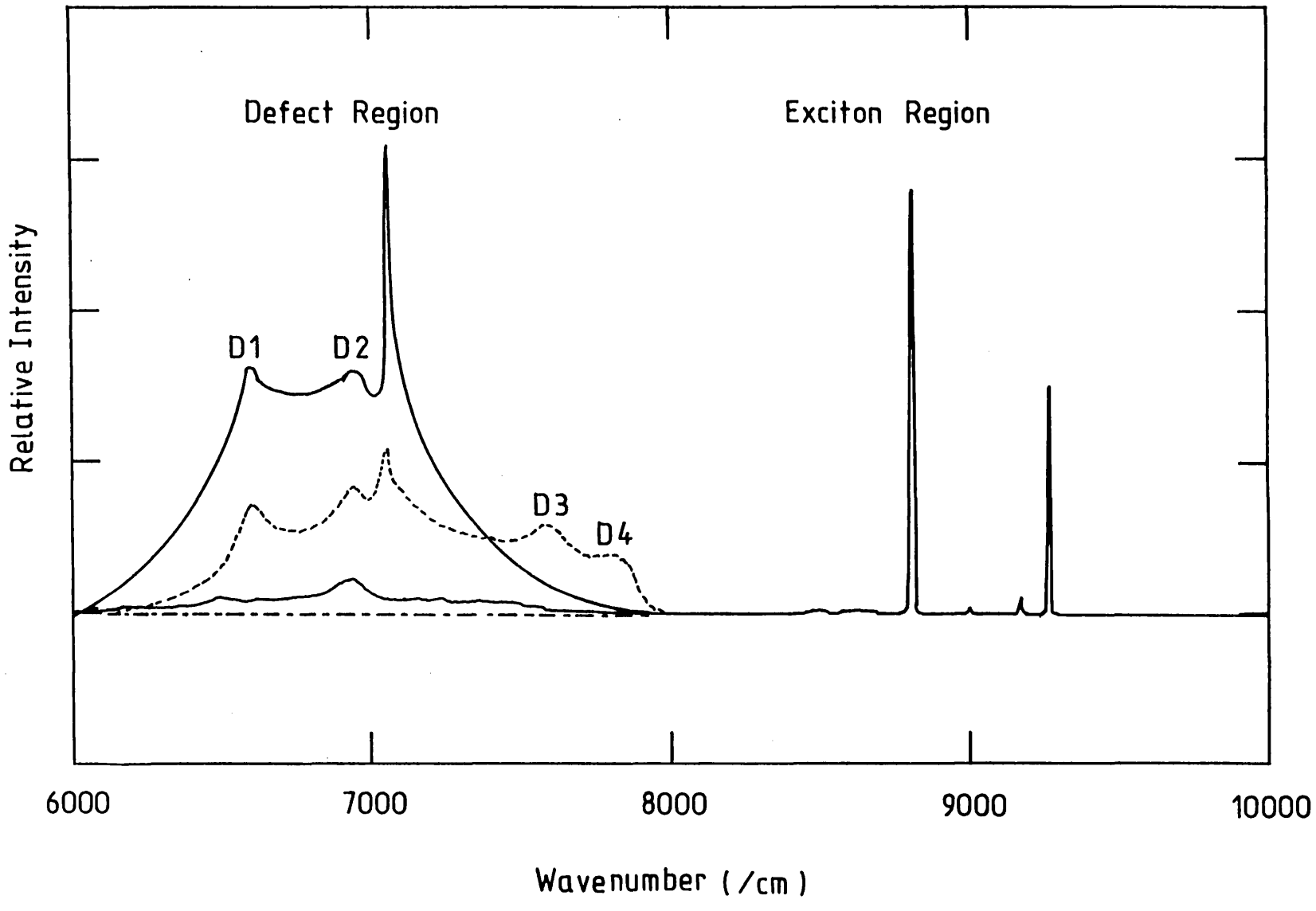


Fig.2.14 Photoluminescence spectra of SIMOX wafers annealed for 2 hours at 1150 (— upper), 1200 (----), 1250 (— lower) and 1275°C (——)

With increased deformation, D3 and D4 were found to shift (≈10meV) towards the lower energy end of the spectrum. This is related to a reduction in the energy band gap, hence the lines were attributed to transitions between allowed bands and levels associated with the dislocations. However, D1 and D2 shifted towards *higher* energies which suggested the lines were due to electron–hole recombination on the dislocation lines.

Later work [96] also found the line widths of D1 and D2 to increase with dislocation density, whereas the widths of D3 and D4 were independent. The dislocation density was also found to affect the intensities of D1, D3 and D4, but not D2. The intensities of D3 and D4 were much greater than those reported by Drozdov *et al* [95], where a different deformation procedure was employed. It was postulated that the different procedures may result in different concentrations of the defects responsible for the two bands in question. This is the most likely explanation since dopant atoms, at relatively low levels, were not found to affect this region of the spectrum. Furthermore, the lines were strongly polarised in directions parallel to the dislocation lines, so it was concluded that the "D" bands are due to dislocations, the discrepancies between intensities being due to different burgers vectors and line directions with respect to the incident beam.

In SIMOX, the "D" bands are also observed [97], although no process–related changes are observed in the extrinsic–to–extrinsic exciton line ratios (see Fig.2.14). This suggests that the doping levels, directly related to the ratios of the donor and acceptor to the intrinsic exciton lines [98], are not altered by oxygen implantation and annealing. Process related changes are, however, observed in the defect region of the spectrum at energies of 0.814, 0.862, 0.935 and 0.995eV, which are almost identical to those reported earlier for bulk silicon. A sharp feature was also observed at 0.874eV for specimens implanted to 1.8 x $10^{18}O^{+}/cm^{2}$, but not for higher doses. The origin of this spike is still unknown.

Fig.2.14 also shows that higher annealing temperatures give much lower band intensities associated with lower dislocation densities and a thicker surface region free from oxide precipitates. In particular, the intensities of D3 and D4 are lower in SIMOX than in deformed silicon or in oxygen–precipitated Cz–Si, where the formation of Thermal or New Donors may be more significant.

It is likely that the "D" line broadening is due to inhomogeneous stress distributions within the overlayers [99], related to both oxide precipitation and the presence of dislocations. However, after annealing at 1405°C, no defect–related lines were found in the spectra, even though $\approx 10^{8}$ dislocations/cm^{2} were known to be present with no

oxide precipitates. Also, the overall photoluminescent intensity was a factor of 2 weaker than that for an untreated specimen, probably the result of non-radiative recombination centres which are still present in this material. The absence of "D" lines was believed to be due to negligible absorption of the incident laser light in the overlayer.

It can be concluded that the "D" lines do arise from defects (probably strongly associated with dislocations), although as yet any results cannot be quantified absolutely - they are only relative from one specimen to another. The comparison of dislocations is easiest when there are no overlayer oxide precipitates to interfere with the spectra, and the penetration depth of the incident light is set so that it lies near the back of the silicon overlayer.

2.6 References For Chapter 2

[1] W.Kaiser, P.H.Keck and C.F.Lange, "Infared absorption and oxygen content in silicon and germanium", Phys. Rev. 101(4) (1956) 1264.

[2] G.D.Watkins, J.W.Corbett and R.S.McDonald, "Diffusion of oxygen in silicon", Japan. J. Appl. Phys. 53(10) (1982) 7097.

[3] W.Kaiser, "Electrical and optical properties of heat-treated silicon", Phys. Rev. 105(6) (1957) 1751.

[4] J.Osaka, N.Inoue and K.Wada, "Homogeneous nucleation of oxide precipitates in Czochralski-grown silicon", Appl. Phys. Lett. 36(4) (1980) 288.

[5] K.H.Yang, R.Anderson and H.F.Kappert, "Identification of oxide precipitates in annealed silicon crystals", Appl. Phys. Lett. 33(3) (1978) 225.

[6] S.Lederhandler and J.R.Patel, "Behaviour of oxygen in plastically deformed silicon", Phys. Rev. 103(2) (1957) 239.

[7] R.C.Newman, M.J.Binns, W.P.Brown, F.M.Livingston, S.Messoloras R.J.Stewart and J.G.Wilkes, "Precipitation of oxygen in silicon: kinetics, solubility, diffusivity and particle size", Physica, 116B (1983) 264.

[8] A.Bourret, J.Thibault-Desseaux and D.N.Seidman, "Early stages of oxygen segregation and precipitation in silicon", J. Appl. Phys. 55(4) (1984) 825.

[9] P.E.Freeland, K.A.Jackson, C.W.Lowe and J.R.Patel, "Precipitation of oxygen in silicon", Appl. Phys. Lett. 30(1) (1977) 31.

[10] J.Burke, "The Kinetics Of Phase Transformations In Metals", (Pergamon, London, 1965) Chaps. 6 & 7.

[11] H.Bender, "Investigation of the oxygen-related lattice defects in Czochralski silicon by means of electron microscopy techniques", Phys. Stat. Sol. (a), 86 (1984) 245

[12] W.Bergholz, J.L.Hutchison and P.Pirouz, "Enhanced oxygen diffusion and precipitation in silicon", Inst. Phys. Conf. Ser. N^0 76, section 1 (1985) 11.

[13] A.Bourret, "Defects induced by oxygen precipitation in silicon: a new hypothesis involving hexagonal silicon", Inst. Phys. Conf. Ser. N^0 87 (1987) 39

[14] T.Y.Tan and W.K.Tice, "Oxygen precipitation and the generation of dislocations in silicon", Phil. Mag. 34(4) (1976) 615.

[15] K.Wada, N.Inoue and K.Kohra, "Diffusion-limited growth of oxide precipitates in Czochralski silicon", J. Crystal Growth, 49 (1980) 749.

[16] C.Jassaud, J.Margail, J.Stoemenos and M.Bruel, "High temperature annealing of SIMOX layers: physical mechanisms of oxygen segregation", Proc. Mat. Res. Soc. Symp. 107 (1988).

[17] J.R.Patel, "Impurity clustering effects on dislocation generation in silicon", Discuss. Faraday Soc. 38 (1964) 201

[18] D.M.Maher, A.Staudinger and J.R.Patel, "Characterisation of structural defects in annealed silicon containing oxygen", J. Appl. Phys. 47 (1976) 3813.

[19] J.R.Patel and A.Authier, "X-ray topography of defects produced after heat treatment of dislocation free silicon containing oxygen", J. Appl. Phys. 46 (1975) 118

[20] J.R.Patel, K.A.Jackson and H.Reiss, "Oxygen precipitation and stacking-fault formation in dislocation-free silicon", J. Appl. Phys. 48(12) (1977) 5279.

[21] K.Wada, H.Takaoka, N.Inoue and K.Kohra, "Growth of stacking faults by Bardeen-Herring mechanism in Czochralski silicon", Japan. J. Appl. Phys. 18(8) (1979) 1629.

[22] B. Leroy, "Kinetics of growth of the oxidation stacking faults: the capture of interstitials by partial dislocations", J. Appl. Phys. 53(7) (1982) 4779.

[23] H.Takaoka, J.Oosaka and N.Inoue, "Stacking faults from oxide precipitates in Cz silicon", Japan. J. Appl. Phys. 18 (1979) supplement 18-1, 179.

[24] K. Wada and N.Inoue, "Diffusion coefficient of self-interstitials determined by bulk stacking fault growth in Cz-Silicon", Inst. Phys. Conf. Ser. Nº 59, (1980) 461.

[25] C.Plougonven, B.Leroy, J.Arhan and A.Lecuiller. "Ring-shaped stacking faults induced by oxide precipitates in silicon", J. Appl. Phys. 49(5) (1978) 2711.

[26] J.F.Ziegler, J.P.Biersack and U.Littmark, "The Stopping And Range Of Ions In Solids", (Pergamon Press, New York, 1985)

[27] S.N.Bunker and A.J.Armini, "Modelling of concentration profiles from very high dose ion implantation", presented at the 6th International conference on Ion Beam Modification of Materials, Tokyo, Japan, (June, 1988).

[28] T.E.Seidel, in "VLSI Technology", 2nd printing, Ed. S.M.Sze (McGraw-Hill, Singapore, 1984) Ch.6.

[29] J.F.Gibbons, W.S.Johnson and S.W.Mylroie, in "Projected Range In Semiconductors", Eds. Dowden, Hutchinson and Ross (Academic Press, New York, 1975) Vol. 2.

[30] W.K.Hofker, "Implantation of boron in silicon", Philips Res. Rep. Suppl. N^0 8 (1975).

[31] D.V.Morgan (Ed.), "Channeling: Theory, Observation And Applications", (Wiley, New York, 1973).

[32] T.A.Woods, E.Antonelli, R.A.Collins, D.J.Chivers and G.Dearnaley, "The formation of buried oxide layers by ion implantatiom", Vacuum, 36(11/12) (1986) 883.

[33] J.P.Ruffell, D.H.Douglas-Hamilton, R.E.Kaim and K.Izumi, "A high current, high voltage oxygen ion implanter", Nucl. Instr. and Meth. in Phys. Res. B21 (1987) 229.

[34] J.A.Kilner, R.J.Chater, S.Biswas, P.L.F.Hemment and K.J.Reeson, "Determination of the nitrogen content of as-implanted and annealed SIMOX substrates", Mat. Res. Soc. Symp. Proc. 107 (1988) 151.

[35] B.Cordts and M.Guerra, "Contamination control in SIMOX implanters", Mat. Res. Soc. Symp. Proc. 107 (1988) 147.

[36] S.S.Lau, S.Matteson, J.W.Mayer, P.Revesz, J.Gyulai, J.Roth, T.W.Sigmon and T.Cass, "Improvement of crystalline quality of epitaxial silicon layers by ion implantation techniques", Appl. Phys. Lett. 34(1) (1979) 76.

[37] R.J.Chater, J.A.Kilner, P.L.F.Hemment, K.J.Reeson and R.F.Peart, "Mass transport studies of buried layer formation by high dose implantation into silicon", Proc. 5th International Symp. on Silicon. Mat. Sci. Tech., Eds. H.R.Huff, T.Abe and B.Kolbesen, (Electrochem. Soc., New Jersey, 1986) 652.

[38] F.F.Morehead and B.L.Crowder, in 1st International Conf. on Ion Implantation, 1000 Oaks, Eds. F.Eisen and L.Chadderton (Gordon and Breach, New York, 1971).

[39] S.S.Gill and I.H.Wilson, "Rutherford backscattering analysis of oxide layers formed by ion implantation into single crystal silicon", Thin Solid Films, 55 (1978) 435.

[40] J.A.Kilner, R.J.Chater, P.L.F.Hemment, R.F.Peart, E.A.Maydell-Ondrusz, M.R.Taylor and R.P.Arrowsmith, "SIMS and ^{18}O tracer studies of the redistribution of oxygen in buried SiO_2 layers formed by high dose implantation", Nucl. Instr. and Meth. In Phys. Res. B7/8 (1985) 293.

[41] S.Maeyama and K.Kajiyama, "Surface silicon crystallinity and anomalous composition profiles of buried SiO_2 and Si_3N_4 layers fabricated by oxygen and nitrogen implantation in silicon", Japan. J. Appl. Phys. 21(5) (1982) 744.

[42] L.Csepregi, J.W.Mayer and T.W.Sigmon, "Regrowth behaviour of ion-implanted amorphous layers on <111> silicon", Appl. Phys. Lett. 29(2) (1976) 92.

[43] I.H.Wilson, "Synthesis of silicon dioxide by ion implantation", Nucl. Instr. and Meth. in Phys. Res. B1 (1983) 331.

[44] W.Bergholz, J.L.Hutchison and P.Pirouz, "Enhanced oxygen diffusion and precipitation in silicon", Inst. Phys. Conf. Ser. Nº 76 (1985) 11.

[45] R.Kelly, "On the nature of the phases formed when metals are implanted with oxygen or nitrogen", Rad. Effects, 64 (1982) 205.

[46] J.Dylewski and M.C.Joshi, "Formation of thin SiO_2 films by high dose oxygen ion implantation into silicon and their investigation by IR techniques", Thin Solid Films, 35 (1976) 327.

[47] P.L.F.Hemment, E.Maydell-Ondrusz, K.G.Stephens, J.Butcher, D.Ioannou and J.Alderman, "Formation of buried insulating layers in silicon by the implantation of high doses of oxygen", Nucl. Instr. Meths. 209/210 (1983) 157.

[48] H.U.Jager, "Modelling of oxygen depth profiles in high dose oxygen-implanted silicon", Presented at the 2nd International Conference on Energy Pulse and Particle Beam Modification Of Materials, Dresden, Sep. 1987.

[49] S.J.Krause, C.O.Jung, T.S.Ravi, S.R.Wilson and D.E.Burke, "Precipitate and defect formation in oxygen implanted silicon-on-insulator material", Proc. Mat. Res. Soc. Symp., Boston, Ma., 107 (1987) 93.

[50] P.L.F.Hemment, K.J.Reeson, J.A.Kilner, R.J.Chater, C.Marsh, G.R.Booker, G.K.Celler and J.Stoemenos, "Ion beam synthesis of thin buried layers of SiO_2 in silicon", Vacuum, 36(11/12) (1986) 877.

[51] M.Watanabe and A.Tooi, "Formation of SiO_2 films by oxygen-ion bombardment", Japan. J. Appl. Phys., 5 (1966) 737.

[52] M.H.Badawi and K.V.Anand, "A study of silicon oxides prepared by oxygen implantation into silicon", J. Phys. D: Appl. Phys. 10 (1977) 1931.

[53] T.Hayashi, S.Maeyama and S.Yoshi, "TEM, AES and XPS studies of Si layer on buried SiO_2 layer formed by high-dose oxygen ion-implantation", Japan. J. Appl. Phys., 19(6) (1980) 1111.

[54] F.Namavar, T.I.Budnick, F.H.Sanchez and H.C.Hayden, Proc. Mat. Res. Soc. Symp. 53 (1986) 233.

[55] P.J.Scanlon, P.L.F.Hemment, A.K.Robinson, K.J.Reeson, R.J.Chater, J.A.Kilner and G.Harbeke, "Evidence for oxygen concentration changes induced by low-temperature O-18 implantation in a SIMOX buried-oxide layer", Proc. Mat. Res. Soc. Symp., 107 (1987) 141.

[56] P.L.F.Hemment, E.Maydell-Ondrusz, K.G.Stephens, J.A.Kilner and J.Butcher, "Oxygen distributions in sysnthesized SiO_2 layers formed by high dose O^+ implantation into silicon", Vacuum, 34(1-2) (1984) 203.

[57] J.A.Kilner, S.D.Littlewood, P.L.F.Hemment, E.Maydell-Ondrusz and K.G.Stephens, "SIMS analysis of silicon-on-insulator structures formed by high-dose O^+ implantation into silicon", Nucl. Instr. and Meths. in Phys. Res., 218 (1983) 573.

[58] R.J.Chater, J.A.Kilner, P.L.F.Hemment, K.J.Reeson and J.R.Davis, "The evolution of the Si/SiO_2 interface in buried oxide layers formed by high dose oxygen implantation into silicon", Nucl. Instr. and Meths. in Phys. Res., B19/20 (1987) 290.

[59] M.Bruel, J.Margail, J.Stoemenos, P.Martin and C.Jassaud, "Formation of buried insulating layers by high dose oxygen implantation under controlled temperature conditions", Vacuum 35(12) (1985) 589.

[60] C.G.Tuppen, M.R.Taylor, P.L.F.Hemment and R.P.Arrowsmith, "Effects of implantation temperature on the properties of buried oxide layers in silicon formed by oxygen ion implantation", Appl. Phys. Lett. 45(1) (1984) 57.

[61] A.E.White, K.T.Short, J.L.Batstone, D.C.Jacobson, J.M.Poate and K.W.West, "Mechanisms of buried oxide formation by ion implantation", Appl. Phys. Lett. 50(1) (1987) 19.

[62] C.Jassaud, J.Stoemenos, J.Margail, M.Dupuy, B.Blanchard and M.Bruel, "Microstructure of silicon implanted with high dose oxygen ions", Appl. Phys. Lett. 46(11) (1985) 1064.

[63] O.W.Holland, T.P.Sjoreen, D.Fathy and J.Narayan, "Influence of substrate temperature on the formation of buried oxide and surface crystallinity during high dose oxygen implantation into Si", Appl. Phys. Lett. 45(10) (1984) 1081.

[64] A.H.van Ommen, B.H.Koek and M.P.A.Viegers, "Ordering of oxide precipitates in oxygen implanted silicon", Appl. Phys. Lett. 49(17) (1986) 1062.

[65] A.H.van Ommen and M.P.A.Viegers, "Structural study of the formation of a buried oxide layer by oxygen implantation", Inst. Phys. Conf. Ser. Nº87 (1987).

[66] A.H.van Ommen, "Low dislocation SOI by oxygen implantation", Proc. Mat. Res. Soc. Symp. 107 (1988) 43.

[67] D.Fathy, O.L.Krivanek, R.W.Carpenter and S.R.Wilson, "TEM, microdiffraction and electrical studies of buried SiO_2 layers formed by high dose oxygen implantation", Inst. Phys. Conf. Ser. Nº67 (1983) 479.

[68] R.L.Minear, D.G.Nelson and J.F.Gibbons, "Enhanced diffusion in Si and Ge by light ion implantation", J. Appl. Phys. 43(8) (1972) 3468.

[69] M.D.Matthews and S.J.Ashby, "The dynamic observation of the formation of defects in silicon under electron and proton irradiation", Phil. Mag. 27(6) (1973) 1313.

[70] K.J.Reeson, C.D.Marsh, K.N.Christensen, A.K.Robinson, R.J.Chater, J.A.Kilner, G.Harbeke, E.F.Steigmeir, P.L.F.Hemment, G.R.Booker and G.K.Celler, "The role of implantation temperature and dose in the control of the microstructure of SIMOX substrates", to be published in Microelectronics Engineering.

[71] P.L.F.Hemment, E.A.Maydell-Ondrusz, J.E.Castle, R.Paynter, M.C.Wilson, G.R.Booker, J.A.Kilner and R.P.Arrowsmith, "Precipitation of oxygen in single-crystal silicon implanted with high doses of oxygen", Thin Solid Films, 128 (1985) 125.

[72] G.Brebec, C.Sella, J.Bevenot and C.Martin, "Diffusion du silicium dans la silice amorphe", Acta. Metal. 28 (1980) 327.

[73] M.K.El-Ghor, S.J.Pennycook, T.P.Sjoreen, C.W.White and J.Narayan, "Cavity formation in SIMOX structures", Mat. Res. Soc. Symp. Proc. 107 (1988) 79.

[74] W.P.Maszara, "Oxygen precipitation along individual ion tracks during high dose O^+ implantation into silicon", Mat. Res. Soc. Symp. Proc. 93 (1987) 143.

[75] K.Izumi, M.Doken and H.Ariyoshi, "C.M.O.S. Devices fabricated on buried SiO_2 layers formed by oxygen implantation into silicon", Electron. Lett. 14(18) (1978) 593.

[76] A.Mogro-Campero, N.Lewis and S.A.Al-Marayati, "Macroscopic defects in epitaxial silicon on SIMOX and in annealed SIMOX", Mat. Res. Soc. Symp. Proc. 107 (1988) 123.

[77] J.Stoemenos and J.Margail, "Nucleation and growth of oxide Precipitates in silicon implanted with oxygen", Thin Solid Films, 135 (1985) 115.

[78] G.K.Celler, P.L.F.Hemment, K.W.West and J.M.Gibson, "High quality Si-on-SiO_2 films by large dose oxygen implantation and lamp annealing", Appl. Phys. Lett. 48(8) (1986) 532.

[79] C.D.Marsh, G.R.Booker, K.J.Reeson, P.L.F.Hemment, R.J.Chater, J.A.Kilner, J.A.Alderman and G.Celler, "The influence of high temperature anneals on the microstructure of silicon-on-insulator (SOI) structures formed by high-dose oxygen implantation into silicon", Proc. Euro. Mat. Res. Soc. Conf, Strasbourg (1986) 137.

[80] C.D.Marsh, J.L.Hutchison, G.R.Booker, K.J.Reeson, P.L.F.Hemment and G.K.Celler, "TEM studies of high-dose oxygen implanted silicon annealed at 1405°C", Inst. Phys. Conf. Ser. Nº 87 (1987).

[81] T.Hayashi, H.Okamoto and Y.Homma, "Defects in Si on buried SiO_2 layer formed by very high dose oxygen-implantation", Inst. Phys. Conf. Ser. Nº59, (1980) 533.

[82] P.D.Augustus, P.Knightly and J.C.Alderman, "Observations of SOI structures made by high-dose oxygen implantation", Inst. Phys. Conf. Ser. Nº87 (1987) 397.

[83] Y.Homma, M.Oshima and T.Hayashi, "An investigation of the properties of an epitaxial Si layer on a substrate with a buried SiO_2 layer formed by oxygen ion implantation", Japan. J. Appl. Phys. 21(6) (1982) 890.

[84] T.F.Cheek and D.Shen, "Dislocation reduction on SIMOX substrates by using multiple implants", Mat. Res. Soc. Symp. Proc. 107 (1988) 53.

[85] J.Blake, J.C.Gelpey, D.M.Lee, L.Rowland and G.A.Rozgonyi, "Rapid thermal processing of multiple low dose oxygen implantation for SIMOX", Mat. Res. Soc. Symp. Proc. 107 (1988) 61.

[86] C-E.D.Chen, "Buried oxide SOI: Materials, devices and VLSI circuits", Mat. Res. Soc. Symp. Proc. 107 (1988) 309.

[87] M.R.Taylor, C.G.Tuppen, R.P.Arrowsmith, R.M.Dobson, A.E.Glaccum, M.C.Wilson, G.R.Booker and P.L.F.Hemment, "TEM and Auger electron spectroscopy observations of C-MOS and n-channal devices incorporating buried oxide implanted isolating regions", Inst. Phys. Conf. Ser. Nº 67 (1983) 485.

[88] S.Cristoloveanu, S.Gardner, C.Jassaud, J.Margail, A.J.Auberton -Hervé and M.Bruel, "Silicon on insulator material formed by oxygen implantation and high-temperature annealing: carrier transport, oxygen activity and interface properties", J. Appl. Phys. 62(7) (1987) 2793.

[89] P.K.Vasudev, K.W.Terrill and S.Seymour, "A high performance submicrometer CMOS/SOI technology using ultrathin silicon films on SIMOX", Mat. Res. Soc. Symp. Proc. 107 (1988) 349.

[90] A.DeVeirman, K.Yallup, J.Van Landuyt, H.E.Maes, K.DeMeyer and L.Dupas, "HVEM and electrical chracterisation of SIMOX structures", Mat. Res. Soc. Symp. Proc. 107 (1988) 129.

[91] J.R.Davis, A.E.Glaccum, K.Reeson and P.L.F.Hemment, "Improved subthreshold characteristics of n-channel SOI transistors", IEEE Electron Device Lett. EDL-7(10) (1986) 570.

[92] J.C.Sturm, "Performance advantages of silicon-on-insulator devices for ULSI", Mat. Res. Soc. Symp. Proc. 107 (1988) 295.

[93] K.Kato, T.Wada and K.Taniguchi, "Analysis of kink characteristics in silicon-on-insulator MOSFET's using two-carrier modelling", IEEE Trans. Electron Devices, ED-32(2) (1985) 458.

[94] S.Cristoloveanu, "Electrical evaluation of SIMOX material and integrated devices", Mat. Res. Soc. Symp. Proc. 107 (1988) 335.

[95] N.A.Drozdov, A.A.Patrin and V.D.Tkachev, "On the nature of the dislocation luminescence in silicon", Phys. Stat. Sol. b), 83 (1977) K137.

[96] M.Suezawa, Y.Sasaki, Y.Nishina and K.Sumino, "Radiative recombination on dislocations in silicon crystals", Japan. J. Appl. Phys. 20(7) (1981) L537.

[97] W.M.Duncan, P.-H.Chang, B.-Y.Mao and C.-E.Chen, "photoluminescence and microstructural properties of high-temperature annealed buried oxide silicon-on-insulator", Appl. Phys. Lett. 51(10) (1987) 773.

[98] M.Tajima, "Determination of boron and phosphorous concentration in silicon by photoluminescence analysis", Appl. Phys. Lett. 32(11) (1978) 719.

[99] J.Weber, H.Baumgart, J.Petruzzello and G.K.Celler, "Photoluminescence characterisation of thin silicon-on-insulator films produced by oxygen implantation", Mat. Res. Soc. Symp. Proc. 107 (1988) 117.

Chapter 3

Experimental Procedure

3.1 Oxygen Ion Implantation

Most of the 3-inch (100) silicon wafers analysed in this study were implanted with 150keV $^{16}O^{+}$ or 300keV O_2^{+} ions in Surrey University's 500keV implanter (i.e. 500keV for singly-charged ions). In this system the ions are post-acceleration mass-analysed. The details of the individual implants (dose etc.) are given in section 3.5. Beam heating was used in each case; a temperature of ≈550°C being achieved with a current of 75μA. The wafers were clamped onto small silicon tips using stainless steel springs, which minimised conductive heat losses and contamination as shown in Fig. 3.1 [1]. The beam was electrostatically scanned at 1-2kHz in both the x and y directions to simulate a direct current flood implantation and to minimise thermal gradients across the wafers.

The remainder of the wafers were implanted by the SPIRE Corporation, Bedford, Ma, at 165keV. Again, electrostatic scanning was used and the (800μA) beam heated the wafers to either 550 or 600°C.

Some of the wafers studied were implanted through a thin (≈100nm) screening layer of SiO_2.

3.2 High Temperature Annealing

The implanted specimens were annealed at the British Telecom Research Laboratories, Martlesham Heath. Prior to annealing, they were capped with an oxide layer (≈0.5μm thick) to protect the wafer surfaces. The first type of cap used was an LTO (low temperature oxide) cap which was deposited in a cantilever-loaded furnace at a temperature of 420°C and a pressure of 300mtorr [2]. Two injection tubes run along the furnace, one for O_2 and the other for silane (SiH_4) and the gases react to form SiO_2, the uniformity of deposition depending on the flows from the injection tubes.

The second method involves the deposition of a plasma oxide cap, where the wafers are mounted on each side of one of 7 carbon plates in a quartz tube. The temperature is 400°C and a low pressure mix of silane and nitrogen oxide (NO) is introduced. The oxide is formed when an rf field is applied, creating a plasma.

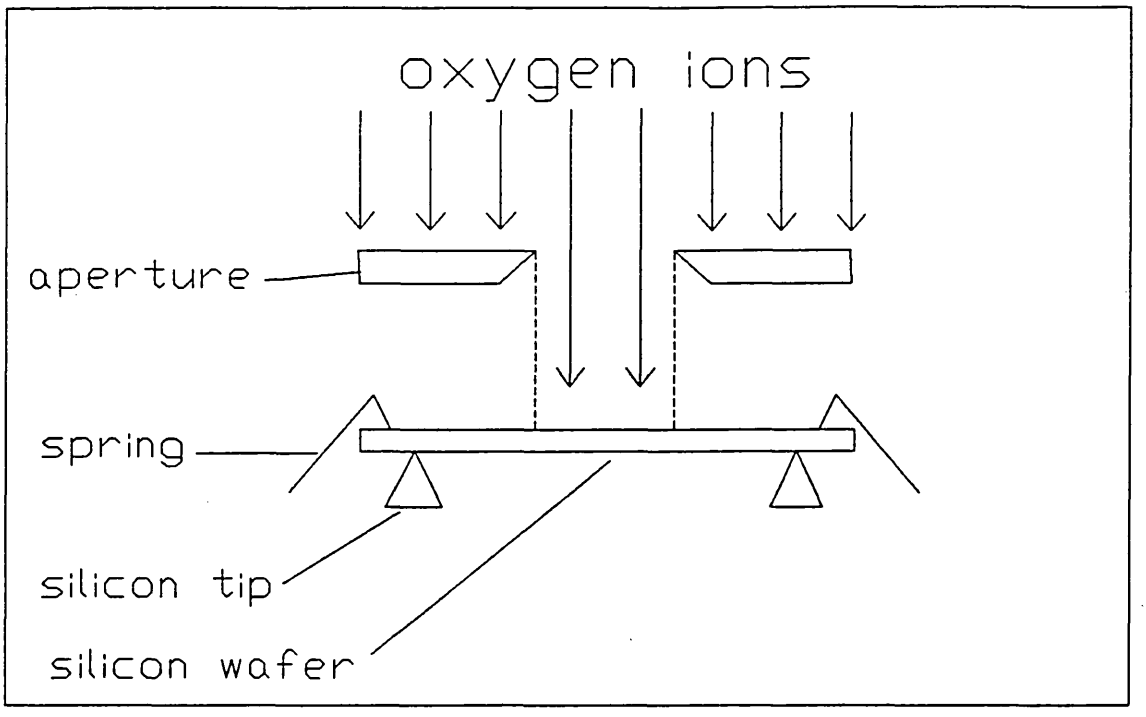


Fig. 3.1 Diagram of wafer holder in the University of Surrey implanter.

The annealing was performed in a conventional 3-zone horizontal diffusion furnace fitted with a single walled silicon carbide tube lined with silicon to fill any pores. The annealing ambients were either pure N_2, N_2 with ½% O_2 or Ar with ½% O_2. The wafers were loaded into a SiC boat mounted on a SiC trolley with wheels, wafer loading and unloading being done at 875°C. The anneals were all at 1300°C for either 2 or 5 hours.

The caps were usually stripped by etching in buffered HF before analysis.

3.3 Transmission Electron Microscopy

3.3.1 Cross-Sectional TEM

XTEM specimens were prepared in a way which has almost become standard in semiconductor research i.e. mechanical thinning followed by ion beam milling [e.g. 3]. However, all workers develop their own variations of the technique, and the method used in this study is based on references 4 and 5.

a) Two slabs of the wafer (≈2mm x 6mm) were cleaned in ethanol and glued together, face-to face, using Araldite. They were clamped in a small press and cured for 24 hours at 150°C.

b) The block was cut in half using a diamond saw, to give two pieces 2mm x 3mm

c) Using "Lakeside Cement" resin, the specimen was mounted edge-on to a 50mm x 25mm piece of 6mm-thick glass, with two pieces of silicon on either side to act as levelling plates (Fig. 3.2a).

d) The first edge was flattened on a grinding wheel using 1200-grade SiC paper. By melting the resin, the specimen was re-mounted with this flat side against the glass.

e) The second side was ground down, again using 1200 paper, until it was level with the silicon plates and was given a final polish with 3 and 1 μm diamond paste.

f) The specimen was then re-mounted with the polished face hard down against the glass. Care was taken to ensure the silicon plates were also flat against the glass and they were in contact with the specimen.

g) The composite structure was ground down to a thickness of 20-30μm. A micrometer was used to check the overall thickness (the glass thickness was known accurately already), the silicon plates giving a large area to ensure the thinning was even. A final diamond polish was given before immersing the whole structure in hot (150°C) dimethylformamide for 3-4 hours to melt and

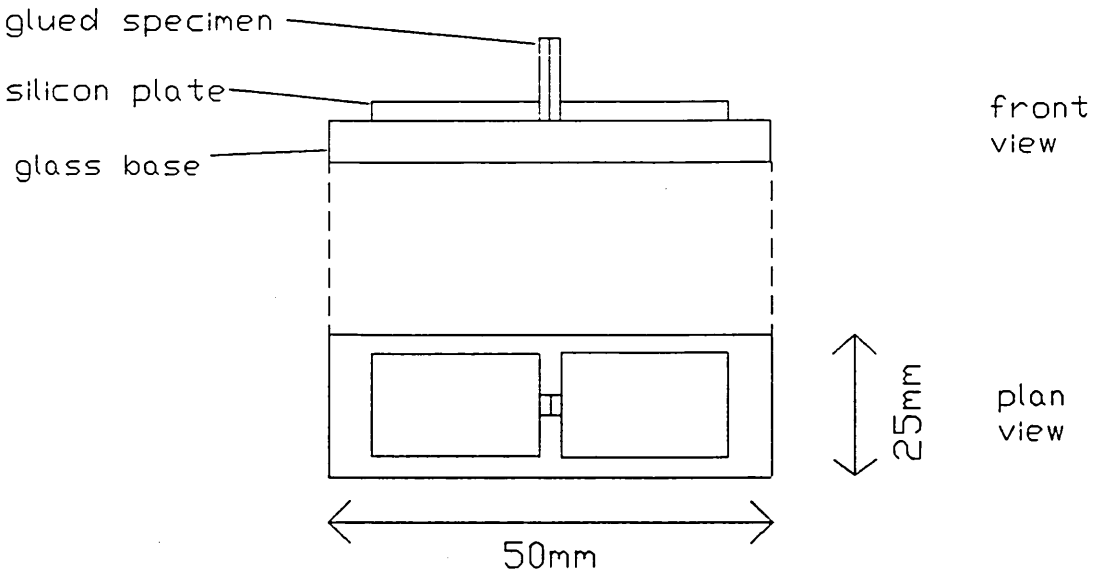


Fig. 3.2a front and plan views of TEM cross-section ready to be mechanically thinned.

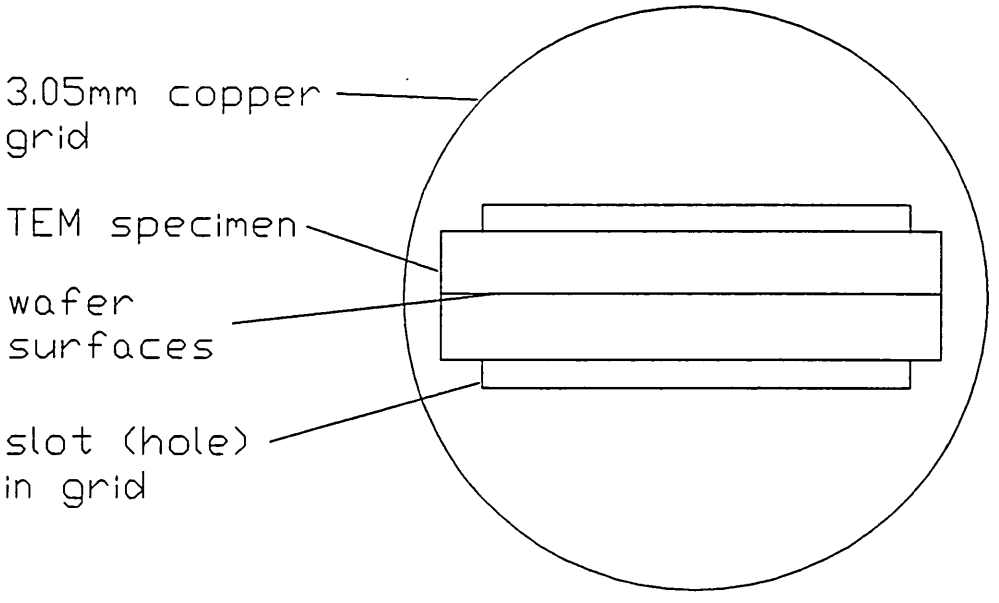


Fig. 3.2b Plan view of TEM cross-section on grid

dissolve the resin.

h) The cross-sectional specimen was carefully removed and mounted onto a 3.05mm TEM slot grid using conducting silver paint (Fig. 3.2b).

i) Ion beam thinning was performed in a Gatan series 600 Ion Beam Miller using 6keV argon ions. Thinning at an angle of 17° from both sides with a total gun current of 1mA, the specimen should be thinned in the centre after 4-6 hours. Final thinning for 1-2 hours at 10° produces a larger thin area for TEM observation.

j) A final clean for 3-4 hours in hot dimethyformamide followed by hot methanol is required to remove any contamination caused by the ion thinning process.

3.3.2 Plan View TEM

Plan view TEM specimens of annealed SIMOX material are prepared simply by dissolving away the buried oxide [6]. This is done by immersing small pieces of the material (1-2mm^2) in 50% hydrofluoric acid for between 2 and 4 hours, although larger specimens can be prepared by etching for longer. The buried oxide dissolves preferentially, leaving the silicon overlayer intact, so it can be floated off on water using the surface tension, and scooped-up with a commercially available copper TEM mesh grid (200 or 400 grade). One drop of ethanol in the water makes this easier since it reduces the surface tension. A methanol rinse is required to clean the specimens, and they can be analysed as soon as they are dry.

3.3.3 TEM Observations

The two transmission electron microscopes employed for this study were a JEOL 120CX and a JEOL 2000FX, operated at 100kV and 200kV respectively. With both microscopes, diffraction contrast imaging was performed in bright field (BF), high-resolution dark Field (HRDF) and weak beam (WB) modes using the guidelines set out by Eddington [7]. A double-tilting stage was found to be essential to obtain the correct specimen orientation for optimum contrast, particularly for dislocation characterisation where a number of two-beam diffracting conditions are required.

Plan view TEM was found to be the best method for calculating dislocation densities since large areas could be studied. Where dislocations were close together, WB imaging was necessary since the strain contrast was limited to less than $\approx$2nm from the dislocation core compared to $\geq$10nm for conventional HRDF imaging [e.g. 8-10].

3.4 Secondary Ion Mass Spectrometry

The SIMS work in this study was performed on an Atomika A-DIDA R-2010 instrument. This instrument is comprised of three main sections which will be discussed in detail along with the depth profiling process.

3.4.1 The Ion Source

The source is evacuated by a turbo-molecular pump to a base pressure below 10^{-8} torr. When a xenon primary beam is used for profiling, the source operates in "hot cathode" mode, a hot filament emitting electrons and providing a xenon plasma from a pure xenon source gas (Fig. 3.3). The application of a longitudinal magnetic field enhances the ionisation probability resulting in a low operating pressure ($\approx 10^{-6}$torr).

The primary ion beam is achieved by extracting ions from the plasma in the source and subsequently accelerating them with an immersion lens. Two pairs of deflection plates in the drift region of the beam provide for the accurate alignment of the xenon ions to transport them into the analysis chamber, and a 1° bend in the beam line helps to suppress the transport of any neutral species.

A caesium primary beam was also used in this study since the presence of Cs^{+} ions in or near the surface region of a material under ion bombardment causes copious emission of negative secondary ions. For elements located in group 4 or to the right in the periodic table, the negative secondary ion yield in the presence of caesium is very high producing good secondary ion mass spectrometric detection limits for those elements.

Caesium, contained in a reservoir, is volatised and delivered to an electrically heated tungsten frit at 1100°C. The delivery rate of caesium from the reservoir is determined by the vapour pressure in the reservoir, which in turn is regulated by the reservoir temperature controlled by a flow of cooling compressed air, and the porosity of the much hotter frit.

The removal of caesium from the frit region is influenced by evaporation due to a thermal process as well as conversion of the neutrals into Cs^{+} ions ($\approx$99%) if they are in contact with the tungsten surface. Upon ionisation, they are rapidly removed from the ionising region by the extraction field. If insufficient ionisation occurs i.e. normal evaporation from the frit predominates, a space charge region may form. This allows a build-up of caesium on the tungsten surface which further reduces the ionisation efficiency. This results from either insufficient heat for ionisation or from

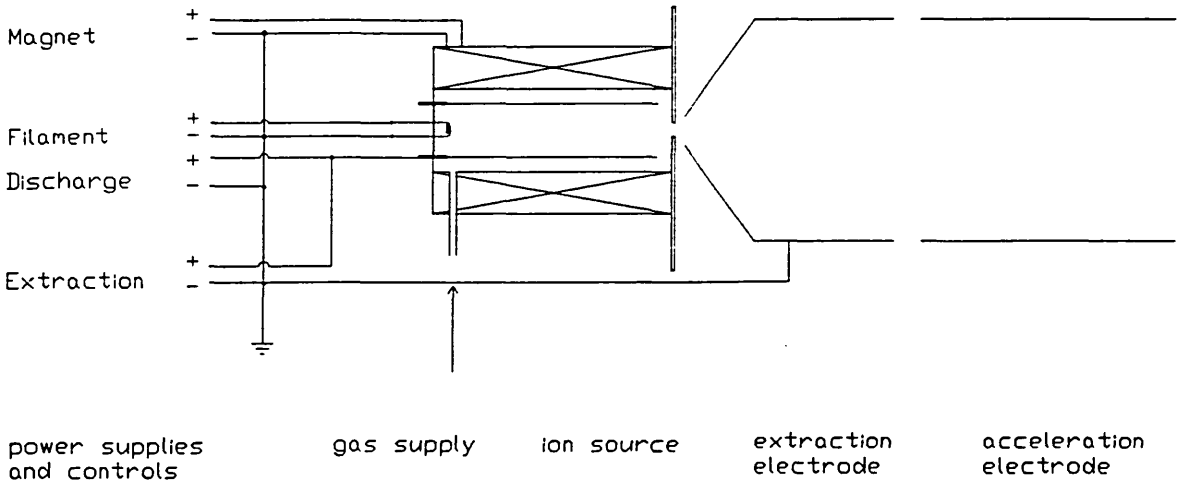


fig. 3.3 Schematic cross-section of the gas ion gun used to obtain a xenon primary beam.

an insufficient electrostatic field.

Once the Cs^+ ions have been produced, they are extracted into the analysis chamber in the same way as for the Xe^+ ions.

3.4.2 The Analysis Chamber

The chamber can be baked to a base pressure of $\approx 10^{-10}$torr, pumped by an ion pump. Operating pressures are typically 10^{-9}torr with a caesium primary beam and 10^{-8}torr with a gas source. This low pressure reduces the effects of beam-divergence, ionisation of residual gas molecules and residual gas adsorption on the specimen which can produce molecular interferences to limit the dynamic range of the depth profile.

An einzel lens focusses the primary beam to $\approx 100\mu$m or less which is raster scanned over a small area of the specimen. As the surface is sputtered away, a square crater is formed, typically with 500-1000μm sides. Since the shape of the crater walls mimics the Gaussian intensity distribution of the beam, an electronic gate aperture is employed so that the secondary ions are only collected from the centre of the crater base. In this work, a 6% (area) aperture was used to give a good depth resolution. It is also essential to have a very flat specimen surface since with a depth resolution of typically 10nm, any surface roughness will result in a distorted profile.

With the layered semiconductor-insulator-semiconductor structures analysed in this study, there are problems with the electrical charge distribution around the crater. This change in surface potential can seriously affect the secondary ion intensities, meaning that the measured depth profiles will not accurately represent the atomic distribution within the specimen. To help overcome this, the specimens were mounted on glass cover slips to produce a wholly insulating structure which was irradiated with a slightly defocussed beam of 450eV electrons. This charge compensation is very successful in maintaining a constant surface potential throughout the depth profile.

3.4.3 The Mass Spectrometer

The specimen and the ion detector are situated away from their line of sight in order to prevent photons, neutrals and fast scattered primary or fast secondary ions from reaching the detector which would result in a high background count inside the mass spectrometer and a loss in the dynamic range of the instrument. Hence there are a series of electrodes (the secondary ion optics) which collect a fraction of the

secondary ions and guide them towards a quadropole mass filter. This can be set to allow a chosen ion through by its charge:mass ratio. It consists of four rods to which dc and rf voltages are applied. The ions *not* selected are forced to follow unstable trajectories such that they strike the rods or the housing and are prevented from reaching the detector. Finally, the selected ions are detected and counted by a Channeltron-type detector. This is also mounted off axis to avoid background counts induced by photons or neutral species.

To suppress the effects of any residual charging or beam instabilities, the final depth profiles are usually plotted as an intensity ratio of the desired ion to a matrix signal. The ratios are always of the same type of ion i.e. atomic:atomic or molecular:molecular. Calibration of the results in terms of atomic concentration is done by scaling to match that of known standards e.g. numerically integrated atomic implants to give a relative sensativity factor (RSF) which directly relates the intensity ratio to the atomic concentration. This is difficult with oxygen (as explained in section 4.1.1) due to secondary ion enhancement, although section 4.1 describes a method by which it can be done).

3.5 Specimen Details

3.5.1 Incremental Doses

Float-zone (100) silicon wafers were implanted at Surrey University with oxygen doses in the range 0.1 to 0.65 x $10^{18}O^+/cm^2$ at 150keV (the actual implanted ion was $^{32}O_2^+$ at 300keV since a higher beam current could be achieved). The beam current was 75±1μA which maintained the wafers at ≈550°C during the implant. The doses are given in Table 3.1.

Half of each wafer was capped and annealed at the British Telecom Research Labs. (BTRL) for 5 hours at 1300°C in an ambient of dry nitrogen with 0.5% oxygen: the other halves were left in the as-implanted state. Each specimen, annealed and unannealed, was analysed by SIMS (Xe^+ primary beam to follow the oxygen distribution) and XTEM.

A detailed analysis of the SIMS data, combined with some modelling of the implantation process, enabled the oxygen profiles to be calibrated accurately in terms of atoms/cm^3. Previously, this had not been possible.

Using this calibration, the corresponding annealed wafers (1300°C for 5 hours) were studied with SIMS in conjunction with cross-sectional TEM, to determine the

mechanisms of:

i) buried oxide layer formation, and

ii) the evolution of overlayer threading dislocations.

Table 3.1 Table showing the wafer number and total oxygen dose.

Wafer	Dose (x $10^{18}O^+/cm^2$)
1	0.1
2	0.2
3	0.25
4	0.3
5	0.4
6	0.45
7	0.55
8	0.65

3.5.2 Defect and Impurity Analysis: SPIRE Wafers

This set of specimens were whole wafer implants from the Spire Corporation, Bedford, Ma. They were implanted to a total dose of 1.8 x $10^{18}O^+/cm^2$ at 165keV under varying conditions and annealed as detailed in Table 3.2.

Table 3.2

Wafer	T_i (°C)	ANNEAL		
		Temp (°C)	Time (h)	ambient
SP10B	600	1300	5	N_2 ½% O_2
SP10C	600	1300	5	Ar ½% O_2
SP13B	600	1300	5	N_2 ½% O_2
SP13C	600	1300	20	Ar ½% O_2

The specimens were analysed using XTEM, plan view TEM and Cs^+ SIMS. Weak-beam TEM was used to characterise dislocations in terms of their Burgers Vectors.

3.5.3 Implantation Temperature Variation

These wafers were implanted to a total dose of 1.6 x $10^{18}O^+/cm^2$ at 150keV. By varying the beam current, the implantation temperature was altered. The three wafers analysed in this study are as shown in Table 3.3:

Table 3.3

Wafer	Dose (x $10^{18}O^+/cm^2$)	T_i ($^\circ C$)
10	1.6	480
11	1.6	540
12	1.6	540*

* Implanted through a 70nm screening oxide

The sections to be annealed were capped with a 0.54μm CVD oxide layer and annealed at 1300$^\circ C$ for (a) 2 hours and (b) 5 hours in dry nitrogen. They were analysed by Xe^+-SIMS, Cs^+-SIMS (to study nitrogen levels), XTEM and plan view TEM.

References for Chapter 3

[1] P.L.F.Hemment, E.Maydell-Ondrusz, K.G.Stephens, J.Butcher, D.Ioannou and J.Alderman, "Formation of buried insulating layers in silicon by the implantation of high doses of oxygen", Nucl. Instr. and Meths. 209/210 (1983) 157.

[2] N.C.Thomas (BTRL), private communication.

[3] D.Fathy, O.L.Krivanek, R.W.Carpenter and S.R.Wilson, "TEM, microdiffraction and electrical studies of buried SiO_2 layers formed by high dose oxygen ion implantation", Inst. Phys. Conf. Ser. N°67 (1983) 479.

[4] K.C.Paus (Oxford University), private communication.

[5] X.M.Zhang, PhD Thesis, University of London (Imperial College), 1987.

[6] T.Hayashi, S.Maeyama and S.Yoshi, "TEM, AES and XPS studies of Si layer on buried SiO_2 layer formed by high-dose oxygen ion-implantation", Japan. J. Appl. Phys. 19(6) (1980) 1111.

[7] J.W.Eddington, "Practical Electron Microscopy In Materials Science", Monographs 1 to 4, Phillips Technical Library, (The Macmillan Press, London, 1975).

[8] D.J.H.Cockayne, I.L.F.Ray and M.J.Whelan, "Investigation of dislocation strain fields using weak beams", Phil. Mag. 20 (1969) 1265.

[9] I.L.F.Ray and D.J.H.Cockayne, "The dissociation of dislocations in silicon", Proc. R. Soc. Lond. A, 325 (1971) 543.

[10] D.J.H.Cockayne and A.Hons, "Dislocations in semiconductors as studied by weak-beam electron microscopy", J. de Physique 40, supplement N°6 (1979) C6.

Chapter 4

Results and discussion

4.1 Calibration of High-Dose Oxygen Implants

4.1.1 Introduction

Calibration of SIMS data to give concentration as a function of depth is normally achieved by performing a numerical integration of the data to match the implanted dose. The depth scale is calculated by measuring the crater depth and by assuming a uniform erosion rate. However, to eliminate the effects of beam instability and charging, the integration is performed on a ratio of the secondary ion intensities i.e. $^{16}O^-/^{28}Si^-$, to give a relative sensativity factor (section 3.4.3). This works well for lower oxygen doses ($\leqslant$ 0.1 x $10^{18}O^+/cm^2$) but fails as the effects of secondary ion yield-enhancement (a function of oxygen concentration) become more prominent. Fig. 4.1 shows the calibrated profile for wafer 1. Since there is no enhancement, this calibration is assumed to be correct.

Fig. 4.2a shows the "raw" SIMS data, using a xenon primary beam, of wafer 1 (0.1 x $10^{18}O^+/cm^2$). The oxygen ($^{16}O^-$) secondary ion yield exhibits the characteristic as-implanted (skew-Gaussian) distribution, whereas the silicon ($^{28}Si^-$) signal is virtually constant (any fluctuations are either due to primary beam instabilities or charging at the specimen surface during analysis). However, Fig. 4.2b is the raw data (using identical experimental conditions to those used for Fig 4.2a) from wafer 7 (0.55 x $10^{18}O^+/cm^2$). Here, the silicon signal is enhanced in the region of highest oxygen concentration. This enhancement occurs for both the silicon and oxygen ion yields, but is more pronounced for the oxygen [1]. The SIMS profiles for wafers 1 to 8 show similar enhancement characteristics, with increasing dose (oxygen concentration) resulting in increased enhancement. Careful observation of Fig. 4.2a suggests there may be a small amount of $^{28}Si^-$ enhancement, but it is assumed to be negligible for the purposes of this work. This is the first important assumption.

The other factor to be taken into consideration is the surface swelling which occurs at high doses. Fig. 4.3 demonstrates how the peak of the as-implanted oxygen distribution moves deeper into the silicon as the dose increases. This swelling makes a direct comparison of the profiles difficult since the depth scales of TRIM-simulated profiles (see section 2.2.1.1) do not match those of the experimental ones. To take account of this, simulated depth distribution profiles were produced, based on the calibrated data for wafer 1, but allowing for swelling as a function of (calculated)

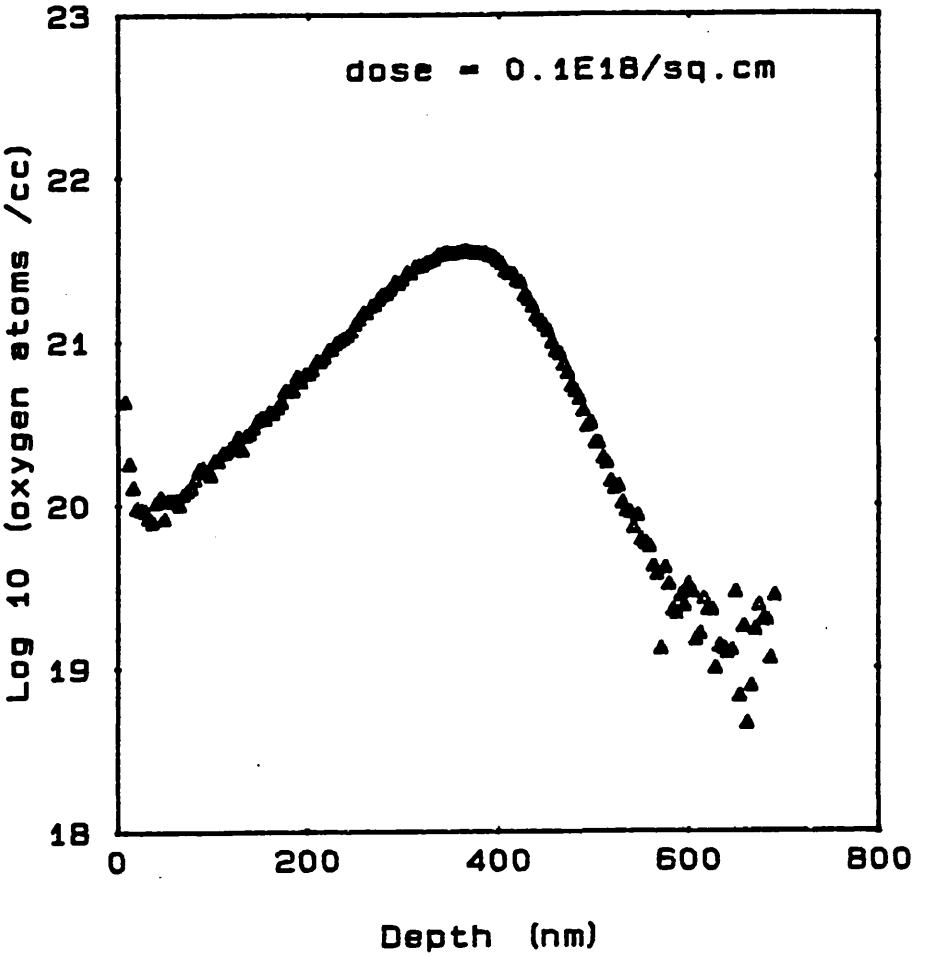


Fig.4.1 Calibrated profile for wafer 1

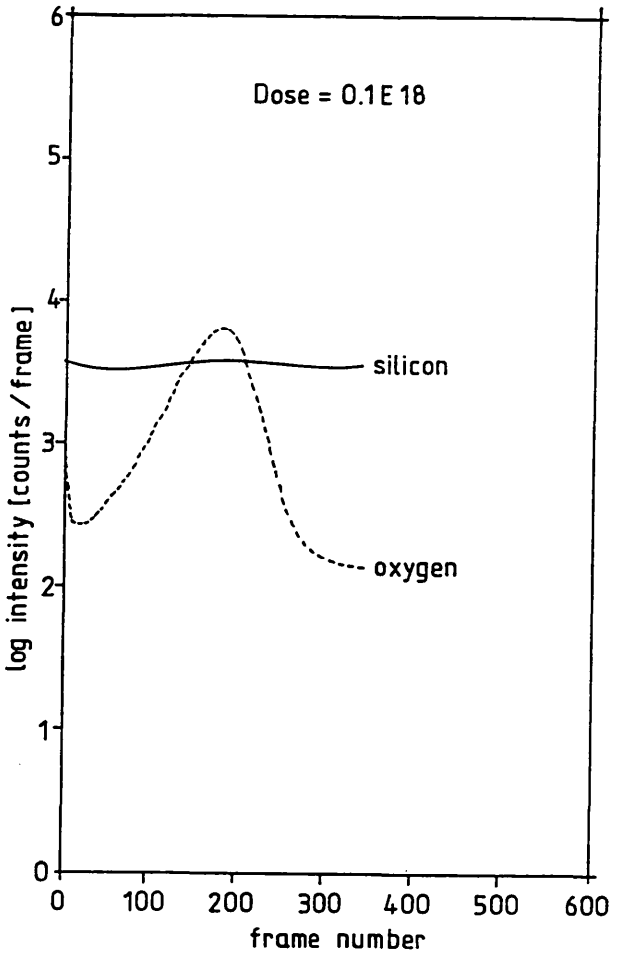


Fig.4.2a Raw data from wafer 1.

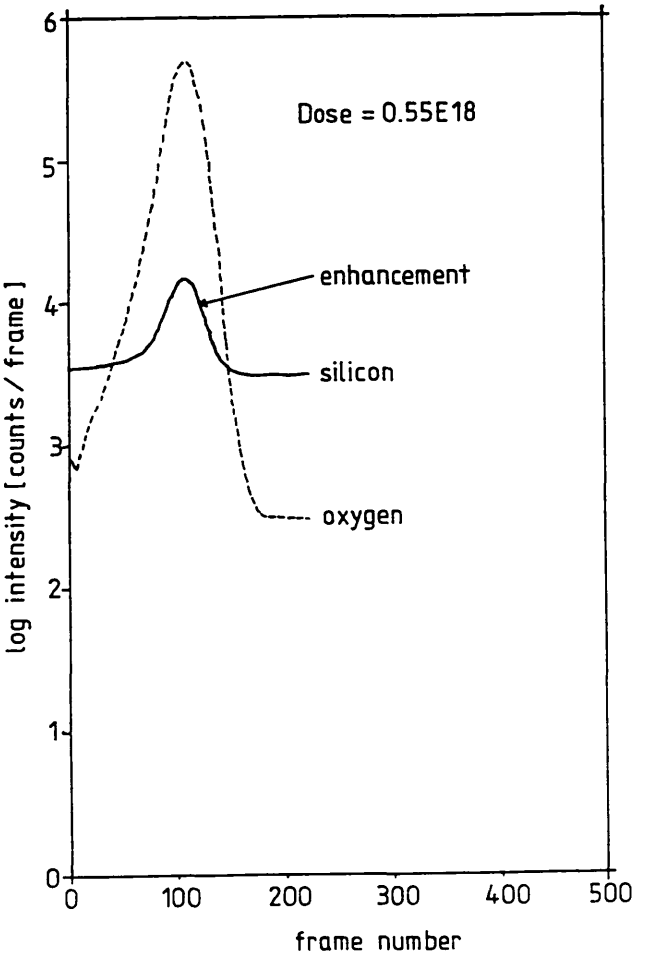


Fig.4.2b Raw data from wafer7.

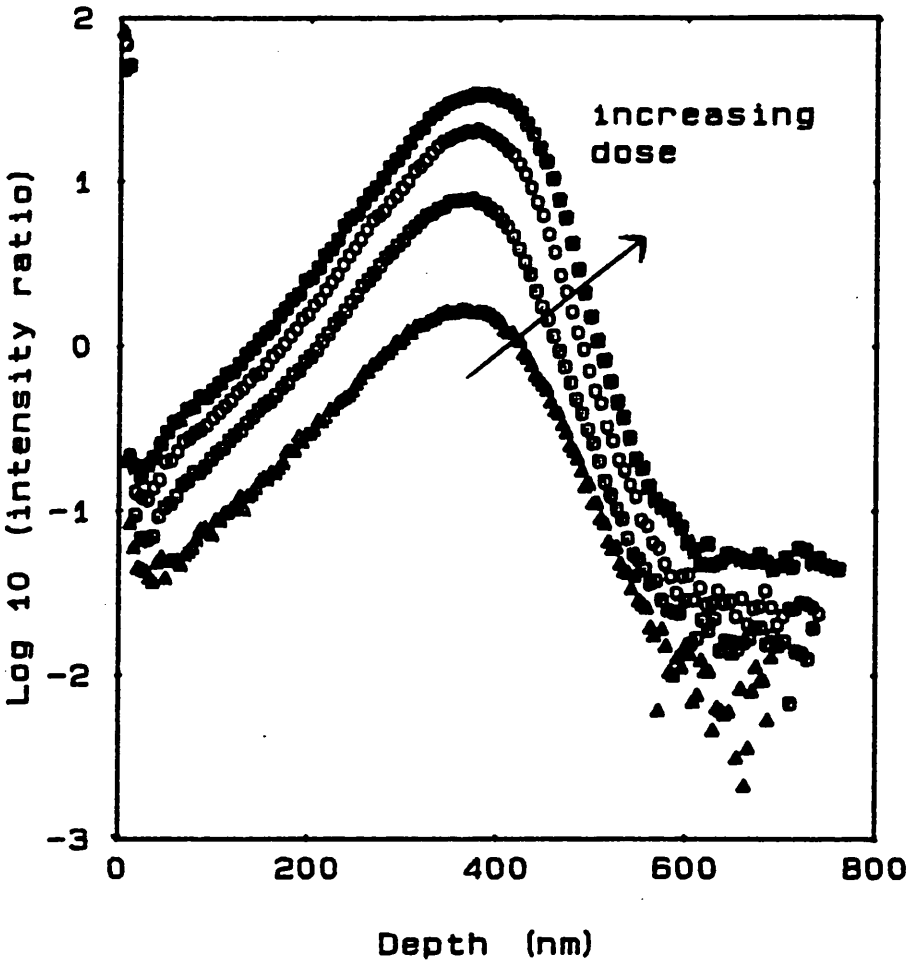


Fig.4.3 Experimental intensity ratios as the dose increases from 0.1E18 to 0.55E18/sq.cm. Note the shift in peak depth.

oxygen concentration. This allowed the enhancement to be quantified. There was assumed to be no swelling at a dose of 0.1 x $10^{18}O^+/cm^2$.

4.1.2 Procedure

The first stage of the simulation was to scale-up the wafer 1 profile to match the higher doses. This was achieved by subtracting a background intensity (4 x $10^{18}O/cm^3$) and multiplying by the appropriate scaling factor (e.g. 2 for 0.2 x $10^{18}O^+/cm^2$, 3 for 0.3 x $10^{18}O^+/cm^2$ etc.) before adding on the background again. It is valid to assume that the profiles can be directly scaled in this manner since there is very little diffusion of the oxygen during implantation at these sub-stoichiometric doses [2]. In order to know how much to correct for the swelling, the peak shifts in the experimental data shown in Fig.4.3 were measured, and are given in Table 4.1.

Table 4.1 The measured peak shift from the experimental data

Wafer	dose (x$10^{18}O^+/cm^2$)	peak shift (nm)
1	0.1	0
2	0.2	5
3	0.25	11
4	0.3	18
5	0.4	17
6	0.45	29
7	0.55	35

To a first approximation, this relationship is linear; any scatter being mainly due to errors in measuring the SIMS crater depths. Linear regression analysis gave the shifts (S_p) used in this model.

Swelling was assumed to occur only when the (simulated) oxygen concentration exceeded the peak value for wafer 1 i.e. 3.5 x 10^{21} at/cm^3 (there was assumed to be no swelling in this specimen). Hence, as shown in Fig.4.4, the amount of oxygen comprising the shaded area (O_t), was calculated using a numerical integration, and was assumed to be responsible for the peak shift, S_p. Hence the swelling per oxygen atom (S_{at}) in this region is calculated to be

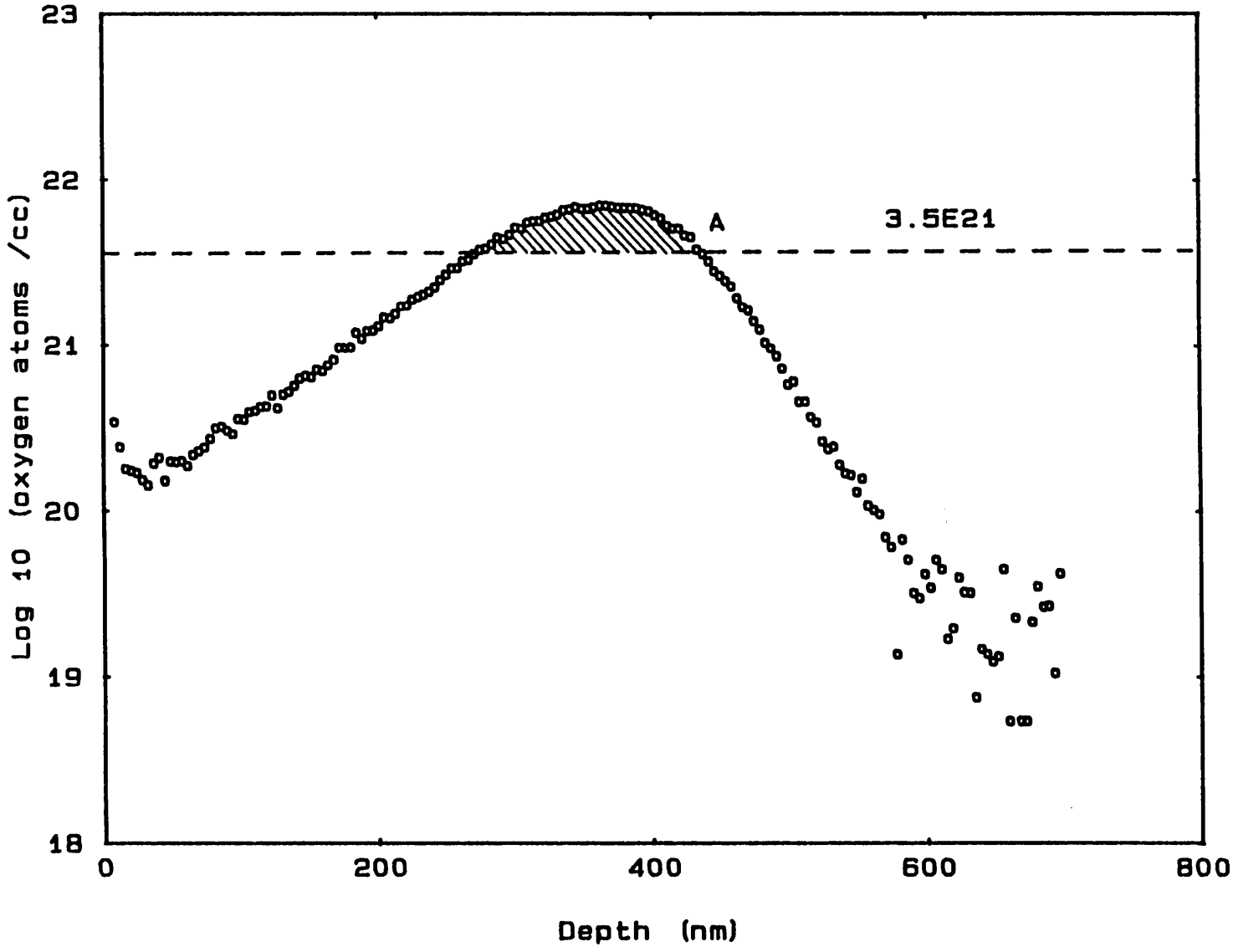


Fig.4.4 Wafer 2. Area used for swelling calculation.

$$S_{at} = \frac{S_p}{O_t} \qquad (4\text{-}1)$$

Sputtering is no taken into account in this simulation.

To start the calculations for the swelling simulation, a base point was chosen on the trailing edge of the profile (point A on Fig.4.4) where the (simulated) oxygen concentration was equal to 3.5×10^{21} at/cm^3.

The depth increment between successive points on the simulated profile is d. With swelling in regions of high oxygen concentration, this needs to be increased in proportion to the oxygen concentration, $[O]_n$, at a particular point d_n. Starting at d_n (point A), the new depth point, d_{n-1}, nearer the surface, is given by

$$d_{n-1} = d_n - \Delta d - S_{at}\,[O]_{n-1}\,\beta$$
$$\text{for } [O]_n \geq 3.5 \times 10^{21}/\text{cm}^3 \qquad (4\text{-}2)$$

The empirical factor, β, was included to ensure that the peaks shifted by the correct amount. This was a consequence of the fact that the total swelling was greater than the peak shift. β had values between 20 and 176 which increased monotonically for doses between 0.2 and $0.55 \times 10^{18} O^+/\text{cm}^2$ respectively.

There are two reasons for the value of β varying, both due to the assumptions made not being entirely true. Firstly, sputtering does occur, meaning that the calculated values of S_{at} will be less than the real values. As the dose increases, sputtering also increases and hence β needs to be larger to compensate for the difference. Secondly, the points on the trailing edges of the profiles used to start the simulations are not constant i.e. their depths will vary slightly, again due to the effects of sputtering. Furthermore, these points are taken at a certain value of the oxygen concentration, below which there is assumed to be no swelling. Again this is not strictly true, although the errors incurred will be very small.

Clearly, the surface was then swollen to a negative value on the depth scale – the modulus being the total swelling at the surface. These values are given in Table 4.2, and correlate very well with previous experimental data [3].

Table 4.2

The simulated total swelling compared with previous experimental data [3].

dose (x $10^{18}O^+/cm^2$)	Simulated total swelling (nm)*	Previous data [3] swelling (nm)
0.1	0	8.5
0.2	10.7	17
0.25	14.9	21.3
0.3	20.2	25.5
0.4	29.5	34
0.45	34.4	38.3
0.55	43.7	46.8

* sputtering not taken into account.

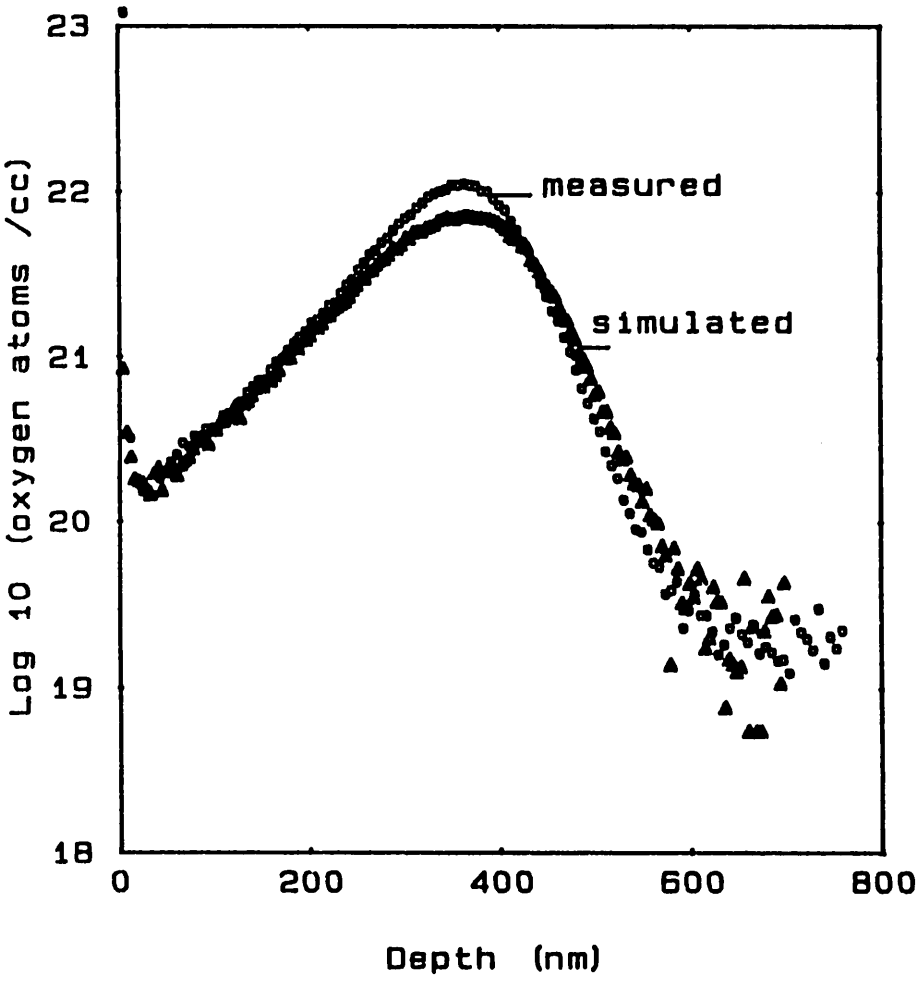
Fig.4.5 shows how the simulated profiles correlate with the experimental data. The leading edges match very well up to the peak as expected, but the trailing edges do not. This is because this simulation is fairly simple and is only intended to match the data between the surface and the concentration peak. In order to get the trailing edges to correlate with the experimental data, the model would have to be built-up by adding one small dose increment at a time, taking account of swelling, range changes and sputtering after each increment.

The model breaks down at a dose of 0.65 x $10^{18}O^+/cm^2$ (Fig. 4.6). This is very close to the onset of buried layer formation during implantation, where diffusion becomes far more prominent and other transport mechanisms determine the oxygen distribution (see section 4.2).

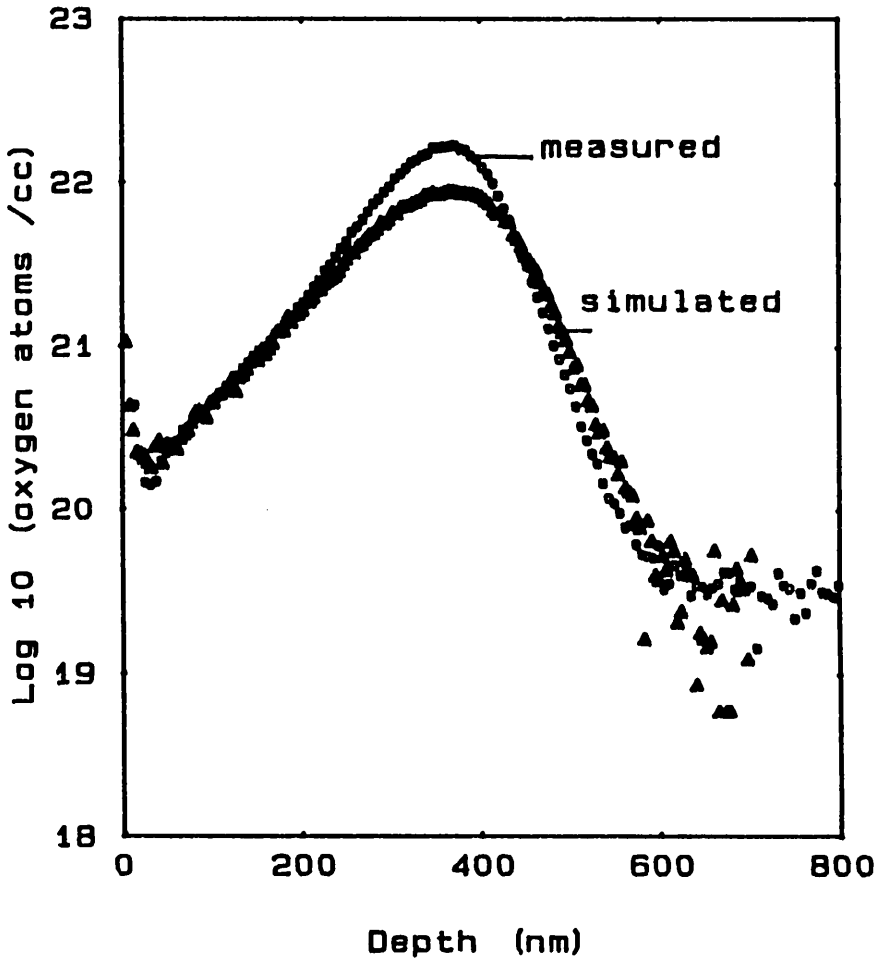
The enhancement factor, E, of the ratioed SIMS data can now be calculated using the definition

$$E = \frac{[O]_{measured}}{[O]_{simulated}} \qquad (4\text{-}3)$$

This will allow all SIMS data measurements of high-dose oxygen profiles in silicon to be simply deconvoluted to give true concentrations.

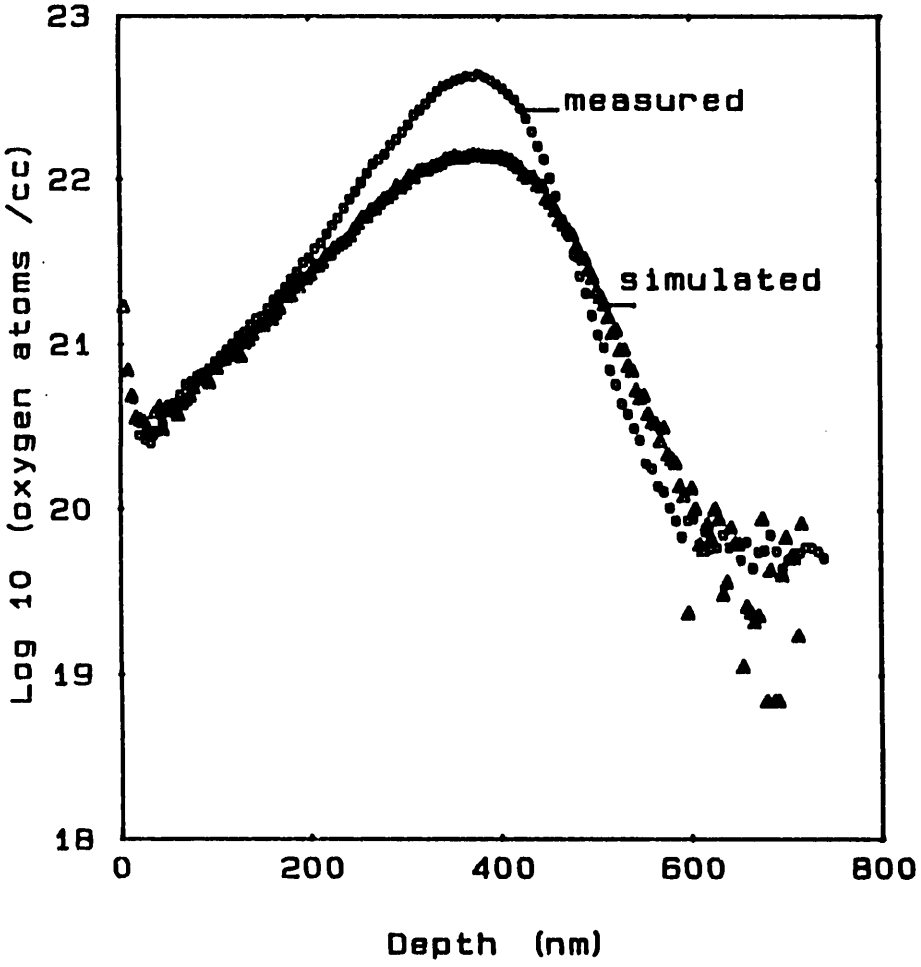


a) Wafer 2 (dose=0.2E18/sq.cm)

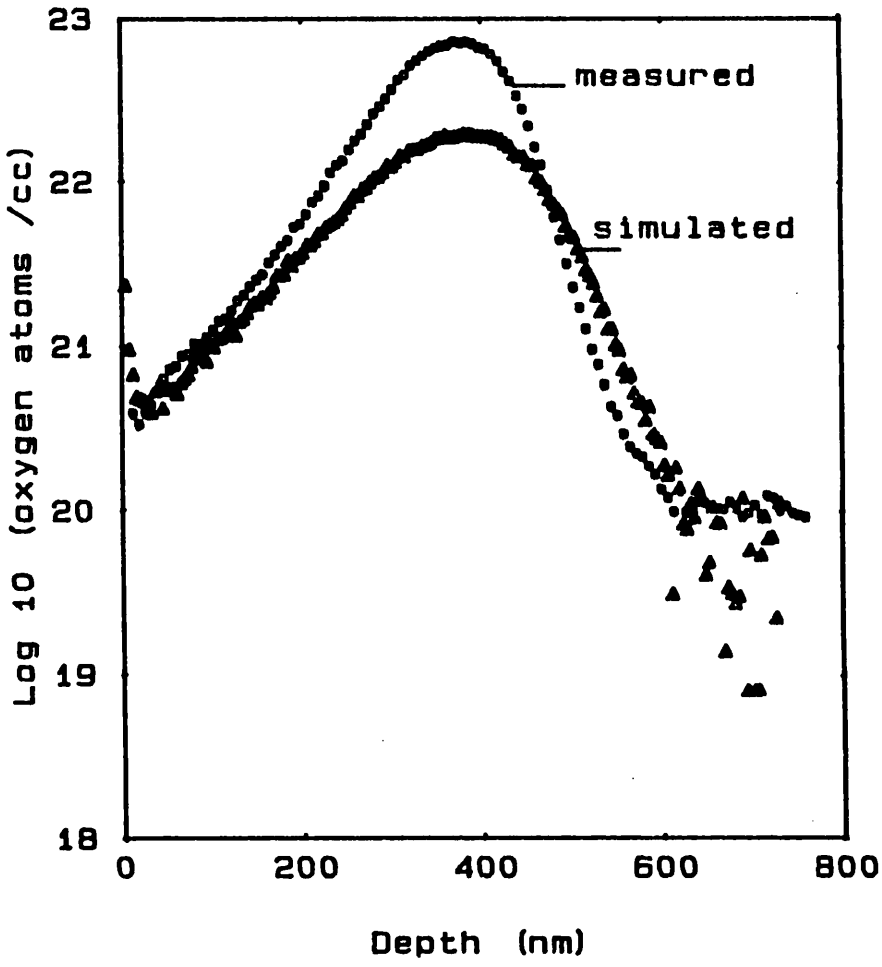


b) Wafer 3 (dose=0.25E18 /sq.cm)

Fig.4.5 Comparison of experimental and simulated data.



C) Wafer 5 (dose=0.4E18)



d) Wafer 7 (dose=0.55E18/sq.cm)

Fig.4.5 continued

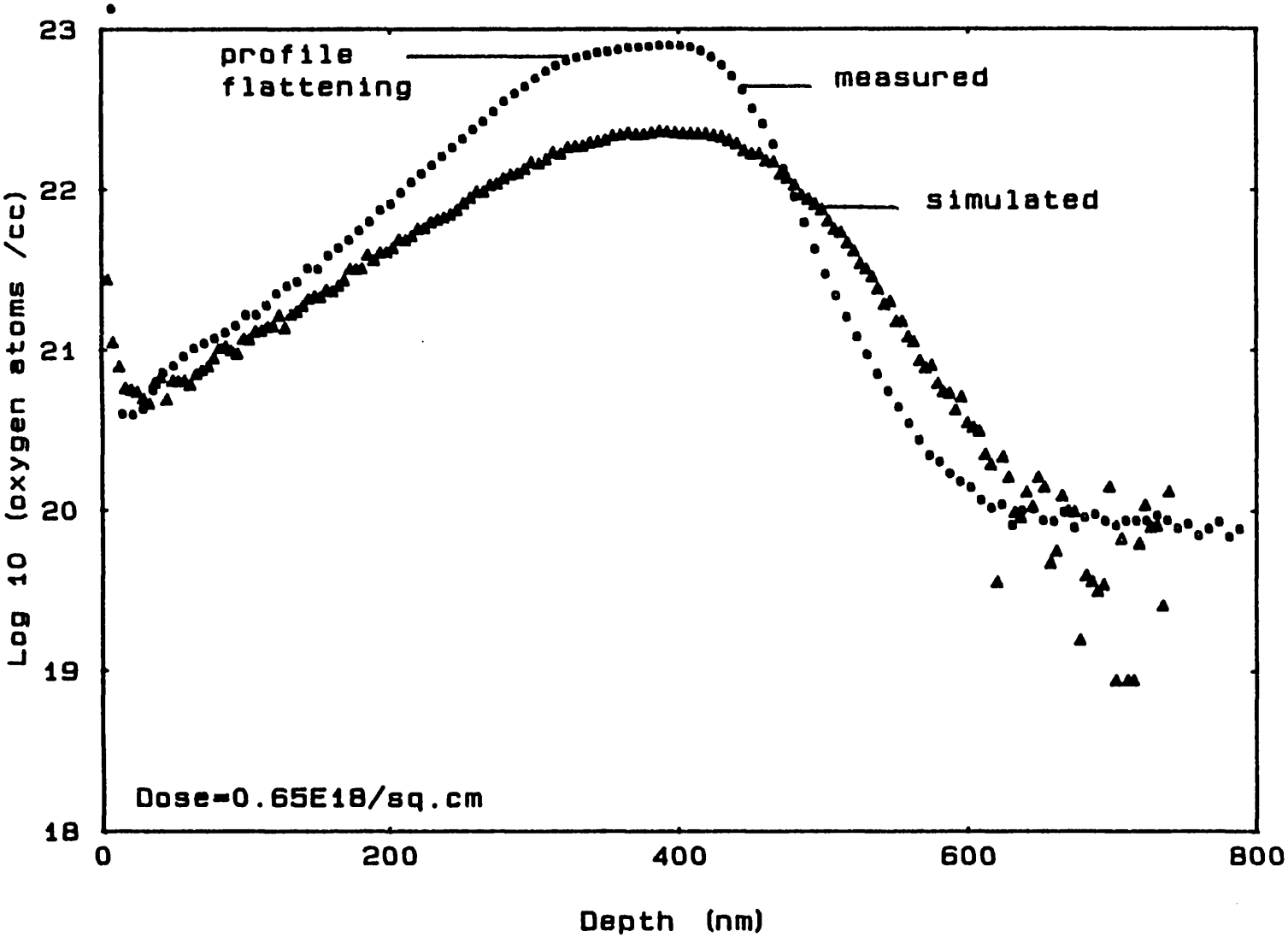


Fig.4.6 Comparison of experimental and simulated data near the onset of continuous buried layer formation.

Fig.4.7 shows the enhancement factor (E) as a function of simulated oxygen concentration. The linear regression line in Fig.4.7 has the equation

$$E = 0.068\ [O] + 1.026 \qquad (4\text{-}4)$$

where [O] is the oxygen concentration (%). The equation has a correlation coefficient of 0.960, and the data agrees very well with the earlier model proposed by Kilner *et al* [1]. Fig.4.8 shows E as a function of the measured intensity ratio. The gradient starts to become much shallower at high oxygen concentrations, and E reaches an almost constant value of approximately 4.

Fig.4.9 shows the deconvoluted SIMS profiles which give the actual oxygen concentrations. This means that although the model to calculate the enhancement factor breaks down at very high doses, it's result can be extrapolated to calibrate higher oxygen levels.

4.1.3 Quantification and Calibration

As reported in section 2.1.1, the amount of oxygen in saturated solid solution is $\approx 10^{18}$at/cm^3. However, from the raw data, it was found that enhancement of the secondary ion intensities did not start until the oxygen concentration exceeded $\approx 10^{21}$at/cm^2, where most of the oxygen will be in the form of very tiny SiO_2 precipitates. Hence the enhancement can be quantified in terms of the volume fraction of SiO_2, V^f_{silica}. This is more realistic since it relates to the microstructure as well as to the oxygen concentration.

At an oxygen concentration of 10^{21}at/cm^3, V^f_{silica} is equal to 0.0226, calculated from the equation

$$V^f_{silica} = \left[\frac{[O]_0 - [O]_s}{2} \right] V_{silica} \qquad (4\text{-}5)$$

where $[O]_0$ is the oxygen concentration, $[O]_S$ the concentration of oxygen in supersaturated solid solution ($\approx 10^{18}$ at/cm^3 in Cz-Si) and V_{silica} is the volume of one SiO_2 "molecule" (4.52×10^{-23} cm^3).

To find the relationship between the oxygen secondary ion intensity (I_O, given in secondary ion counts per second, or c/s) and the volume fraction of SiO_2 (V^f_{silica}) at these low oxygen levels, I_O (minus a background count from the analysis) was plotted

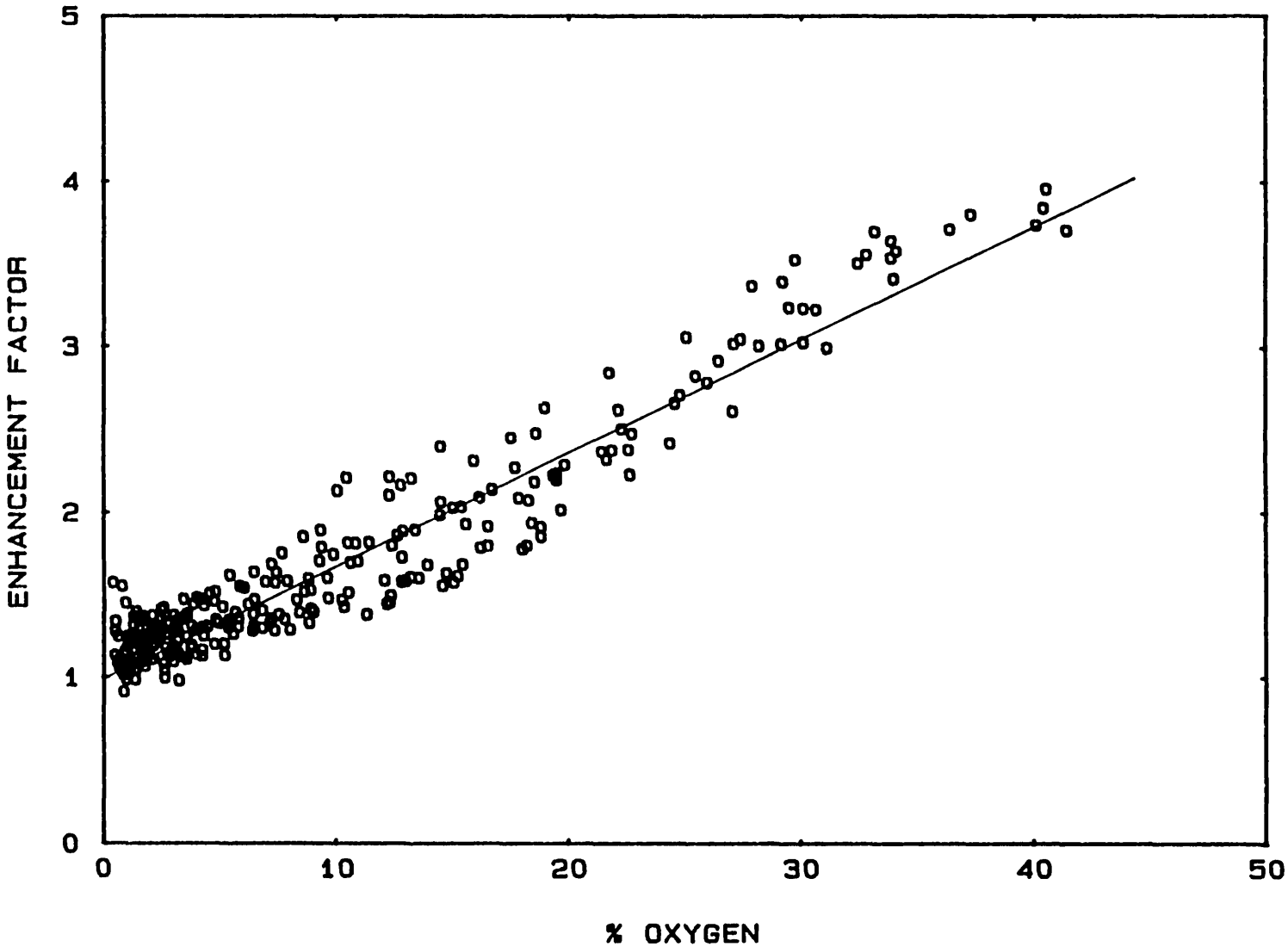


Fig.4.7 Enhancement factor as a function of simulated oxygen concentration.

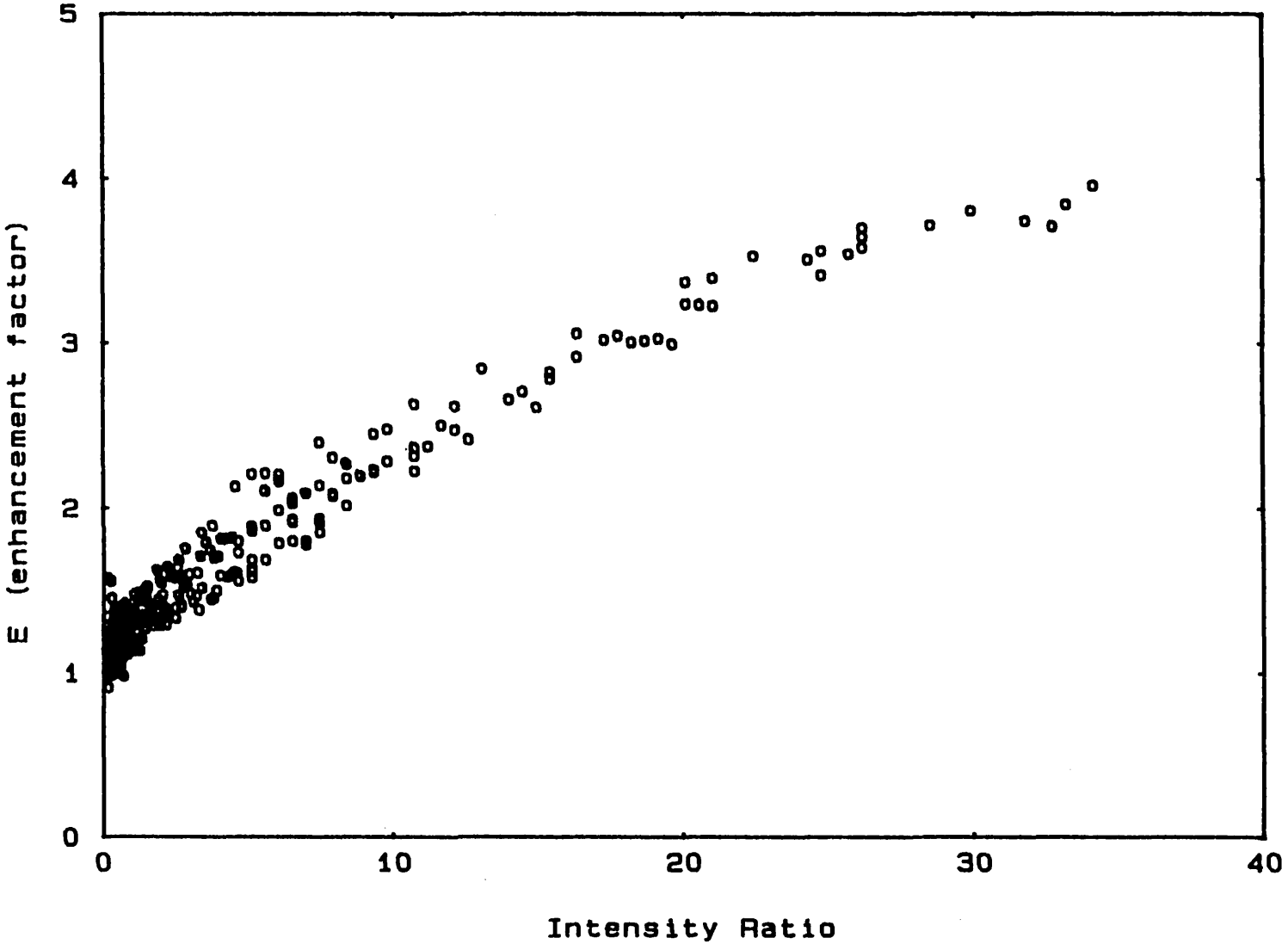
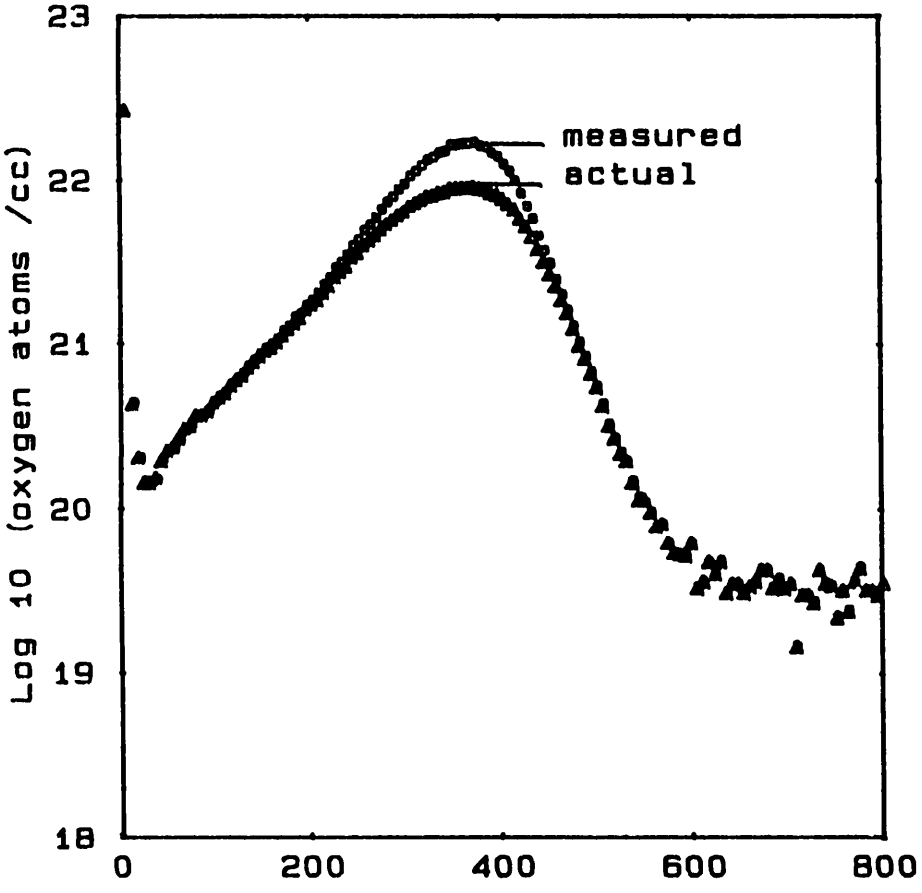
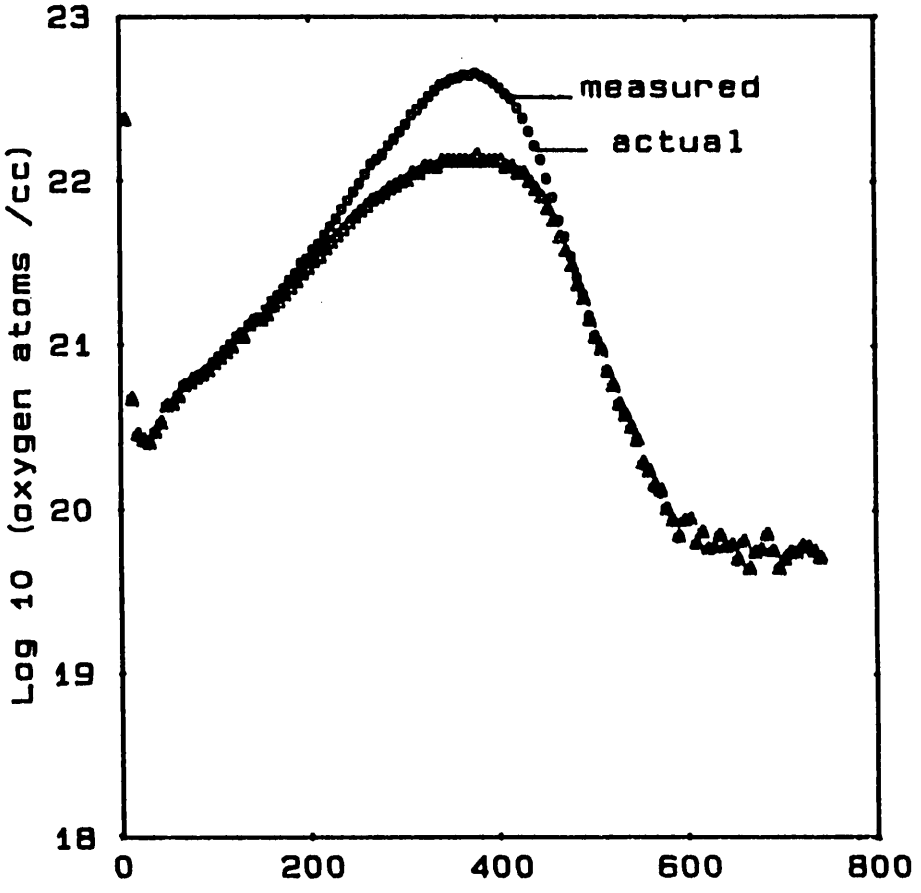


Fig.4.8 Enhancement factor as a function of measured intensity ratio

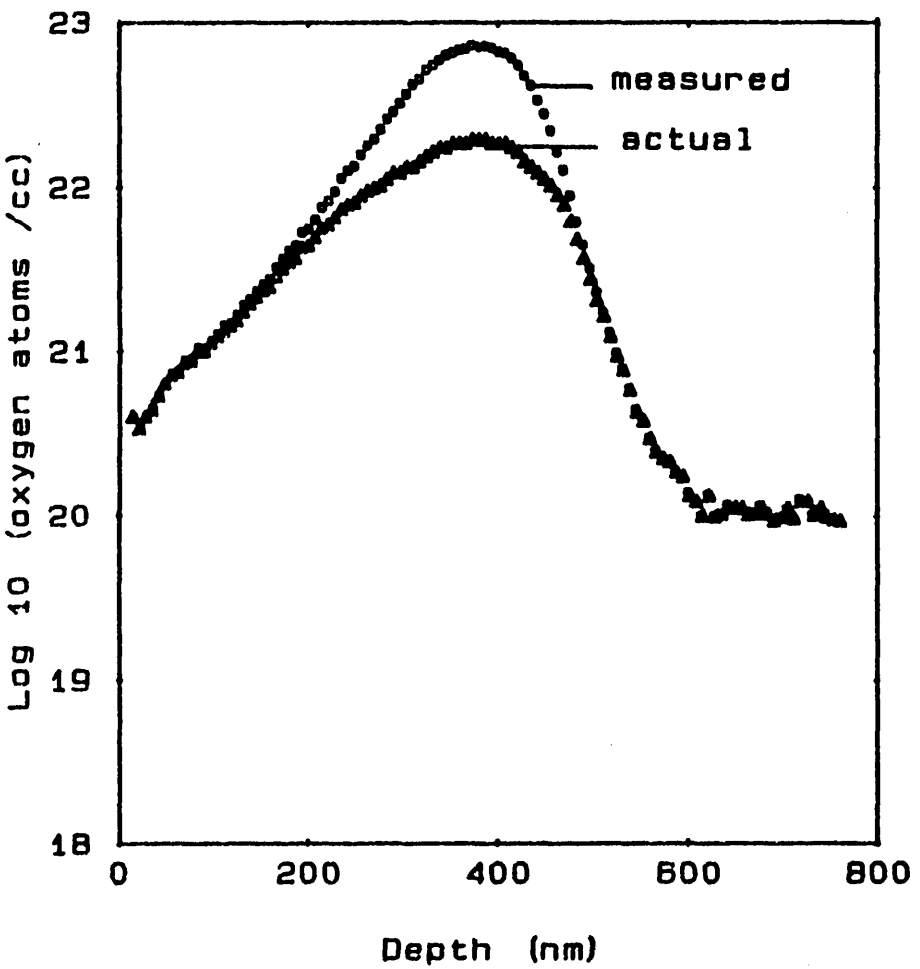


a) Wafer 3 (dose=0.25E18/sq.cm)

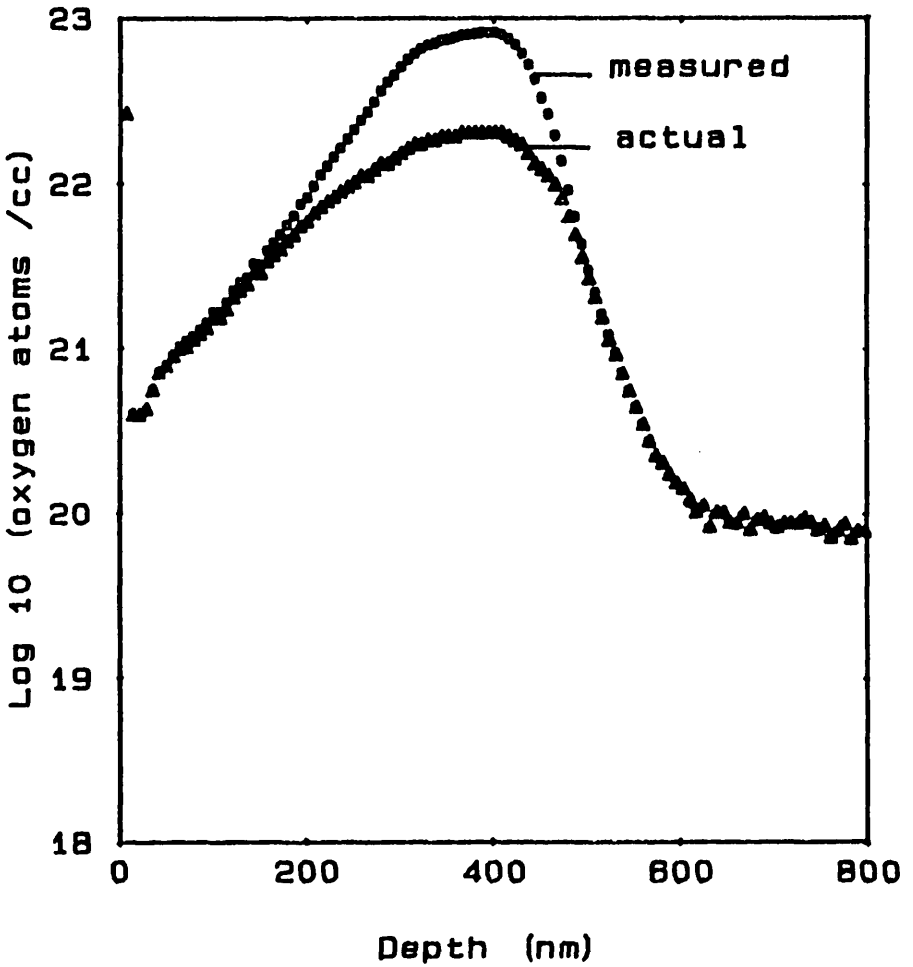


b) wafer 5 (dose=0.4E18/sq.cm)

Fig.4.9 Deconvoluted SIMS data showing real oxygen concentrations



c) Wafer 7 (dose=0.55E18/sq.cm)



d) Wafer 8 (dose=0.65E18/sq.cm)

Fig.4.9 Continued

as a function of V^f_{silica} for each wafer, up to the point where I_0 started showing signs of enhancement (an oxygen concentration of $\approx 10^{21}$at/cm^3). In each case, the result was a linear relationship of the form

$$I_o = k\, V^f_{silica} + c \qquad (c/s) \qquad (4\text{–}6)$$

Table 4.3 gives the values of the constants k and c together with the correlation coefficient, R, for each wafer.

Table 4.3 Values of the constants in equation 4-6.

Wafer	dose ($\times 10^{18} O^+/cm^2$)	k c/s	c c/s	R
1	0.1	65044	39	0.968
2	0.2	78023	-6.8	0.9995
3	0.25	115623	-12.3	0.9997
4	0.3	107093	-42.2	0.9993
5	0.4	78869	-42.2	0.9995
6	0.45	70096	12.9	0.9992
7	0.55	73520	-22.6	0.9997

Hence equation 4–6 holds for oxygen concentrations up to 1 x 10^{21}at/cm^3 ($V^f_{silica} < 0.0226$). Since this concentration is much greater than $[O]_s$, the bulk of the oxygen signal originates from very tiny oxide precipitates, which could even be considered as small clusters of interstitial oxygen atoms.

If a similar equation to 4–6 also applied to the secondary ion yield of silicon, I_{Si}, then we would have the relationhip

$$I_{Si} = k'\, V^f_{Si} = k'\,(1 - V^f_{silica}) \qquad (c/s) \qquad (4\text{–}7a)$$

However, since V^f_{silica} is small, I_{Si} will be virtually constant, hence equation 4–7a can be written as

$$I_{Si} = k' \qquad (c/s) \qquad (4\text{-}7b)$$

where k' is a constant.

The experimentally determined values of k' are given in Table 4.4 with the standard deviations and equivalent errors in %.

Table 4.4 Values of k' in equation 4-7b with standard deviations and % errors.

Wafer	dose ($x10^{18}O^+/cm^2$)	k' ($=I_{Si}$, c/s)	sd	±%
1	0.1	3244	68	2.1
2	0.2	3752	54	1.4
3	0.25	5504	94	1.7
4	0.3	4983	97	1.9
5	0.4	3437	71	2.1
6	0.45	3441	32	0.9
7	0.55	3467	46	1.3

This confirms that at oxygen concentrations at or below 1 x 10^{21}at/cm^3, the secondary ion intensities of silicon and oxygen vary linearly with the volume fraction of the relevant phase. Variations in the values of the constants in equation 4-6 and 4-7 are simply due to unavoidable differences in the analysis conditions, such as surface potential or the collection efficiency of the secondary ion optics. However, the values obtained for each wafer can be used to characterise the enhancement process at higher oxygen concentrations, for the same wafers.

The situation becomes more complex at higher oxygen concentrations where enhancement dominates. I_O increases very rapidly with V^f_{silica}, so Log $[I_O - (0.0226k + c)]$ was plotted against $(V^f_{silica} - 0.0226)$, assuming the relationship

$$I_O = (0.0226k + c) + m \exp [n(V^f_{silica} - 0.0226)] \qquad (4\text{-}8)$$

where m and n are constants. The first term (0.0226k + c) corresponds to the secondary ion intensity at the onset of enhancement (where $V^f_{silica} = 0.0226$), given by equation 4-6, and the term $(V^f_{silica} - 0.0226)$ is the volume fraction of SiO_2 which causes the enhancement i.e. the volume fraction minus the volume fraction of SiO_2 at the onset of enhancement. The results of this plot for three of the wafers

are shown in Fig.4.10, the constant on the y-axis being (0.0226k + c). The other data matched very well, but is omitted for reasons of clarity. Up to V^f_{silica} =0.05, it is predominantly linear although the region 0.025 < V^f_{silica} < 0.05 appears to be undergoing a transition from linear to exponential. The relationship is then exponential up to V^f_{silica} = 0.3. Above V^f_{silica} = 0.3, the relationship is still exponential but with a different gradient. This is the region where the enhancement factor vs intensity ratio relationship (Fig.4.8) also deviates from linearity.

For the first exponential region, the constants in equation 4-8, determined graphically, are

$$m = 2000 \pm 500$$
$$n = 13.8$$

i.e. $$I_o = (0.0226k + c) + 2000 \exp[\ 13.8(V^f_{silica} - 0.0226)]$$

"m" is a measure of I_o at the onset of enhancement, and as such, is prone to the variations described for I_{Si} earlier in this section. In fact, all the values of I_o at the onset of enhancement fall within this range which corresponds to V^f_{silica} = 0.025. The value of n, however, appears to be more fundamental since it is very similar for all the experimental data.

At volume fractions above 0.3, deviation from the behaviour described above is related to non-linear enhancement. The constants, for an expression similar to 4-8, are

$$m = 10000$$
$$n = 8.3$$

In this region, a less-effective mode of enhancement seems to dominate. The exponential constant, n, is about half the value of n for the first mode, and the constant m is about five times greater, corresponding to $V^f_{silica} \approx 0.125$.

If the values of m do represent the oxygen concentrations (or volume fractions) at which enhancement starts, we can say that the first mode of enhancement starts at $V^f_{silica} \approx 0.025$, but does not dominate until $V^f_{silica} \approx 0.05$, and the second mode starts at $V^f_{silica} \approx 0.125$ but does not dominate until $V^f_{silica} \approx 0.3$.

If the silicon secondary ion enhancement behaves in a similar way to the oxygen, then I_{Si}, the total intensity, is the sum of a matrix signal, I^m_{Si}, and a signal from

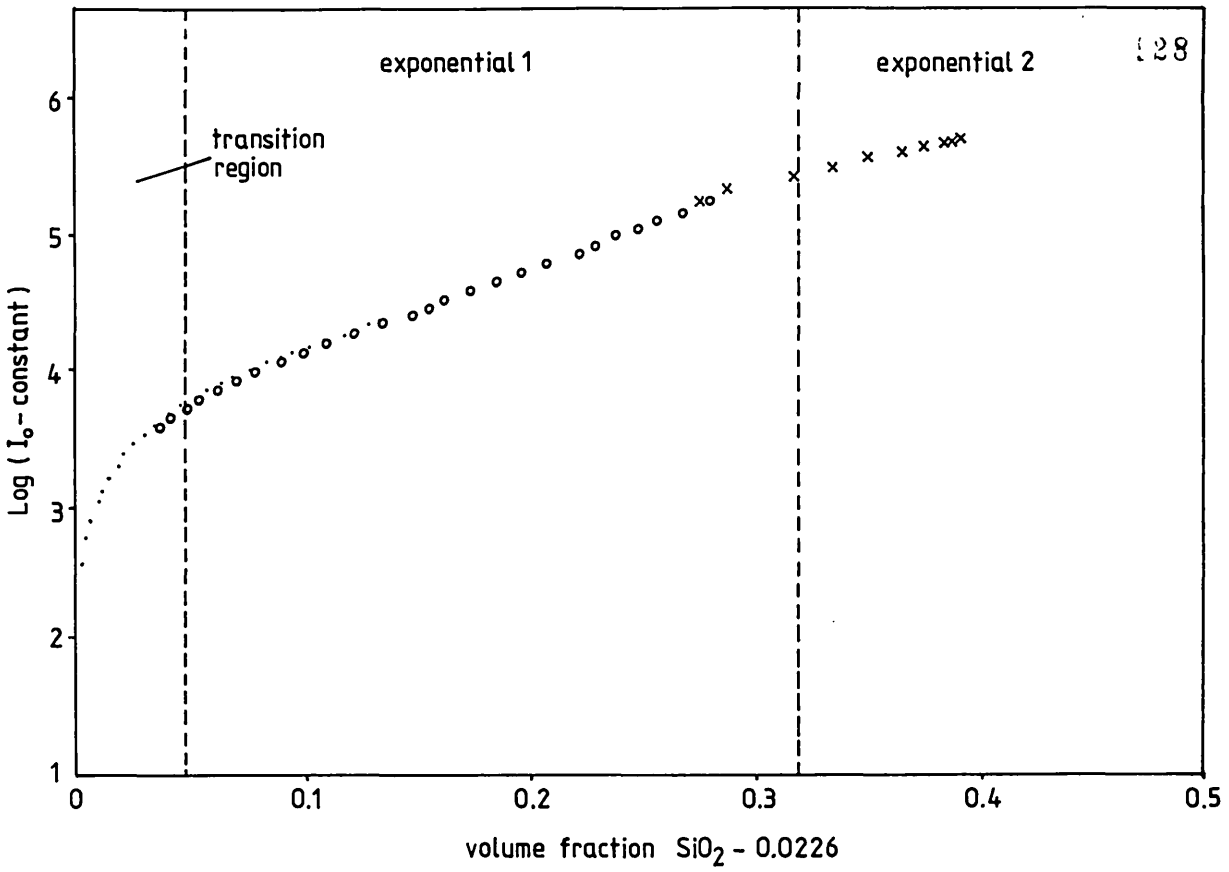


Fig.4.10 Plot to find the constants in equation 4-8.
Data from wafers 9(·), 12(∘) and 14(×).

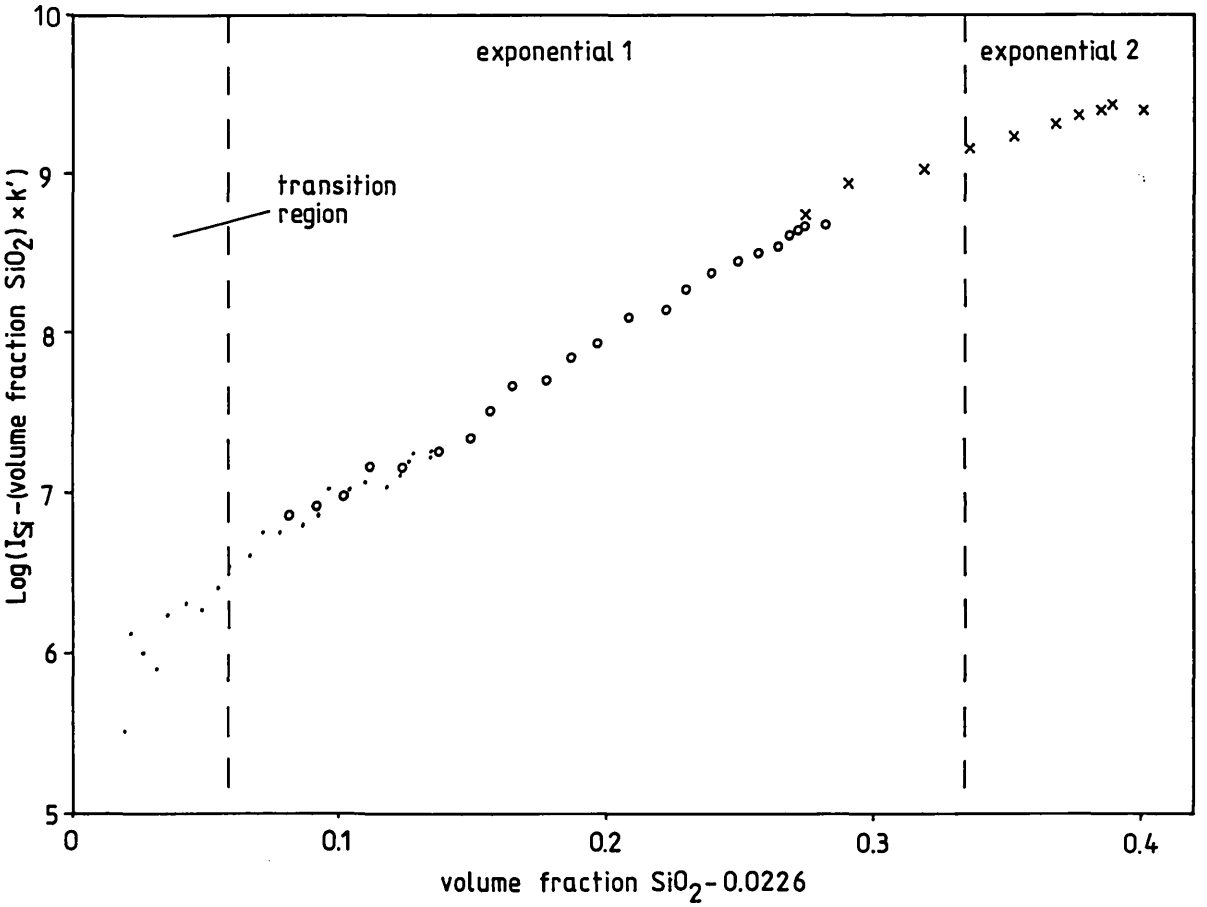


Fig.4.11 Plot to find the constants in equation 4-9.
Data from wafers 9(·), 12(∘) and 14(×).

the oxide, I^{s}_{Si}. Since V^{f}_{Si} is always greater than 0.5 in the data being analysed, I^{m}_{Si} will always be significant, and is given by equation 4-7a. If I^{s}_{Si} does depend on an exponential term, the overall equation for I_{Si} will be

$$I_{Si} = k' (1-V^{f}_{silica}) + m' \exp[\, n'(V^{f}_{silica} - 0.0226)] \qquad (4-9)$$

where m' and n' are constants (k' is given for each wafer in Table 4.4). To find the values of m' and n', Fig.4.11 is a plot of $Log_e[\, I_{Si} - k' (1-V^{f}_{silica})]$ as a function of $(V^{f}_{silica} - 0.0226)$.

As with the oxygen ion enhancement, there are two exponential regions, with a non-exponential transition region at the lowest oxygen concentrations. For the first exponential region, the constants are

$$m' = 400 \pm 100$$

and

$$n' = 9.5$$

whereas for the second region

$$m' = 2000$$

and

$$n' = 4.7$$

Again there are similarities with the behaviour of the oxygen signals. The constant, n', in the second exponential region is approximately half that for the first region. However, in the case of silicon, the m' values do not represent absolute intensities, rather the enhanced part of the signal i.e. the difference between the total intensity and that due to the silicon matrix. The first enhancement mode starts at $V^{f}_{silica} \approx 0.03$, but does not dominate until $V^{f}_{silica} \approx 0.05$, whereas the second mode starts at $V^{f}_{silica} \approx 0.15$, but does not dominate until until $V^{f}_{silica} \approx 0.3$.

Hence there appear to be three processes which contribute to the secondary ion intensity:

a) up to $V^{f}_{silica} \approx 0.0125$, the secondary ion intensities of oxygen and silicon are proportional to the volume fractions of Si and SiO_2 respectively.

b) At $V^{f}_{silica} \approx 0.0125$, an exponential term is superimposed on the linear term but it does not dominate until $V^{f}_{silica} \approx 0.05$. The intermediate range results in a transition region shown in Figs. 4.10 and 4.11.

c) At $V^{f}_{silica} \approx 0.125$, a second (exponential) mode of enhancement starts to operate, but it does not dominate until $V^{f}_{silica} \approx 0.3$.

4.1.4 Cross-Sectional TEM

The microstructure of the as-implanted material is shown in Plates 4.1 and 4.2. Plate 4.1a is a cross-section of wafer 2 (0.2 x $10^{18}O^{+}/cm^{2}$) with a SIMS profile overlay. Three main regions are indicated and are characterised as follows:

a) D: 60nm near-surface damage layer with a low oxygen concentration (the oxygen peak at the surface is due mainly to a native surface oxide). The damage is in the form of point defects and possibly small stacking faults and dislocation nuclei.
b) M1: 200nm layer of defect-free silicon with an oxygen concentration increasing to ≈3 atomic %. This oxygen is in the form of interstitial atoms and micro-precipitates of SiO_2.
c) M2: a region comprising of SiO_2 precipitates in a silicon matrix.

Regions M1 and M2 can be seen more clearly in plate 4.1b, a thinner part of the TEM specimen.

Plate 4.2a is a cross-section of wafer 6 (0.45 x $10^{18}O^{+}/cm^{2}$) showing the same regions as Plate 4.1. However at this higher dose, region D has increased in thickness to 150nm and M1 has decreased to 100nm with a corresponding increase in the thickness of region M2, the region containing SiO_2 precipitates. Some stacking faults (SF) are evident in this structure and are shown more clearly in Plate 4.2b. They are likely to be due to an increased stress and silicon interstitial concentration as the dose is increased and more oxide is formed.

4.1.5 Discussion

At first sight, the values of the exponential coefficients (n and n') appear to be very high, which tends to question their physical significance. It may be that the constants are related to the product of a number of factors such as secondary ion emission and post (emission) ionisation. However, using the constants to predict the SIMS secondary ion intensities from a calibrated oxygen depth profile (Fig.4.12), they do so quite accurately, indicating that they are correct. Any differences are mainly due to statistical fluctuations in the general model, the constants derived for the equations being an average for the whole range of data analysed. Even so, it is still unclear as to which physical mechanisms are responsible for this exponential-type enhancement.

Plate 4.1

Cross-sectional TEM of (unannealed) wafer 2 (0.2 x $10^{18}O^{+}/cm^{2}$).

a) with SIMS overlay and showing near-surface damage region (D), defect-free silicon layer (M1) and two-phase microstructure of Si and SiO_2 (M2),

b) clearer view of regions M1 and M2.

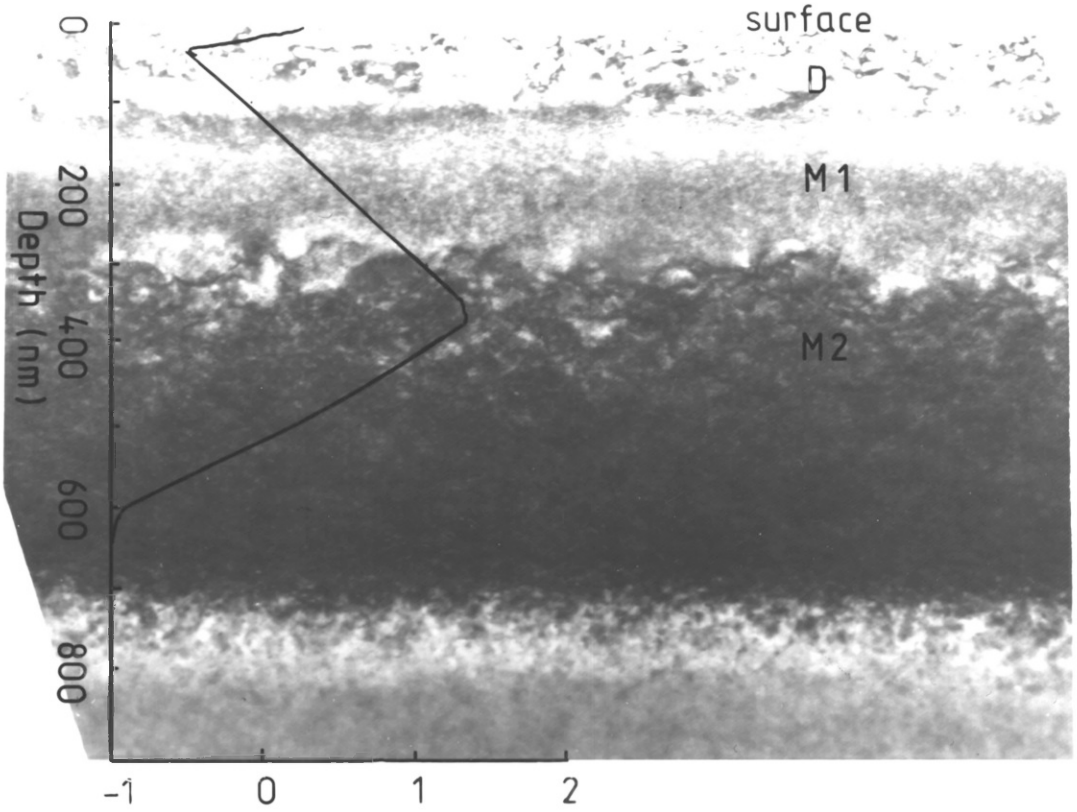


Plate 4.1a

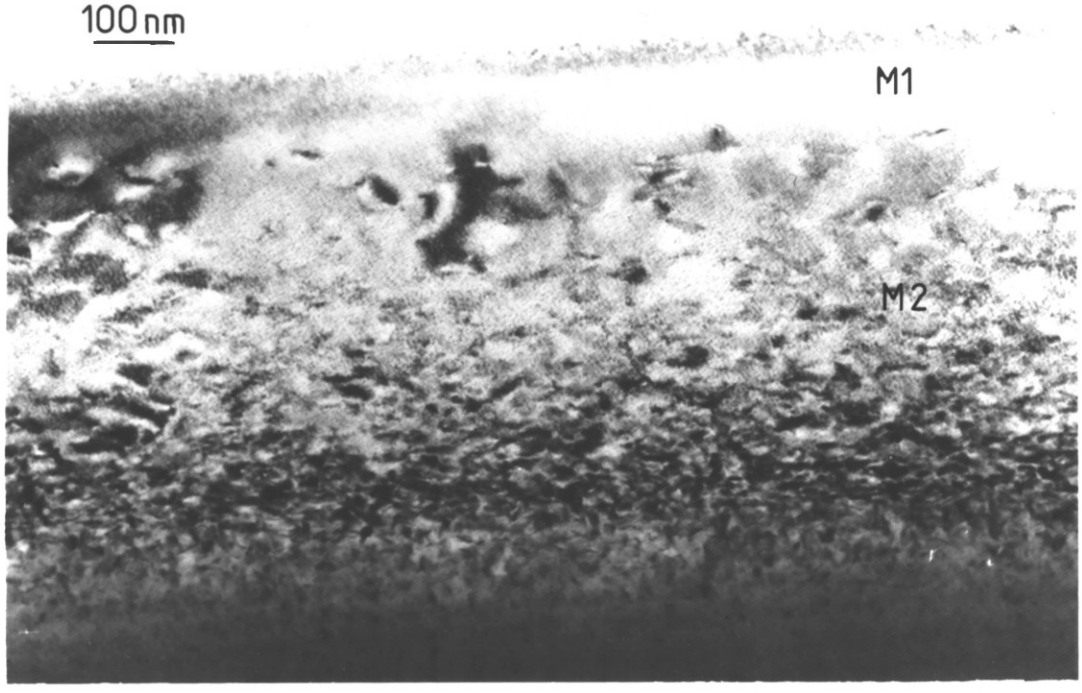


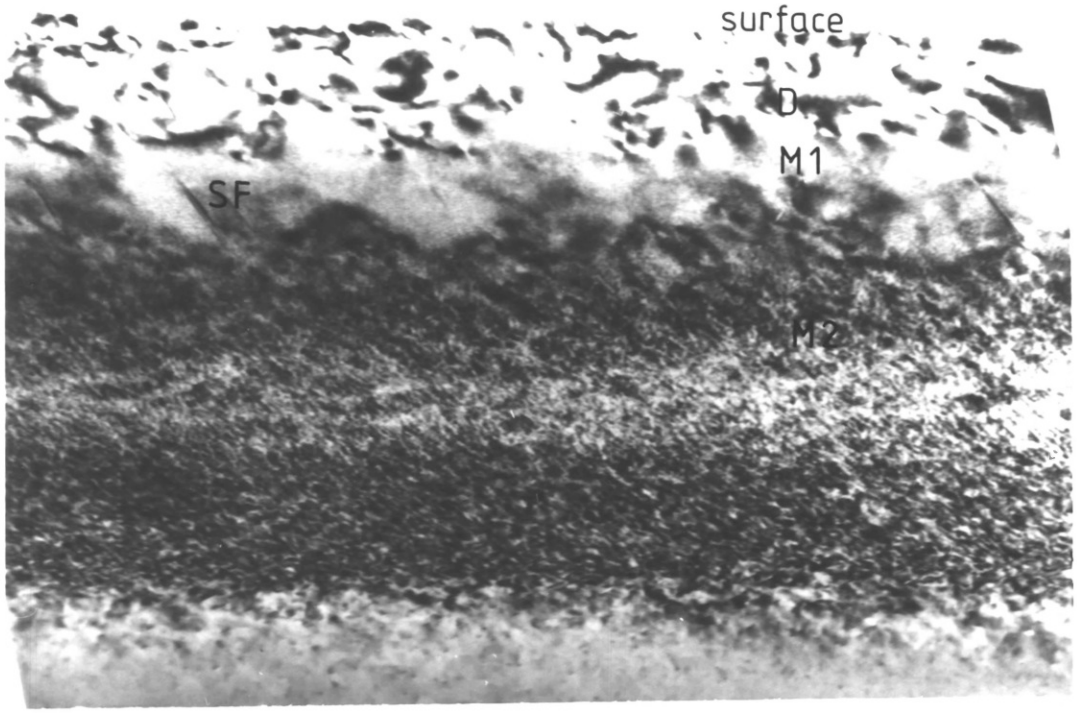
Plate 4.1b

Plate 4.2

Cross-sectional TEM of (unannealed) wafer 6 (0.45 x $10^{18}O^{+}/cm^{2}$).

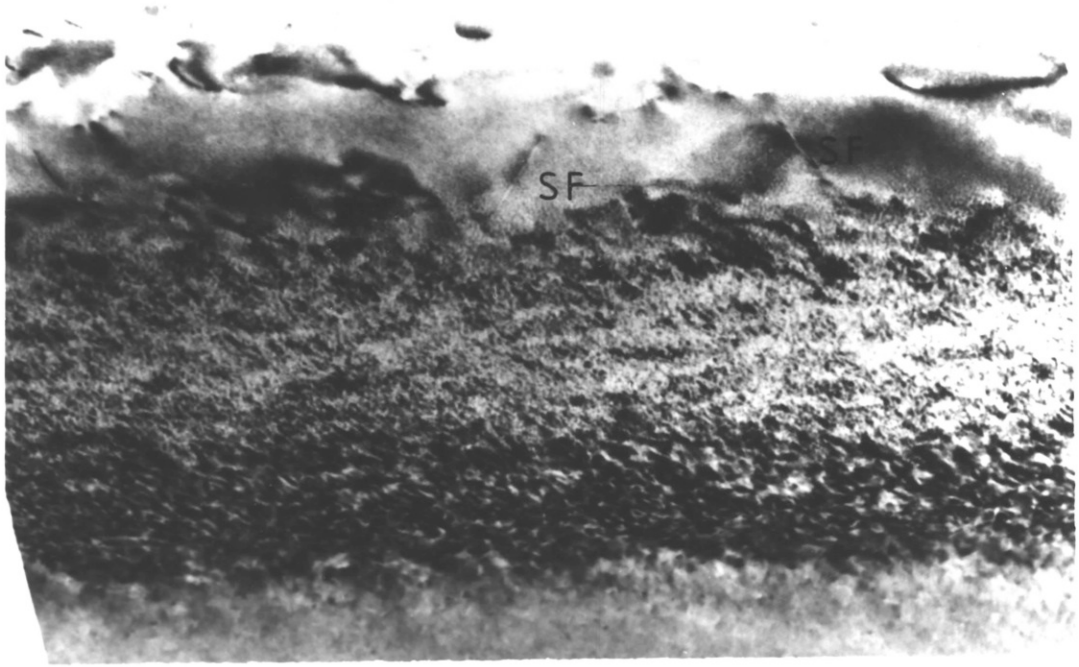
a) showing regions D, M1 and M2 and a stacking fault (SF).

b) clearer view of stacking faults.



100nm

Plate 4.2a



100nm

Plate 4.2b

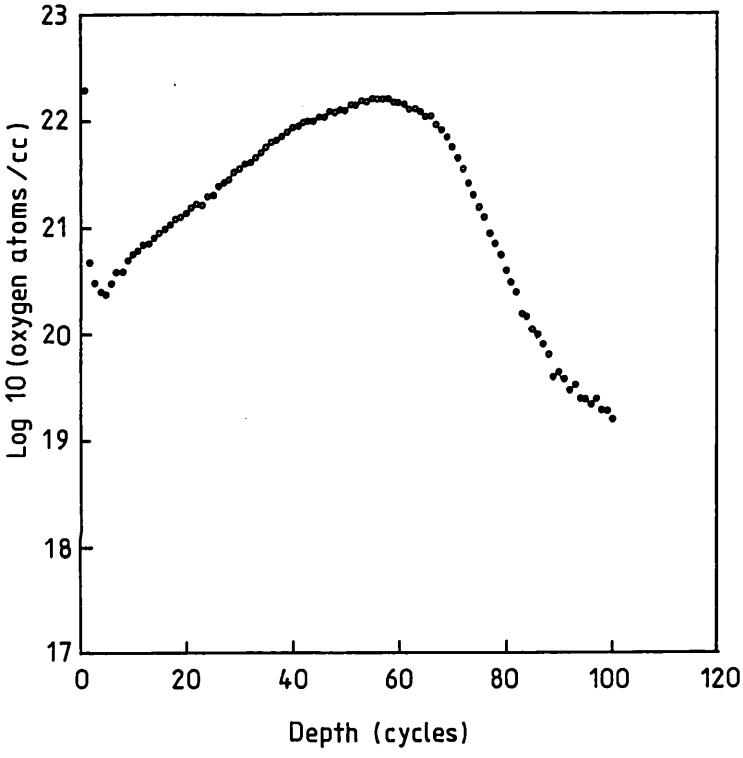


Fig.4.12a Calibrated profile for wafer 6
(dose = 0.45E 18/sq.cm).

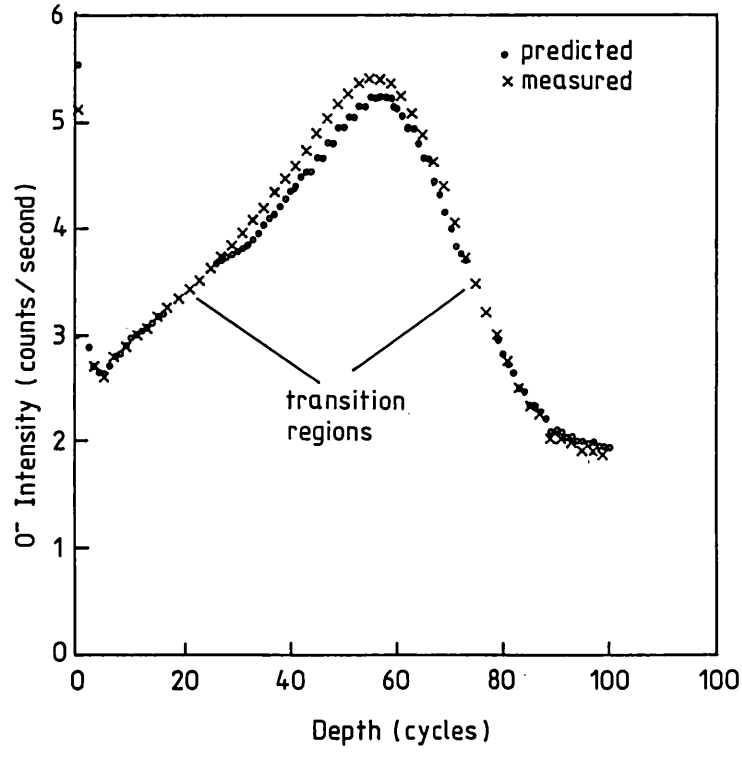


Fig.4.12b Measured and predicted O^- secondary ion intensities from the distribution shown above in Fig.4.12a.

Wittmaack [4] found the O^- and Si^- secondary ion intensities to be proportional to the oxygen concentration up to ≈3 atomic %. Above this, I_O was found to vary as $[O]^{3.7}$ whereas I_{Si} was linear up to ≈20 atomic %, above which there was an unquantified deviation from linearity. This clearly disagrees with the results of the current study above 3% oxygen.

Below 3% oxygen, the oxygen atoms are either in isolated interstitial sites (trapped in supersaturated solid solution) or they are tiny (≈nm) clusters of interstitials which may alternatively be considered to be micro-precipitates of oxide. When the oxygen is in this form, there is no detectable enhancement of the O^- and Si^- secondary ion intensities.

At higher oxygen concentrations, "the mechanism of secondary ion yield enhancement due to the presence of oxygen is not easy to ascertain" [4]. From the current study, it can simply be said that enhancement occurs when the microstructure of the target changes from silicon (with a low concentration of dispersed oxygen atoms as described above) to a two phase structure of silicon and SiO_2 precipitates (Plates 4.1 and 4.2). The presence of oxygen in "bulk" SiO_2 precipitates enhances the secondary ion yields exponentially.

Wittmaack [4], who studied mainly the O^- and Si^+ secondary ion yields, believed the O^- signal to come from SiO secondary fragments which dissociate to give O^- and Si^+. Whilst this may be the most intense (most likely) source, much more detailed analyses [5,6,7] concluded that all secondary ion species are a result of the sputtering and subsequent dissociation of a whole range of secondary ions and neutrals e.g. Si_2O, Si_3O, Si_2O_2...Si_xO_y. The secondary ions collected for SIMS analysis i.e. Si^- and O^- depend on the intensities of the ion molecules being emitted, this depending in turn on the target composition and the molecules' emission energies.

Up to 3% oxygen, the microstructure of the target changes very little, hence the types of nascent ion molecules being emitted would be expected to be the same (or very similar). With a higher concentration of oxygen (i.e. a higher volume fraction of SiO_2), more SiO molecules would be emitted, giving a linear relationship with the O^- secondary ion intensity. Since the probability of SiO dissociating into O^+ and Si^- is very small (due to the electronegativity of oxygen), another molecule must be responsible for the Si^- ion e.g. Si, Si_2, Si_3 etc. The intensity of this ion/molecule would be expected to remain approximately constant, as is observed experimentally, since the volume fraction of silicon remains approximately constant.

As the oxygen concentration increases and the target's microstructure changes,

different molecules will be emitted – there will obviously be a much higher proportion of those containing oxygen. From the current work, it is not possible to say what they are. However, they do dissociate into a wide range of ions, predominantly Si^+ and O^- with a smaller amount of Si^- and O^+ (any others are not really of interest here). This accounts for the large intensity difference observed between Si^- and O^-. Since the intensities of all oxygen–carrying molecules increase, the molecule(s) responsible for the majority of the Si^- production will also increase, although an exponential increase, which is quite dramatic, may not have been predicted beforehand.

At very high oxygen concentrations, where we find a second exponential region, it is possible that the emission of SiO (and the Si^-–carrying) molecules becomes unfavourable, and molecules with a higher proportion of oxygen are emitted (e.g. Si_2O_3, SiO_2 etc. become more favoured). If these do not have enough energy to dissociate entirely to atomic ions, the degree of enhancement will tail–off as found experimentally and described in section 4.1.3.

This hypothesis may help to explain the observed phenomena, but it does not speculate as to where the emitted molecules originate from.

If the O^- ion does originate from SiO molecules, these molecules may be produced most favourably from the surfaces of oxide precipitates – "surface" in this case also including the atoms in interstitial clusters and even isolated interstitial oxygen atoms where any micro–particles may be considered to be comprised entirely of "surface". As the oxygen concentration increases, an increasing proportion of the oxygen is in the "bulk" of oxide particles and the relative area of Si/SiO_2 interface will decrease. If "bulk" oxide favours the formation of more or larger secondary ion molecules, the ultimate secondary ion intensities will be altered.

As stated above, from the current work it is not possible to predict which emitted molecules dramatically increase their intensities and perhaps also their dissociation efficiencies. However it *is* possible to state that different volume fractions of SiO_2 produce different types of emitted ion–molecules with different energy spectra and different dissociation probabilities. In the oxygen range studied, three stages were observed and described in section 4.1.3, which probably relate to at least three different ion molecules and/or dissociations.

4.2 The Evolution Of Buried Oxide Structures And Overlayer Threading Dislocations

This section reports on the evolution of SIMOX structures after annealing as the dose is increased from 0.1 to 0.65 x $10^{18}O^+/cm^2$. It follows the segregation of oxygen, initially to form discrete precipitates of SiO_2 and eventually a continuous buried oxide layer. This is explained in terms of thermodynamics; the influence of point defects is also considered. The distribution of point defects has also allowed a mechanism for the formation of overlayer threading dislocations to be postulated.

4.2.1 SIMS Analysis

The SIMS results in this section were obtained using a primary beam of Xe^+ ions and detecting the O^- and Si^- secondary ions. Fig 4.13 is the SIMS profile for the wafer implanted to a dose of 0.1 x $10^{18}O^+/cm^2$ and annealed at 1300°C for 5 hours, showing two peaks: a thin peak centred around a depth of 230nm and a thicker, slightly more intense peak centred around 350nm. The oxygen concentrations at the peaks (calibrated using the method described in section 4.1) are $\approx$ 1.2 and 1.5 x 10^{22} at/cm^3 respectively (corresponding to SiO_2 volume fractions of $\approx$ 0.3 and 0.35). Thus, although all the oxygen has segregated to two distinct layers (and probably also to the surface), neither one is likely to consist of a continuous buried oxide layer.

As the dose increases to 0.25 x $10^{18}O^+/cm^2$ (Fig.4.14), the deeper peak increases in height at the expense of the shallower one, until there is just one broad peak at a dose of 0.3 x $10^{18}O^+/cm^2$ (Fig.4.15). This peak is still not level across the top, and corresponds to an oxygen concentration of $\approx$ 3 x 10^{22} at/cm^3 (the volume fraction of SiO_2 is $\approx$ 0.7). Hence a continuous oxide layer would still not be expected, rather a diphasic microstructure of Si and SiO_2.

For doses of 0.4 and 0.45 x $10^{18}O^+/cm^2$ (Fig.4.16a), the peak broadens from 120 to 135nm, the top flattens and the lower interface becomes more abrupt. The flattened peak has an oxygen concentration corresponding to 3.5 to 4 x 10^{22} at/cm^3, very similar to that in stoichiometric SiO_2, suggesting that a buried oxide layer is present. However, this is not the case for the corresponding as-implanted wafer (also Fig.4.16b), which clearly shows no evidence of a continuous buried layer, the peak oxygen concentration being only $\approx$ 2 x 10^{22} at/cm^3.

At the two highest doses (Figs. 4.17 and 4.18), the processes of peak broadening (155-175nm) and interface-sharpening continue. The buried oxide layer now appears to be well-established with a silicon overlayer thickness of $\approx$300nm. The oxygen

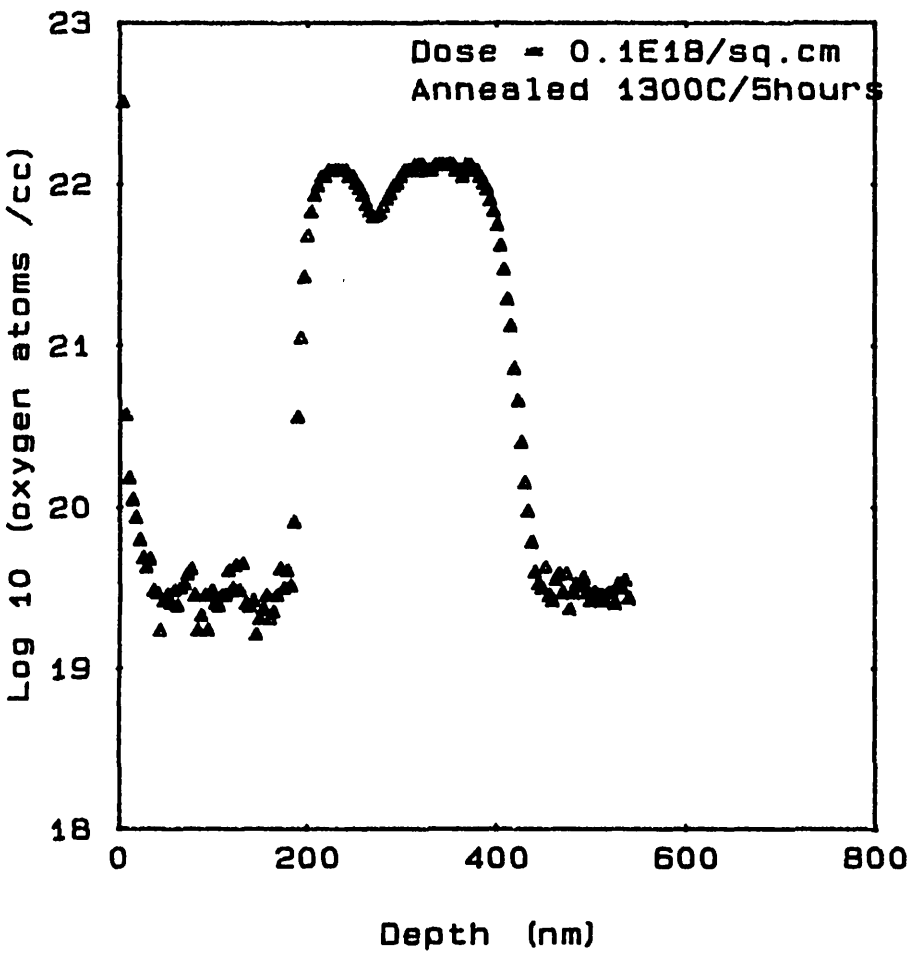


Fig.4.13 Calibrated profile for annealed wafer 1.

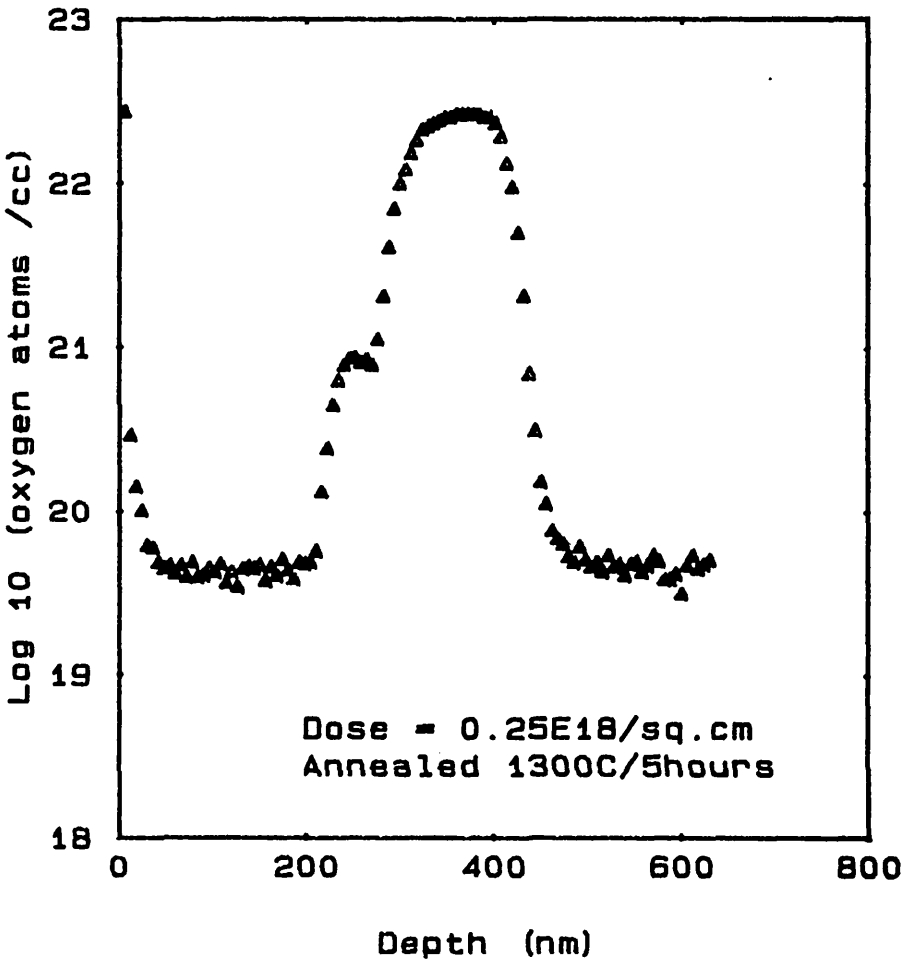


Fig.4.14 Calibrated profile for annealed wafer 3

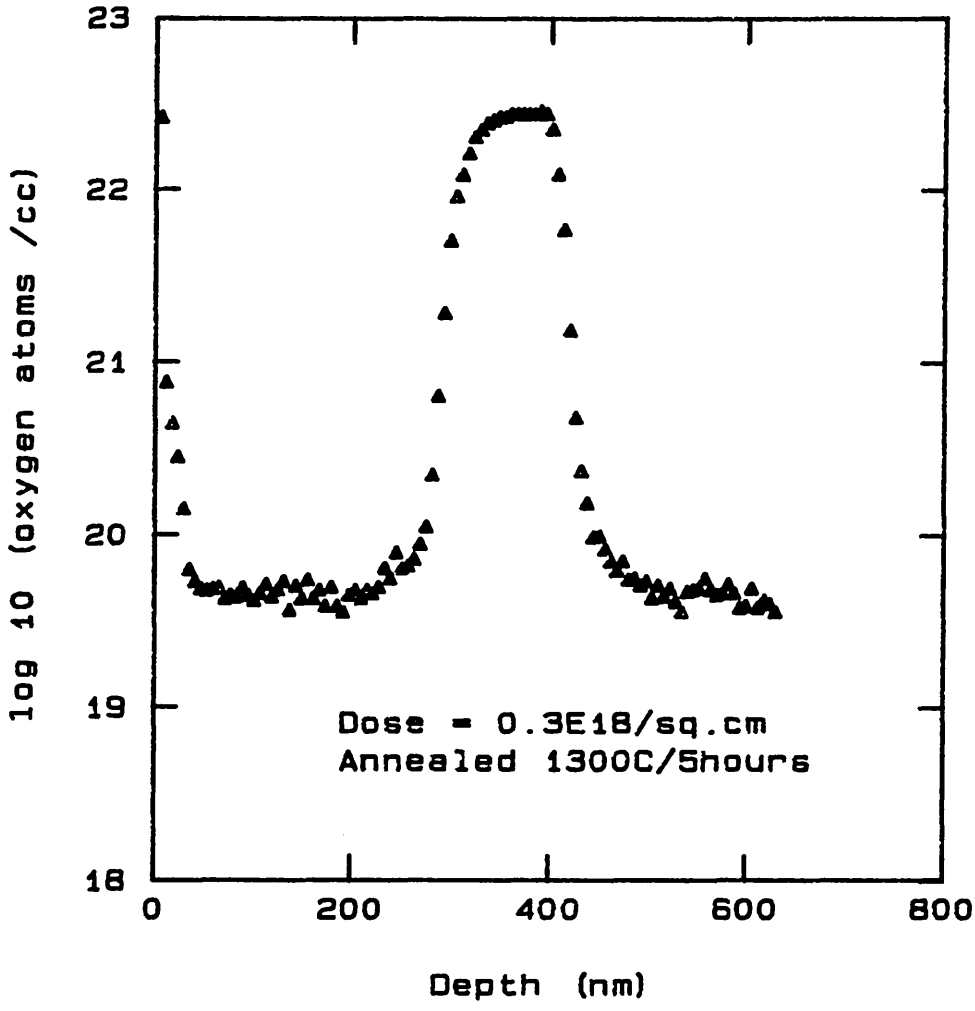


Fig.4.15 Calibrated profile for annealed wafer 4.

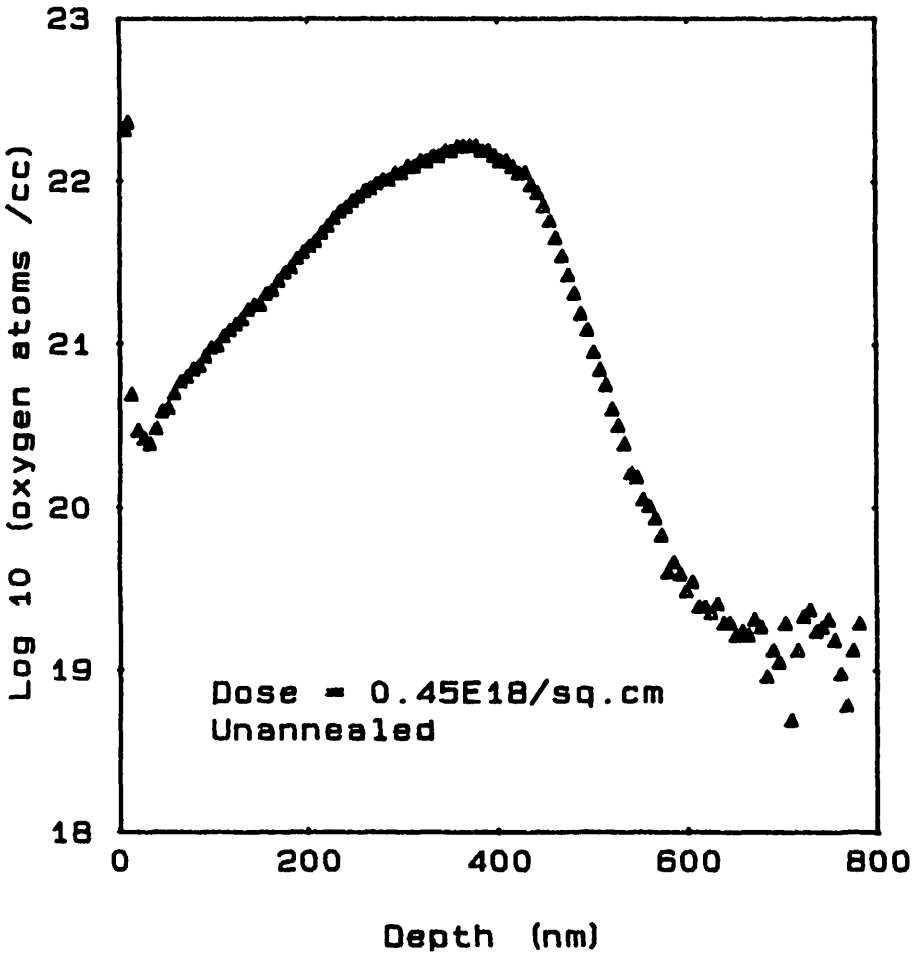


Fig.4.15a Calibrated profile for wafer 6 (no anneal).

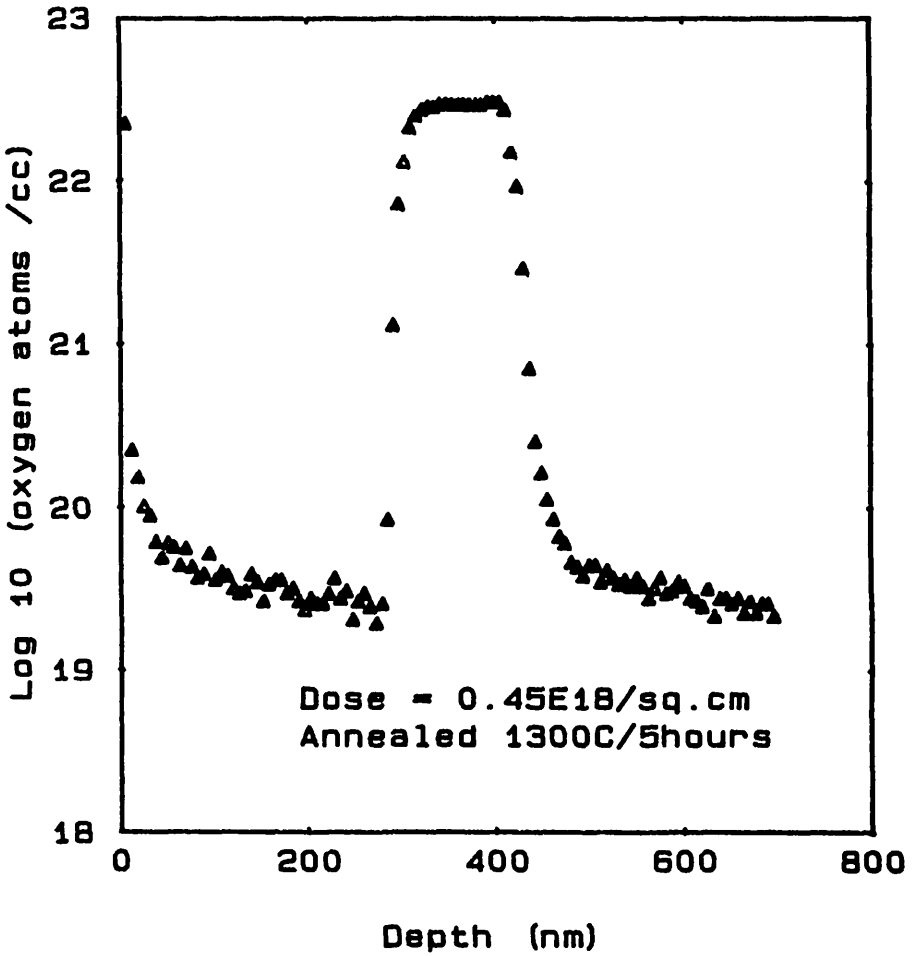


Fig.4.15b Calibrated profile for wafer 6 (annealed)

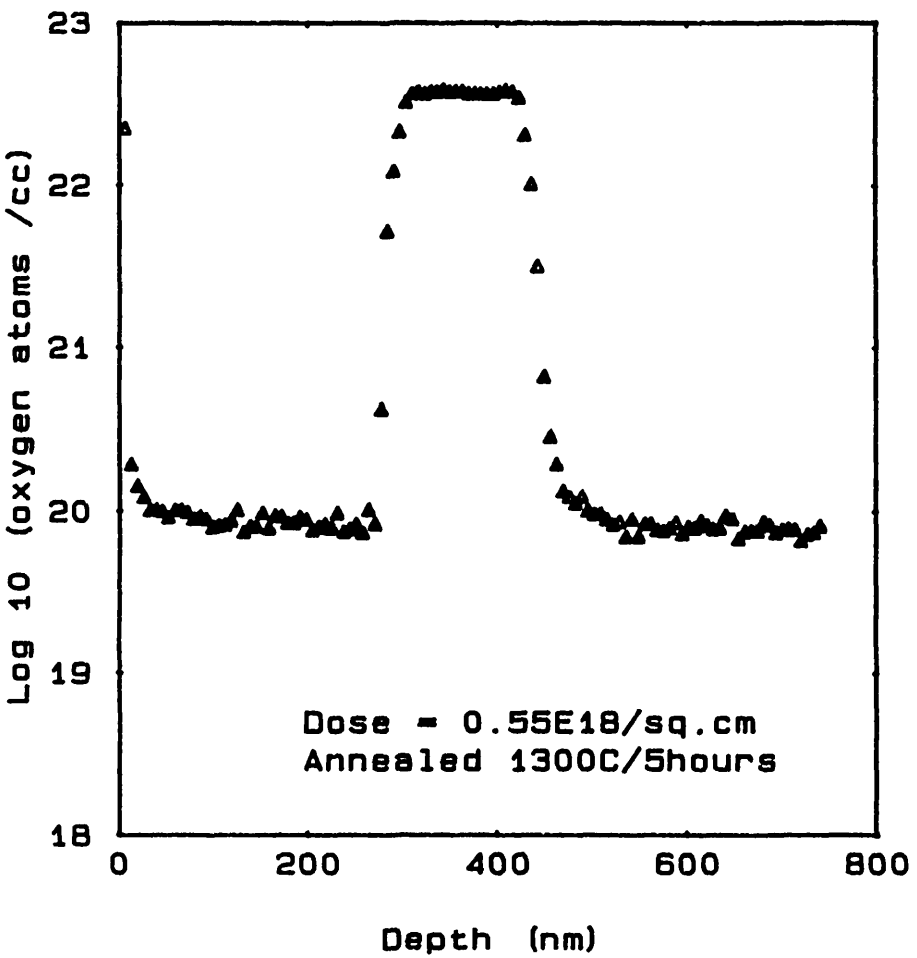


Fig.4.17 Calibrated profile for wafer 7 (annealed).

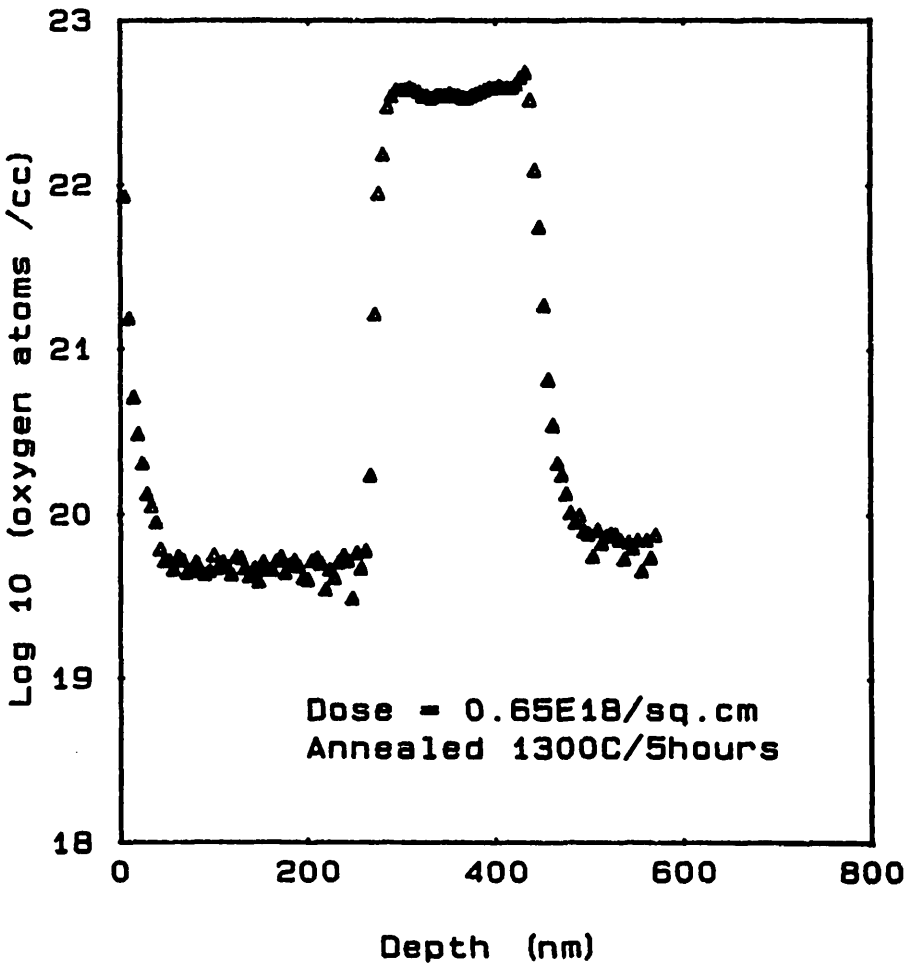


Fig.4.18 Calibrated profile for wafer 8 (annealed)

content of the overlayer is $\approx 10^{20}$ at/cm^3, close to the detection limit of the SIMS technique under these operating conditions.

4.2.2 Cross-Sectional TEM

4.2.2.1 Low Doses: 0.1 to 0.25 x $10^{18}O^+$/cm^3

The cross-sectional TEM results in this section support the SIMS results very well. Plate 4.3 is a cross-sectional micrograph of the wafer implanted to a dose of 0.1 x $10^{18}O^+$/cm^2 and annealed at 1300°C for 5 hours. It shows two layers of SiO_2 precipitates (corresponding to the peaks in the SIMS profile shown in Fig. 4.13): the first at a depth of 250-260nm and the second at a depth of 360-390nm. The precipitates in the upper layer are polyhedral and are bounded by the {111} and {100} silicon planes. They are typically 60nm in diameter and their density/cm^2 in the plane of the precipitates decreases from 3 x 10^9 to 7 x 10^8 to 3 x 10^8 as the dose increases from 0.1 to 0.2 to 0.25 x $10^{18}O^+$/cm^2 respectively. The precipitates comprising the lower layer, typically 10^9/cm^2, are also polyhedral but they become more elongated, parallel to the wafer surface along the (100) plane, as the dose increases. Once the precipitates start to elongate at around 0.2 x $10^{18}O^+$/cm^2, they remain ≈100nm thick but their length increases to as much as 300nm at 0.25 x $10^{18}O^+$/cm^2 (Plate 4.4). The few precipitates which remain in the upper layer tend to be the larger ones, which can be explained in terms of an "Ostwald Ripening" of the microstructure i.e. during annealing, the largest precipitates are the most stable, hence they grow at the expense of the smaller ones (see section 2.1.2). The precipitates in the lower layer correspond to the peak range during implantation and they become larger as the dose increases simply because more oxygen is available for precipitate growth.

The upper precipitate layer is at a depth corresponding to the peak of the damage distribution from the implantation process, this damage aiding heterogeneous nucleation. Since there is less oxygen at this depth, the precipitates are generally smaller, but as the dose increases, there is likely to be a higher damage level between the precipitate layers which would aid oxygen diffusion between them. This radiation-enhanced diffusion would mean that the larger (lower) precipitates grow whilst the smaller ones (including those in the upper layer) dissolve, until we end up with a situation where there is only one layer of precipitates, as is observed.

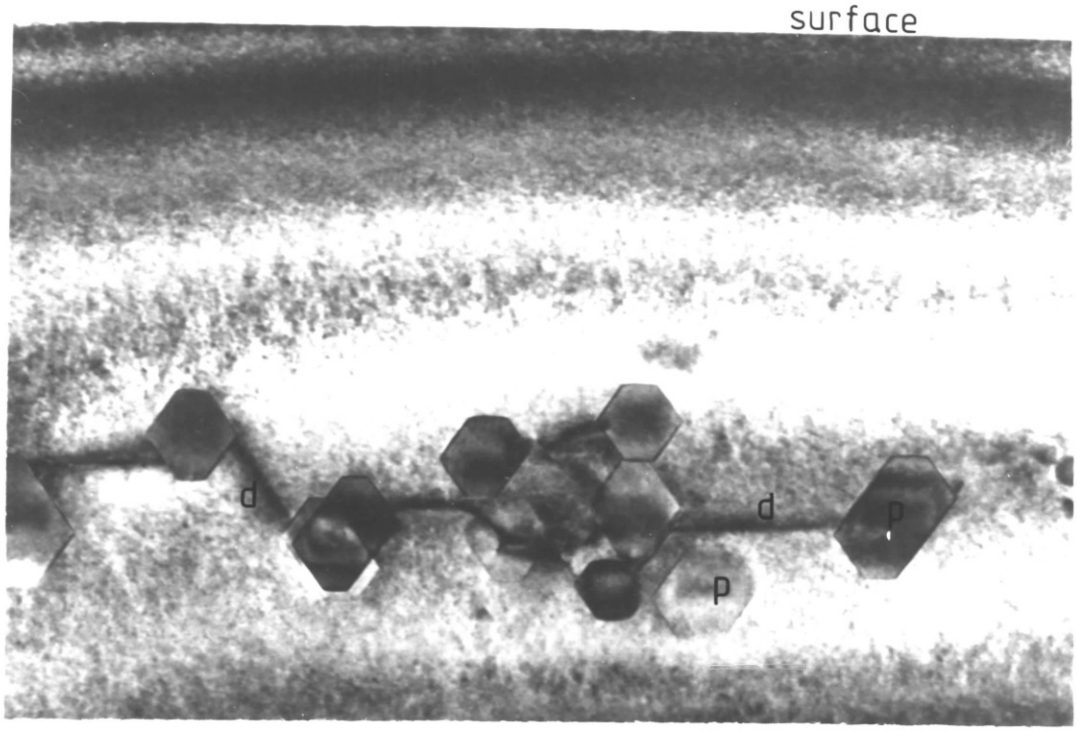
There are no overlayer threading dislocations in any of these wafers as determined by XTEM (i.e. $\leqslant 10^5$-10^6/cm^2). There are, however, dislocations between the precipitates, both within the layers and between them (Plate 4.5), with a density of

Plate 4.3

Cross–section of wafer 1 (0.1 x $10^{18}O^{+}/cm^{2}$), annealed at 1300°C for 5 hours showing faceted SiO_2 precipitates (p) and dislocations (d).

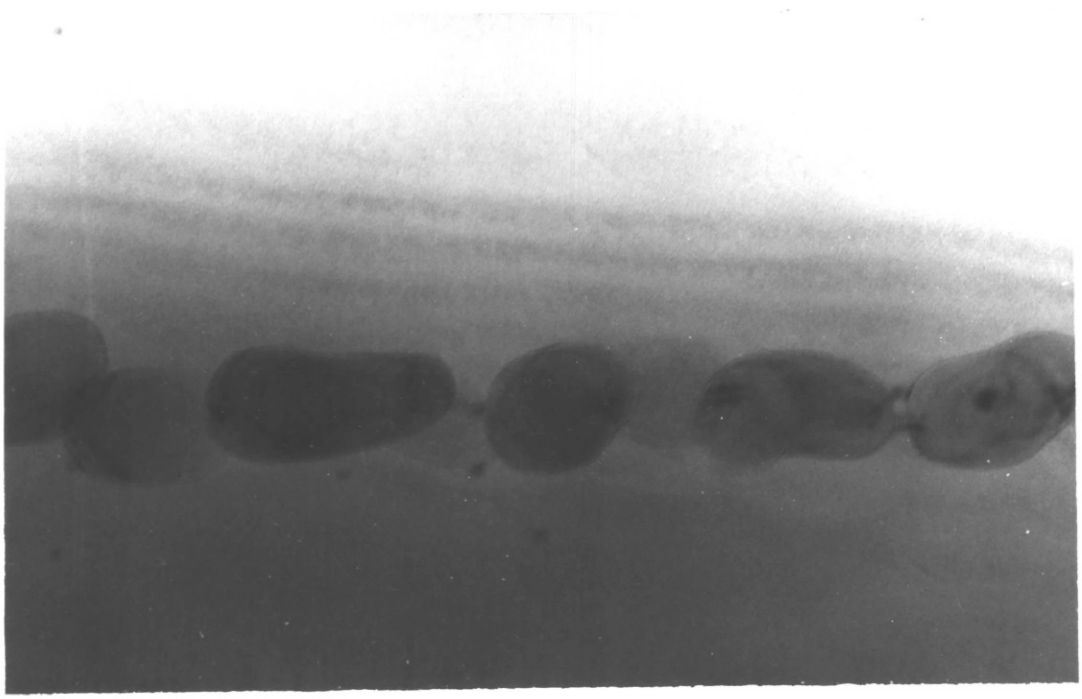
Plate 4.4

Cross–section of wafer 3 (0.25 x $10^{18}O^{+}/cm^{2}$), annealed at 1300°C for 5 hours showing how the oxide precipitates, mainly in one layer, have started to elongate.



100nm

Plate 4.3



100nm

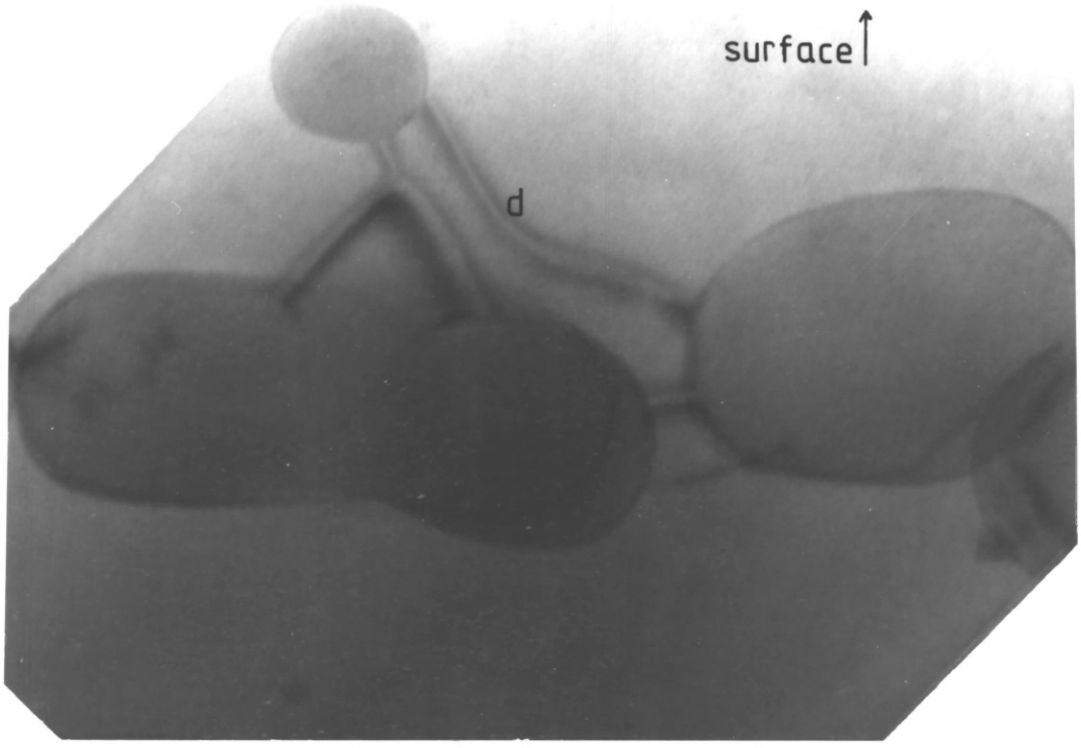
Plate 4.4

Plate 4.5

Cross-section of wafer 3 (0.25 x $10^{18}O^{+}/cm^{2}$), annealed at 1300°C for 5 hours. This high-magnification image shows large precipitates in the lower layer and a smaller precipitate in the upper layer, all connected by dislocations (e.g. d). The dislocation double-images are due to multi-beam diffraction conditions.

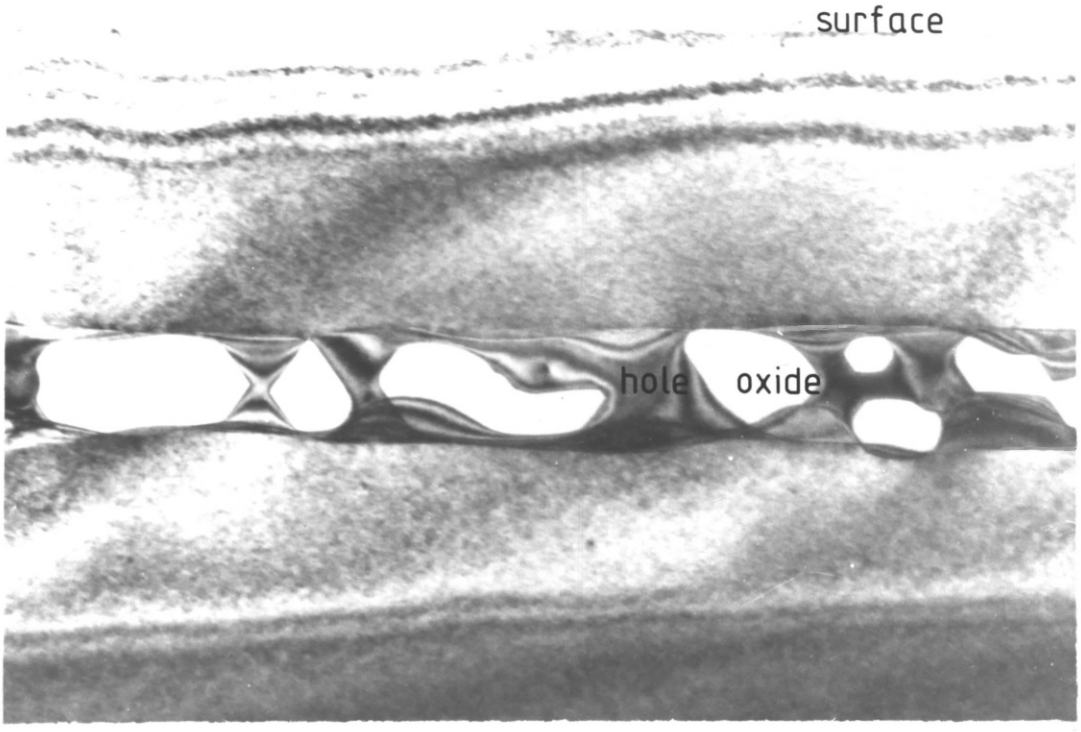
Plate 4.6

Cross-section of wafer 5 (0.4 x $10^{18}O^{+}/cm^{2}$), annealed at 1300°C for 5 hours showing the discontinuous oxide network (white) and the holes in it. The layer almost constitutes a continuous buried oxide.



100 nm

Plate 4.5



100 nm

Plate 4.6

$\approx 10^9/cm^2$ in the plane of the precipitates. It has not been possible to characterise these dislocations in terms of their Burgers vectors. It is likely that they are the result of oxidation-induced stress and silicon interstitial production as discussed in section 2.1.3. Most likely, they lie between precipitates to minimise the total line length and/or because they have reacted with each other, perhaps by the interaction of expanding loops.

4.2.2.2 Medium Doses: 0.3 to 0.4 x $10^{18}O^+/cm^2$

The wafers implanted with 0.3 and 0.4 x $10^{18}O^+/cm^2$ are both characterised by a 100-110nm thick continuous oxide network (Plate 4.6). Although the network is continuous, it cannot be described as a continuous buried layer since it contains a large number of dicontinuities or "holes" still occupied by the silicon. These holes are important in terms of silicon interstitial migration (which will be discussed in section 4.2.3). They are ≈100nm in diameter at a dose of 0.3 x $10^{18}O^+/cm^2$ and 40-50nm at 0.4 x $10^{18}O^+/cm^2$, although they still remain ≈250nm apart corresponding to a density of $10^9/cm^2$ in the plane of the oxide. This reduction in size is a result of the oxide growing laterally rather than vertically towards the surface. The edges of the oxide, at the holes, are still characterised by facets on the {111} silicon planes.

It seems likely that the discrete oxide precipitates have coalesced to form an oxide network. However, since there is not enough oxygen present to form a complete 100nm buried oxide, holes are left in the buried layer.

In both wafers, the silicon overlayers are ≈330nm thick and contain no dislocations. In fact no dislocations or any other type of crystallographic defect were found during XTEM analysis of these specimens.

4.2.2.3 High Doses: ≥0.45 x $10^{18}O^+/cm^2$

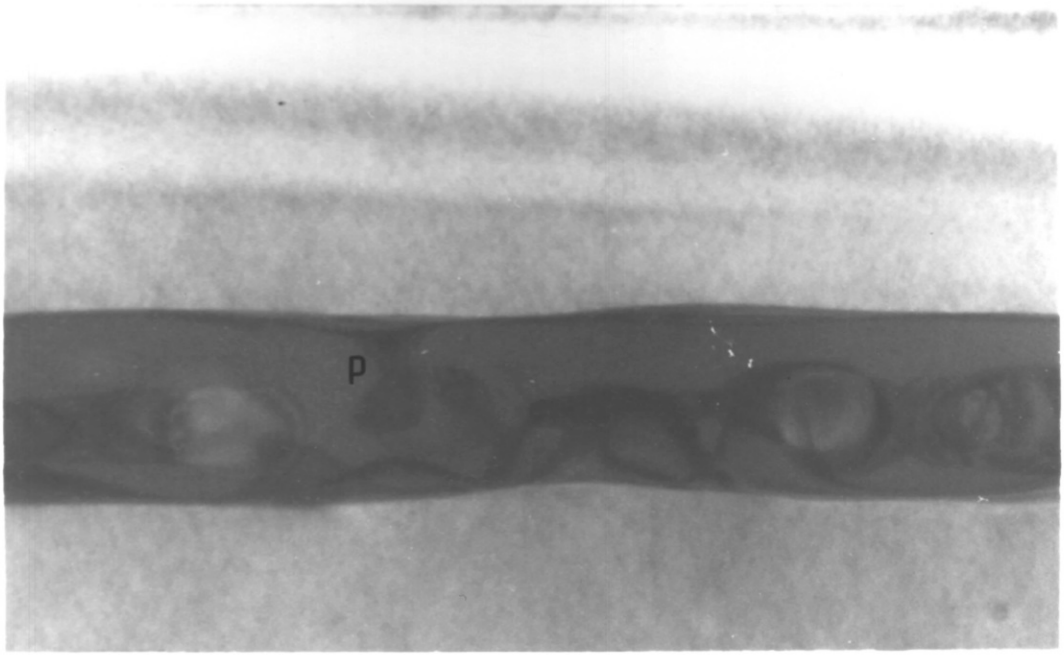
In this dose range, we can see a continuous buried oxide layer e.g. Plate 4.7. In each case, the lower Si/SiO_2 interface is at a depth of ≈500nm, and the oxide thickness increases from 130 to 160 to 180nm as the dose increases from 0.45 to 0.55 to 0.65 x $10^{18}O^+/cm^2$ respectively. However, it must be stressed that this thickness includes a large number of silicon isthmuses from the overlayer protruding into the oxide making the upper interface very uneven as opposed to the relatively flat and planar lower interface. Some of these isthmuses are almost totally surrounded by the growing oxide front.

Plate 4.7

Cross-section of wafer 8 (0.65 x $10^{18}O^{+}/cm^{2}$), annealed at 1300°C for 5 hours showing a deep silicon protrusion into the buried oxide layer.

Plate 4.8

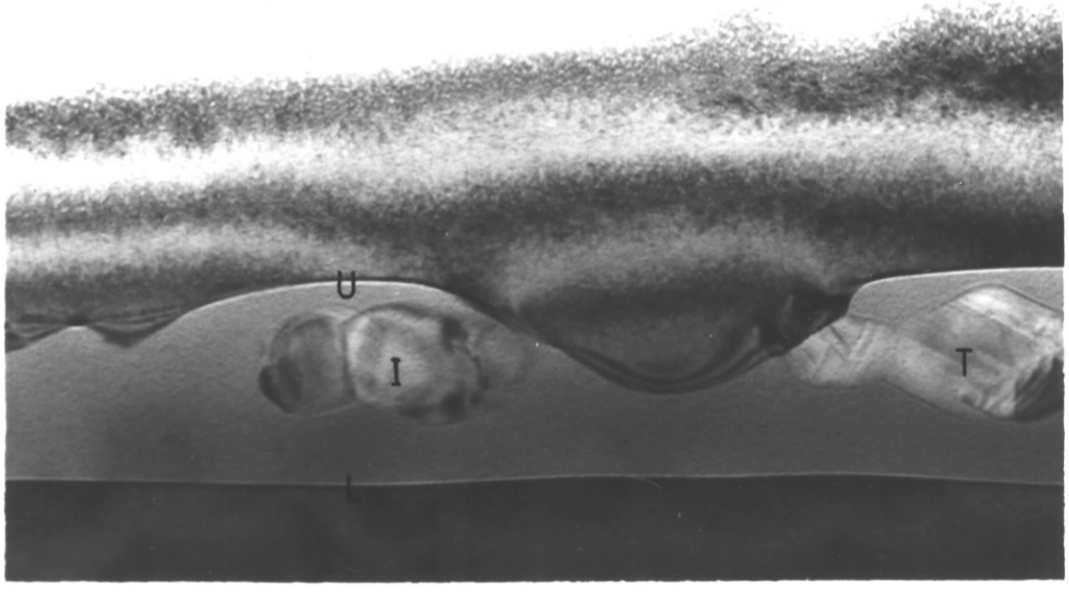
Cross-section of wafer 7 (0.55 x $10^{18}O^{+}/cm^{2}$), annealed at 1300°C for 5 hours. The upper interface (U) is very wavy compared to the lower one (L). Silicon inclusions (I) can be seen within the buried oxide, some of them twinned (T).



100nm

Plate 4.7

surface



100nm

Plate 4.8

The buried layers contain a high density of twinned silicon inclusions which tend to be situated closer to the upper interface (Plate 4.8). This region is likely to have undergone the most regrowth during annealing and once the buried layer has formed near the lower interface (see section 2.2.3.1). The inclusions can be considered to be isthmuses which have become totally surrounded by oxide and are now trapped. Hence the lower 40–60nm of oxide is free from all but the smallest silicon inclusions, which are also twinned.

The most interesting feature of these wafers is that for the first time we can see crystallographic defects in the overlayer. There are none of the characteristic threading dislocations, but instead there is a high density of small twins (Plate 4.9) and stacking faults (Plate 4.10) along the upper Si/SiO_2 interface. Where the silicon protrudes a long way into the oxide, we tend to find both microtwins and thin stacking faults, whereas in the shallower protrusions and on the more planar regions of the upper interface, we tend to find only stacking faults.

4.2.3 Discussion

From previous work on the growth of buried oxides during annealing (section 2.3), it is most likely that the oxidation-induced silicon interstitials play a key role in the formation of crystallographic defects in the silicon overlayers. In fact, work reported in section 2.2.3.3 suggested that once a continuous buried oxide layer had formed, any interstitials formed by further oxide growth (predominantly at the upper Si/SiO_2 interface) were trapped in the silicon overlayer.

In the current work, no threading dislocations (or any other overlayer defects) were observed up to a dose of $0.4 \times 10^{18} O^+/cm^2$. This dose range also corresponds to the absence of a buried oxide layer, even after annealing, meaning there will be no trapping of silicon interstitials in the overlayer. It seems fair to assume that even if no dislocations are present after annealing, the damage regions present after implantation would still have contained the dislocation nuclei. However, with no excess of silicon interstitials, the dislocation nuclei are prevented from growing and they are annealed out.

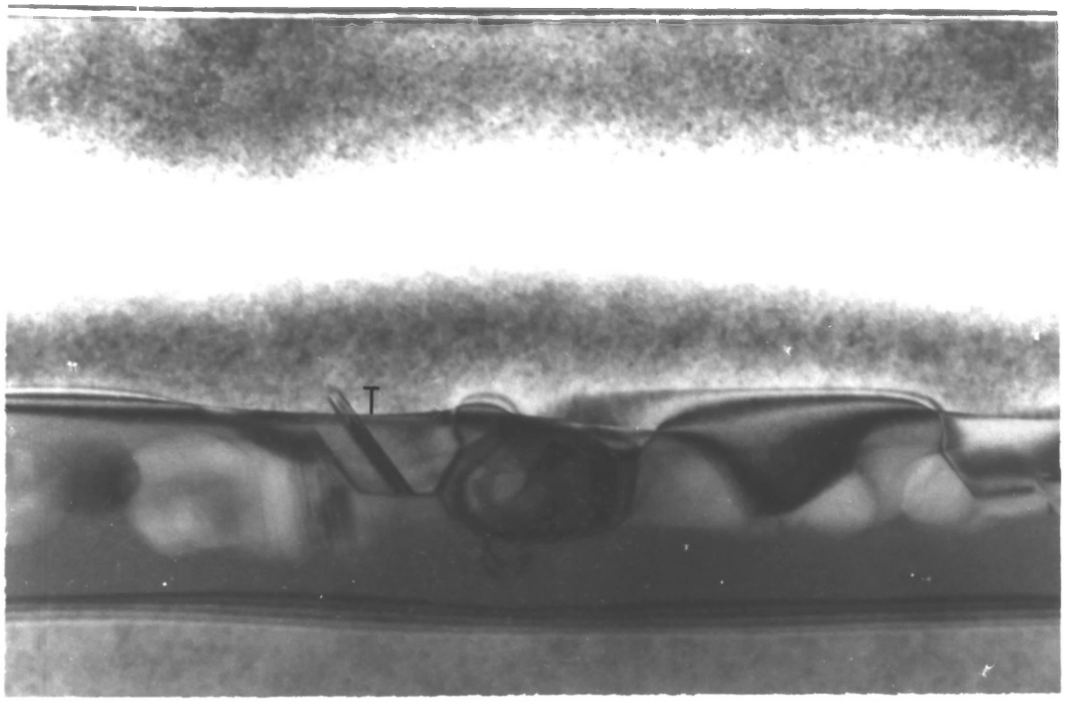
At doses of 0.45 to $0.55 \times 10^{18} O^+/cm^2$, there is no continuous buried layer after implantation, although such a layer is present after annealing at 1300°C for 5 hours, indicating that the layer formed sometime during the anneal. Up to the point of buried layer formation (i.e. in the early stages of the anneal), the silicon interstitials would not have been trapped and hence the dislocation nuclei would have annealed out. At the onset of continuous buried layer formation, two processes would have

Plate 4.9

Cross-section of wafer 7 (0.55 x $10^{18}O^{+}/cm^{2}$), annealed at 1300°C for 5 hours showing a very distinct twin (T) growing upwards from the upper interface in one of the silicon isthmuses.

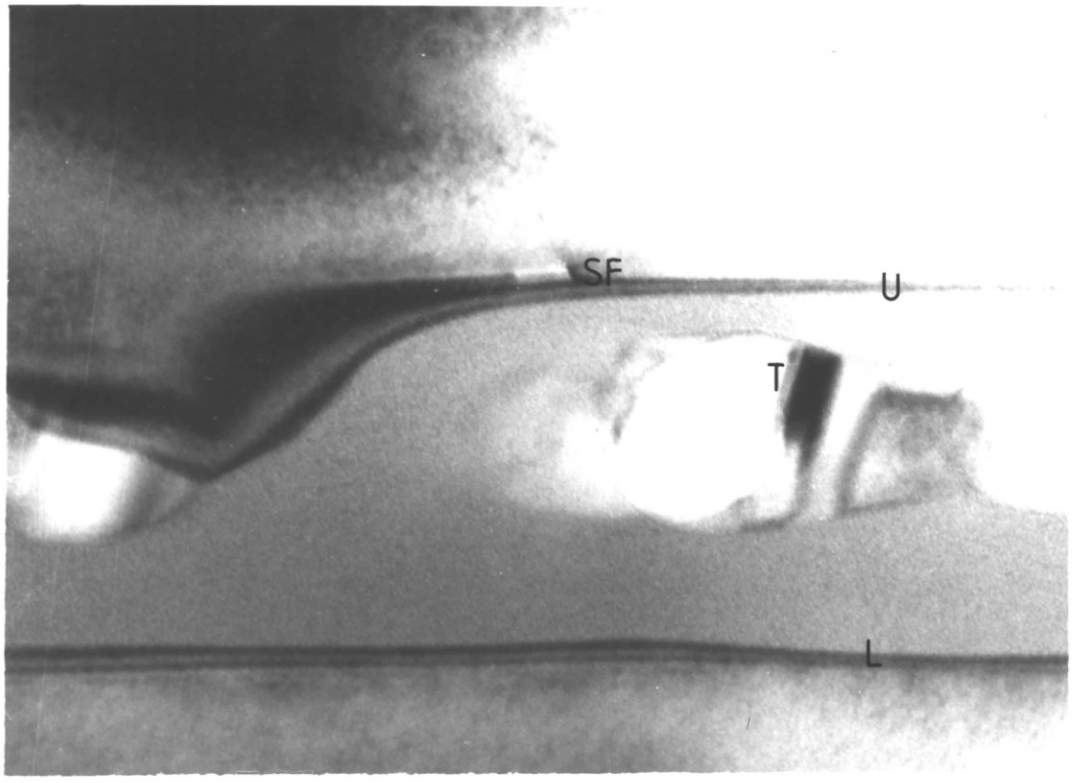
Plate 4.10

High-magnification cross-section of wafer 7 (0.55 x $10^{18}O^{+}/cm^{2}$) showing a wavy upper interface (U), a planar lower interface (L) and twinned silicon inclusions (T). A small stacking fault (SF) can be seen on one of the more planar areas of the upper interface.



100nm

Plate 4.9



100nm

Plate 4.10

occurred:

i) an increase in stress, particularly at the Si/SiO_2 interfaces, and

ii) an increase in the silicon interstitial concentration within the overlayer.

The combination of these two factors would explain the formation of the observed twins and stacking faults. To relieve the interfacial stress, the silicon interstitials could provide extra atomic planes which comprise the twins and stacking faults. The structure and formation of these two types of defect are very similar on an atomic scale, hence it is possible that they are formed by the same mechanism. The fact that twins are only observed in the silicon isthmuses may be explained by a modified stress field in those isthmuses due to the silicon, in some cases, being almost totally surrounded by oxide. A detailed stress analysis, which may help to explain the result, is beyond the scope of this work.

To summarise, it is clear that the formation of a continuous buried oxide layer during implantation is not a prerequisite for the formation of one after annealing. Indeed, to produce a SIMOX structure with no overlayer threading dislocations, it seems best to implant to a dose which will not form a buried layer during implantation. This allows dislocation nuclei to be annealed out before excess silicon interstitials are trapped, so only micro-defects will be formed at the upper Si/SiO_2 interface.

Some very recent work [8] strongly suggests that the dislocations are a result of the growth of nuclei present near the wafer surfaces after implantation. This surface damage layer can clearly be seen in Plate 4.1. These nuclei are believed to propagate downwards towards the upper Si/SiO_2 interface as the excess interstitials are trapped by them. This seems likely in the light of the present work although it contradicts the work of van Ommen in section 2.3.4, who believed the dislocations to nucleate near the bottom of the silicon overlayer. Hence the summary should be amended to state that no overlayer threading dislocations will be formed if no dislocation nuclei are present *when an excess of silicon interstitials are trapped in the silicon overlayer.*

A closer examination of the work of van Ommen [9] and the French group [10,11], who were able to produce SIMOX material with few or no dislocations, reveals that in each case, no damage region was present at the surface of the as-implanted wafers. This is most likely to be the result of pre-heating the wafers to a stable temperature and maintaining stability of the other implantation parameters such as beam current and voltage. This stability may allow the surface damage to anneal out during the implant, leaving no nuclei for the propagation of dislocations during

annealing.

This theory can also be applied to the multiple low-dose implants described in section 2.3.4. For the first one or two implants, a buried layer may not be present, even after the intermediate anneals, so it does not really matter if there is a surface layer of damage since the interstitials will not be trapped. As the total dose is increased to the point where a continuous buried oxide is formed, the implantation of small doses may not produce enough silicon interstitials to saturate the overlayer and/or there may not be many dislocation nuclei at the surface, hence they can anneal out.

The material analysed in this study, implanted to a dose of $1.6 \times 10^{18} O^+/cm^2$ in a single step, was always found to have a surface damage layer and was always found to contain 10^8 to 10^9 dislocations/cm^2 (see section 4.4). Hence it can be said that the material implanted at the University of Surrey in this manner will probably never result in dislocation-free SIMOX after annealing. However, with wafer pre-heating to $\approx 600^{\circ}C$, the surface damage layer may be annealed out during the implant, resulting in dislocation-free structures.

4.3 Defect And Impurity Analysis: SPIRE Wafers

4.3.1 Dislocation Characterisation

Plate 4.11 consists of a selection of Bright Field (BF) and Weak-Beam (WB) images of the same area of a plan view TEM specimen from wafer SP10B. They are all imaged from two-beam diffraction conditions using the diffracted beams indicated.

Plates 4.11a and b are BF and $(1\,1\,\bar{1})$ WB images, and Plates 4.11c and d are BF and $(0\,\bar{2}\,2)$ WB images respectively. Five dislocations (A to E) are indicated on each of these micrographs (B has another dislocation joined to it and there is a triangular stacking fault at the node). Most of the dislocations do not rigidly follow a particular crystallographic direction. In Plates 4.11e ($g = 1\,\bar{1}\,\bar{1}$) and 4.11f ($g = 0\,\bar{4}\,0$), dislocations A to E are no longer visible. Hence it can be deduced that they have the Burgers vectors $a/2[1\,0\,1]$.

The dislocations are inclined to the wafer and specimen surfaces, as shown by these results and from cross-sectional TEM. In $<0\,1\,1>$ cross-sections, the dislocations usually appear straight and inclined at 50-60° to the surface, indicating that they lie on the $\{1\,1\,1\}$ planes. Working on this basis, the dislocation images in Plate 4.11 (which are projected onto the image plane), have lines approximately along the $[0\,\bar{1}\,1]$ direction. This indicates that the dislocations lie on the $(\bar{1}\,1\,\bar{1})$ plane with the lines approximately along the $[\bar{2}\,\bar{1}\,1]$ directions or on the $(1\,1\,\bar{1})$ plane approximately along the $[\bar{2}\,1\,\bar{1}]$ direction. With a Burgers vector of $a/2[1\,0\,1]$, the angle they make with the overall line vector is ≈73°, indicating an orientation between 60° and edge for the dislocations. Hence, for dislocation E (Plate 4.11b), section 1 of the dislocation appears to be predominantly edge and section 2 has more 60° character.

Plate 4.12 is a $(1\,1\,\bar{1})$ WB image showing some other characterised dislocations. Both 2a and 2b lie in the $(1\,1\,\bar{1})$ plane, and have the Burgers vector $a/2[1\,1\,0]$. Dislocation 2a, which is almost straight, follows the line $[\bar{1}\,0\,\bar{1}]$ and is a 60° dislocation, but 2b has two parts: one with direction $[\bar{1}\,0\,\bar{1}]$ (60°) and the other lying between the $[\bar{2}\,1\,\bar{1}]$ and $[\bar{1}\,1\,0]$ directions (giving it more edge character). Due to difficulties associated with the WB imaging technique, it has not been possible to characterise every dislocation.

From observations of dislocations in bulk silicon [14], the dislocations have the lowest energy when they are dissociated (≈7nm), they lie in straight lines and are either pure screw, pure edge or have 60° character. The fact that most of the dislocations in the current study are not straight i.e. are of mixed edge and 60° character is

Plate 4.11

Plan view TEM micrographs from wafer 10B, at different specimen orientations.

a) $(1\,1\,\bar{1})$ BF image showing five dislocations (A to E).

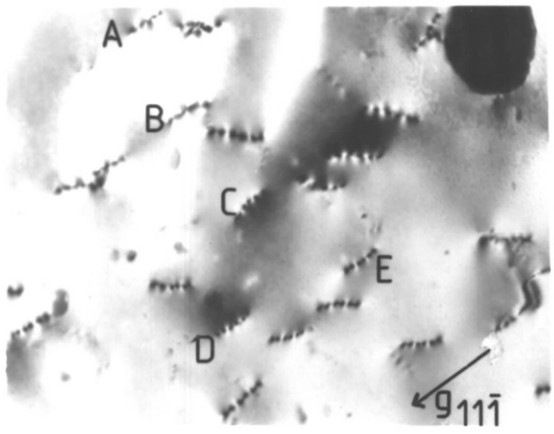
b) $(1\,1\,\bar{1})$ WB image showing clearer images of the dislocations A to E.

c) $(0\,\bar{2}\,2)$ BF showing the same dislocations.

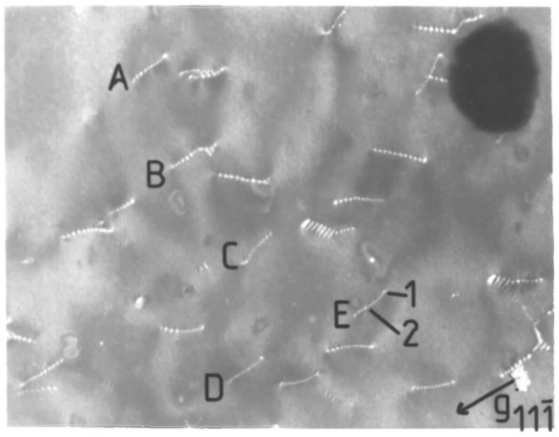
d) $(0\,\bar{2}\,2)$ WB image

e) $(1\,\bar{1}\,\bar{1})$ WB image – dislocations A to E are no longer visible.

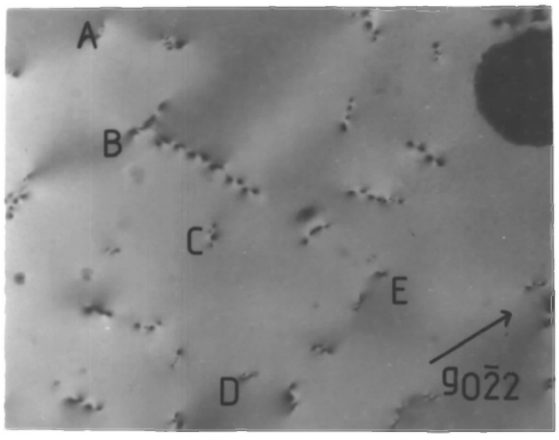
f) $(0\,\bar{4}\,0)$ WB image – again the dislocations A to E are invisible.



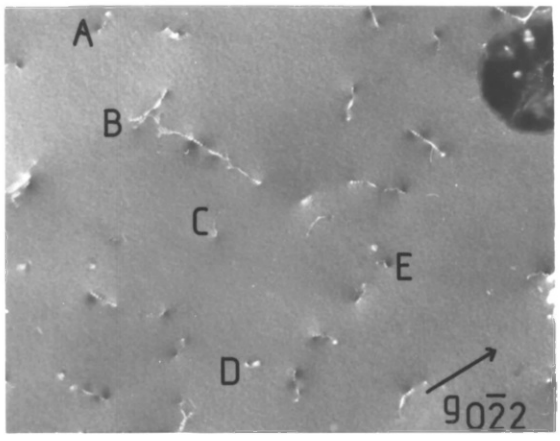
200nm a)



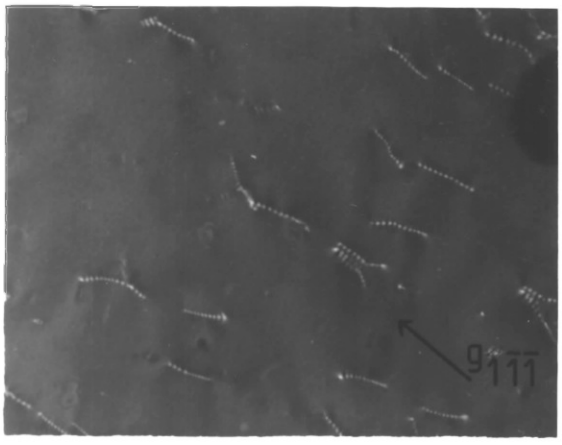
200nm b)



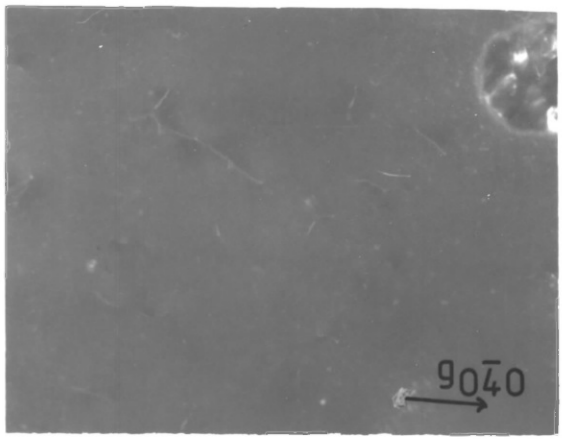
200nm c)



200nm d)



200nm e)



200nm f)

Plate 4.11

Plate 4.12

WB image using the $(1\,1\,\bar{1})$ planes, showing dislocation types 1 ($a/2\langle 1\,0\,1\rangle$) and 2 ($a/2\langle 1\,1\,0\rangle$). It has not been possible to characterise all of the others.

Plate 4.13

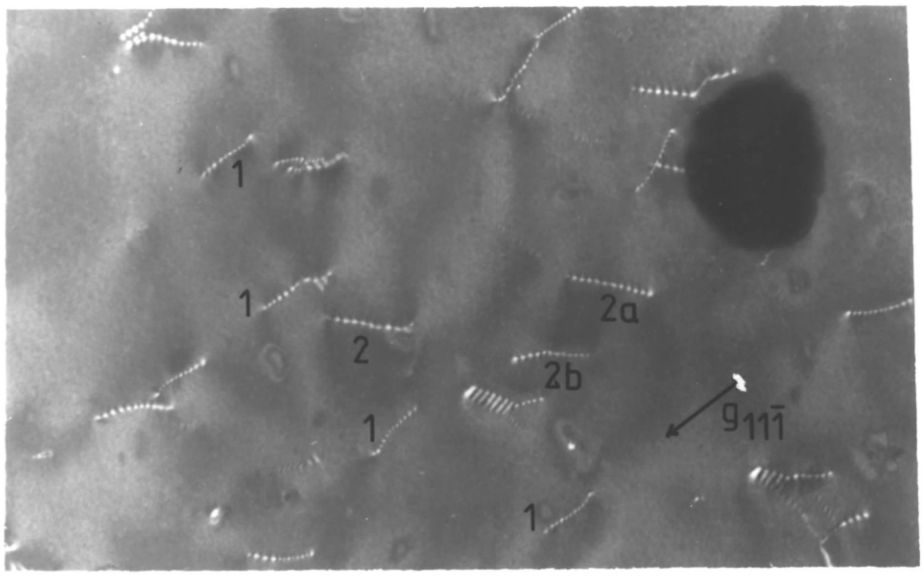
Micrographs to show the dissociation of two unit dislocations into partial dislocations, separated by a stacking fault.

a) BF image ($[0\,1\,1]$ beam direction) of a complex dislocation structure, D.

b) $(1\,1\,\bar{1})$ WB image of D, now seen to comprise of dislocations (d_1, d_2, a and b) and stacking faults (SF).

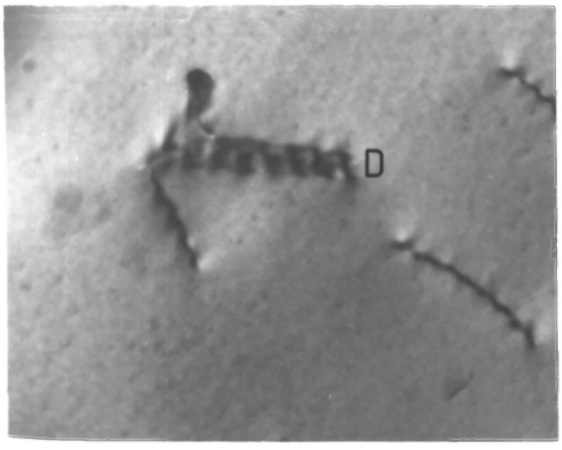
c) $(1\,\bar{1}\,1)$ WB image of D showing the same features.

d) $(\bar{3}\,\bar{1}\,1)$WB image showing no stacking fault contrast. Three very faint lines can be seen corresponding to partial dislocations with a separation of ≈15nm.

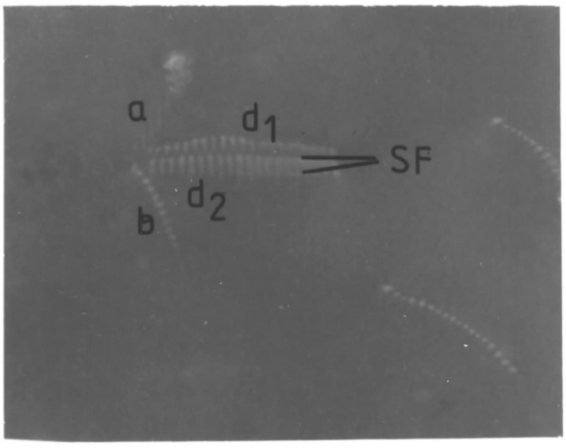


200nm

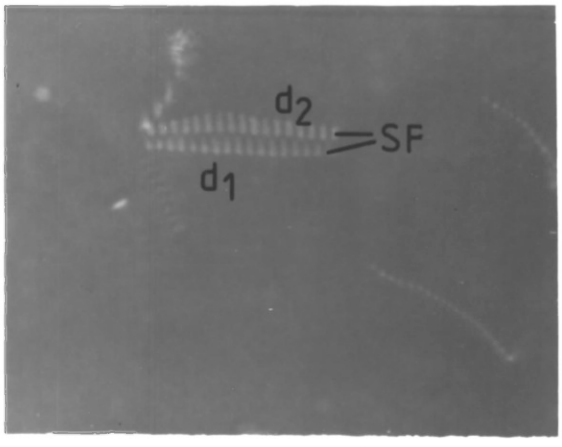
Plate 4.12



a) 100nm



b) 100nm



c) 100nm



d) 100nm

Plate 4.13

because they will tend to change their line directions near the surfaces, where they are pinned. This may explain why segments of the dislocations are not clearly defined as being totally of edge or 60° character. In all cases where the dislocations were able to be characterised, the orientation was found to vary between pure edge and 60° with no screw orientations being observed.

Early work on the dissociation of dislocations in silicon [14] found the equilibrium partial separation to be ≈7.5nm with a corresponding stacking fault energy (SFE) of ≈50mJ/m^2. These values were for intrinsic stacking faults. From the current WB investigations, there is definite evidence that some of the dislocations are extended i.e. they have dissociated into two partial dislocations separated by a stacking fault. Plate 4.13 shows an example of this under different diffracting conditions. Not all of the dislocations were observed to be dissociated; this does not mean they are not, just that the resolution of this WB technique is not good enough to image the individual partial dislocations.

Plate 4.13a is a BF image showing a complex defect (D) comprising of dislocations and stacking faults. The WB images (Plates 4.13b and c) show the right hand side of the defect to be comprised of two overlapping stacking faults bounded by partial dislocations (the stacking faults, SF, and the positions of the sets of partials, d_1 and d_2, are indicated). Both d_1 and d_2 are joined to other dislocations (a and b), which are also dissociated. Although the fault contrast is clearly visible under these diffracting conditions, it is not possible to say whether or not the partials are visible because of the strong, overlapping stacking fault contrast.

Plate 4.13d is a $(\bar{3}\bar{1}1)$ WB image of the same defect structure. Although it is a very low contrast image, three lines can just be seen which represent three of the four partial dislocations and there is no stacking fault contrast. This indicates that the partial dislocations are most likely to have $a/6\langle 112\rangle$-type Burgers vectors with the fault vector of the stacking fault being of the $a/3\langle 111\rangle$-type i.e they are probably Shockley partials. The separation of the partials is 15 ± 3nm, most of this error being due to uncertainties in the absolute positions of the dislocations. This is larger than the partial separation in bulk silicon [14], because surface-pinning effects are likely to mean that the partials are not at a true "equilibrium" separation, a term usually applied to isolated dislocations in bulk material. In the results reported here, the dislocations are close enough to interact with each other and they are pinned at either end by the silicon surfaces/interfaces, both of which are likely to affect the partial separation.

Two further features are shown in Plate 4.14, which is comprised of images from a different area of the same specimen. Plate 4.14a shows a complex defect structure, D, with a very wide (≈25nm) region of contrast compared to the other dislocations (≈3nm). Although this is a WB image, the resolution is still not good enough to ascertain the actual structure of the defect. However, it looks very similar to D in Plate 4.13 i.e. it probably consists of two overlapping stacking faults bounded by partial dislocations. The relationship between the stacking fault contrast and the reciprocal lattice vectors ±g in Plates 4.14b and c (where g = $1\bar{1}\bar{1}$) shows that the stacking faults are extrinsic. Since this type of complex defect is only seen when two dissociated dislocations are in close proximity to each other, it is possible to say that this wide dissociation is aided by the interaction of the two dislocations.

The second feature on plate 4.14 is seen most clearly in plate 4.14d. This dislocation network contains two types of stacking faults: the triangular SF1 types which appear at dislocation nodes and the SF2 types which occur along the dislocation lines. The SF1 types are very similar to those reported for dislocation nodes in bulk silicon [14]. The SF2 types appear to be due to the dissociation of a unit dislocation in certain places along its line. The stacking fault width in this case is 10 ± 3nm. Again the resolution is not good enough to give any more accurate information.

The results of the present study are very similar to previous results reported for dislocations in bulk silicon [12,14], in that

a) the dislocations have $a/2<1\,1\,0>$-type Burgers vectors,
b) the orientations of the dislocations, most of which were not straight, were found to vary between 60° and edge,
c) some of the dislocation nodes are dissociated, resulting in triangular stacking faults,
d) some pairs of dislocations, which are close enough to interact with each other, are dissociated along the whole of their lines, giving extrinsic stacking faults, and
e) some of the dislocations are only dissociated along segments of their lines.

155

Plate 4.14

TEM images of widely–spaced dissociated dislocations.

a) $(1\,1\,\bar{1})$ WB image showing image of defect, D.

b) $(1\,\bar{1}\,\bar{1})$ WB image of the same structure showing stacking fault contrast in one of the dislocations.

c) $(\bar{1}\,1\,1)$ WB image showing a shift in the stacking fault contrast from one dislocation to the other.

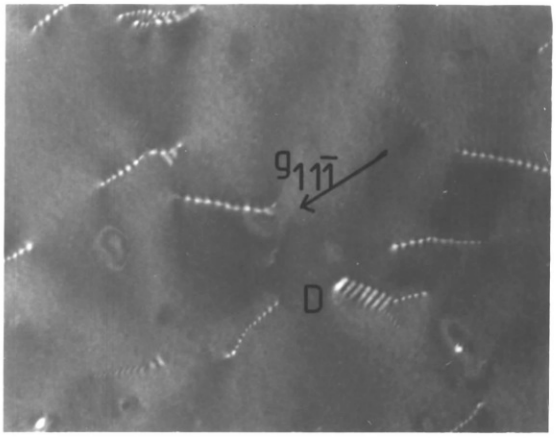
d) $(0\,0\,4)$ WB image showing triangular stacking faults formed at the dislocation nodes (SF1) and stacking faults along parts of dislocation lines (SF2).

Plate 4.15

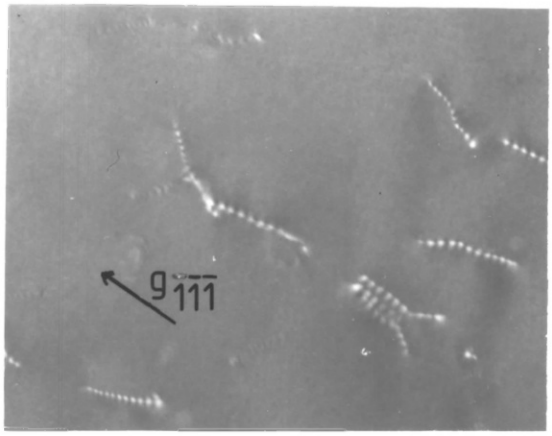
Cross–sectional TEM of silicon implanted with oxygen to a dose of $1.6 \times 10^{18} O^+/cm^2$ at 480°C (unannealed)

Plate 4.16

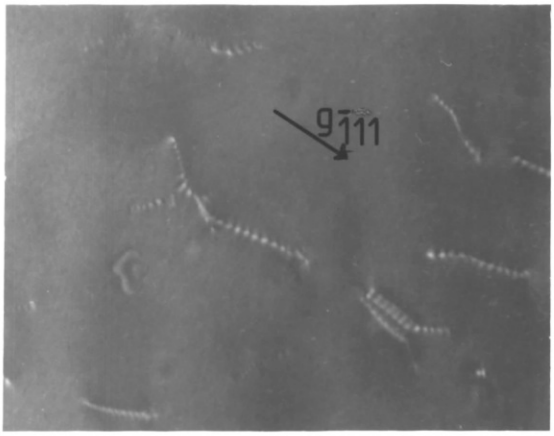
Cross–sectional TEM of silicon implanted with oxygen to a dose of $1.6 \times 10^{18} O^+/cm^2$ at 540°C (unannealed)



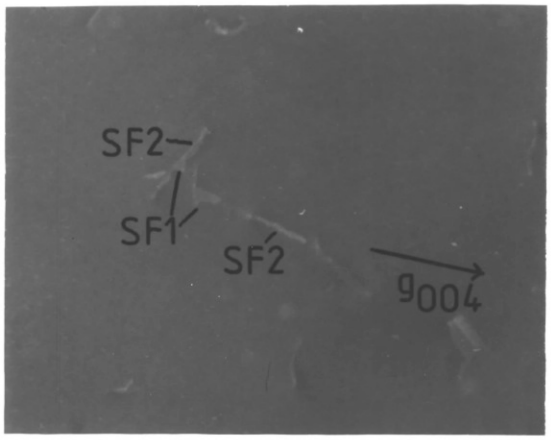
a) 100nm



b) 100nm



c) 100nm



d) 100nm

Plate 4.14

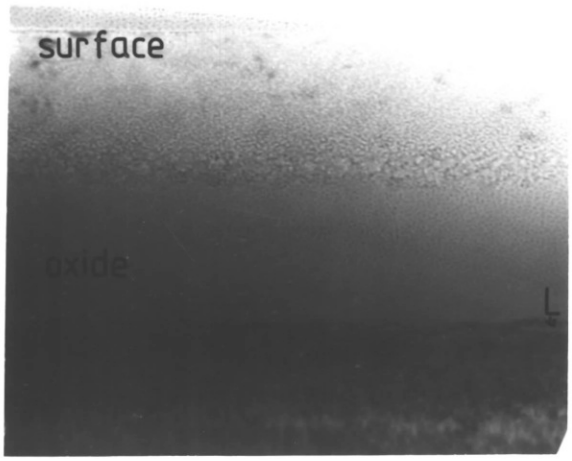


Plate 4.15 100nm

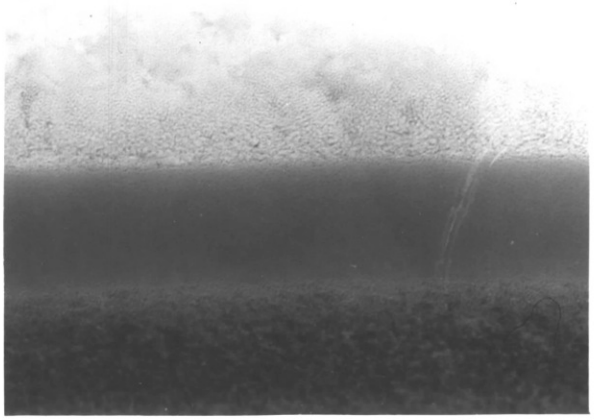


Plate 4.16 100nm

4.3.2 Nitrogen Contamination

As explained in section 3.4.1, the presence of caesium (Cs^+) ions in or near the surface region of a material under ion bombardment causes copious emission of negative secondary ions. This emission is enhanced for elements located in group 4 or to the right in the periodic table. Hence to follow the nitrogen distribution, a Cs^+ primary beam was used. However, due to the chemical nature of nitrogen, the N^- intensity is very low, so the $^{42}SiN^-$ secondary ion was followed since it gave a better dynamic range and detection limit.

The Cs^+ SIMS profiles for the SPIRE wafers SP10B, SP10C, SP13B and SP13C, the details of which were given in section 3.5.2, are shown in Fig.4.19. The nitrogen (SiN^-) secondary ion yield is plotted to compare the effects of nitrogen and argon annealing at 1300°C. The absolute intensity (rather than an intensity ratio) is given since with the nitrogen-annealed specimens, there were charging problems in the buried oxide which distorted the intensity ratios.

The nitrogen concentration in the overlayers was very nearly the same for each wafer, corresponding to $\approx 5 \times 10^{17} at/cm^3$ which is very close to the detection limit of $\approx 10^{17} at/cm^3$, determined by comparing with the SIMS profile of a known standard in bulk silicon. The differences in the profiles occur at the upper Si/SiO_2 interface where the nitrogen concentration increases dramatically to $10^{20} - 10^{21} at/cm^3$ for the wafers annealed in nitrogen. Also, the nitrogen appears to have diffused slowly away from the interface into the buried oxide. There is no evidence of an interfacial nitrogen build-up in the argon-annealed wafers.

These results show that during the anneals in nitrogen, nitrogen diffuses through the capping oxide and the silicon overlayer to the buried oxide where it collects at the upper Si/SiO_2 interface. This being the case, nitrogen would also be expected to collect at the interface between the silicon surface and the capping oxide, although this cannot be proved here since the capping oxide layer was etched away before SIMS profiling.

The fact that the nitrogen concentration in the overlayers is the same for both nitrogen and argon annealing suggests that the nitrogen diffuses through the silicon via a mechanism which involves very little atomic exchange with silicon atoms in the lattice (the nitrogen concentration is very close to the detection limit). An interstitial mechanism is likely, but during the very early stages of the anneal, there is an excess of silicon interstitials, so it may be that the nitrogen does not start to accumulate at the buried oxide at the very start of the anneal, but once the buried

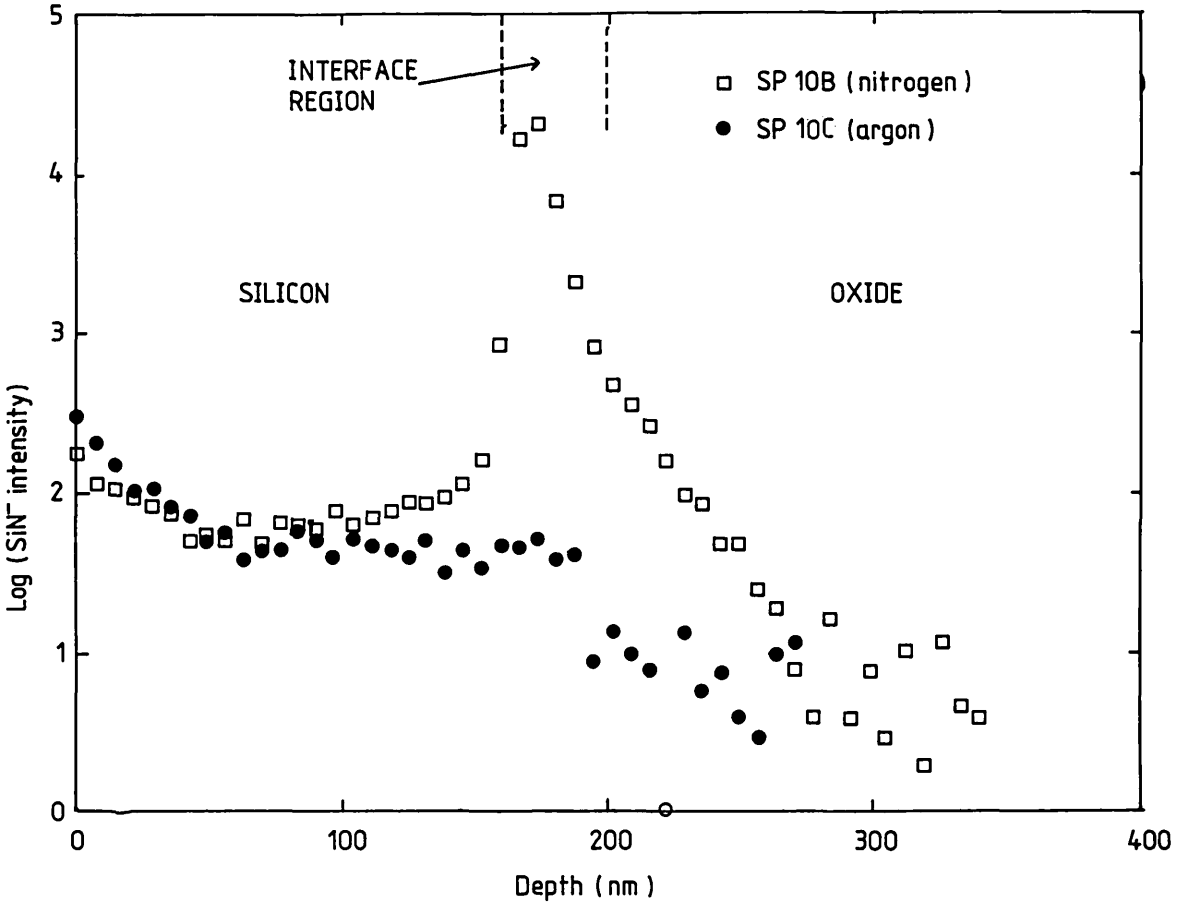


Fig.4.19 Nitrogen SIMS profiles of wafers SP10B and SP10C.

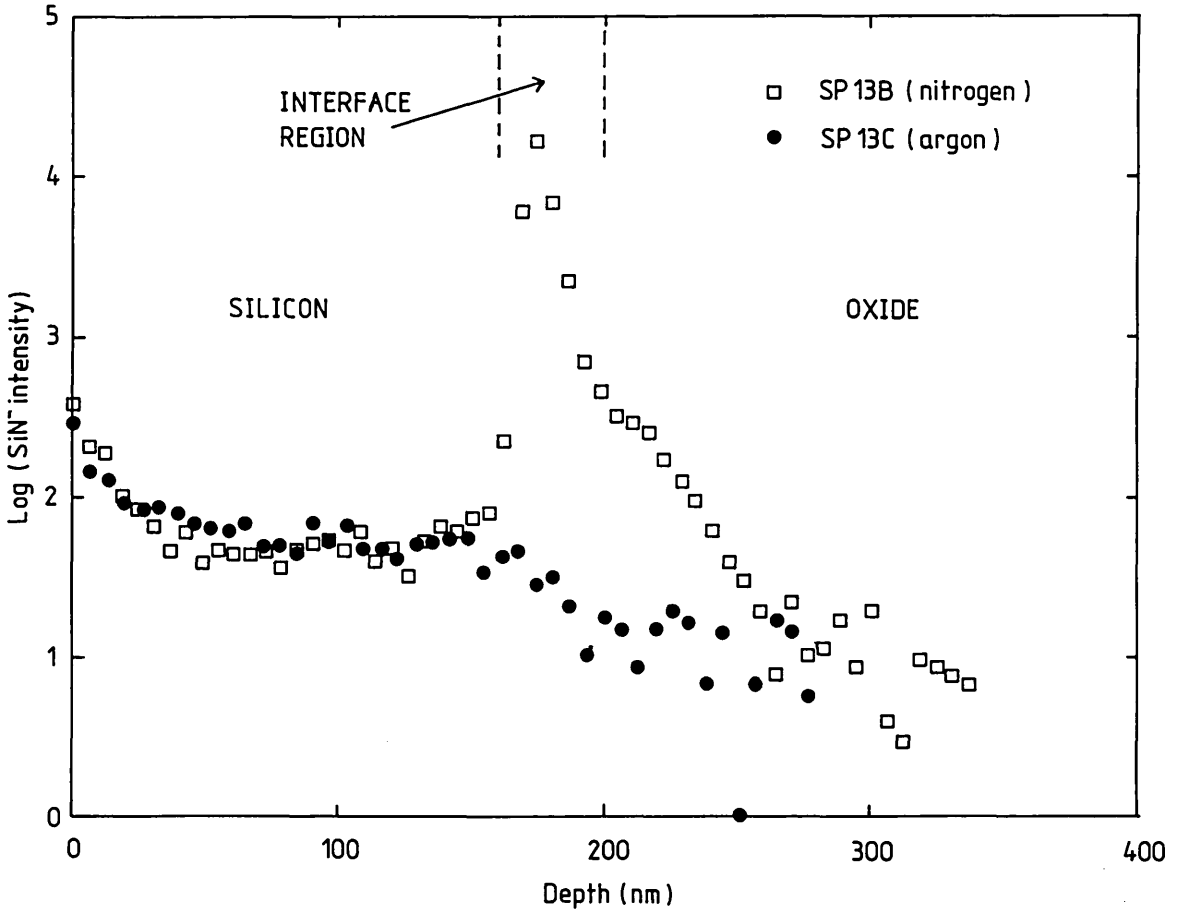


Fig.4.19b Nitrogen SIMS profiles of wafers SP13B and SP13C.

oxide has started to establish itself.

Previous work concerning the diffusion of nitrogen in buried oxides [15,16] has shown that nitrogen implanted into the oxide diffuses rapidly to the two Si/SiO_2 interfaces, forming thin oxy-nitride layers. This suggests that a fast diffusion mechanism is operating, such as nitrogen molecules moving through micro-channels in the atomic structure of the oxide (a phenomena well-known in the oxidation of silicon). However, the SIMS profiles in reference 15, like the ones for nitrogen in Fig.4.19, showed evidence of nitrogen diffusing slowly from the interfaces into the buried oxide (particularly at the upper interface). This slow diffusion suggests that there is a slower diffusion mechanism operating simultaneously.

The results of the current study, together with those from reference 15, suggest that during high-temperature annealing in nitrogen, the following processes occur:

a) nitrogen diffuses rapidly through the capping oxide to the silicon surface. There is likely to be a build-up of nitrogen at this interface, perhaps in the form of an oxy-nitride layer.

b) Some of this nitrogen diffuses rapidly (via an interstitial-type mechanism) through the silicon overlayer where there is a further build-up of nitrogen at the upper Si/SiO_2 interface. It is possible that this nitrogen may again be in the form of a very thin oxy-nitride layer, although such a layer has never been observed during cross-sectional TEM analysis. The presence of some kind of nitride layer may locally alter the electrical properties of the structure, which would help to explain the charging problem encountered during SIMS profiling. A similar charging problem was found by Kilner *et al* [17] when profiling buried nitride structures.

c) Some nitrogen difuses into the buried oxide layer via an atomic-exchange mechanism. From previous work [15,16], it is also likely that some nitrogen will diffuse rapidly through the buried oxide to the lower Si/SiO interface, although this cannot be proved from the present work.

The nitrogen has already diffused over $0.5\mu m$ through the capping oxide by the time it reaches the silicon surface, but within the buried oxide, the nitrogen has only diffused over a distance of $\approx$50nm (and from previous work is also likely to have diffused rapidly to the lower interface [15]). Hence it is certain that two different diffusion mechanisms are operating within the oxide.

For the nitrogen to diffuse through the silicon overlayer during annealing (a distance of $\approx$200nm), the diffusion coefficient, D, would have to be $\geq 10^{-15} cm^2/s$. This is quite feasible since D was reported as having a value of $\approx 10^{-13} cm^2/s$ at 1300°C

[17]. It is possible that there is also some radiation-enhanced diffusion due to the implantation damage.

To determine the diffusion coefficient for the slow nitrogen diffusion in the buried oxide, using the raw SIMS data, the following assumptions must be made:

a) the intensity of the SiN^- secondary ion signal from the buried oxide is directly proportional to the nitrogen concentration in the buried oxide, and

b) the background concentration of nitrogen in the buried oxide is the same as that in the silicon overlayer i.e. $\approx 5 \times 10^{17} at/cm^2$.

The first assumption should be valid as far as oxygen-induced secondary ion enhancement is concerned: the oxide has a constant oxygen concentration so the degree of enhancement will be the same for all SiN^- intensities. Hence from the SIMS data, using the nitrogen concentration, C, at distance x from the upper Si/SiO_2 interface (x being positive going into the buried oxide), after time t, it is possible to find the diffusion coefficient from the equation

$$C = \frac{M}{(\pi Dt)^{\frac{1}{2}}} \exp\left[- \frac{x^2}{4Dt} \right] \qquad (4\text{-}10)$$

where M is the total amount of substance diffusing [19]. This equation applies to the case of diffusion in only one direction in a semi-infinite medium, from a planar interface. Equation 4-10 can be simplified to

$$Ln(C) = constant - \frac{x^2}{4Dt} \qquad (4\text{-}10a)$$

Hence by plotting Ln(C) against x^2, the diffusion coefficient, D, can be determined from the gradient. Such a plot is shown in Fig.4.20. The gradients are similar for both wafers, giving a diffusion coefficient of $\approx 10^{-16} cm^2/s$ (within an order of magnitude). This corresponds to diffusion lengths of 5-50nm for a 5 hour anneal at 1300°C, which seems to fit the diffusion profiles fairly well.

The presence of nitrogen in SIMOX structures is known to increase the residual doping levels resulting in an increased carrier scattering rate on ionized impurities and a consequent decrease in carrier mobilities [20]. The current work has shown that annealing in a nitrogen ambient increases the amount of nitrogen present, whereas no nitrogen has been found in the argon-annealed wafers. Hence argon annealing would be expected to produce SIMOX structures with improved electrical characteristics.

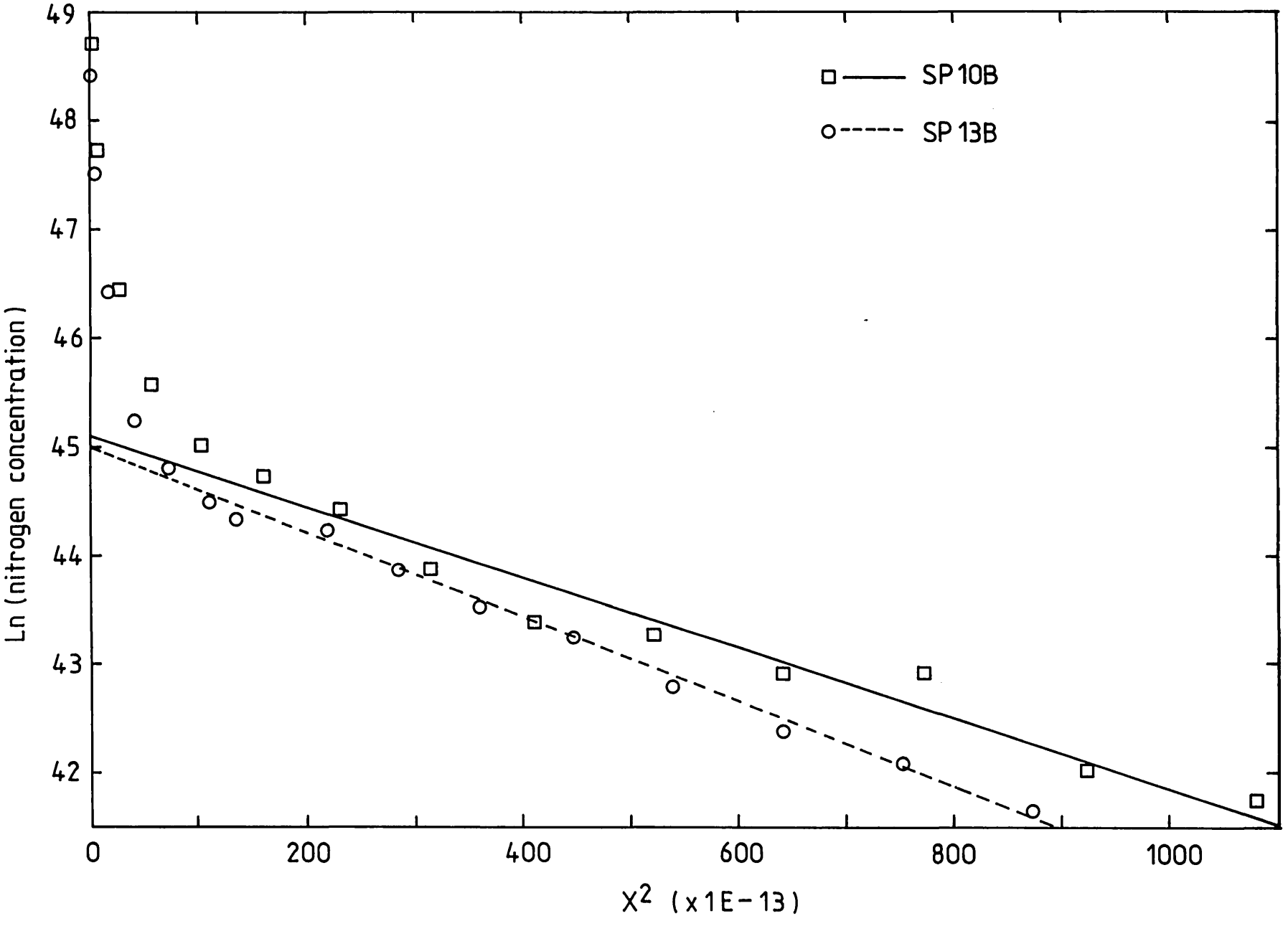


Fig. 4.20 Plot of Ln (nitrogen concentration) vs (distance)^2 to determine the diffusion coefficient of nitrogen in buried oxide

160

4.3.3 Dislocation Density

Using plan view TEM to analyse large areas of the silicon overlayers allowed the dislocation densities of these specimens to be determined as a function of annealing ambient at an implantation temperature (T_i) of 600°C. Table 4.5 gives the dislocation densities for the four wafers examined.

Table 4.5 Dislocation densities of the SPIRE wafers

Wafer	T_i (°C)	annealing ambient	annealing time	dislocation density/cm^2
SP10B	600	nitrogen	5	2.2x10^9
SP10C	600	argon	5	4.0x10^9
SP13B	600	nitrogen	5	1.2x10^9
SP13C	600	argon	20	3.5x10^9

It can immediately be seen that the dislocation densities are all very similar and of the order of magnitude expected for this type of implant where no wafer pre-heating is used (see section 2.3.3). However, there appears to be a difference of a factor of ≈2 between the argon-annealed wafers and those annealed in nitrogen, the dislocation density being lower after a nitrogen anneal (large enough areas were examined to make this comparison realistic). Both SP10B and C come from the same implanted wafer as do SP13B and C, hence any variation or instability in the implantation parameters would be reflected in the dislocation counts for both B and C specimens. For this reason it would be less viable to compare values between the wafers SP10 and SP13; comparisons between annealing conditions on the same wafers will give far more realistic results. It is clear that annealing for 20 hours in argon has very little effect on the dislocation density compared to a 5 hour anneal.

From the previous section (4.3.2) it is known that there is a build-up of nitrogen, most likely in the form of a very thin oxy-nitride layer, at the upper Si/SiO_2 interface during annealing in nitrogen. If this is the case, it is possible that this has some effect on the overall dislocation densities. There has been no indication that any other differences exist, so it seems likely that this nitrogen-rich layer in some affects the formation of the overlayer threading dislocations.

It is known that nitrogen atoms at an Si/SiO_2 interface attatch themselves to the silicon dangling bonds along the interface to inhibit further oxidation [16]. In the same way, the presence of nitrogen was also found to slow down the process of SiO_2

precipitate dissolution in the silicon overlayers of SIMOX structures [21]. In that report, it was unusual to find such large (≈40nm) oxide precipitates in the overlayers, especially after a 150keV implant and a 1250°C anneal, so the effect of the nitrogen appeared to be quite significant.

In the current study, it is proposed that the nitrogen, which diffuses to the buried oxide during annealing, retards the growth of the buried oxide at the upper Si/SiO_2 interface; not by a great amount (as suggested by Davis *et al* [21]) but enough to slightly reduce the rate of silicon interstitial emission and the interstitial saturation within the overlayer. This reduces the rate of dislocation growth and allows more of the dislocation nuclei to anneal out.

The observed reduction in dislocation density by a factor of approximately 2 is not significant enough to state that nitrogen annealing is preferable to argon annealing since other properties of the SIMOX structures have to be taken into consideration, particularly the electrical characteristics. However, it can be stated that as far as the dislocation density is concerned, there is no need to anneal for 20 hours in argon; 5 hours appears to be enough to reach a stable microstructural condition. This shows that the dislocations really are very stable, giving further evidence that they can only be eliminated by stopping the formation of nuclei during implantation and not by annealing for long times.

Cristoloveanu *et al* have always annealed in argon since it was shown to give better all round electrical properties than nitrogen [20,22]. However, that same group have developed a method of producing (almost) dislocation-free SIMOX by pre-heating the silicon wafers (see section 2.3.4). This reduction in dislocation density, by a factor greater than 10^4, is a far more significant reduction than that produced by nitrogen annealing alone. Hence argon annealing can be tolerated in this case – the resultant increase in dislocation density is far outweighed by a general improvement in the electrical characteristics.

Overall, it appears that nitrogen annealing is preferable if it is only desirable to have the lowest possible dislocation density. However, if the dislocation density is already low (as occurs with pre-heating), argon annealing may be preferred to improve the all round electrical properties of the SIMOX substrates.

4.4 Implantation Temperature Variation

In this series of experiments, silicon wafers were implanted using different beam currents to alter the implantation temperature, T_i. The other implantation parameters were kept constant to study only the effect of temperature, and at the higher temperature, one wafer was implanted through a screening oxide to see whether this had any effect on the unannealed and annealed microstructures.

Plates 4.15, 16 and 17 are cross-sections of the material implanted to a dose of 1.6 x $10^{18}O^+/cm^2$ at 480, 540 and 540°C with a 70nm screening oxide respectively. The buried oxide layer can clearly be seen in each case, surrounded on both sides by damaged regions of silicon containing SiO_2 precipitates. Table 4.6 gives the values of the buried oxide and silicon overlayer thicknesses. It should be noted that in Plate 4.16, the specimen is tilted from the $<0\,1\,1>$ orientation to obtain the desired contrast in the overlayer, hence in this micrograph the thicknesses may not appear to correspond to the measurements shown in the table.

Table 4.6 Overlayer and oxide thicknesses

T_i (°C)	Layer Thicknesses (nm)	
	silicon	oxide
480	260	240
540	260	240
540*	260	260

* implanted through a 70nm screening oxide

There are errors of ±20nm in these measurements since the interfaces are not clearly defined. It can be seen that increasing the implantation temperature from 480 to 540°C does not have any measurable affect on the layer thicknesses.

At lower doses (e.g. <0.5 x $10^{18}O^+/cm^2$ as shown in Plates 4.1 and 4.2), there is a region of defect-free silicon lying between the surface damage layer and the peak of the damage depth distribution. In Plates 4.15, 16 and 17, the two damage regions have merged, because the higher doses result in more damage at the surface (directly related to the implantation process), an increase in the amount of oxygen (oxide precipitates) within the overlayer, and an increase in the number of silicon interstitials (from oxide growth and from Frenkel pairs generated by the collision cascades). Also, the growing oxide front at the upper interface has moved nearer to the surface so that oxidation-induced silicon interstitials, being produced at a constant rate, are confined to a smaller and smaller volume of silicon. These factors all contribute to

Plate 4.17

Cross-sectional TEM of silicon implanted with oxygen to a dose of 1.6 x $10^{18}O^{+}/cm^{2}$ at 540°C through a 70nm screening oxide (unannealed)

Plate 4.18

High magnification image of the upper Si/SiO_2 interface for the 480°C specimen.

Plate 4.19

Microstructure of the 480°C wafer annealed for 5 hours at 1300°C showing a threading dislocation (d) and two rows of silicon inclusions (A and B) within the buried oxide.

Plate 4.20

TEM of 540°C wafer annealed for 5 hours at 1300°C showing a dislocation (d) and a lower layer of silicon inclusions (A).

Plate 4.21

540°C wafer, annealed for 2 hours at 1300°C showing a wavy upper Si/SiO_2 interface.

Plate 4.22

High magnification image of the upper Si/SiO_2 interface in Plate 4.21.

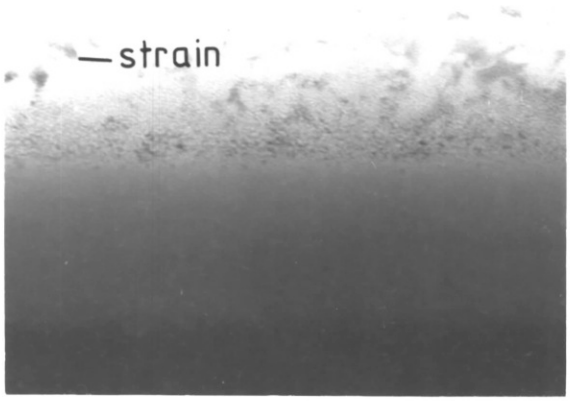


Plate 4.17 100nm

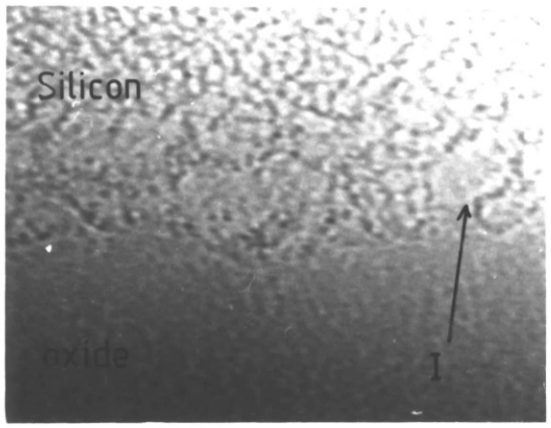


Plate 4.18 100nm

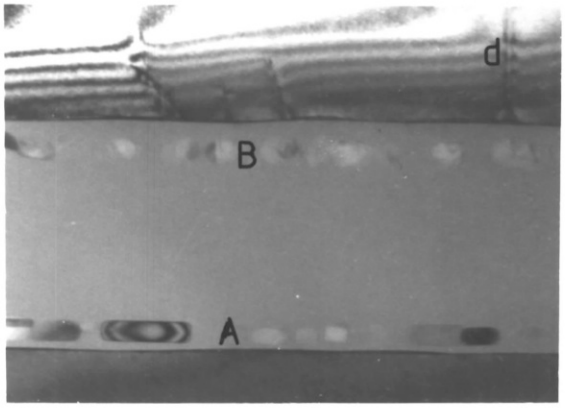


Plate 4.19 100nm

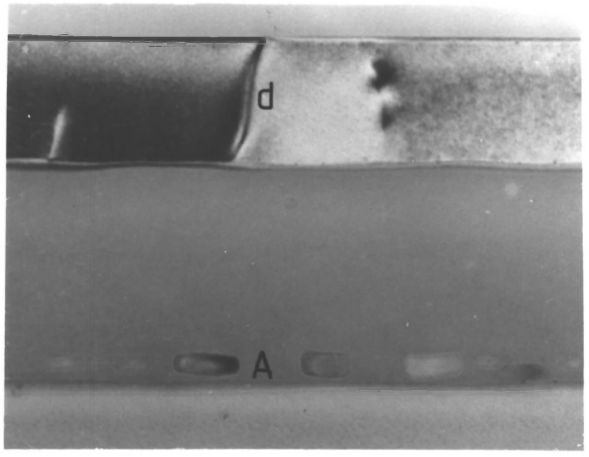


Plate 4.20 100nm

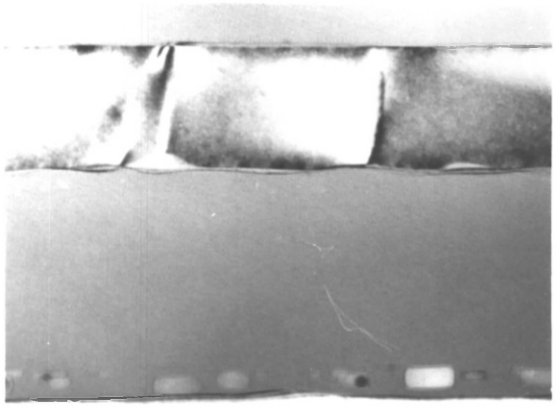


Plate 4.21 100nm

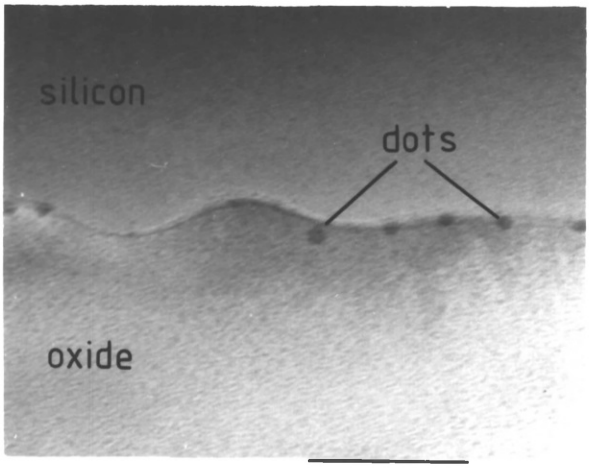


Plate 4.22 100nm

a higher concentration of damage and defects in the region between the buried oxide and the surface.

The regions near the interfaces, indicated in Plate 4.16, contain the largest (observable) oxide precipitates which are ≈40nm across. The mottled contrast in the silicon overlayer is attributed to smaller precipitates which decrease in size with distance from the upper Si/SiO_2 interface. The darker regions of contrast in the silicon overlayer are due to stress and strain in the silicon lattice associated with implantation damage (e.g. point defect clusters) and expansion as the oxide precipitates grow.

The oxygen depth distribution of the wafer implanted at 480°C is shown in Fig. 4.21 (it has been calibrated using the method described in section 4.1). It exhibits a flat–topped peak characteristic of a stoichiometric buried oxide layer. The wings of the distribution, where the oxygen concentration increases (or decreases) exponentially with depth, are the regions containing oxide precipitates, the concentration representing the volume fraction of SiO_2. There were no observable differences in the as–implanted profiles of the three wafers analysed.

It is clear that the microstructures of these three specimens are all very similar – the only difference observed is at the the upper Si/SiO_2 interface. For the 480°C implant (Plate 4.15) the interface can just be seen to be undulating on a small scale (≈30nm). This is shown more clearly in Plate 4.18 which is a higher magnification image of the interface at a very thin part of the TEM specimen. 30–40nm oxide isthmuses can be seen protruding into the silicon overlayer (e.g. feature I). They are almost spherical oxide precipitates, but are joined to the buried layer by thin strands of oxide. These could alternatively be interpreted as being spherical silicon isthmuses protruding into the oxide layer. This type of structure is not present in any of the material implanted at 540°C.

The lower Si/SiO_2 interfaces are all very similar to each other, but they are different to the upper interfaces in that there are no actual isthmuses, although laminar–shaped oxide precipitates exist e.g. feature L on plate 4.15. The interface itself is more planar than the upper interface and the oxide laminae, ≈100nm x 10nm in cross–section, are at a distance of 10–20nm from the interface, decreasing in size further into the substrate.

During implantation (and to a certain extent during annealing) it is known that most of the buried oxide growth occurs at the upper Si/SiO_2 interface (see section 2.2.5), so the lower interface will undergo a greater amount of *in situ* annealing and hence

Fig.4.21 SIMS profile of 480C wafer

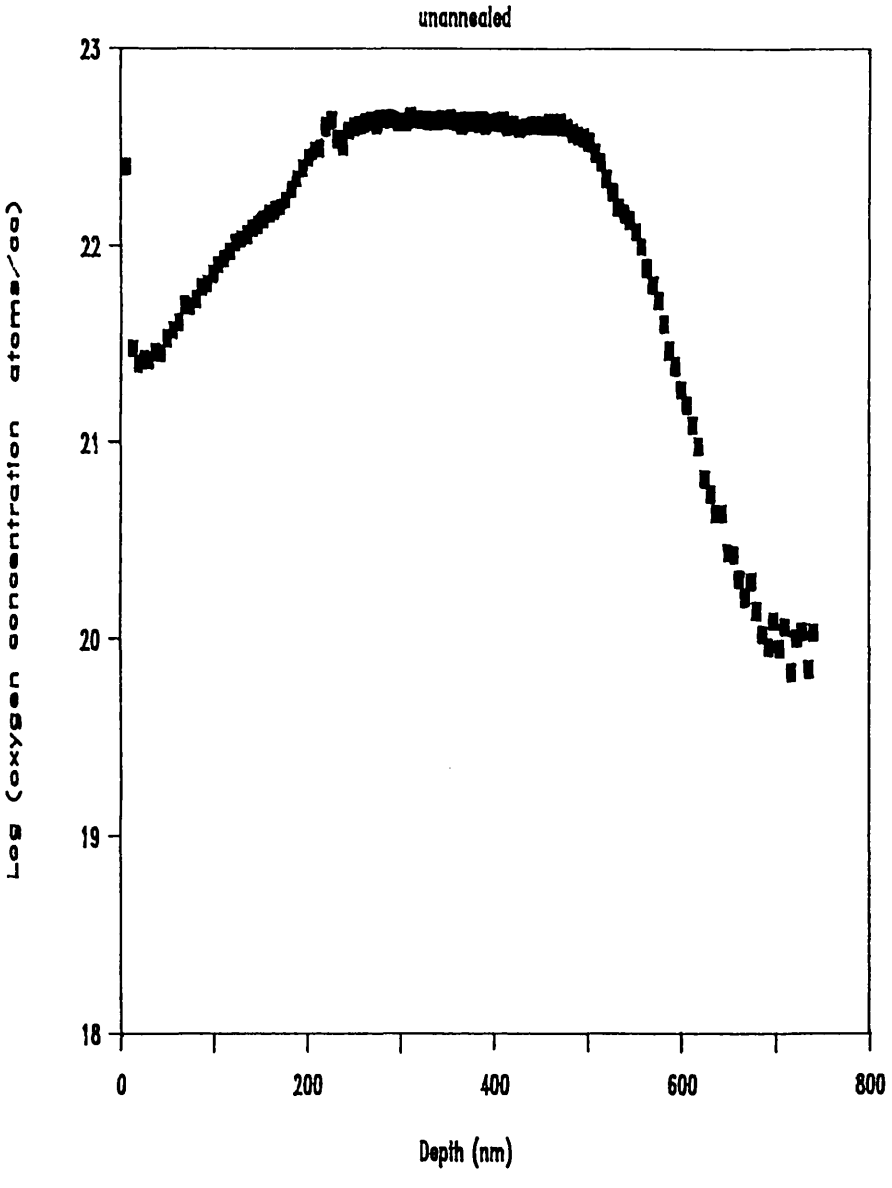
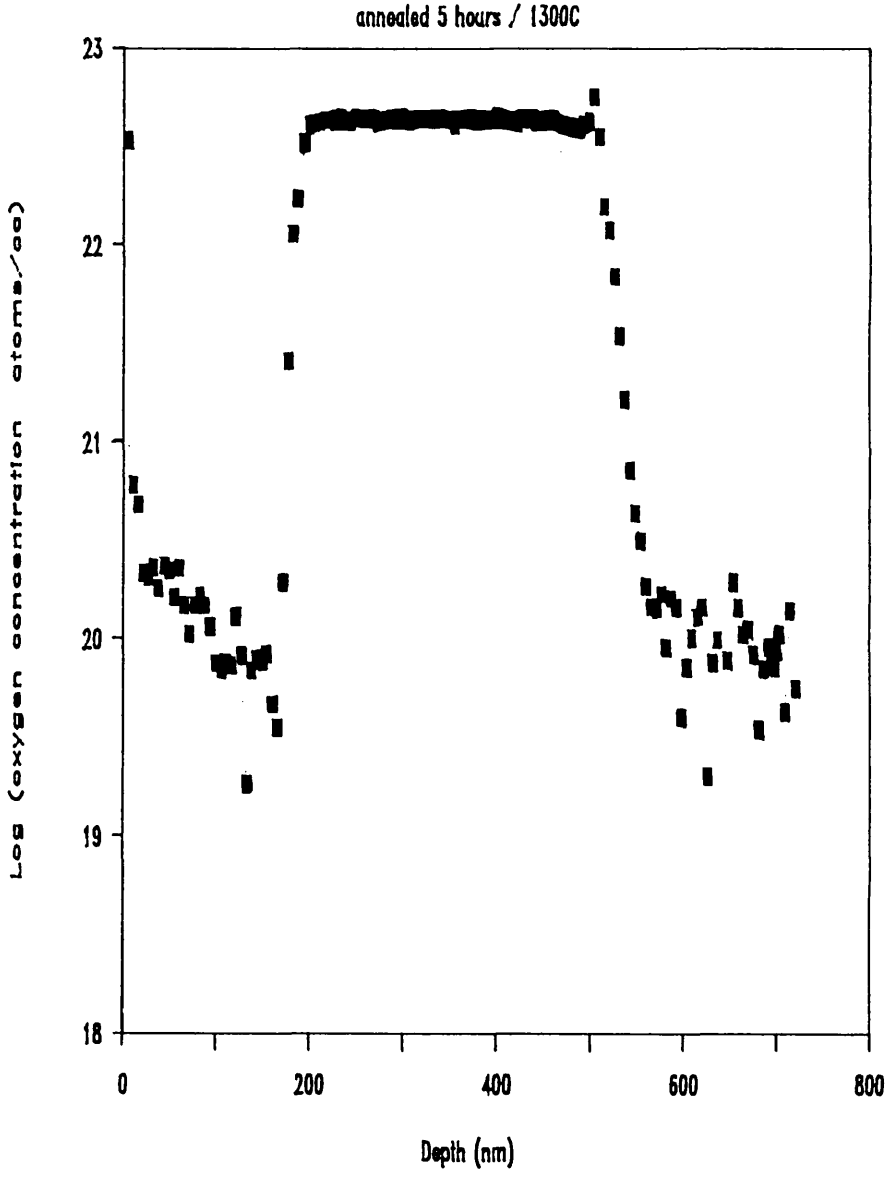


Fig.4.22 SIMS profile of 540C wafer



will be more static. It is clear from the fact that buried oxide layers form at all in silicon that the oxide grows along the (100) plane parallel to the surface, so the lower interface would be expected to be more planar than the upper one since it is in a less-disturbed state; the *in situ* annealing means that the microstructure of the interface will be nearer to equilibrium. For the same reasons, the oxide precipitates near the interface would perhaps be expected to take up more elongated shapes along the (100) plane, as is observed.

At the upper interface, however, during implantation, although there is some annealing, the oxide is continually growing and implantation damage is continually being created. This disturbance means that the upper interface would be expected to be rougher than the lower one. It seems that between 480 and 540°C, there is a transition point where the temperature is high enough to increase the amount of annealing such that the interface becomes more planar.

The annealed microstructures (5 hours at 1300°C) of the 480 and 540°C wafers are shown in Plates 4.19 and 4.20 respectively with the corresponding oxygen depth profile in Fig. 4.22 for the 540°C wafer implanted through a 70nm screening oxide. This profile is typical of each of the annealed structures, and no differences were observed between them. The buried oxides can be seen to have very flat, planar interfaces, their thicknesses increasing to 360nm whilst the overlayer decreases to 190nm. The lower interfaces are at a depth of ≈550nm, only 50nm deeper than the lower interfaces in the lower dose implants (see section 4.2), giving further proof that most of the oxide growth during implantation occurs at the upper interface. The characteristic overlayer threading dislocations (e.g. d) can also be seen, and they have a density of $\approx 10^9/cm^2$.

Both micrographs show a layer of silicon inclusions in the buried oxide near the lower Si/SiO_2 interface (feature A). They are typically 50nm long, 30nm high and centred at an almost constant distance of 30-40nm from the interface. They are faceted at the edges (in cross-section), and plan view TEM has shown them to be discs [23]. The lower interface is slightly more planar than the upper one which is to be expected since it is known to form first and hence has more time to reach an equilibrium microstructure. The shape of the silicon inclusions in cross-section i.e. long and thin, is very similar to the shape of the oxide lamallae described for the as-implanted material, and hence very similar to the shape of the silicon regions between the lamallae and the interface. It appears that during high temperature annealing, the lower interface forms in the region of the oxide lamellae, trapping discs of silicon within the buried oxide. The long, high temperature anneal allows the inclusions to take up low energy configurations, hence their faceted appearance,

and the low diffusion coefficient of Si in SiO_2 prevents them from dissloving by the out-diffusion of silicon to the substrate.

It is clear that the oxide in the 480°C specimen (Plate 4.19) also contains a row of silicon inclusions near the upper interface (feature B). These inclusions are more rounded than those near the lower interface. Again this rounded shape corresponds to the rounded (probably spherical) regions of silicon almost totally surrounded by oxide in the as-implanted material, as described earlier.

Both layers of inclusions are a result of silicon being trapped in the regions between the largest oxide precipitates (i.e. those nearest to the interfaces) and the buried oxides during high-temperature annealing. Further evidence is given by the fact that the distance between the bottom of the upper layer of inclusions and the top of the lower layer is identical to the thickness of the continuous buried oxide layer in the as-implanted material. The presence of this upper inclusion layer after implanting at 480°C does not appear to affect the dislocation density, although it is not known whether or not it will have any effect on the electrical properties.

Plate 4.21 is a cross-section of the 540°C wafer annealed at 1300°C for only 2 hours. It can be seen that although the layer thicknesses are the same, the interfaces are more wavy than after a 5 hour anneal. The lower interface is the more planar of the two. This can be seen more clearly in Plate 4.22 which is a higher magnification image of the upper interface. Again the effect of this waviness on the electrical properties is unknown, but working on the general assumption that flatter, more planar interfaces are more desirable, it appears that a 5 hour anneal at 1300°C is preferable to a 2 hour anneal.

The small (≈6nm) dots along the interface in Plate 4.22 remain uncharacterised. They are unlikely to be associated with nitrogen since this nitrogen would be expected to form a thin nitride or oxy-nitride layer along the interface, the atoms attatching themselves to the silicon dangling bonds. It is possible that they are small particles of silicon carbide, although they are too small to be characterised using conventional diffraction techniques.

Finally, these investigations have shown there to be no difference between the material implanted with and without a screening oxide. The only time a screening oxide has been found to affect the microstructure is where the oxides have suppressed the formation of cavities by reducing the efficiency of the surface as a sink for silicon interstitials (see section 2.2.5.3). However, the dose rates used to produce the material in the current study were not high enough to produce cavities. Also, the

screening oxide would be expected to have sputtered away in the very early stages of the implantation process, meaning that most of the implant would not be through a screen, suggesting that a significant effect would not be expected.

4.5 References For Chapter 4

[1] J.A.Kilner, R.J.Chater and S.D.Litlewood, "Quantification of high levels of oxygen in silicon", 6th Int. Conf. on Secondary Ion Mass Spectroscopy, Versailles, France, (1987), Eds. Benninghoven, Huber and Werner (J.Wiley & Sons, London, UK) 299.

[2] R.J.Chater, (Imperial College, London), unpublished.

[3] P.L.F.Hemment, E.Maydell-Ondrusz, K.G.Stephens, J.A.Kilner and J.Butcher, "Oxygen distributions in synthesized SiO_2 layers formed by high dose O^+ implantation into silicon", Vacuum 34(1-2) (1984) 203.

[4] K.Wittmaack, "Oxygen-concentration dependence of secondary ion yield enhancement", Surface Science, 112 (1981) 168.

[5] W.Gerhard and C.Plog, "Secondary ion emission by nonadiabatic dissociation of nascent ion molecules with energies depending on solid composition: part 1", Z. Phys. B - Condensed Matter, 54 (1983) 59.

[6] C.Plog and W.Gerhard, "Secondary ion emission by nonadiabatic dissociation of nascent ion molecules with energies depending on solid composition: part 2", Z. Phys. B - Condensed Matter, 54 (1983) 71.

[7] C.Plog and W.Gerhard, "Secondary ion production by latent energy of neutrally emitted particles", Surface Science, 152/153 (1985) 127.

[8] A.deVeirman, presented at SIMOX Workshop 1, University of Surrey, Guildford, U.K. (November 1988).

[9] A.H.van Ommen, "Low dislocation SOI by oxygen implantation", Proc. Mat. Res. Soc. Symp. 107 (1988) 43.

[10] M.Bruel, J.Margail, J.Stoemenos, P.Martin and C.Jassaud, "Formation of buried insulating layers by high dose oxygen implantation under controlled temperature conditions", Vacuum 35(12) (1985) 589.

[11] C.Jassaud, J.Stoemenos, J.Margail, M.Dupuy, B.Blanchard and M.Bruel, "Microstructure of silicon implanted with high dose oxygen ions", Appl. Phys. Lett. 46(11) (1985) 1064.

[12] D.J.H.Cockayne and A.Hons, "Dislocations in semiconductors as studied by weak-beam electron microscopy", J. de Physique, 40, supplement N°6 (1979) C6.

[13] J.W.Eddington, "Practical Electron Microscopy In Materials Science", Monograph 3, "Interpretation of Transmission Electron Micrographs", Philips Technical Library, (The Macmillan Press, London, 1975).

[14] I.L.F.Ray and D.J.H.Cockayne, "The dissociation of dislocations in silicon", Proc. R. Soc. Lond. A, 325 (1971) 543.

[15] K.J.Reeson, P.L.F.Hemment, J.A.Kilner, R.J.Chater, C.D.Meekison, C.Marsh and G.R.Booker, "Formation mechanisms and structures of buried oxy-nitride layers produced by ion beam synthesis", Vacuum 36(11/12) (1986) 891.

[16] W.J.M.J.Josquin and Y.Tamminga, "The oxidation inhibition in nitrogen-implanted silicon", J.Electrochem. Soc. 129(8) (1982) 1805.

[17] J.A.Kilner, R.J.Chater, P.L.F.Hemment, R.F.Peart, K.J.Reeson, R.P.Arrowsmith and J.R.Davis, "SIMS analysis of buried silicon nitride layers formed by high dose implantation of ^{14}N and ^{15}N", Nucl. Instr. and Meths. in Phys. Res. B15 (1986) 214.

[18] N.V.Denbova, E.I.Zorin, P.V.Pavlov, D.I.Tetelbaum and A.F.Khoklov, Izv. Akad. Nauk. SSSR, Neorg. Mater. 11(12) (1975) 2236.

[19] J.Crank, "The Mathematics of Diffusion", 2nd Edition, (Oxford University Press, New York, 1975) Ch.2.

[20] S.Cristoloveanu, S.Gardner, C.Jassaud, J.Margail, A.J.Auberton -Hervé and M.Bruel, "Silicon on insulator material formed by oxygen implantation and high-temperature annealing: Carrier transport, oxygen activity, and interface properties", J.Appl. Phys. 62(7) (1987) 2793.

[21] G.E.Davis, K.S.Jones and S.Prussin, "Nitrogen contamination in SIMOX wafers", Mat. Res. Soc. Symp. Proc. 107 (1988) 111.

[22] S.Cristoloveanu, private communication (1988).

[23] C.D.Marsh, J.L.Hutchison, G.R.Booker, K.J.Reeson, P.L.F.Hemment, and G.K.Celler, "TEM studies of high-dose oxygen implanted silicon annealed at 1405°C", Inst. Phys. Conf. Ser. N°.87 (1987).

Chapter 5

Conclusions

5.1 Calibration Of High Levels Of Oxygen In Silicon

It is possible to model (and predict) the oxygen concentration depth profiles which are a result of high doses (10^{17} - $10^{18} O^+/cm^2$) of oxygen being implanted into silicon at high energy (≈150keV). In order to do this, it is necessary only to know the calibrated oxygen distribution at a low dose ($\leqslant 10^{17} O^+/cm^2$) and the amount of surface swelling caused by each additional oxygen atom above a certain oxygen concentration ($\approx 10^{21}/cm^3$ or 2.5 atomic %). This concentration corresponds to the point where the oxygen becomes observable as small, discrete SiO_2 precipitates, which are known to cause a volume increase of ≈2.2x. It also corresponds to the point where secondary ion yield enhancement in the SIMS becomes detectable. This enhancement then causes the secondary ion yields to increase exponentially with the volume fraction of SiO_2 in the target material. Above 35–40 at. % oxygen, there is a second, less intense exponential region. Both types of enhancement are due to the emission of different secondary ion fragments with different yields and different post-emission dissociation probabilities, which depend on the amount of SiO_2 present.

The oxygen in interstitial sites and near Si/SiO_2 interfaces does not cause any measurable secondary ion yield enhancement. However, the oxygen in "bulk" SiO_2 produces different, and probably higher yields of secondary ion fragments, which results in yield enhancement.

5.2 Growth Mechanisms of Buried Oxide Layers and Overlayer Threading Dislocations

The mechanisms of buried layer formation at 150keV appear to be similar to those at 200keV (see section 2.3). When annealed at 1300°C for 5 hours, a continuous buried oxide layer is formed at a dose of 0.45 x $10^{18} O^+/cm^2$. However, it is clear that the formation of a buried oxide layer during implantation is not a prerequisite for the formation of one after subsequent annealing. Indeed, to produce a silicon overlayer with no threading dislocations, it seems best to implant to a dose which will not form a buried layer during implantation. In this way there are fewer silicon interstitials trapped in the silicon overlayer (and less produced by further oxide growth at the upper Si/SiO_2 interface) once the overlayer becomes isolated from the rest of the wafer. Also, the dislocation nuclei, which are a result of the implantation

damage (probably near the surface), are able to anneal out. However, the combination of interfacial stress and interstitial production causes microtwins and small stacking faults to form at the upper interface. Although this prevents dislocation formation, it is possible that the undulating upper interface, together with its associated defects, may have a detrimental effect on the electronic properties of the structure. There may also be problems if the buried oxide is not thick enough to support SOI device action.

5.3 Dislocation Characterisation

The overlayer threading dislocations have been found to be very similar to dislocations in bulk silicon. They have $a/2\langle 1\,1\,0\rangle$ type Burgers vectors, they lie in the $\{1\,1\,1\}$-type planes and the ones it was possible to characterise had orientations varying between pure edge and 60°, both commonly found in bulk silicon. It is possible that all of the dislocations are dissociated, but in many cases, any separation was too small to be observed. Most of the dislocations were found to be bent, probably due to their proximity to the specimen's surfaces/interfaces, meaning that the dislocations were of mixed edge and 60° character.

Some of the dislocations were found to dissociate as follows:

a) all along the dislocation lines, to give extrinsic stacking faults with a partial separation of 15 ± 3nm. These partials are likely to have $a/6\langle 1\,1\,2\rangle$-type Burgers vectors with fault vectors of $a/3\langle 1\,1\,1\rangle$. They were only observed in positions where two closely spaced dislocations were interacting with each other.

b) at dislocation nodes, resulting in triangular stacking faults, and

c) along segments of dislocation lines, to give a partial separation of 10 ± 3nm. This was not observed for all of the dislocations, and occurred when there appeared to be no dislocation interactions.

5.4 Nitrogen Contamination

Annealing in a nitrogen ambient at 1300°C for 5 hours results in a build-up of nitrogen at the upper Si/SiO_2 interface. This nitrogen is likely to be in the form of a thin oxy-nitride layer, and it is possible (from the results of previous work) that a similar layer exists both at the lower interface and at the interface between the silicon surface and the capping oxide layer.

It appears that nitrogen from the annealing gas behaves as follows:

a) the nitrogen molecules diffuse rapidly through the capping oxide (micro-channel mechanism) possibly forming an oxy-nitride layer at the interface between the

capping oxide and the silicon surface.

b) The nitrogen then diffuses through the silicon overalyer via a mechanism that involves very little atomic exchange with silicon atoms in the lattice (interstitial mechanism) to form another oxy-nitride layer at the upper Si/SiO_2 interface.

c) It is possible that some of this nitrogen diffuses rapidly to the lower Si/SiO_2 interface (micro-channel mechanism), and some diffuses more slowly into the buried oxide via an atomic-exchange mechanism. The diffusion coefficient for the latter process, within an order of magnitude, has been found to be $10^{-16}cm^2/s$.

Since none of these nitrogen-related features were observed in the argon-annealed wafers, and since nitrogen is known to be an undesirable electrically-active impurity, argon annealing seems to be preferable to nitrogen-annealing as far as electrical properties are concerned.

5.5 Dislocation Density

Annealing SIMOX wafers, implanted to a dose of $1.6 \times 10^{18}O^+/cm^2$, at 1300°C for 5 hours results in material with an overlayer threading dislocation density of $\approx 10^9/cm^2$. However, during nitrogen annealing, the nitrogen build-up at the upper Si/SiO_2 interface inhibits the oxidation (oxide growth) rate, resulting in a lower rate of silicon interstitial emission and a subsequent reduction in the dislocation density by a factor of two. No such effect occurs for argon annealing.

For this high-dislocation density material, nitrogen annealing is preferable if it is most important to reduce the dislocation density. However, for low-dislocation SIMOX, formed by pre-heating the wafers, argon annealing is preferable since the overall improvement in the electrical properties outweighs the relatively small increase in the dislocation density.

5.6 Implantation Temperature Variation

Silicon, implanted with oxygen to a dose of $1.6 \times 10^{18}O^+/cm^2$ at 150keV, produces a 250nm-thick buried oxide layer, the upper interface being ≈260nm below the wafer surface.

Annealing at 1300°C for between 2 and 5 hours results in a 360nm buried oxide with sharp interfaces below a 190nm single crystal silicon overlayer containing $\approx 10^9$ dislocations/cm^2. The wafers implanted at 480 and 540°C have a layer of disc-shaped silicon inclusions in the buried oxide near the lower interface. These are

a result of the largest, lamellar-shaped oxide precipitates, formed during the implantation process, coalescing and trapping small regions of silicon. A similar process occurs at the upper interface in the 480°C-implanted wafer, but the inclusions are much more rounded, mimicking the shapes of the oxide (or silicon) isthmuses at this interface after implantation. This layer of inclusions is not present after implantation at 540°C where the temperature is great enough to anneal out more of the implantation damage and allow the oxygen to redistribute itself, promoting the growth of a more planar oxide front.

The SIMS and TEM results show no other differences between the wafers, even the one implanted through a 70nm screening oxide. However, in each case, the lower interfaces were flatter and more planar than the upper ones. This was most obvious after only a 2 hour anneal, and occurs because there is less implantation damage near the lower interface allowing more *in situ* annealing to occur during implantation. There is also less oxide growth at this interface, allowing it to stabilise.

The effect of these features on the electrical properties is unknown at present, although it is likely that flat interfaces and the absence of an upper layer of silicon inclusions would be preferred (the inclusions near the lower interface appear to be unavoidable). Hence a 540°C implant followed by a 5 hour anneal at 1300°C would appear to give the best material.

5.7 Suggestions For Future Work

For the high-dose implant modelling, it would be useful (and more accurate) to start at a low dose e.g. $10^{16}O^{+}/cm^{2}$, so there is absolutely no detectable secondary ion yield-enhancement at the peak of the oxygen distribution. Using this more accurate model, the effects of diffusion near the onset of continuous buried layer formation could be determined (these effects were ignored in the current study). It would also be useful to have deep buried marker layers (e.g. thin nitride layers) to act as fixed reference points for all measurements. Not enough use has been made of this technique.

A study of a much wider range of positive and negative secondary ions (perhaps simultaneously) may give information about which secondary ions are responsible for the ultimate exponential increase in the O^{-} and Si^{-} secondary ion yields with the volume fraction of SiO_2. High-resolution TEM may also be helpful in comparing the calculated and actual volume fractions of SiO_2.

To test the proposed model for the evolution of overlayer threading dislocations, implanting into pre-heated wafers (but keeping the other implantation conditions identical to those described in this study) will show whether or not a near-surface damage layer is produced. Subsequent annealing will reveal if this has any effect on the dislocation density i.e whether this surface damage layer really does contain most of the dislocation nuclei.

From this study, it is clear that more high-resolution TEM (and lattice imaging) is required to accurately determine the dislocation structure in detail. This would show if all the dislocations are dissociated and would also reveal whether intrinsic as well as extrinsic stacking faults are present.

It would be interesting to study the effect of annealing in combinations of nitrogen and argon i.e. mixtures of the gases in varying proportions, to see how the nitrogen build-up at the interfaces is affected. It would also be interesting to start the anneal in nitrogen and then change to argon (or *vice versa*) to see whether the excess of silicon interstitials in the early stages of annealing does indeed reduce the diffusion rate of nitrogen to the buried oxide. This may give more information about the diffusion mechanisms.

Overall, a lot of the unanswered questions involve the relation between the observed chemical and microstructural features and the electronic properties of the substrates. Hence it is most important to correlate the material properties with an electrical evaluation of the SIMOX substrates, since it is the electrical properties which will ultimately determine the processing conditions.

Finally, since better device characteristics have been produced on very thin (<100nm) silicon overlayers, it may be necessary to implant at lower energies. Hence a study of the materials science of 100keV implants may be needed in the near future.

ACKNOWLEDGEMENTS

And Finally.....

I would like to give my greatest thanks to Dr. John Kilner and Dr. Anne Staton-Bevan who have shown the upmost patience in supervising, helping and guiding me through this thesis. Extra thanks are due to Dr. Kilner for providing the odd holiday here and there and for being very understanding on Friday afternoons.

Thanks are also due to Professor D.W.Pashley for the provision and use of his laboratory facilities.

Very special thanks must go to Mr. Richard Chater and Mr. Graham Briers for their instruction and help concerning the use (and abuse!) of of the SIMS and TEM equipment respectively.

For financial support, I would like to thank the SERC, Dr. Derek Godfrey (GEC), Mr. A.Tarring (Lloyds Bank plc) and Fred and Peter (M&R).

Of course, the completion of this work would not have been possible without the help of Dr. Peter Hemment and Dr. Karen Reeson (Surrey University), Dr. John Davis (British Telecom Research Labs) and John Alderman (Plessey). Dr. Reeson also offered to translate a few references which were written in French.

Last, but by no means least, I would like to thank Sujata, Chris, Louise and Martin for helping to preserve my sanity.

Next time, I'll be sure to have one I prepared earlier!